



2007

INTEGRATED APPROACH TO THE SUPERPLASTIC FORMING OF MAGNESIUM ALLOYS

Fadi K. Abu-Farha

University of Kentucky, rurouni@engr.uky.edu

[Click here to let us know how access to this document benefits you.](#)

Recommended Citation

Abu-Farha, Fadi K., "INTEGRATED APPROACH TO THE SUPERPLASTIC FORMING OF MAGNESIUM ALLOYS" (2007).
University of Kentucky Doctoral Dissertations. 493.
https://uknowledge.uky.edu/gradschool_diss/493

This Dissertation is brought to you for free and open access by the Graduate School at UKnowledge. It has been accepted for inclusion in University of Kentucky Doctoral Dissertations by an authorized administrator of UKnowledge. For more information, please contact UKnowledge@lsv.uky.edu.

ABSTRACT OF DISSERTATION

Fadi K. Abu-Farha

The Graduate School
University of Kentucky

2007

INTEGRATED APPROACH TO THE SUPERPLASTIC FORMING OF
MAGNESIUM ALLOYS

ABSTRACT OF DISSERTATION

A dissertation submitted in partial fulfilment of the
requirements for the degree of Doctor of Philosophy in the
College of Engineering at the University of Kentucky

By
Fadi K. Abu-Farha

Director: Dr. Marwan K. Khraisheh, Professor of Mechanical Engineering

2007

Copyright © Fadi K. Abu-Farha 2007

ABSTRACT OF DISSERTATION

INTEGRATED APPROACH TO THE SUPERPLASTIC FORMING OF MAGNESIUM ALLOYS

The economical and environmental issues associated with fossil fuels have been urging the automotive industry to cut the fuel consumption and exhaust emission levels, mainly by reducing the weight of vehicles. However, customers' increasing demands for safer, more powerful and luxurious vehicles have been adding more weight to the various categories of vehicles, even the smallest ones. Leading car manufacturers have shown that significant weight reduction, yet satisfying the growing demands of customers, would not be feasible without the extensive use of lightweight materials.

Magnesium is the lightest constructional metal on earth, offering a great potential for weight-savings. However, magnesium and its alloys exhibit inferior ductility at low temperatures, limiting their practical sheet metal applications. Interestingly, some magnesium alloys exhibit superplastic behaviour at elevated temperatures; mirrored by the extraordinarily large ductility, surpassing that of conventional steels and aluminium alloys. Superplastic forming technique is the process used to form materials of such nature, having the ability to deliver highly-profiled, yet very uniform sheet-metal products, in one single stage. Despite the several attractions, the technique is not widely-used because of a number of issues and obstacles.

This study aims at advancing the superplastic forming technique, and offering it as an efficient process for broader utilisation of magnesium alloys for sheet metal applications. The focus is primarily directed to the AZ31 magnesium alloy, since it is commercially available in sheet form, possesses good mechanical properties and high strength/weight ratio. A general multi-axial anisotropic microstructure-based constitutive model that describes the deformation behaviour during superplastic forming is first developed. To calibrate the model for the AZ31 magnesium alloy, systematic uniaxial and biaxial stretching tests are carried out over wide-ranging conditions, using

specially-designed fixtures. In a collaborative effort thereafter, the calibrated constitutive model is fed into a FE code in conjunction with a stability criterion, in order to accurately simulate, control and ultimately optimise the superplastic forming process. Special pneumatic bulge forming setup is used to validate some proposed optimisation schemes, by forming sheets into dies of various geometries. Finally, the material's post-superplastic-forming properties are investigated systematically, based on geometrical, mechanical and microstructural measures.

KEYWORDS: Superplastic Forming of the AZ31 Magnesium Alloy, Constitutive Modelling, Elevated Temperature Mechanical Testing, Pneumatic Bulge Forming, Post-Forming Analysis

Fadi K. Abu-Farha

15th May, 2007

INTEGRATED APPROACH TO THE SUPERPLASTIC FORMING OF
MAGNESIUM ALLOYS

By

Fadi K. Abu-Farha

Dr. Marwan Khraisheh
Director of Dissertation

Dr. Scott Stephens
Director of Graduate Studies

15th May, 2007

DISSERTATION

Fadi K. Abu-Farha

The Graduate School
University of Kentucky

2007

INTEGRATED APPROACH TO THE SUPERPLASTIC FORMING OF
MAGNESIUM ALLOYS

DISSERTATION

A dissertation submitted in partial fulfilment of the
requirements for the degree of Doctor of Philosophy in the
College of Engineering at the University of Kentucky

By
Fadi K. Abu-Farha

Director: Dr. Marwan K. Khraisheh, Professor of Mechanical Engineering

2007

Copyright © Fadi K. Abu-Farha 2007

Dedicated To:

My beloved family; for the years of patience & support

*Those who have influenced my life; Rurouni, Simone, Wagner & Marwan
Khraisheh*

*The United States of America; for offering me this magnificent opportunity, & for
the enormous kindness of its people*

Germany; the unsurpassed motivation of my life

ACKNOWLEDGEMENTS

I would like to express my gratitude to all who have assisted me, in anyway, in accomplishing this work:

My advisor, Dr. Marwan Khraisheh; for the enormous help, support, guidance, patience and encouragement throughout those five years, and without whom this work would not be what it is. RJ Robinson, and his team; who did not spare any effort in assisting me, in every possible way. Larry crocket, Richard Anderson and Mark Smith; who have machined hundreds of parts and thousands of test specimens. Mohammad Nazzal; for the collaborative effort in some parts of this work. Nathir Rawashdeh; for his assistance in building some of the experimental setups. Daniel Bortz; who instructed and assisted me in the microstructural examination. Center for Manufacturing staff, for their assistance, support, courtesy and kindness.

To you all; I cannot thank you enough.

TABLE OF CONTENTS

TABLE OF CONTENTS.....	iv
LIST OF TABLES.....	viii
LIST OF FIGURES	ix
CHAPTER ONE: PREFACE	1
1.1 Problem Definition.....	1
1.2 Motivations.....	2
1.2.1 Modelling Issues.....	2
1.2.2 Material Formability Issues.....	3
1.2.3 Testing Issues	3
1.2.4 Forming Issues.....	4
1.2.5 Post-Forming Issues.....	4
1.3 Objective and Methodology.....	4
1.4 Dissertation Layout	6
CHAPTER TWO: INTRODUCTION.....	8
2.1 Superplasticity and Superplastic Forming Technique	8
2.1.1 Definition and Historical Overview.....	8
2.1.2 Requirements for Superplasticity.....	9
2.1.3 Mechanical Aspects of Superplastic Deformation	10
2.1.4 Superplastic Materials	12
2.1.5 Superplastic Forming Technique (SPF).....	12
2.1.6 Current Applications of SPF	14
2.2 Light Weighting	17
2.3 Magnesium	19
2.3.1 General Overview.....	19
2.3.2 Magnesium’s History in the Automotive Industry.....	20
2.3.3 Advantages	21
2.3.4 Problems and Limitations	22
2.3.4.1 Formability Issues.....	22
2.3.4.2 Material’s Mechanical and other Properties.....	22
2.3.4.3 Components’ Mechanical Properties:.....	23
2.3.4.4 Cost issues.....	23
2.3.4.5 Raw Material Supply Issues	24
2.3.4.6 Alloy Development Issues	24
2.3.4.7 SF ₆ Shielding Gas Issues.....	24
2.3.5 Current Applications	24
2.3.5.1 Power Train	25
2.3.5.2 Interior	25
2.3.5.3 Chassis.....	26
2.3.5.4 Body Structure.....	27

CHAPTER THREE: GENERALISED CONSTITUTIVE MODELLING OF SUPERPLASTIC DEFORMATION.....	30
3.1 General Multiaxial Constitutive Model.....	30
3.2 Anisotropic Yield Function.....	32
3.3 Evolution of Microstructure and Internal Variables.....	34
3.3.1 Grain Growth.....	34
3.3.2 Cavitation.....	35
3.3.3 Isotropic and Kinematic Hardening.....	36
3.3.5 Anisotropic Angle.....	37
3.4 Model Reduction to Various Loading Cases.....	38
3.4.1 Uniaxial Simple Tension.....	38
3.4.2 Simple Shear.....	40
3.4.3 Combined Tension-Torsion.....	41
3.4.4 Biaxial Stretching.....	43
3.5 Model Validation under Various Loading Cases.....	45
3.5.1 Material Parameters.....	46
3.5.2 Simple Tension.....	49
3.5.3 Simple Shear.....	50
3.5.4 Combined Tension-Torsion.....	54
3.5.5 Biaxial Stretching.....	55
3.5.5.1 Stress/Strain Behaviour.....	56
3.5.5.2 Yield Surface.....	57
3.5.5.3 Bulge Forming.....	58
4. CHAPTER FOUR: DESIGN AND BUILDING OF EXPERIMENTAL SETUPS.....	64
4.1 Uniaxial Tensile Testing at Elevated Temperatures.....	64
4.1.1 Testing Machine and Heating Chamber.....	66
4.1.2 Standard Grips and Related Gripping Issues.....	67
4.1.2.1 Slippage.....	67
4.1.2.2 Imposed Twisting Torque.....	68
4.1.2.3 Material Flow.....	68
4.1.2.4 Gauge Length Issues.....	69
4.1.3 Modified Testing Grips.....	69
4.2 Effects of Testing Parameters on the Accuracy of Test Results.....	74
4.2.1 Heating Issues.....	75
4.2.1.1 Protecting the Specimen.....	75
4.2.1.2 Thermal Expansion.....	75
4.2.2 Effect of heating time on Stress/strain curves.....	76
4.2.3 Effect of Heat on Load Cell Measurements.....	79
4.2.4 Straining Mode; Constant Strain Rate vs Constant Speed.....	80
4.2.5 Testing Procedure.....	81
4.3 Pneumatic Bulge Forming at Elevated Temperatures.....	81
4.3.1 Controlled Pressurised Gas Line.....	82
4.3.2 Forming Die Assembly.....	82
4.4 Controlled Biaxial Testing at Elevated Temperatures.....	87

5. CHAPTER FIVE: TESTING AND CHARACTERISATION OF THE SUPERPLASTIC BEHAVIOUR IN THE AZ31 MAGNESIUM ALLOY.....	91
5.1 Properties of the As-Received Material.....	93
5.1.1 Initial Grain Size	93
5.1.2 Room Temperature Mechanical Properties	95
5.1.3 Initial (Planar) Anisotropy	96
5.2 High Temperature Tensile Testing and Superplastic Behaviour	98
5.2.1 High Temperature Anisotropy.....	98
5.2.2 Constant Strain Rate Uniaxial Tensile Tests	100
5.2.2.1 Mechanical Behaviour	100
5.2.2.2 Flow Stress.....	104
5.2.2.3 Fracture Strain.....	105
5.2.3 Strain Rate Jump Tests.....	106
5.2.3.1 Strain Rate Sensitivity Index m	106
5.2.3.2 Effect of Plastic Strain on m	109
5.2.3.3 Jump Test versus Slope of the Stress/Strain Rate Curve.....	110
5.3 High Temperature Biaxial Testing at Controlled Rates	111
6. CHAPTER SIX: MODELLING, SIMULATING AND OPTIMISING THE SUPERPLASTIC FORMING OF THE AZ31 MAGNESIUM ALLOY.....	118
6.1 Modelling the Material's Tensile Behaviour at 400 °C	119
6.1.1 Reduced Model	120
6.1.2 Grain Growth	121
6.1.2.1 Static Grain Growth	121
6.1.2.2 Dynamic Grain Growth	122
6.1.3 Cavitation	124
6.1.4 Model Calibration	127
6.2 Simulation of Superplastic Forming Using the Calibrated Model	129
6.2.1 Model Capabilities in Superplastic Forming of Simple Geometries ..	129
6.2.1.1 Analytical Expressions.....	129
6.2.1.2 Calibrated Model Combined with FE	132
6.2.2 Model Predictions in Superplastic Forming of Complex Geometries	134
6.3 Optimising the Superplastic Forming Process.	136
6.3.1 Optimisation in 1D	137
6.3.2 Optimisation in 2D	142
7. CHAPTER SEVEN: POST-SUPERPLASTIC FORMING ANALYSIS	148
7.1 General Approach.....	150
7.2 Detailed Investigation of Post-SPF in 1D at 400 °C	152
7.2.1 Superplastic deformation at 400C	152
7.2.2 Deformation Uniformity.....	153
7.2.3 RT Tensile Tests and Post-SPF Mechanical Properties.....	158
7.2.4 Post-SPF Mechanical Properties versus Microstructural Evolution ..	163
7.3 Post-SPF Mechanical Properties in 1D at Various Temperatures.....	165
7.4 Post-SPF Mechanical Properties in 2D at 400 °C	169

8. CHAPTER EIGHT: REMARKS AND FUTURE RECOMMENDATIONS....	173
8.1 Concluding Remarks.....	173
8.2 Importance and Contributions.....	174
8.3 Recommendations for Future Work.....	175
REFERENCES	176
VITA	186

LIST OF TABLES

<i>Table 3.1: A list of the material parameters for the modelled Pb-Sn alloy</i>	<i>48</i>
<i>Table 4.1: Percentage change in gauge length due to the thermal expansion ...</i>	<i>76</i>
<i>Table 4.2: Holding and heating times corresponding to various temperatures ...</i>	<i>79</i>
<i>Table 5.1: Chemical composition of the AZ31B-H24 magnesium alloy</i>	<i>93</i>
<i>Table 6.1: A summary of the calibration material parameters for the AZ31 magnesium alloy.....</i>	<i>128</i>
<i>Table 6.2: Forming time versus achieved bulge height following the three different forming pressure profiles</i>	<i>133</i>
<i>Table 6.3: Summary of the tensile tests at constant versus optimum variable strain rate loading paths</i>	<i>139</i>
<i>Table 6.4: Summary of the bulge forming experiments at constant versus optimum variable strain rate loading paths</i>	<i>144</i>
<i>Table 7.1: Summary of several studies on the post-superplastic forming properties of various superplastic alloys.....</i>	<i>149</i>

LIST OF FIGURES

<i>Figure 1.1: A schematic flow chart of the whole dissertation</i>	7
<i>Figure 2.1: Superplasticity in the Pb-Sn eutectic alloy pulled in tension at 140 °C to 4850% elongation [Pilling and Ridley 1989].....</i>	8
<i>Figure 2.2: A typical sigmoidal-shaped logarithmic stress/strain rate curve and the corresponding bell-shaped sensitivity curve for a superplastic material</i>	11
<i>Figure 2.3: Schematic of the superplastic blow forming technique</i>	13
<i>Figure 2.4: Superplastic forming used for aeroplane applications [Superform Aluminium] (a) Eclipse 500 Jet (b) Boeing 777 (c) Boeing 737.....</i>	15
<i>Figure 2.5: Superplastic forming used for automotive applications [Superform Aluminium] (a) Aston Martin Vanquish (b) Morgan Aero 8.....</i>	15
<i>Figure 2.6: Superplastic forming used for medical applications [Curtis 2005]</i>	16
<i>Figure 2.7: Superplastic forming used for art and architectural applications [Superform Aluminium]</i>	17
<i>Figure 2.8: (a) Energy consumption during full life cycle (b) Impact of vehicle weight on total fuel consumption [Jambor and Beyer 1997].....</i>	18
<i>Figure 2.9: Means for reducing fuel consumption [Mertz 2002]</i>	19
<i>Figure 2.10: Magnesium gear box housing [Friedrich and Schumann 2000].....</i>	25
<i>Figure 2.11: Magnesium seat frame for the SL-type, Mercedes Benz [Jambor and Beyer 1997]</i>	26
<i>Figure 2.12: (a) Steering column lock housing (b) sealing flange (c) Steering column [Mordike and Ebert 2001, Mertz 2002]</i>	26
<i>Figure 2.13: Magnesium die-cast fuel tank partition panel in the SLK type, Mercedes-Benz [Mertz 2002].....</i>	27
<i>Figure 2.14: CL-type magnesium casting door inner part [Burk and Vogel 2002]</i>	28
<i>Figure 2.15: Magnesium extrusions [Mertz 2002].....</i>	29
<i>Figure 3.1: Anisotropic angle ϕ with respect to the reference axes x_i ($i = 1, 2$ & 3)</i>	34
<i>Figure 3.2: Stresses and strains in the biaxial stretching loading case.....</i>	43
<i>Figure 3.3: Model-generated versus experimentally-constructed stress/strain rate sigmoidal curve for the Pb-Sn Alloy</i>	46
<i>Figure 3.4: Modelled grain growth at different strain rates for the Pb-Sn alloy ...</i>	47
<i>Figure 3.5: (a) Experimentally-obtained vs model-predicted stress/strain curves in simple tension (b) Effect of accounting for grain growth on the model capabilities</i>	49
<i>Figure 3.6: Effects of the initial anisotropic angle ϕ_0 on (a) Tensile stress (b) Back stress (kinematic hardening)</i>	50

Figure 3.7: Experimentally-obtained versus model-predicted stress/strain curves in pure torsion tests	51
Figure 3.8: Induced axial stresses (a) Experimentally-measured in fixed-end torsion tests (b) Model-generated	51
Figure 3.9: (a) Evolution of anisotropic angle ϕ (b) Model-generated induced axial stresses assuming a fixed anisotropic angle.....	52
Figure 3.10: Effect of various parameters on the evolution of ϕ (a) ϕ_0 (b) β (c) μ (d) ξ	52
Figure 3.11: Effect of various parameters on shear stresses (a) ϕ_0 (b) β (c) μ (d) ξ	53
Figure 3.12: Effect of various parameters on induced axial stresses (a) ϕ_0 (b) β (c) μ (d) ξ	54
Figure 3.13: Anisotropic model-generated yield surface compared to experiments and isotropic von-Mises at (a) $1 \times 10^{-3} \text{ s}^{-1}$ (b) $6.5 \times 10^{-4} \text{ s}^{-1}$	54
Figure 3.14: Effect of various parameters on yield surfaces (a) ϕ_0 (b) c_1 (c) c_2 (d) c_3	55
Figure 3.15: Model-predicted stress/strain curves for different biaxial strain ratios k (a) σ_{11} vs ϵ_{11} (b) σ_{22} vs ϵ_{22}	56
Figure 3.16: Anisotropic yield surfaces for different ϕ_0 values compared to von-Mises	57
Figure 3.17: Effect of k on the evolution of ϕ	58
Figure 3.18: Schematic of the free bulge forming of circular sheets	58
Figure 3.19: The effect of anisotropy and grain growth on the pressure–time profile for (a) Strain-balanced biaxial stretching [$k = 1$] (b) Stress-balanced biaxial stretching [$\rho = 1$] (c) Comparison between (a) & (b)	61
Figure 3.20: Expected shapes of a bulged circular sheet for different values of k (a) Incomplete hemisphere [$k < 1$] (b) Perfect hemisphere [$k = 1$] (c) Over-bulged hemisphere [$k > 1$]	62
Figure 3.21: Longitudinal and transverse cross sections of the three domes (a) $k < 1$ (b) $k = 1$ (c) $k > 1$	63
Figure 4.1: Load frame equipped with a heating chamber.....	66
Figure 4.2: INSTRON grip and a simple-geometry test specimen	67
Figure 4.3: Slippage marks on a test specimen.....	68
Figure 4.4: Material flow from the grip region into the gauge length region	68
Figure 4.5: (a) Geometrically defined gauge length [H_0] (b) Grip inserts' edges inside the geometrical gauge length [$H_1 < H_0$] (c) Grip inserts' edges outside the geometrical gauge length [$H_2 > H_0$] (d) Combination of (b) and (c).....	69
Figure 4.6: Type-I grips for high temperature tensile testing	71
Figure 4.7: Dimensions of type-I tensile test specimen	72
Figure 4.8: Type-II grips for high temperature tensile testing (for post-SPF in particular).....	73
Figure 4.9: Dimensions of type-II tensile test specimen	74

Figure 4.10: Different orientations for machining test specimens with respect to the rolling direction of the sheet.....	74
Figure 4.11: Effect of holding time on stress/strain curves at 400 °C and (a) $1 \times 10^{-3} \text{ s}^{-1}$ (b) $5 \times 10^{-4} \text{ s}^{-1}$	78
Figure 4.12: Effect of heat on load cell reading (a) Detected by the stress/strain curve at 375 °C and $1 \times 10^{-5} \text{ s}^{-1}$ (b) Measured directly in a zero-load test at 500 °C	80
Figure 4.13: (a) Difference between constant strain rate and constant cross-head speed tests (b) Deviation from constant strain rate when applying constant cross-head speed.....	81
Figure 4.14: Controlled pressurised gas lines with 120 & 6000 psi capacities ...	83
Figure 4.15: Schematic of type-I forming die assembly	83
Figure 4.16: Type-I forming die assembly with different die geometries.....	84
Figure 4.17: Examples for magnesium sheets formed into different shapes using type-I forming dies	84
Figure 4.18: Schematic of type-II forming die assembly	85
Figure 4.19: Type-II forming die assembly with different die geometries.....	86
Figure 4.20: Examples for magnesium sheets formed into different shapes using type-II open elliptical forming dies.....	86
Figure 4.21: Biaxial testing fixture (a) CAD model (b) A photo	88
Figure 4.22: Biaxial testing fixture fitted to the INSTRON load frame	89
Figure 4.23: A cruciform-shaped test specimen for biaxial testing.....	90
Figure 5.1: Pictures of the grain structure for samples taken from the 1.65mm thick sheets (a) Cross section view (b) Top view.....	93
Figure 5.2: Software used for grain size measurement in a T-oriented sample taken from the 3.22 mm thick sheet (a) Photo of the microstructure (b) Captured grain boundaries (c) Captured grains (d) Results	94
Figure 5.3: Stress/strain curves for six 0° oriented specimens tested at RT and 1.5 mm/s (a) A test specimen before and after failure	96
Figure 5.4: Stress/strain curves at room temperature and various strain rates for (a) 0° (b) 45° (c) 90° oriented specimens.....	97
Figure 5.5: Stress/strain curves for 0°, 45° and 90° oriented specimens indicating RT initial anisotropy at (a) $5 \times 10^{-4} \text{ s}^{-1}$ (b) $2 \times 10^{-4} \text{ s}^{-1}$	97
Figure 5.6: Stress/strain curves for 0°, 45° and 90° oriented specimens at (a) 375 °C and $2 \times 10^{-4} \text{ s}^{-1}$ (b) 400 °C and $2 \times 10^{-4} \text{ s}^{-1}$ (c) 400 °C and $5 \times 10^{-5} \text{ s}^{-1}$	99
Figure 5.7: (a) Stress/strain curves for two tensile tests at 400 °C and $5 \times 10^{-5} \text{ s}^{-1}$ (b) A test specimen before and after testing	101
Figure 5.8: (a) Stress/strain curves for various strain rates at 400 °C (b) Corresponding deformed specimens (c) Extracted flow stress and fracture strain curves	101
Figure 5.9: Stress/strain curves for various strain rates at (a) 225 °C (b) 325 °C (c) 350 °C (d) 375 °C (e) 425 °C (f) and 450 °C	103

Figure 5.10: (a) Sigmoidal-shaped stress/strain rate curves at different temperatures (b) Flow stress versus temperature for various strain rates.....	104
Figure 5.11: (a) Fracture strain versus strain rate at different temperatures (b) Fracture strain versus temperature for various strain rates.....	105
Figure 5.12: (a) Stress/strain curves for two strain rate jump tests between 5×10^{-4} and 10^{-3} s^{-1} at $400 \text{ }^\circ\text{C}$ (b) Estimated strain rate sensitivity index values	106
Figure 5.13: (a) A complete set of strain rate jump tests at $400 \text{ }^\circ\text{C}$ (b) Corresponding strain rate sensitivity index curves for four different strains (c) Continuous and stepped averaged curves for m	107
Figure 5.14: Average strain rate sensitivity index m versus (a) Average strain rate (b) Temperature.....	108
Figure 5.15: Strain rate sensitivity index m at $400 \text{ }^\circ\text{C}$ versus (a) Average strain rate at different strains (b) Plastic strain at different strain rates....	110
Figure 5.16: (a) Sensitivity index m derived from the slope of the stress/strain rate curve at $400 \text{ }^\circ\text{C}$ (b) Comparison with the curve generated by strain rate jump tests	110
Figure 5.17: A heat gun used to produce localised heating inside the heating capsule	112
Figure 5.18: A calibration test specimen with two thermocouples for temperature measurement.....	112
Figure 5.19: Dimensions of the cruciform-shaped biaxial test specimen	113
Figure 5.20: localised deformation in the neck region between the centre region and one of the four specimen arms	114
Figure 5.21: A recess introduced to the centre region of the specimen.....	114
Figure 5.22: An example of a uniform biaxial deformation localised at the centre part of the test specimen (a) Before and after (b) Zoomed before (c) Zoomed after	115
Figure 5.23: Fracture taking place at the centre of the test specimen	116
Figure 5.24: Measured forces along the x and y axes of the test specimen	117
Figure 6.1: Selected photos for the grain-structure of the AZ31 mg alloy taken after heating at $400 \text{ }^\circ\text{C}$ for (a) 75 (b) and 252 minutes.....	121
Figure 6.2: Static grain growth curve at $400 \text{ }^\circ\text{C}$ (a) Normal time scale (b) Logarithmic time scale	122
Figure 6.3: Selected photos for the grain-structure of the material taken after straining at $1 \times 10^{-4} \text{ s}^{-1}$ and $400 \text{ }^\circ\text{C}$ to different strains (a) 0.3 (b) 0.7 (c) 1.1.....	123
Figure 6.4: Dynamic grain growth curve at $400 \text{ }^\circ\text{C}$	124
Figure 6.5: Evident cavitation in a specimen deformed at $400 \text{ }^\circ\text{C}$ and $5 \times 10^{-5} \text{ s}^{-1}$	124
Figure 6.6: Selected photos for cavitation in the material taken after straining at $400 \text{ }^\circ\text{C}$ to different strains (a) 0.5 (b) 1.15 (c) 1.45 (d) 1.6 (e) 1.68 (f) 1.75.....	125

Figure 6.7: Software used for area fraction of voids' measurement in a sample taken from a specimen strained at $1 \times 10^{-4} \text{ s}^{-1}$ and 400 °C (a) Photo of the microstructure (b) Captured voids (c) Results.....	126
Figure 6.8: Area fraction of voids versus strain at 400 °C.....	127
Figure 6.9: Model-predicted versus experimentally-obtained stress/strain curves at 400 °C.....	128
Figure 6.10: Schematic of the free bulge forming of circular sheets.....	130
Figure 6.11: Forming pressure-time profiles for the AZ31 mg alloy based on (a) Dutta and Mukherjee [1992] (b) Banabic et al. [2001].....	131
Figure 6.12: Forming pressure-time profile generated by the calibrated model in comparison with two analytical models.....	132
Figure 6.13: Formed domes using the three different forming pressure profiles.....	133
Figure 6.14: Formed domes using the three different forming pressure profiles.....	134
Figure 6.15: Pressure-time profiles for forming at $2 \times 10^{-4} \text{ s}^{-1}$ into multi-deep cylindrical dies (b) The corresponding formed parts.....	135
Figure 6.16: Optimum forming path for the AZ31 magnesium alloy at 400 °C..	137
Figure 6.17: (a) Continuous versus approximated variable strain rate loading (forming) path (b) Corresponding variable speed loading path.....	138
Figure 6.18: Stress/strain curve based on the optimum loading path compared to those corresponding to constant strain rates.....	138
Figure 6.19: (a) Specimens deformed to 250% at various strain rates (b) Width distribution (c) Thickness distribution along each specimen.....	140
Figure 6.20: (a) Specimens deformed to 300% at various strain rates (b) Width distribution (c) Thickness distribution along each specimen.....	141
Figure 6.21: (a) Specimens deformed to 350% at various strain rates (b) Width distribution (c) Thickness distribution along each specimen.....	142
Figure 6.22: Forming pressure-time profiles generated for constant versus optimum variable strain rate loading paths.....	143
Figure 6.23: (a) Dome profile (b) Thickness distribution along the perimeter of sheets formed following constant versus optimum strain rate paths to 31.75 mm height.....	145
Figure 6.24: (a) Dome profile (b) Thickness distribution along the perimeter of sheets formed following constant vs optimum strain rate paths to 35.5 mm height.....	146
Figure 6.25: (a) Domes formed at different strain rate paths to 35.5 mm height (b) A section showing thickness variation along each dome.....	146
Figure 7.1: Schematic approach to investigating the post superplastic forming properties.....	151
Figure 7.2: (a) Interrupted stress-strain curves of specimens strained at $2 \times 10^{-4} \text{ s}^{-1}$ to different strain values (b) The corresponding deformed specimens.....	153

Figure 7.3: (a) Schematic of the deformed specimen (b) Normalised width and (c) Thickness distributions along specimens strained at $5 \times 10^{-4} \text{ s}^{-1}$ to various strains.....	154
Figure 7.4: (a) Normalised width and (c) Thickness distributions along specimens strained to 110% at various strain rates.....	155
Figure 7.5: Maximum thinning at various combinations of strain and strain rate in terms of (a) Width (b) Thickness.....	156
Figure 7.6: 2D Maps for maximum thinning at various combinations of strain and strain rate in terms of (a) Width (c) Thickness	157
Figure 7.7: Post-SPF analysis mirrored by the changes underwent by test specimens.....	158
Figure 7.8: RT Stress/strain curves for specimens already superplastically deformed (a) At the same strain rate (b) To the same strain limit..	159
Figure 7.9: Normalised post-SPF mechanical properties for various strains and strain rates (a) Yield strength (b) Tensile strength (c) Fracture strain	160
Figure 7.10: 3D post-SPF maps for various strains and strain rates (a) Ultimate tensile strength (b) Fracture strain	162
Figure 7.11: (a) Effect of heating on the post-SPF yield strength (b) Cavitation versus post-SPF tensile strength and fracture strain	164
Figure 7.12: Specimens deformed at $5 \times 10^{-4} \text{ s}^{-1}$ to different strain values at $350 \text{ }^\circ\text{C}$	165
Figure 7.13: Maximum thinning at various combinations of strain and temperature in terms of (a) Width (b) Thickness	166
Figure 7.14: Maximum thinning map at various strains and temperatures	167
Figure 7.15: Normalised post-SPF mechanical properties for various strains and temperatures (a) Yield strength (b) Tensile strength (c) Fracture strain.....	168
Figure 7.16: 3D post-SPF fracture strain map for various strains and temperatures.....	169
Figure 7.17: Post-SPF analysis in 2D mirrored by the changes underwent by test sheets	170
Figure 7.18: (a) A schematic plot for a tensile specimen machined out of the formed cup (b) Thickness strains corresponding to the three different cup heights	171
Figure 7.19: Effect of heating and strain on post-SPF mechanical properties in 2D	171

CHAPTER ONE: PREFACE

1.1 Problem Definition

Environmental and economical issues, embodied by the increasing prices of exhaustible fossil fuels, lack of feasible alternative fuel sources, pollution and global warming, have been the source of a continuously growing pressure on the automotive industry to cut fuel consumption and exhaust emission levels. Among the different proposed means to achieve such cuts, reduction of mass remains the most influential and least costly one, provided that large cuts of 20-40% are realised [Cole 1999]. Leading automotive manufacturers have shown in separate studies that more than 50% of fuel consumption is mass dependent [Engelhart and Moedel 1999, Jambor and Beyer 1997, Schumann and Friedrich 1998]. Audi showed that a 6% drop in fuel consumption could be achieved by a 10% mass drop [Engelhart and Moedel 1999, Barnreiter and Eichberg 1997]. However, customers' increasing demands for safer, more powerful and luxurious vehicles have been adding more weight to the various categories of vehicles, even the smallest ones, making the realisation of lighter cars even more difficult and challenging. Therefore, significant weight reduction would not be feasible without the extensive use of light yet strong-enough materials; lightweight materials [Dick 1999, Burk and Vogel 2002, Mertz 2002, Holste et al. 2002, Friedrich and Schumann 2000, Jambor and Beyer 1997, Schumann and Friedrich 1998].

Magnesium is the lightest constructional metal on earth; a fact that explains the great attention it has been receiving over the past decade. With its low density, magnesium is 35% lighter than aluminium and 78% lighter than steel. These numbers accentuate the great weight-saving potentials promised by the metal (*and its alloys*), if it could be successfully utilised in particular areas. In fact, several examples of magnesium auto parts that have evolved recently prove the initial signs of such promising potentials [Jambor and Beyer 1997, Friedrich and Schumann 2001, Burk and Vogel 2002, Aghion et al. 2001]. Despite that, the success magnesium has been living so far is confined to die casting, and the aforementioned examples fall primarily into the cast-components' category. Unless magnesium's usage is expanded to cover other areas, mainly sheet metal body panels, feasible weight reduction will be quite limited. The problem is; magnesium (*and its alloys*) exhibits inferior ductility at room temperature due to its hexagonal close-packed (*HCP*) crystal structure, which continues to hinder such an expansion. In fact, that's why exploitation of magnesium is practically paralysed, and its sheet metal applications are hardly in existence!

Surprisingly, several magnesium alloys exhibit extraordinarily enhanced tensile ductility at elevated temperatures; a phenomenon known as superplasticity. This phenomenon has gained a lot of interest over the past few decades, and was put into practice to form several titanium and aluminium alloys

by means of the superplastic forming (*SPF*) technique [Sanders 2001, Osada 1997, Bonet et al. 2000]. The technique offers several advantages over conventional forming practices; the ability to produce rather complicated shapes from hard-to-form metals in one single step, is definitely the most attractive of all. And as magnesium's feeble formability dampens the hopes, the SPF technique brings new possibilities and opens more doors for magnesium's use in sheet metal applications.

Expectedly, this technique has been confronted by a number of obstacles and issues that hindered its widespread use on a larger scale; the most critical of all is the limited predictive capabilities of deformation and failure. In other words, there is a lack of accurate models that can describe the behaviour of superplastic materials during deformation and thence predict its failure. This lack has been mirrored practically by the uncontrolled forming practices, where most SPF operations are carried out by trial and error routines. And since superplastic deformation is rate dependent, it is a common practice to avoid premature failure by forming at lower rates, which as a consequence, makes the SPF technique a rather slow forming process.

As it stands, the SPF technique has proven to be an efficient cost-worthy process in forming various components for aerospace and medical applications [Sanders, 1998; Kistner, 1998; Piltch et al, 1998; Curtis, 2001]. But for the highly competitive automotive sector, for instance, where production rate is of a prime interest, problems related to SPF need to be tackled, if the process is to get a chance for forming automotive sheet-metal components.

1.2 Motivations

The superplastic forming technique seems to go hand-in-glove with lightweight alloys; magnesium alloys in particular. The limited room temperature formability and the inability of conventional processes to effectively form these alloys uniquely position the SPF technique to become the process of choices in the future. The superior formability associated with SPF offers a chance to take magnesium to whole new level. But for this magnesium/SPF partnership to succeed, several issues associated to both sides need to be tackled.

1.2.1 Modelling Issues

There is a general lack of constitutive models that has the ability to describe the behaviour of different superplastic materials, at various forming conditions. Most of the available modelling efforts:

- i. Are based on the uniaxial loading case, which does not represent the state of loading during actual superplastic forming practices [Hamilton et al. 1991, Johnson et al. 1993].
- ii. Assume isotropic behaviour, ignoring the possibility of initial and/or deformation-induced anisotropy [Dutta and Mukherjee 1992].
- iii. Do not account for microstructural evolution; though heating combined with large plastic strains suggest the possibility of significant changes in the microstructure [Khraisheh et al. 1997].

Despite the fact that the aforementioned points were studied separately by different investigators, there is no available work that combines all of these aspects together.

1.2.2 Material Formability Issues

Several magnesium alloys behave superplastically at elevated temperatures, yet the alloy of choice should satisfy certain criteria for potential use in structural sheet-metal, automotive for instance, applications. The AZ31 is one such alloy; commercially available in sheet form, offers very good room temperature mechanical properties, and its strength-to-weight ratio is higher than many competitive steel and aluminium alloys [Friedrich and Schumann 2000]. To model and characterise the superplastic behaviour of this alloy requires a large number of diverse tests (*both mechanical and microstructural*), covering wide ranges of forming conditions. Unfortunately, investigators' efforts and therefore the available experimental data on this alloy are scattered. There is a need for a systematic work to establish a comprehensive quantitative database of the alloy's superplastic behaviour.

1.2.3 Testing Issues

Just like modelling, most testing efforts in superplastic studies are confined to the uniaxial loading case. Better understanding of the material behaviour in actual superplastic forming operations requires other multiaxial tests, biaxial stretching at the very least. And though gas bulge forming has been used to simulate such condition [Atkinson 1997, Dutta and Mukherjee 1992, Carrino and Giuliano 1997, Ding et al. 1997], many limitations, such as the control of deformation and relating stresses to strains, make it unsatisfactory in this regard.

On the other hand, it is quite surprising that there are no available ASTM testing standards for studying the behaviour of superplastic materials! Since superplasticity is usually achieved at elevated temperatures, it has been a common practice to follow the guidelines offered by available standards on

elevated temperature tensile testing, like the ASTM E21 [2003]. However, there are so many specific issues, particularly associated with superplastic materials, which were not addressed by such standards. The lack of standards makes it hard to compile experimental data on any specific alloy from different investigators.

1.2.4 Forming Issues

The vast majority of actual superplastic forming operations is carried out by trial and error routines, where the different part geometries are formed by applying randomly chosen pressure-time profiles. This lack of controlling capabilities is particularly critical in superplasticity because of its deformation rate dependence. Consequently, efforts to minimise thinning and/or prevent failure usually conclude in using reduced pressure levels, leading to slow forming. There is a vital need to control the deformation rate during superplastic forming practices, and thereafter, optimise the forming process in order to reduce the relatively-high forming times.

1.2.5 Post-Forming Issues

The issue of post-forming material properties has been generally ignored, not only in superplastic forming studies, but in most metal forming processes. However, this issue is particularly critical in the case of SPF because of the large plastic strains, the exposure to elevated temperatures for prolonged periods of time, and the significant microstructural changes during deformation. Despite that, there are only a few available post-superplastic forming (*post-SPF*) studies, targeting mainly aluminium and titanium alloys over narrow ranges of forming conditions [Wisbey et al. 1993, Cope et al. 1987]. There are no available studies on the post-superplastic forming properties of any magnesium alloy, the AZ31 in particular.

1.3 Objective and Methodology

The overall objective (*goal*) of this work is to advance the superplastic forming technique to effectively form magnesium alloys, the AZ31 in particular, for potential sheet metal applications. This objective will be achieved by the following:

- I. Develop a multi-axial constitutive model that has the ability to accurately capture the behaviour of superplastic materials during deformation. The model is to be based on the continuum theory of viscoplasticity, employ an anisotropic dynamic yield function, and account for microstructural changes within the material; namely grain growth and cavitation.
- II. Design an appropriate testing methodology that specifically suits superplastic materials. The methodology should comprehensively and adequately cover issues related to testing apparatus, specimen geometry, detailed experimental procedures and data measurements.
- III. Characterise the superplastic behaviour of the AZ31 magnesium alloy quantitatively, by establishing a wide-ranging comprehensive database of its deformation aspects. Such characterisation requires mechanical testing followed by microstructural examination, covering wide ranges of forming temperatures and loading strain rates.
- IV. Employ the superplastic bulge forming technique to form AZ31 magnesium sheets into different geometries, at various operating conditions, based on specific optimisation forming schemes. This task will be carried out in collaboration with a fellow student (*M. Nazza*), who is working on stability analysis and finite element simulation of superplastic forming. These optimum forming schemes will be generated by combining the developed constitutive model with a modified stability criterion in a finite element code, followed by actual forming practices in order to validate the optimisation approach.
- V. Investigate the post-superplastic forming properties of the AZ31 magnesium alloy systematically, covering wide ranges of superplastic forming conditions. Material properties following uniaxial and biaxial superplastic deformation are to be evaluated, in order to quantify the changes in the mechanical and microstructural properties in reference to those of the as-received material.

The AZ31 magnesium alloy is the focus of this study for several reasons:

- i. Commercially available in sheet form
- ii. Good room-temperature mechanical properties
- iii. High strength-to-weight ratio compared to many competitive steel and aluminium alloys
- iv. Exhibits superplastic behaviour at elevated temperatures

1.4 Dissertation Layout

After describing the general problem, and identifying the specific issues that need to be investigated, several steps were then proposed to tackle those issues, and therefore help solving the problem. The following chapters in this dissertation present the details of the work that has been done to achieve that.

Following the preface, an introductory chapter (*two*) provides some background information about both the superplastic forming technique and magnesium separately.

Chapter three deals with constitutive modelling of superplastic deformation. A general multiaxial constitutive model based on the theory of viscoplasticity, and incorporating both microstructural features and anisotropy, is developed, and its capabilities are thence tested at different loading conditions.

For the mechanical tests that will be carried out to study the superplastic behaviour of the AZ31 magnesium alloy, the details on the design and building of the experimental setups, the experimental procedures to conduct these tests, are all presented in chapter four. Also, due to the lack of accurate guiding standards on the issue, a closer look on the commonly-ignored testing issues in superplasticity is given in a specific section of the chapter.

In characterising the superplastic behaviour of the AZ31 magnesium alloy, uniaxial tensile tests covering wide ranges of temperatures and strain rates are carried out; the results of which are discussed in chapter five. The preliminary results of the effort to study the material's behaviour in biaxial stretching are also presented.

The focus in chapters six is directed towards a selected optimum superplastic forming temperature, where the capabilities of the model presented earlier in chapter three are tested again, but using the AZ31 magnesium alloy instead. The details of a collaborative effort aiming at controlling and thence optimising the superplastic forming process are presented with experimental validation in both simple tension and bulge forming.

After modelling, testing and optimising the superplastic forming of the AZ31 magnesium alloy, chapter seven is dedicated to investigating the issue of its post-superplastic forming properties.

Finally, the concluding remarks and major contributions by this work, in addition to some recommendations for future work, are all listed in chapter eight.

At the end, the overall picture of “what and how” this work is trying to achieve, is presented schematically by the flow chart describing the whole dissertation, shown in figure 1.1.

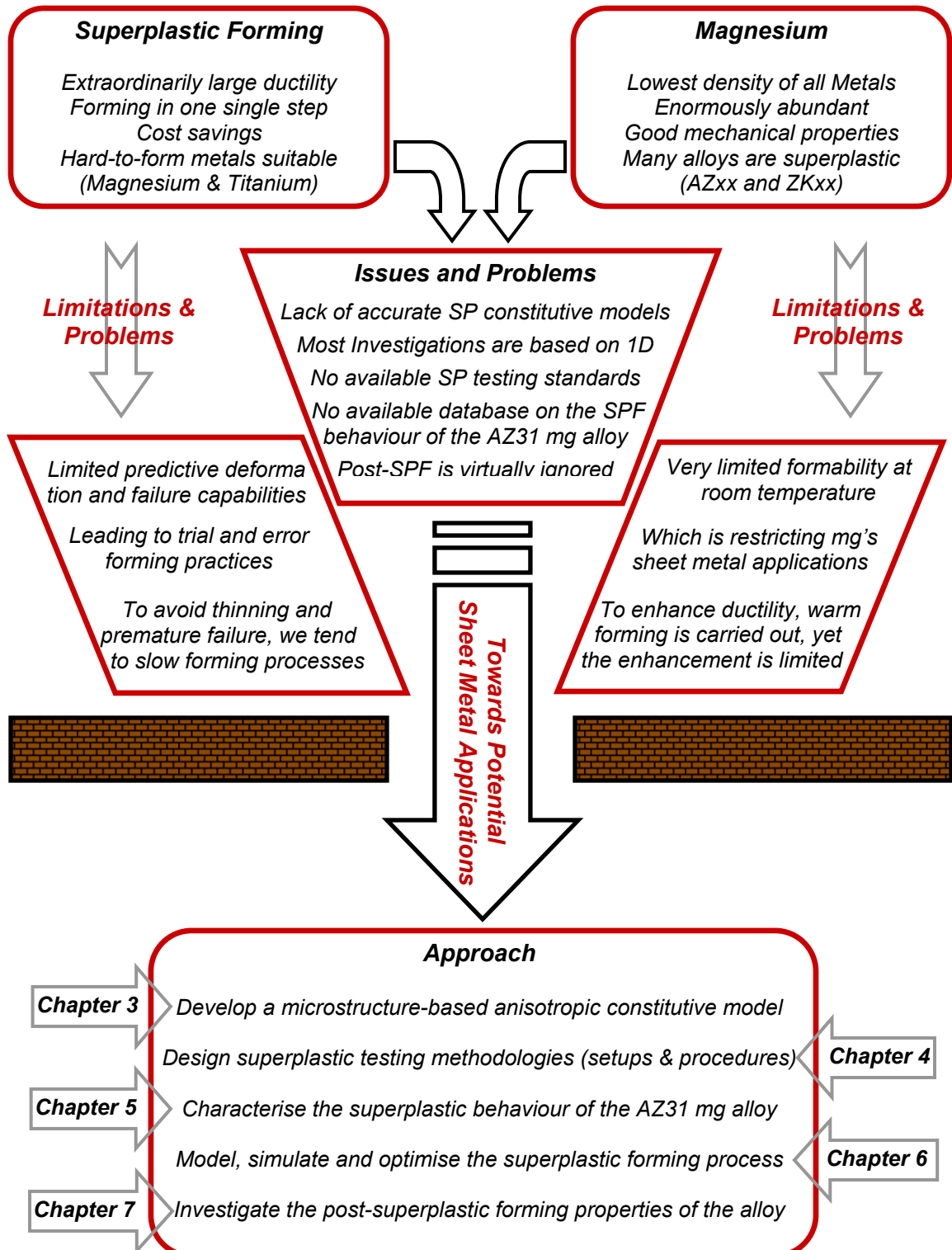


Figure 1.1: A schematic flow chart of the whole dissertation

CHAPTER TWO: INTRODUCTION

In this chapter, some background information about the main topics of this work is presented; superplasticity and the superplastic forming technique, lightweight materials and lightweight structures and the need for it in the automotive sector, and finally magnesium alloys as the main target with highest potentials in the whole family of lightweight materials.

2.1 Superplasticity and Superplastic Forming Technique

2.1.1 Definition and Historical Overview

Superplastic materials are unique class of polycrystalline solids that have the ability to undergo extraordinarily uniform strains prior to failure. For deformation in simple tension, an elongation in excess of 200% is usually indicative of superplasticity. Several materials of this class can attain extensions greater than 1000%; the highest elongation reported for a Pb-Sn eutectic alloy was 4850%, as shown in figure 2.1 [Ahmed and Langdon 1977, Pilling and Ridley 1989].

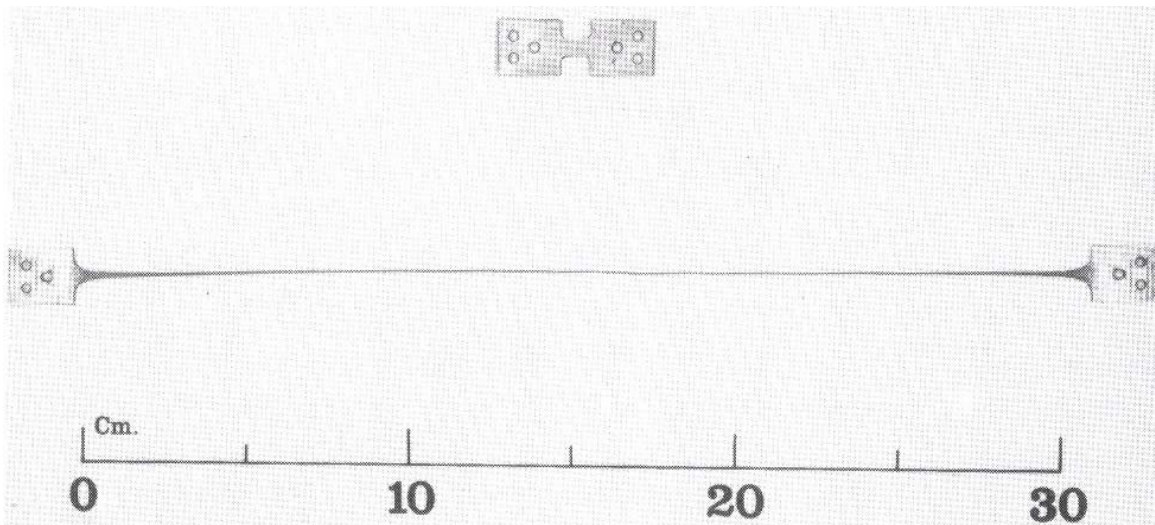


Figure 2.1: Superplasticity in the Pb-Sn eutectic alloy pulled in tension at 140 °C to 4850% elongation [Pilling and Ridley 1989]

Historically, it is not clear where the first observation of superplasticity was made. Some presume that superplasticity was first observed in USSR, and others say that it was in the UK. Whether here or there, it is believed that those early observations of this phenomenon were made in the early 1920's. The most

spectacular of the earlier observations was that made by Pearson in 1934, where he reported a tensile elongation of 1950% without failure in a Bi-Sn eutectic alloy [Pearson 1934]. After those early observations, there was little interest in this phenomenon in the western world, and the whole issue of superplasticity was regarded as a laboratory curiosity. Nevertheless, studies were carried out in the USSR, and the term superplasticity was given by Bochvar and Sviderskaya in 1945, when they were studying the extended ductility observed in Zn-Al alloys [Pilling and Ridley 1989].

After the Second World War, superplasticity was revived in the western world, and extensive studies started to take place on different scales. Most of that research work was done in the late 60's and early 70's. Many years later, superplasticity started to gain the interest in industry, and parts in different applications started to be produced by the superplastic forming (*SPF*) technique.

Nowadays, the interest in this phenomenon and its forming technique is growing up, and continues to gain more and more potential. Large amount of literature is available, and research activities are expanding more to cover the various aspects of superplasticity; in addition, larger numbers of different parts are being produced by the superplastic forming technique. However, and despite the advances that have been achieved so far, it will be a certain period of time before this forming technique is brought into commercial use.

2.1.2 Requirements for Superplasticity

Three main requirements are generally needed to achieve superplastic behaviour in the material:

1. Fine and Stable Grain Structure:

Generally speaking, grain structure with average grain size of less than 10 μm is usually required to attain superplasticity. As it will be shown later, the dominant deformation mechanism in superplasticity is the accommodated grain boundary sliding. And so, the smaller the grains are, the easier for them to rotate and slide over each other, and accommodate larger strains before failure. It should be emphasised that 10 μm is not a critical limit above which superplasticity is not feasibly achieved, as diverse superplastic materials behave differently. In fact, superplasticity in some coarse-grained magnesium alloys had been reported [Liu et al. 2000, Wu and Liu 2002]. Yet, it can be generalised that the smaller the grain size is, the larger the deformation that can be attained before failure.

2. High Forming Temperature:

In a similar manner and as it is the case with grain size, different alloys behave differently in terms of forming temperature. But generally speaking,

superplasticity takes place at relatively elevated temperatures, usually above 50% the absolute melting point of the material. Some magnesium alloys, for instance, exhibit superplasticity at temperatures around that limit [Watanabe et al. 1999 & 2001]. As a rule of thumb, the higher the forming temperature, the larger the deformation can be attained before failure.

By combining the effects of both the grain size and temperature, it is generally known that the smaller the grain size, the lower the temperature than can be used to achieve superplasticity, and vice versa.

3. Controlled Rate of Deformation:

Superplasticity is often confined within a certain range of strain rates, typically between 1×10^{-5} and $1 \times 10^{-1} \text{ s}^{-1}$ [Padmanabhan et al. 2001]. To explain this, it is necessary to address some of the mechanical aspects of superplastic deformation, which is covered next.

2.1.3 Mechanical Aspects of Superplastic Deformation

The basic mechanical aspects of a superplastic material are the low flow stress and the high sensitivity of flow stress to strain rate. As it is known, rate independent materials at room temperature behave as rate-dependent ones at higher temperatures. And as it was mentioned before, one of the main requirements for superplastic flow is the relatively high temperature; accordingly, it is expected that superplastic materials behave in a rate-dependent manner.

The general expression for flow stress in a rate-dependent material is given in terms of the strain rate by the following simple relation:

$$\sigma = K\dot{\epsilon}^m \quad (2.1)$$

where σ is the flow stress, $\dot{\epsilon}$ is the strain rate, K is the strength coefficient, and m is the strain rate sensitivity index.

For a superplastic material, the value of m ranges between 0.3 and 0.7. The larger the value of this index, the more resistance the material has to necking, and so the higher the capability of the material to undergo large plastic deformation prior to failure. A typical logarithmic stress/strain rate curve for a superplastic material is shown in figure 2.2. The slope of this sigmoidal-shaped curve at any point represents (*merely an estimate for comparison*) the value of the strain rate sensitivity index m at that point.

Accordingly, the curve can be divided into three main regions where different microstructural mechanisms are believed to dominate the deformation behaviour. Superplasticity occurs only in region-II, where the strain rate

sensitivity index m has high values at moderate strain rates, which is accompanied by very large elongation. And unlike conventional materials, which rely on work hardening to develop neck resistance, superplastic materials achieve neck resistance because of the high strain rate sensitivity of flow stress. Although the deformation process in this region is not very well understood, it is believed that grain boundary sliding accompanied by diffusion or dislocation glide and climb is the dominant mechanism.

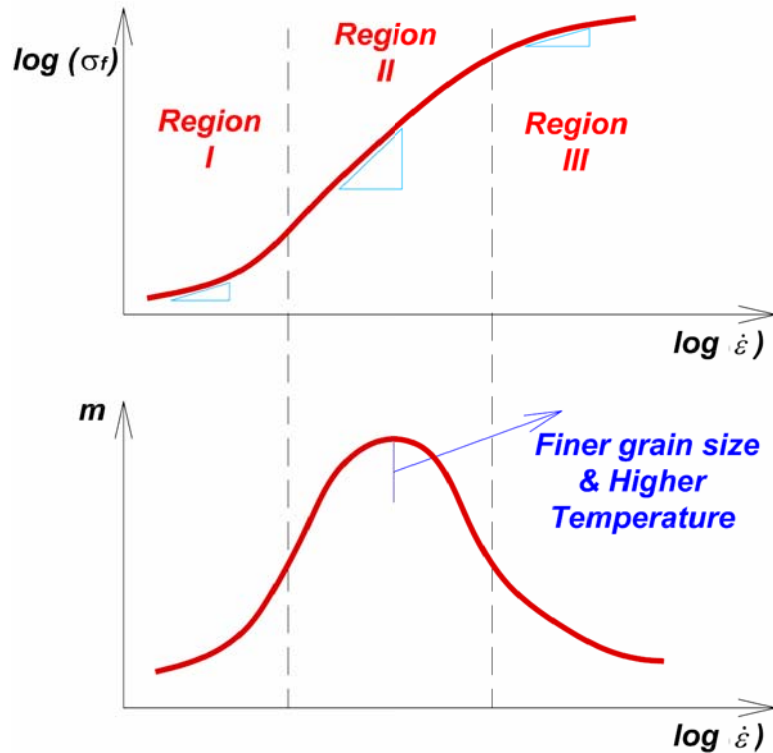


Figure 2.2: A typical sigmoidal-shaped logarithmic stress/strain rate curve and the corresponding bell-shaped sensitivity curve for a superplastic material

Based on the sigmoidal curve shown in figure 2.2, and in order to stay inside the superplastic region, the rate of deformation (*strain rate*) used to deform a superplastic material shall be kept within the limits of the superplastic region-II. More specifically, it should be as close as possible to the peak value of m . As mentioned before, the superplastic region usually falls between the 1×10^{-5} and $1 \times 10^{-1} \text{ s}^{-1}$, although this is more often between 2×10^{-4} and $2 \times 10^{-3} \text{ s}^{-1}$ [Pilling and Ridley 1989]. All the same, these strain rates are lower than typical hot forming rates, and they are practically very small. Consequently, it is always desirable to have region-II shifted to the right (*towards the higher strain rates*) as possible; this can be attained (*generally speaking*) by increasing the forming temperature, and/or refining the grain structure of the superplastic material prior to the forming process.

2.1.4 Superplastic Materials

Despite the wide variety of methods available for obtaining fine-grained microstructures, only a limited number of distinct alloys showing extensive superplasticity, or have the potential to be, are exploited on a commercial scale; these include:

1. Aluminium Alloys:

Of the aluminium alloys that have been specially developed or processed for superplasticity, only two are extensively used in structural applications; AA7475 and Supral 100, 150 & 220. Alloys such as Supral 5000 (*Al-2Mg-0.4Zr*) and Neopral (*Al-5Mg-0.15Cr*) are used for decorative panels in architectural applications.

2. Titanium Alloys:

It is somewhat fortuitous that conventionally processed alloys such Ti-6Al-4V and Ti-6Al-2Sn-4Zn-2Mo when hot rolled to sheets can show some exceptional superplasticity during deformation in the $\alpha+\beta$ phase field. These alloys have already found their applications in many areas of superplastic forming, the aircraft and aerospace fields in particular.

3. Iron Alloys:

Iron-based alloys are the most versatile and in many contexts the most important of all structural materials. So, it is not strange that superplasticity has been developed in a number of these alloys. However, the increased potential or weight-reduction at different scales, and the bias to utilise more lightweight materials hinder the use of these alloys in commercial applications.

4. Magnesium Alloys:

On contrast to Iron, the increasingly strong potentials to achieve lighter weight constructions make magnesium and its alloys very promising targets. On the other hand, superplastic forming provides a solution for the inferior formability characteristics of these alloys at room temperature. This combination makes a number of magnesium alloys that exhibit superplasticity, such as AZ31 and ZK 61, promising future materials for various applications.

5. Other Materials:

Other materials that show superplastic behaviour include some nickel alloys, copper alloys, ceramics and composites.

2.1.5 Superplastic Forming Technique (SPF)

It is the large ductility observed in superplastic materials that attracted many investigators to the potential benefits in the area of metal forming. The

Superplastic Forming (SPF) Technique is the process used to form this class of materials, and considered a near-net shape forming process, with tremendous cost and weight saving potentials over conventional forming operations. Blow forming of superplastic sheets uses a single die surface rather than the matched dies used in typical sheet metal forming operations. The superplastic sheet material is usually formed onto a fixed die cavity, shaped to the geometry of the desired part, using pressurised gas in one single step. This is schematically illustrated by figure 2.3.

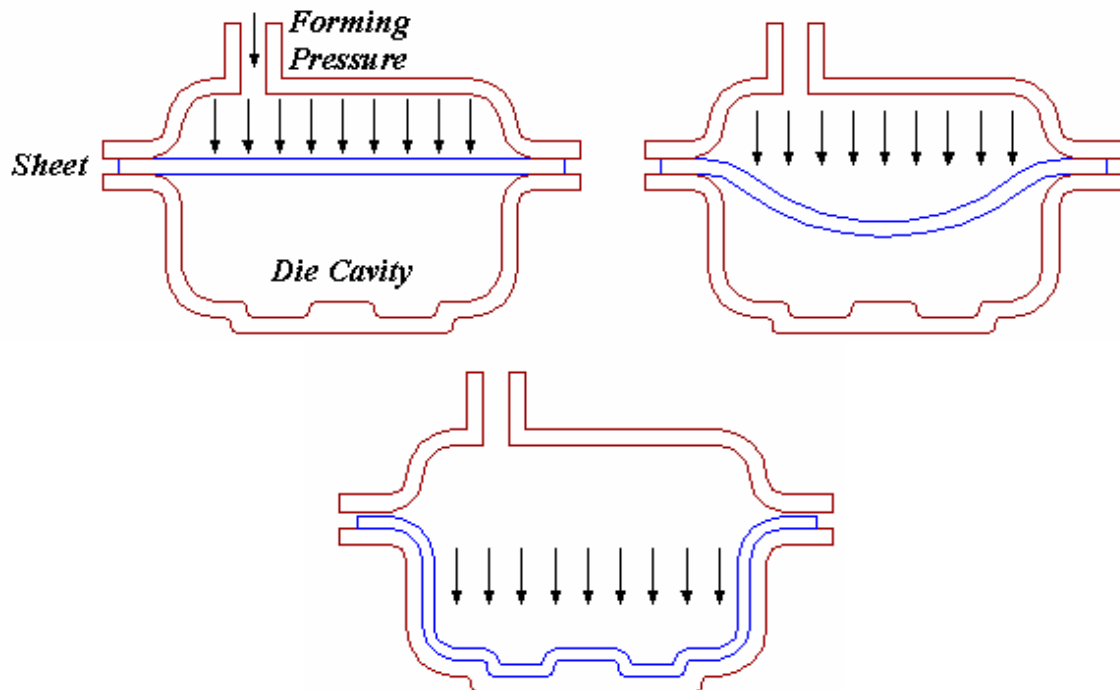


Figure 2.3: Schematic of the superplastic blow forming technique

The superplastic forming technique offers many advantages over conventional forming operations, such as:

- i. The ability to form very complex shapes, which cannot be formed by conventional methods, or can be accomplished by a larger number of parts and steps.
- ii. The ability to form very hard materials, with relatively small flow stresses.
- iii. Significant cost reduction, in terms of the low die cost.
- iv. Reduced number of forming steps, since SPF is usually carried out in one single step.
- v. Reduction of the total number of parts, and consequently the number of fasteners and joints, which leads to safety improvement in certain applications (*aerospace for instance*).
- vi. Greater design flexibility and dimensional control.

However, the technique still faces some obstacles that limits its use on a large scale, such as:

- i. Slow and speed-limited forming process, which makes it unfavourable for mass-production applications.
- ii. Expensive pre-forming steps, like the preparation of the fine grain-structured material, and heating to the desired forming temperature.
- iii. Limited predictive capabilities of deformation and failure, mirrored by the trial and error practices in forming operations.
- iv. Lack of comprehensive data regarding superplastic materials.

2.1.6 Current Applications of SPF

Despite the fact that superplastic forming technique is still considered a recent technique that has not been completely formulated, and the number of obstacles hindering its widespread use, SPF has found its place in many applications. The aerospace industry is the biggest market for SPF, yet automotive, medical, sports, cookware and architectural applications have their share too.

Aerospace titanium alloy Ti-6Al-4V is the most popular superplastic alloy used in aircrafts and submarines, covering almost one third of SPF applications in these fields. Superplastic forging of nickel-base alloys has been used to form turbine discs with integral blades.

The superplastic aluminium alloy 5083 has been formed successfully by the superplastic forming technique; producing electric devices and ticket vending machines, window frames for trains, and gate panels. This and other aluminium alloys can be used in the fabrication of airframe control surfaces and other small-sale structural elements, where lightweight and high stiffness are required. Figure 2.4 shows several aeroplane components formed from different aluminium alloys, produced by Superform Aluminium [www.super-form.com].



(a)

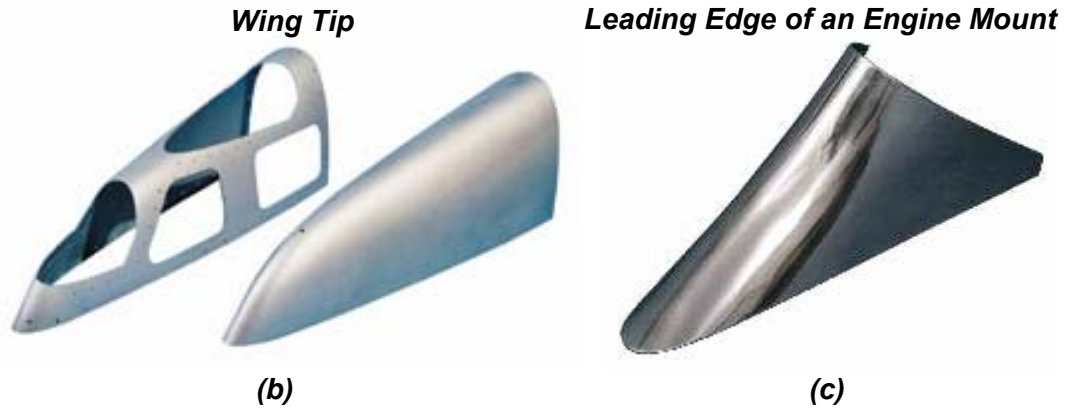


Figure 2.4: Superplastic forming used for aeroplane applications [Superform Aluminium] (a) Eclipse 500 Jet (b) Boeing 777 (c) Boeing 737

The biggest aluminium fabricator by the superplastic forming technique (*superform aluminium*) also produces parts for automotive applications. Expectedly, such parts are not found in mass-produced cars, but rather in high tag price cars produced at much lower rates, as the two examples shown in figure 2.5.

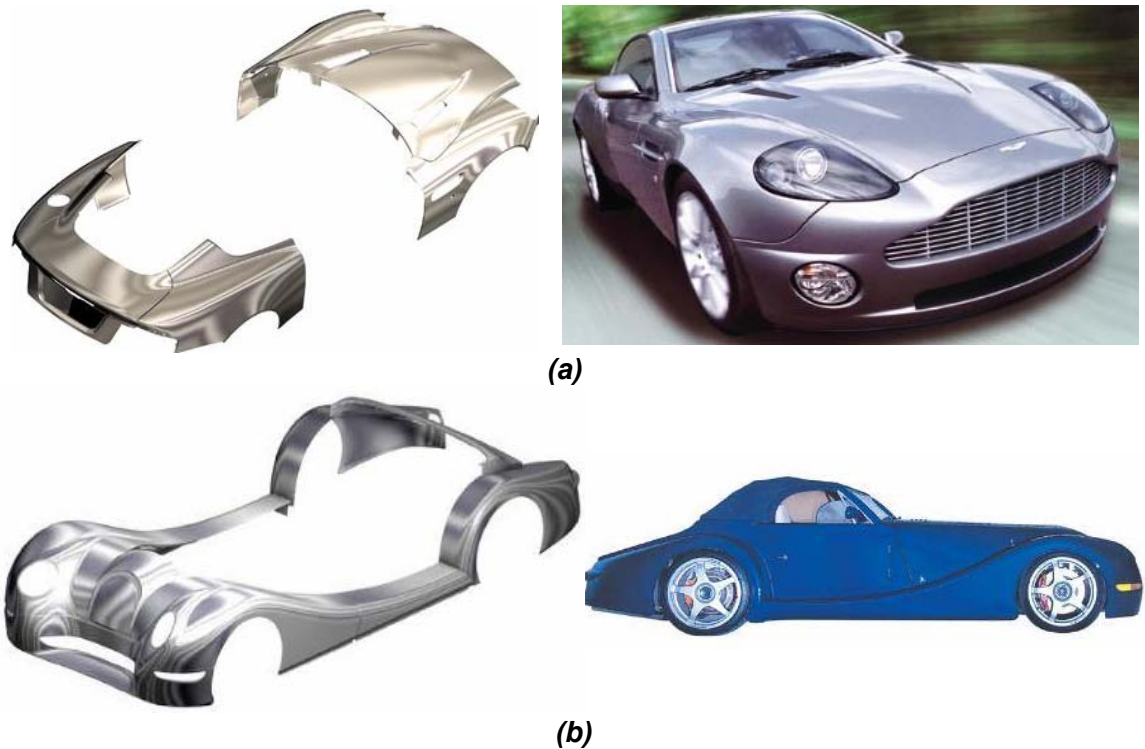


Figure 2.5: Superplastic forming used for automotive applications [Superform Aluminium] (a) Aston Martin Vanquish (b) Morgan Aero 8

All exterior body panels of the new Aston Martin Vanquish are superplastically formed using aluminium, with each panel hand tailored to the central structure to ensure a perfect fit. The Morgan Motor Company's all-new supercar (*Aero 8*) is a completely new car with advanced aluminium chassis, superplastically-formed and hand-formed highly-detailed, light yet strong aluminium outer body panels.

One of the areas of application where superplastic forming capabilities clearly surpass other forming processes is the medical field. The components shown in figure 2.6, for example, are superplastically formed using titanium, a metal known for its bio-compatibility [Curtis 2005]. Such highly detailed profiles can't be produced efficiently by any other forming process.

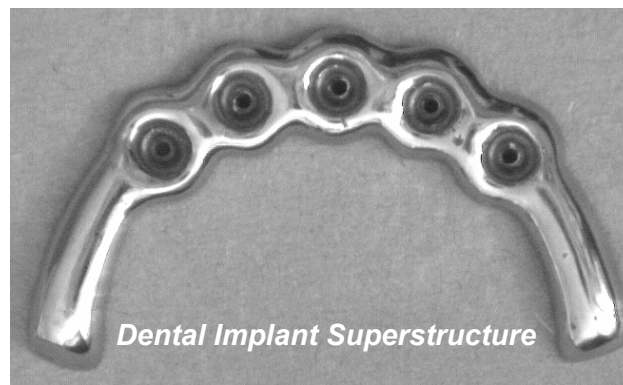


Figure 2.6: Superplastic forming used for medical applications [Curtis 2005]

In sports, different titanium alloys (*like SP700*) have been used to produce some equipment by superplastic forming; a successful example is the golf-club head produced by Yamaha [Osada 1997]. Duplex stainless steel is superplastically formed into different cookware equipments, and sink decks for passenger aircrafts. This superplastic material covers almost 30% of the Japanese market demand for such applications [Osada 1997].

Finally, even artists and architects sighted the capabilities of SPF in producing intricate geometries, and used it in many occasions. In the development of Victoria Station in London, McColl Architects used a multi-barrel vault design that required bull nosed terminal detailing around the arches at the junction with glazed walls. Due to the complexity and high specification, SPF was considered the only viable process for the production of the component [Superform Aluminium]. Some other exciting examples are found in the art sculptures shown in figure 2.7, where SPF eliminates wrinkles and ensures very smooth surfaces [Superform Aluminium].



Figure 2.7: Superplastic forming used for art and architectural applications [Superform Aluminium]

2.2 Light Weighting

The automotive industry has made a voluntary commitment to reduce fuel consumption levels by 25%, by the year 2005 in comparison with the 1990 level [Schumann and Friedrich 1998, Friedrich and Schumann 2000]. Also in 1995, the German car industry, in particular, promised to reduce fuel consumption by 25% by 2005 [Mertz 2002]. The seriousness of these commitments were translated by the development of 3L/100km (80Mpg) fuel consumption level vehicles, such as *Lupo* by VW [Dick 1999], and *A2* by Audi [Engelhart and Moedel 1999]. In spite of the success of these projects, and whether those commitments were really satisfied or not; they indicate the pressure exerted on the automotive industry to reduce fuel consumptions, and hence exhaust gas emissions, due to both economical and environmental issues.

There are many ways to reduce fuel consumption in a vehicle, such as improved power-train efficiency, IC-diesel hybrids, alternative fuels, aerodynamics, and mass reduction. Among all, mass reduction is just about the most effective and least costly, but only if the reductions are large, such as in the

range of 20-40% [Cole 1998]. Consequently, many leading car manufacturers have investigated the impact of mass reduction on fuel consumption.

From a study by Daimler-Benz, the percentage allotment of energy consumed over a full life cycle of a vehicle is shown in figure 2.8a [Jambor and Beyer 1997]. The figure shows that more than 70% of the total energy consumption goes as fuel consumed for driving the car. Moreover, the influence of vehicle mass on the average fuel consumption is shown in figure 2.8b, which shows a distribution of the total driving fuel consumption among the different modules in the C180-type model. In addition to the direct mass influence contributing to more than 50% of the consumption, it should be taken into account that both acceleration and rolling resistances are mass dependent.

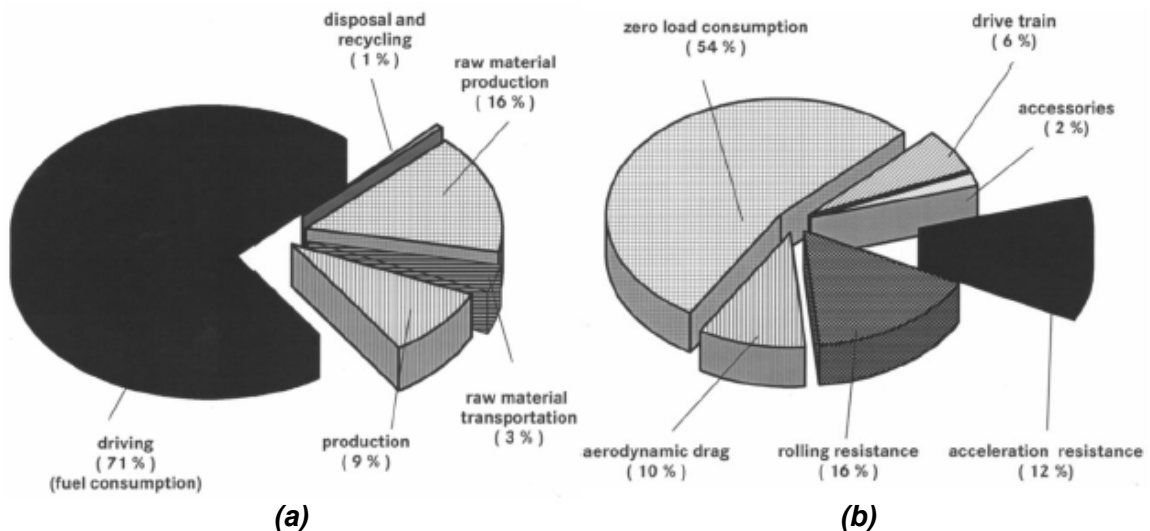


Figure 2.8: (a) Energy consumption during full life cycle (b) Impact of vehicle weight on total fuel consumption [Jambor and Beyer 1997]

In a similar study, Volkswagen showed that 80% of the full life energy consumption of VW-Golf is used during its period of utilisation, and that the mass dependent component of fuel consumption is around 60%. For that, and as a general rule of thumb, 100 kg weight reduction lowers fuel consumption by approximately 5% [Schumann and Friedrich 1998].

More clearly, Audi in one of its studies showed the direct effect of each of the different modules on the average fuel consumption; the results of this study are shown schematically in figure 2.9. According to this graph, 10% weight reduction leads to about 6% reduction in the fuel consumption level [Mertz 2002].

In spite of the abovementioned numbers, achieving mass-reduction on such scales would be quite hard to realise with conventional materials, even by employing lightweight designs. More importantly, the increasing customers' demands have led to fully equipped cars in all the different classes; even small

cars are getting more luxurious and comfortable. In addition, customers pay more attention to occupants' safety, calling again for stronger and more rigid bodies. And to keep the performance of the car, stronger engines and power-trains are needed, which requires heavier chassis and higher rigidity structure. The final result is that in any automobile class, each new model is getting heavier than the old [Carle and Blount 1999]. Therefore, and to escape this circle, the automotive industry is forced to look for new lightweight materials if the proposed mass reductions are to be realised.

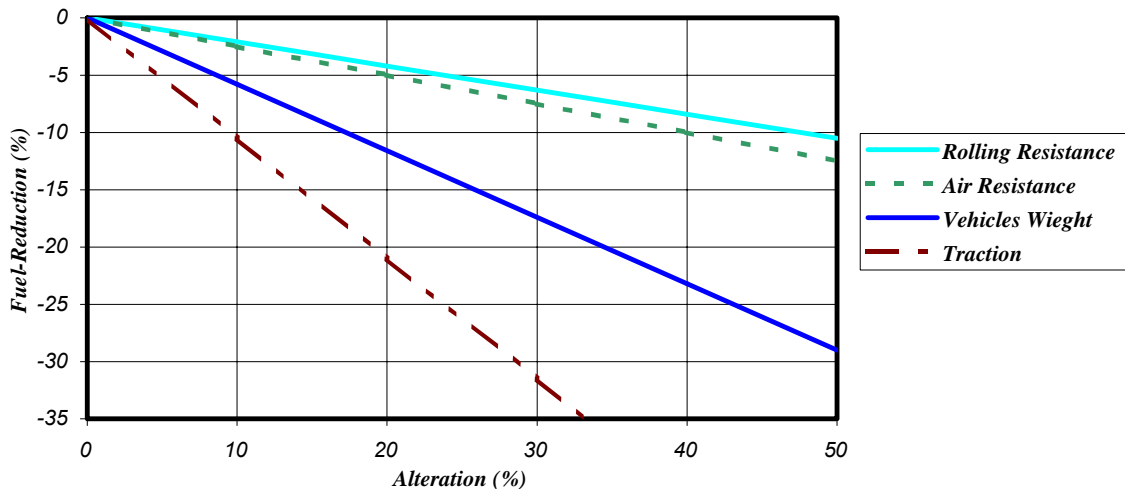


Figure 2.9: Means for reducing fuel consumption [Mertz 2002]

Finally, just to indicate the significance and seriousness of this issue, annual surveys by the society of automotive engineers showed that fuel economy was considered the leading engineering challenge by 7% of the surveyed in 2003; the figure rose to 11% in merely two years. For the year 2006, light-weighting was on the top of the environmental issues by 24.5% of the surveyed, compared to recycling/recyclability, which was second at 12.6% [SAE 2006].

2.3 Magnesium

2.3.1 General Overview

Magnesium is the chemical element that has the symbol *Mg*, the atomic number 12, and an atomic mass of 24.31. It is the lightest structural metal, the eighth most abundant element on earth, comprising 2% of the earth's crust by weight, and the third most plentiful element dissolved in seawater, constituting 13% of its elements [Tabellenbuch Metall 2001, Emley 1966, www.wikipedia.org, www.magnesium.com]. Magnesium is a very reactive metal, that's why it does

not exist in the free state, but usually found in nature in the form of oxide, carbonate, chloride or silicate. This reactivity is one of the reasons why the production of magnesium metal requires large amounts of energy.

Producing magnesium is quite interesting example of an industry where little information is shared. Unlike for example the aluminium industry where almost all of the world production is made by the Hall-Héroult process, there are many production processes used commercially to produce magnesium. They do however fall into two basic groups:

1. Silicothermic production routes:

Which includes the Pidgeon process, Magnetherm process and Bolzano process. These processes rely on the use of ferrosilicon to reduce magnesium oxide in a molten slag at temperatures between 1200 °C and 1600 °C under a reduced gas pressure above the slag to produce a magnesium vapour. This vapour is then condensed at a location, and removed from the main furnace. The crowns of condensed magnesium are then re-melted, refined and cast. These processes can produce magnesium of purity as high as 99.95%.

2. Electrolytic processes:

Commercial magnesium electrolysis is conducted in a chloride melt of mixed alkali metals at temperatures usually below 700 °C. The feed to the electrolysis process is either anhydrous magnesium chloride produced from dehydration of carnallite or partially dehydrated magnesium chloride. Unlike the high temperature production routes, it is hard to achieve a metal purity higher than 99.8% in the electrolysis processes. However, for production of greater than 10,000 tonnes per annum, the electrolysis process develops cost benefits over the high temperature processes

Magnesium has a hexagonal close-packed (*HCP*) crystal structure, to which its limited room temperature ductility is mainly attributed. In fact, magnesium's inferior formability is one of the main critical problems that limit the applications of the metal and its alloys. To strengthen, harden and alter its chemical reactivity, magnesium is usually alloyed by the addition of other elements. The most common magnesium alloys are the AZxx (*Al, Zn and Mn*), the AMxx (*Al and Mn*) and the ASxx (*Al and Si*) alloys.

2.3.2 Magnesium's History in the Automotive Industry

Volkswagen, as one of the pioneer automotive producers to utilise magnesium in its cars, has started using magnesium with the Beetle after World War II, and reached its peak in 1971 with an annual production volume of 42,000 tonnes. AS41 & AZ81 magnesium alloys were used to produce mainly air-cooled

engines and gearboxes; comprising up to 20 kg of the weight of the car at that time. In the subsequent few years, the introduction of water-cooled front engine designs, and the inadequate heat and corrosion resistances of magnesium alloys, in addition to the cheaper prices and technical superiority of aluminium alloys, all that started to diminish the importance of magnesium as a material [Schumann and Friedrich 1998, Friedrich and Schumann 2000]. In 1982, production of magnesium gearbox housings in Germany ceased altogether [Schumann and Friedrich 1998].

Economical in addition to environmental issues, mainly the continuous debate on the CO₂ emissions since the early nineties, raised the desire of the automotive industry to save energy by reducing fuel consumption, which brought the interest in more lightweight materials, and consequently revived magnesium as the lightest constructional metal.

Again, Volkswagen was one of the first to realise the strategic significance of magnesium in this regard, for that a joint venture between VW and Dead Sea Magnesium (*DSM*) for the production of magnesium was established [Friedrich and Schumann 2000]. And because the magnesium industry cannot serve for the specific demands of the automotive industry, in terms of alloys and process development, the Magnesium Research Institute (*MRI*) was established as a part of that joint venture. With this joint, the research strategy at VW aimed at the technical design of the entire material production/properties process chain (*DSM/MRI*), design and methods of construction and application in automotive components production (*VW & VW suppliers*).

Currently, many magnesium components are being produced by different auto makers, few examples will be shown in section 2.3.5.

2.3.3 Advantages

- i. Low density: magnesium has a density of 1.77 kg/L, which makes it 35% lighter than Aluminium (2.7 kg/L) and 78% lighter than steel (7.9 kg/L) [Tabelnbuch Metall 2001].
- ii. High strength-to-weight ratio: depending on strength and bending requirements, many magnesium alloys surpass aluminium alloys and even some steels in their high strength-to-weight ratio.
- iii. Very abundant: magnesium is the third most plentiful element dissolved in sea water [www.wikipedia.org]. One cubic kilometre of seawater contains 1.5 million tons of magnesium metal; there is 1375 million cubic kilometres of seawater on earth [www.magnesium.com]. Moreover, magnesium is the eighth most abundant element, constituting about 2% of earth's crust by weight [www.wikipedia.org].

- iv. Outstanding cast-ability: 1-1.5 mm wall-thickness and 1-2° draft angle components can be cast from magnesium; these numbers are half those associated with aluminium castings. Magnesium's extensive fluid flow capability allows many steel fabrications to be replaced by one large cast magnesium component [Cole 1999 Mordike and Ebert 2001]. Magnesium die-casting process is especially suited to produced highly integrated components with low wall thickness; compared to metal sheet weld-aments or machined light metal components, the near-net shape die-casting process allows a significant reduction of joining and/or machining processes [Cole 1999].
- v. Enhanced surface properties: magnesium die-castings demonstrate a significant skin effect, in which the material/mechanical properties near the surface are much improved over the bulk. Thinner magnesium die-castings may have sufficient strength per unit area to withstand better than thicker sections, and thereby competing with heavier aluminium and plastic sections [Cole 1999].
- vi. Excellent machine-ability: magnesium is easier for machining than aluminium, requiring less horsepower (50% less) at faster material removal rates (50% faster). [Cole 1999, Mordike and Ebert 2001].
- vii. Longer die-life: magnesium's lower latent heat of fusion reduces die thermal fatigue, and its low reactivity with steel limits welding to the die [Cole and Sherman 1995].
- viii. Faster solidification: due to the lower latent heat, approximately 25-50% more castings can be produced per unit time compared to aluminium [Cole and Sherman 1995].
- ix. Better corrosion resistance: corrosion resistance of high purity magnesium alloys is better than that of conventional aluminium die-cast alloys. [Mordike and Ebert 2001].
- x. Good weld-ability under controlled atmospheres.

2.3.4 Problems and Limitations

2.3.4.1 Formability Issues

The HCP crystal structure makes magnesium and its alloys some of the hardest metals to form at low temperatures, due to the corresponding limited formability. This has been paralysing almost all sheet metal forming operations, resulting in total focus on casting as a means to produce magnesium components of practical significance.

2.3.4.2 Material's Mechanical and other Properties

Generally speaking, magnesium alloys are weaker than aluminium and steel alloys in different regards [Cole 1999]:

- i. Magnesium has a low modulus of elasticity of 45 GPa ; which is 37% less than aluminium (71 GPa) and 78% less than carbon steels (207 GPa).
- ii. It has 18% larger coefficient of expansion ($26 \text{ vs } 22 \mu\text{m/m.K}$), and 25% lower thermal conductivity ($72 \text{ vs } 96 \text{ W/m.K}$) compared to aluminium.
- iii. Compared to aluminium, magnesium has 25% lower ultimate tensile strength, 35% lower fatigue strength and 25% lower hardness [Cole and Sherman 1995].

2.3.4.3 Components' Mechanical Properties:

To replace a steel or aluminium component by a magnesium one, the component must be redesigned to compensate for magnesium's reduced mechanical properties, namely stiffness and strength. This compensation is usually acquired by proper use of ribs, darts and webs, and the result is magnesium parts having the same stiffness as their aluminium counterparts. Another critical issue in this regard is the lack of the database of these parts and components under vehicle's operation loading conditions; that is tension, compression, torsion, bending, impact, and cyclic fatigue loadings. Temperature is to be taken into account, so data is needed from -40 to $100 \text{ }^\circ\text{C}$ for structural applications, and up to $180 \text{ }^\circ\text{C}$ for engine and transmission ones. In addition, environmental factors like humidity, salt, silt, sand and stones, and their effects on the functional durability of the parts shall be realised [Cole 1999].

2.3.4.4 Cost issues

The cost of a new material (*always compared to the presently employed one*) is one of the most important variables that determines whether that material has the opportunity to replace the current one in a certain vehicle component. Cost issues include three components: actual cost of raw material, added manufacturing value, and the cost to design and test the product. And because magnesium alloys are more costly than steel and aluminium, approaching the cost level of competition requires lower manufacturing costs [Cole and Sherman 1995].

The automotive industry is highly cost sensitive, therefore, and because of the fluctuation in different materials prices, a product designed now might not meet the cost targets required by the different vehicle programs later on. Because of the advantages of magnesium over aluminium, it is estimated that a magnesium part is about the same price as its aluminium counterpart when the Mg/Al price ratio is 1.8 or less. However, the Mg/Al price ratio is usually higher than that required limit, mainly because of the drop aluminium prices; even when magnesium price drops, aluminium's drops more. If this ratio is brought to the 1.5 level, there would be no limit to magnesium's demand, and that's the long term goal of the automotive industry [Cole 1999].

2.3.4.5 Raw Material Supply Issues

Despite the high growth rate of magnesium's demand, especially for the automotive industry, the current worldwide supply of magnesium is still small compared to aluminium. This makes designers feel insecure, as they need to assure sufficient supplies of material for their long-term needs.

2.3.4.6 Alloy Development Issues

As a part of the lack of database issues, most of magnesium alloys that do exist cannot be used for structural applications because of their bad mechanical properties (*compared to aluminium and/or steel*), as described before. For instance, the AZ91 magnesium alloy has *1/3* fatigue strength, *1/3* modulus of elasticity, *50%* less creep resistance at *60 °C*, and *80%* less at *130 °C* in comparison with the *380* aluminium alloy. VW/Audi introduced the B80 gearbox housings made of AZ91 in *1996*, where its greater creep and contact corrosion, and its lower elevated temperature strength were all tackled by design strategies [Friedrich and Schumann 2000]. However, for high performance gearboxes and engine crankcases, temperatures exceeding *130 °C* must be withstood (*up to 175 °C, about the same as AE42*).

2.3.4.7 SF₆ Shielding Gas Issues

98% of the engineering components made for automotive applications from magnesium are produced by pressure die-casting. One of the most serious problems when casting magnesium is its high flammability, and because of that, shielding gas must be used while doing so. The one being used for this purpose is the SF₆; however, this gas is a greenhouse one, and so an alternative shall be found.

Work is being conducted to find some replacements for this gas, and the SO₂ mixtures seem to be a good solution. However, safety, alarm systems, piping, equipment and operational protocols are not standardised for commercialised SO₂ containing systems yet [Cole 1999].

2.3.5 Current Applications

The major area of magnesium's usage remains the die-cast components, with the USA in the lead in terms of the volume of utilisation. This covers components like steering wheel core, steering column components, dashboard mounting brackets, and the 4WD transmission housing. In Japan, the applications are restricted to the steering wheel core, steering lock housing, and cylinder head cover. In Germany on the other hand, car manufacturers utilise magnesium in the four different modules, from engine block and transmission housing, to steering wheel frames, even to inner door panels. Several examples are covered next by category.

2.3.5.1 Power Train

Shown in figure 2.10, VW/Audi introduced in 1996 the *B80* gearbox housing made of AZ91 mg alloy, which marked the evolution of magnesium as a material for such applications. Weight saving of 20-25% compared to aluminium was achieved. Automatic transmission housing is also due to go into mass production [Friedrich and Schumann 2000]. The greater creep and contact corrosion of AZ91hp, and its lower elevated temperature strength were all tackled by design strategies; on the other hand, AZ91hp can be used without chromating or wax coating [Friedrich and Schumann 2001]. Moreover, to withstand temperatures exceeding 130 °C for high performance gearboxes and engine crankcases, VW has initiated a research project with MRI for this purpose. The result was several alloys among which two attractive alloys with very strong potentials for these applications were developed; *MRI153M* for temperature application range up to 150 °C, and *MRI1230D* for temperature up to 200 °C [Friedrich and Schumann 2001, Schumann and Friedrich 2003].

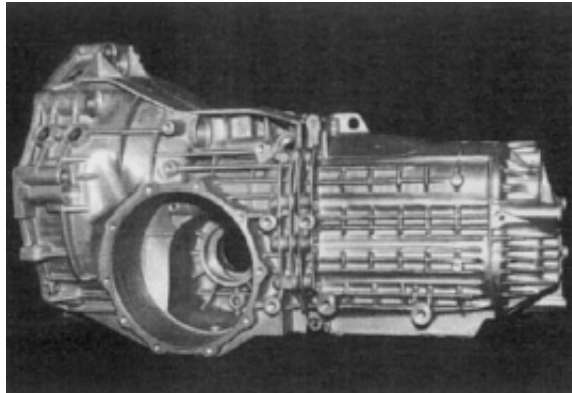


Figure 2.10: Magnesium gear box housing [Friedrich and Schumann 2000]

2.3.5.2 Interior

This area represents for many car producers the main section where the most magnesium components are in use, mainly because there are no corrosion resistance requirements. The most common alloys used in this area are AM50 & AM60, which possess 8-10% elongation to fracture [Friedrich and Schumann 2000, Burk and Vogel 2002]. Mercedes-Benz used magnesium successfully in the SL-type seat frame since 1989; the seat, shown in figure 2.11, is entirely made of die-cast magnesium, with total weight of about 8 kg only. Weight saving was achieved through the integration of many functions into a few casting parts. Despite the fact that no technical problems have occurred with this seat frame, the 1999 CL-type has gone to high strength aluminium extrusions, mainly due to cost issues, and long lead times for tooling [Jambor and Beyer 1997, Burk and Vogel 2002].



Figure 2.11: Magnesium seat frame for the SL-type, Mercedes Benz [Jambor and Beyer 1997]

2.3.5.3 Chassis

The use of magnesium in this area is still hindered, and represents a great challenge, because of the demanding safety requirements placed on chassis components. The main issue in this regard that requires more research and development is the fatigue resistance under vibrational stresses in corrosive conditions. Optimised die-casting does not produce the required level of fatigue resistance for such an application, and neither Thixo-casting nor squeeze casting have yet produced a remarkable level of improvement in this regard. Some promising techniques that might provide considerable improvement are Rheo-casting, optimised wrought alloys and forged components [Friedrich and Schumann 2000]. Different magnesium-made components like steering lock housings, steering mounting brackets and some brake components have been produced by UNITECH and Honsel, some examples are shown in figure 2.12 [Mordike and Ebert 2001, Mertz 2002].

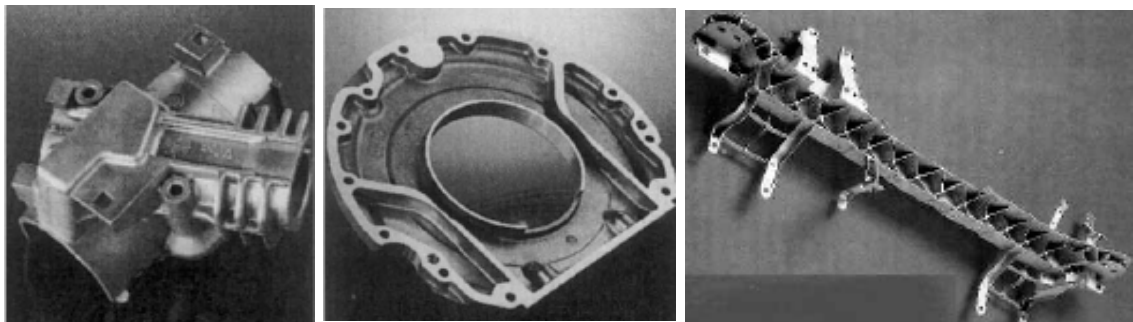
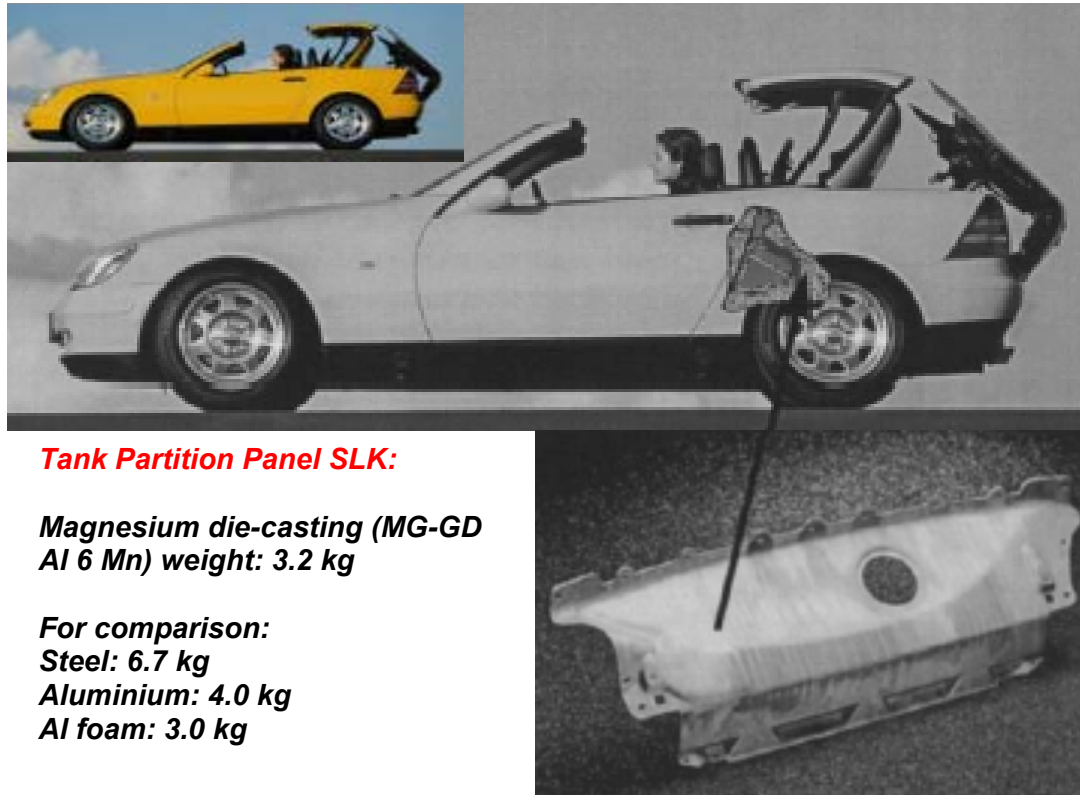


Figure 2.12: (a) Steering column lock housing (b) sealing flange (c) Steering column [Mordike and Ebert 2001, Mertz 2002]

Despite its higher cost, a fuel tank partition panel made from magnesium is used in the SLK230-type since 1996. The weight of the magnesium die-casting is 3.2 kg, which yielded 3.5 kg weight saving compared to the original steel panel, and 0.8 kg compared to the aluminium one, as shown in figure 2.13 [Jambor and Beyer 1997, Burk and Vogel 2002].



Tank Partition Panel SLK:

Magnesium die-casting (MG-GD Al 6 Mn) weight: 3.2 kg

For comparison:

Steel: 6.7 kg

Aluminium: 4.0 kg

Al foam: 3.0 kg

Figure 2.13: Magnesium die-cast fuel tank partition panel in the SLK type, Mercedes-Benz [Mertz 2002]

2.3.5.4 Body Structure

Cast Components

Components like the instrument panel cross-car beam became one of the familiar components in this field. Because of its ability to be cast in components of 1-1.5 mm wall thickness, magnesium die-castings gained the potential for making door interior components. An example is the inner boot lid of the 3L-Lupo by VW, which is made of an integral magnesium die-casting on the inner side, and aluminium sheet on the outside with Al lock reinforcing. The total weight of this Mg/Al boot lid is 5.4 kg, which is 49% weight saving compared to steel (10.5 kg), and 36% compared to aluminium (8.5 kg) [Friedrich and Schumann 2000]. Another example is the magnesium inner door casting of the 1999 CL500, by Mercedes-Benz, shown in figure 2.14. Due to the demanding corrosive environment, the inner door is protected with a yellow chromating and a

powder coating. Aluminium is used for the outer door sheet, because class A surface requirements cannot be obtained with the currently available magnesium casting technology [Burk and Vogel 2002].



Figure 2.14: CL-type magnesium casting door inner part [Burk and Vogel 2002]

Sheets

Outer panels of body components (*like doors, boot lid and engine hood*) involve large surface area and small thickness sheets, exposed primarily to bending stresses, which requires the satisfaction of flexural/buckling stiffness. In such areas, magnesium can achieve about 50% weight saving compared to steel, and 20% compared to aluminium, depending on stress profiles relevant to practical applications. However, magnesium sheets are yet unable to satisfy the corrosion resistance and surface finish requirements for body outer panels components [Friedrich and Schumann 2000].

More important, due to its hexagonal crystal structure, magnesium sheets' formability at room temperature is very limited, compared with aluminium and steel. In warm forming at 225 °C, however, the AZ31 magnesium alloy exhibits similar forming behaviour to steel and aluminium at room temperature, and achieves maximum drawing ratios comparable to steel. Under these conditions, VW was able to produce initial research demonstrators for the inner section of a door for Golf A2 without cracking [Friedrich and Schumann 2000]. Yet, more research and development are needed in order to bring magnesium sheet applications into light.

Extrusions

The main advantage of using magnesium extrusions comes from its better mechanical properties in comparison with cast components. An AZ31 extrusion achieves 15% elongation to fracture. Due to its hexagonal atomic structure, the energy absorption capabilities under dynamic axial stresses are lower than aluminium; yet, the difference is much less marked under dynamic transverse and diagonal loadings [Friedrich and Schumann 2000]. In terms of cost, magnesium extrusions are usually less expensive than comparable die-castings, especially for low and medium series production, mainly due to the low tooling cost [Mertz 2002].

The use of magnesium-extrusions in vehicles depends primarily on the type of stresses a certain component is exposed to. Mass-requirement characteristics are used as the criteria for the choice of material, based on stability under certain loading conditions. According to the mass-requirement characteristics for essential single-axis stresses, magnesium (*in comparison with steel and aluminium*) offers the potential for component mass reduction with regard to strength requirements (*tensile and bending stress*). Therefore, if thin-walled large-cross-section components are produced, weight saving is conceivable in applications like window frames and chassis members [Friedrich and Schumann 2000].

Possible geometries of the cross section of magnesium extrusions are similar to those extrusions made of high strength aluminium alloys; hollow profiles and wall thickness of less than *1.5 mm* can be produced, as demonstrated by the examples shown in figure 2.15 [Mertz 2002].

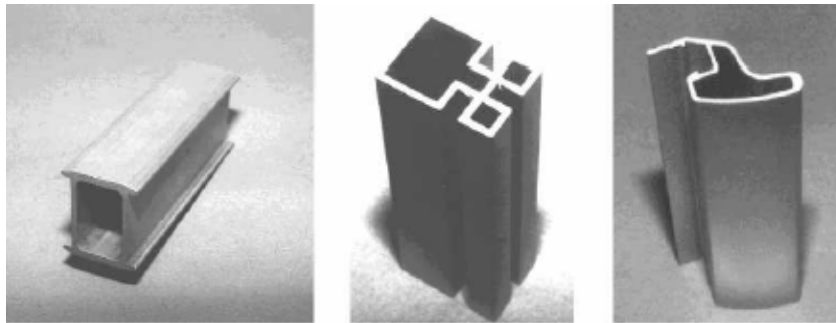


Figure 2.15: Magnesium extrusions [Mertz 2002]

CHAPTER THREE: GENERALISED CONSTITUTIVE MODELLING OF SUPERPLASTIC DEFORMATION

Flow stress during superplastic deformation can be generally defined as a function of strain, strain rate and temperature. Constitutive relations for superplastic materials are based on either continuum mechanics or atomistic mechanisms [Davies et al. 1970]. Continuum models are of two types: one which considers the macroscopic response of superplastic materials to mechanical forces [Hart 1967, Avery and Backofen 1965] and the other type accounts for the measured values of the activation energy of flow [Mukherjee 1971, Suery and Baudelet 1978]. Atomistic models vary according to the rate controlling mechanism that determines the microstructural and mechanical characteristics of the flow. The most viable atomistic models describing superplastic deformation are those that involve grain boundary sliding in association with some accommodation mechanism to achieve compatibility at grain boundaries. These models may include a combination of grain boundary sliding and diffusion creep, grain boundary sliding and grain boundary migration, and grain boundary sliding, grain boundary migration and localised dislocation motion by glide and climb [Davies et al. 1970, Gifkins and Langdon 1970]. Other researchers [Hamilton et al. 1991, Khraisheh et al. 1997] combined mechanical parameters with microstructural parameters to describe the superplastic flow based on the sigmoidal shape of the stress/strain rate curve.

Khraisheh et al. [1997] modelled the multiaxial deformation behaviour of superplastic materials within the continuum theory of viscoplasticity using the isotropic von-Mises yield function, without accounting for microstructural evolution. In this work, the general frame of the same constitutive model is employed, and then modified by taking anisotropy and microstructural changes into account. This is done by incorporating a dynamic anisotropic yield function, and introducing a set of evolution equations for the various internal and microstructural parameters, into the model. The capabilities of the modified model are thence tested using data available in the literature, obtained from different multiaxial tests on the Pb-Sn superplastic alloy.

3.1 General Multiaxial Constitutive Model

Constitutive modelling of superplastic deformation is based on large viscoplastic deformation, where elastic strain is neglected, since its very small compared to the plastic one. By the multiplicative decomposition of the rate of deformation into elastic and plastic parts [Lee 1969, Zbib and Aifantis 1988, Zbib 1993], this leads to:

$$\mathbf{D} = \mathbf{D}^E + \mathbf{D}^P \cong \mathbf{D}^P \quad (3.1)$$

where \mathbf{D} is the rate of deformation (*strain rate*) tensor, \mathbf{D}^E and \mathbf{D}^P are the elastic and plastic parts of \mathbf{D} , respectively.

For viscoplastic deformation, the general associated flow rule is given by [Dafalias 1990, Lubliner 1990, Khan 1996]:

$$\mathbf{D}^P = f \frac{\partial J}{\partial \boldsymbol{\sigma}} \quad (3.2)$$

where f is the overstress function, $J(\boldsymbol{\sigma}-\boldsymbol{\alpha})$ is a positive scalar-valued function of the state variables having the dimension of stress, $\boldsymbol{\sigma}$ is the Cauchy stress tensor, and $\boldsymbol{\alpha}$ is the back stress tensor.

The overstress function f has been presented in different forms in literature. Hamilton et al. [1991] developed a model for the uni-axial loading case, using a microstructure-based overstress function that describes the characteristics of superplastic materials during deformation. In his model, the overstress function is split into a strain rate term and a creep term, which enables capturing the sigmoidal stress-strain rate behaviour of superplastic materials, shown earlier in figure 2.2. Motivated by Hamilton's work, the following form for f is proposed:

$$f = \frac{C_I [J - (K_0 + R)]^{\frac{1}{m}}}{d^p} + C_{II} J^n \quad (3.3)$$

where $(K_0 + R)$ is a reference stress, whose variable part R represents the isotropic hardening, d is the average grain diameter, p is the grain size exponent, m is the strain rate sensitivity index, n is the hardening exponent, and C_I & C_{II} are material constants.

The first term in the equation represents the superplastic region (*region II of the logarithmic stress/strain rate curve, figure 2.2*), while the second represents the creep region (*region III*).

Substituting equation (3.2) in (3.3) gives the generalised multi-axial constitutive equation in the following form:

$$\mathbf{D}^P = \left[\frac{C_I [J - (K_0 + R)]^{\frac{1}{m}}}{d^p} + C_{II} J^n \right] \frac{\partial J}{\partial \boldsymbol{\sigma}} \quad (3.4)$$

Equation (3.4) is a tensor equation, from which six independent equations, corresponding to six independent strain rate and stress components, can be obtained. However, and for any specific loading case, the six equations can be

reduced to a lesser number of equations that can be solved for the corresponding stresses and strains. In later sections, four different loading cases will be considered and analysed, and it will be shown how the constitutive equations are reduced and solved for the corresponding stresses and strains.

Moreover, the presented constitutive model is microstructure-based, since it accounts for various microstructural and internal variables, and allows for changes in their values during deformation. For instance, equation (3.4) not only accounts for the initial grain size d_0 , but also takes grain growth into account, if the value of grain diameter d is updated during deformation. Similarly, the evolution of the internal variables; namely the isotropic hardening R , and the kinematic hardening, which is represented by the internal (*back*) stress tensor α in the yield function J , is accounted for through a set of evolution equations that will be discussed in details.

3.2 Anisotropic Yield Function

Experimental observations showed that the Pb-Sn eutectic alloy exhibits transient behaviour during deformation, which could be associated with the internal stresses [Zhang et al. 1995]. In another study, and in fixed-end torsion tests in particular, Khraisheh et al. [1995] showed experimentally that the same material exhibits a strong degree of deformation induced anisotropy, though it is initially isotropic.

Khraisheh et al. [1997] employed von-Mises isotropic yield function (J_2 Theory) in the framework of the same model, without accounting for grain growth. The model was able to describe the superplastic behaviour of the model material in both simple tension and pure torsion; nevertheless, it was not able to predict the induced axial stresses in fixed-end torsion tests.

Based on the work of Dafalias [1990], departing from the classical J_2 theory would enhance the constitutive model. In addition, Miller et al. [1992] indicated that incorporating the J_3 theory in the hardening laws and/or the yield function would adequately predict the secondary response in pure torsion. For that, Khraisheh et al. [1997] replaced von-Mises with a yield function that includes J_3 . The output was improved; but still, the model could not accurately capture the induced axial stresses in fixed-end torsion tests. For the model to be able to capture the superplastic deformation-induced anisotropy, an anisotropic yield function shall be employed.

A generalised anisotropic yield function defined in reference to the reference axes x_i ($i = 1, 2 \text{ \& } 3$) will be used here [Hill 1950, Dafalias 1990, Khraisheh and Abu-Farha 2003, Khraisheh 2000, Abu-Farha and Khraisheh

2004]. The anisotropic yield function is capable of describing the evolution of the initial state of anisotropy through the evolution of unit vectors defining the direction of anisotropy, and has the following form:

$$J = \left[\frac{3}{2} (\mathbf{S} - \boldsymbol{\alpha})(\mathbf{S} - \boldsymbol{\alpha}) + c_1 (\mathbf{M}(\mathbf{S} - \boldsymbol{\alpha}))^2 + c_2 (\mathbf{N}_1(\mathbf{S} - \boldsymbol{\alpha}))^2 + c_3 (\mathbf{N}_2(\mathbf{S} - \boldsymbol{\alpha}))^2 \right]^{\frac{1}{2}} \quad (3.5)$$

$$\mathbf{M} = \frac{1}{2} [\mathbf{a}_1 \otimes \mathbf{a}_2 + \mathbf{a}_2 \otimes \mathbf{a}_1] \quad \mathbf{N}_1 = \mathbf{a}_1 \otimes \mathbf{a}_1 \quad \mathbf{N}_2 = \mathbf{a}_2 \otimes \mathbf{a}_2 \quad (3.6)$$

where \mathbf{S} is the deviatoric part of Cauchy stress tensor, $\boldsymbol{\alpha}$ is the deviatoric part of the back stress (*kinematic hardening*) tensor, c_1 , c_2 & c_3 are the anisotropic constants. For $c_1 = c_2 = c_3 = 0$, the anisotropic yield function reduces to the isotropic von-Mises yield function. \mathbf{a}_1 , \mathbf{a}_2 & \mathbf{a}_3 are orthonormal vectors along the axes of anisotropy \mathbf{x}_i' ($i = 1, 2$ & 3), where $\mathbf{a}_3 = \mathbf{a}_1 \times \mathbf{a}_2$. The directions of \mathbf{a}_1 and \mathbf{a}_2 are defined by the angle of anisotropy ϕ , measured positive counter clockwise between \mathbf{x}_1 and \mathbf{x}_1' , as shown in figure 3.1.

Referring to figure 3.1, \mathbf{a}_1 and \mathbf{a}_2 are expressed in terms of ϕ as:

$$\begin{aligned} \mathbf{a}_1 &= \cos \phi \bar{\mathbf{i}} + \sin \phi \bar{\mathbf{j}} \\ \mathbf{a}_2 &= -\sin \phi \bar{\mathbf{i}} + \cos \phi \bar{\mathbf{j}} \end{aligned} \quad (3.7)$$

The direction tensors \mathbf{M} , \mathbf{N}_1 & \mathbf{N}_2 can be also expressed in terms of ϕ by substituting equation (3.7) in (3.6):

$$\mathbf{M}_{ij} = \frac{1}{2} \begin{bmatrix} -2 \cos \phi \sin \phi & \cos^2 \phi - \sin^2 \phi & 0 \\ \cos^2 \phi - \sin^2 \phi & 2 \cos \phi \sin \phi & 0 \\ 0 & 0 & 0 \end{bmatrix} \quad (3.8a)$$

$$\mathbf{N}_{1ij} = \begin{bmatrix} \cos^2 \phi & \cos \phi \sin \phi & 0 \\ \cos \phi \sin \phi & \sin^2 \phi & 0 \\ 0 & 0 & 0 \end{bmatrix} \quad (3.8b)$$

$$\mathbf{N}_{2ij} = \begin{bmatrix} \sin^2 \phi & -\cos \phi \sin \phi & 0 \\ -\cos \phi \sin \phi & \cos^2 \phi & 0 \\ 0 & 0 & 0 \end{bmatrix} \quad (3.8c)$$

$\boldsymbol{\alpha}$ and $\boldsymbol{\sigma}$ are tensors; so even though J given by equation (3.5) is a scalar quantity, the final form for J is still determined by the loading case, as it will be shown later. It is to be mentioned that the yield function used here is a dynamic yield function, with the rate dependence appears explicitly via the strain rate, and implicitly via the internal variables, which will be covered next.

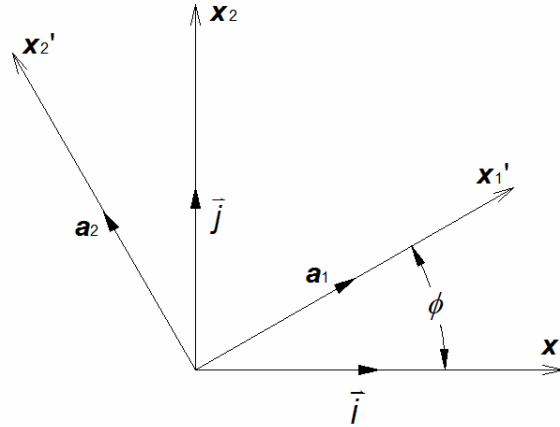


Figure 3.1: Anisotropic angle ϕ with respect to the reference axes x_i ($i = 1, 2$ & 3)

3.3 Evolution of Microstructure and Internal Variables

3.3.1 Grain Growth

Stress/strain rate behaviour of many superplastic materials is known to be grain size dependent. Ti6Al4V titanium alloy was found to have strong grain size dependency; in addition, it has been shown that grain coarsening occurs and causes flow hardening as well as changes in the value of m [Johnson et al. 1993]. Grain growth in the Pb-Sn eutectic alloy was found to be both strain and strain rate dependent [Zhang 1996], with direct effect on the hardening and softening behaviour observed in stress/strain curves at different strain rates [Khraisheh and Abu-Farha 2003]. Influence of grain growth on the behaviour of the 5083 aluminium alloy was similarly observed, and accounted for in a modelling effort by Khaleel et al. [1998].

The grain growth model used here is similar to the one used by Johnson et al. [1993]. To fully describe grain growth, both static grain growth (SGG) and deformation-enhanced dynamic grain growth (DEGG) are considered. And since both static and dynamic growth rates are assumed to be independent mechanisms, the total grain growth rate is obtained by simply combining both terms:

$$\dot{d} = \dot{d}_{static} + \dot{d}_{dynamic} \quad (3.9)$$

Static grain growth is assumed to follow the kinetics of particle stabilised growth rates and is used to account for thermal exposure, since superplastic forming is usually conducted at relatively high temperatures. The static grain growth rate equation has the following form:

$$\dot{d}_{Static} = \frac{k_S}{d^g} \quad (3.10)$$

where d is the grain size, k_S is the static grain growth constant and g is a material constant. The two constants are determined by fitting the rate equation to the experimentally-measured grain size after thermal exposure for various times.

Several mechanisms were proposed to describe dynamic (*deformation-enhanced*) grain growth; including grain switching, grain sliding and migration, grain cellular dislocation glide and climb, and enhanced grain boundary mobility [Johnson et al. 1993, Khaleel et al. 2001]. Unlike the static one, dynamic grain growth is quite different for different materials, so is the form of the rate equation. The following form for dynamic grain growth, which assumes increased grain boundary mobility due to an increase in the grain boundary vacancy concentration resulting from grain boundary sliding, was proposed by Clark and Alden [1973], and is used here:

$$\dot{d}_{Dynamic} = \frac{k_D \tau \dot{\epsilon}}{d^g} \left(1 - \exp\left(-\frac{\epsilon}{\dot{\epsilon} \tau}\right) \right) \quad (3.11)$$

where k_D is the dynamic grain growth constant, and τ is another material constant, and they are also determined by fitting the experimental data. Equation (3.11) shows that the dynamic grain growth rate in its general form is a function of both strain and strain rate.

3.3.2 Cavitation

Most superplastic materials develop internal cavitation during deformation [Miller et al. 1979, Stowell et al. 1984, Pilling and Ridley 1989, Khaleel et al. 1997, Nicolaou et al. 2000, Chino and Iwasaki 2004, Khraisheh et al. 2006]. Excessive cavitation not only causes premature failure, but also imposes significant limitations on the industrial use of superplastically-formed parts. Cavity growth is a result of diffusion-controlled mechanism or plasticity-controlled mechanism. Diffusional cavity growth rate is stress-dependent and drops sharply after a rapid growth rate. Eventually, void growth rate during superplastic deformation is dominated by plastic flow of the surrounding matrix. Because of the large plastic deformation associated with superplasticity, void growth is believed to be dominated by a plasticity-controlled mechanism [Stowell 1983, Pilling and Ridley 1989]. Cavitation model used here accounts for the growth of pre-existing cavities (*nucleation of new voids is not considered*), where the area fraction of voids f_a is exponentially related to the effective plastic strain $\bar{\epsilon}$:

$$f_a = f_{a0} \exp(\nu \bar{\epsilon}) \quad (3.12)$$

where f_{a0} is the initial area fraction of voids, and ψ is a void growth material parameter that depends on the strain rate sensitivity index m , and the ratio between the mean stress σ_m and the effective stress $\bar{\sigma}$.

It should be noticed that cavitation does not appear anywhere in the constitutive model, therefore, a simple approach to account for it is to consider the direct impact of cavities on reducing the cross section of the material under loading. In other words, to correct the cross sectional area by subtracting the total area of voids, and then calculating the stress based on the corrected area. Doing so, based on the area fraction of voids defined by equation (3.12), a corrected cross sectional area and stress component would be:

$$A_{Corr} = A(1 - f_a) \quad (3.13a)$$

$$\sigma_{Corr} = \frac{\sigma}{(1 - f_a)} \quad (3.13b)$$

Since σ is embedded in every J term in equation (3.4), accounting for cavitation would be hard to express, for the constitutive equation in its general form. However, the case would be easier when the model is reduced to a specific loading case, as it will be shown later. All the same, even if a stress/strain curve is generated ignoring cavitation, correction to account for it could be easily done quite independently in an additional step, as inferred by equation (3.13b).

3.3.3 Isotropic and Kinematic Hardening

The evolution equations for the Isotropic Hardening R and the Kinematic Hardening α , employed here, are similar to those used for viscoplastic materials [Dafalias 1990]. These equations include hardening, static recovery and dynamic recovery terms. The static recovery term is very important due to the very viscous nature of superplastic materials, embodied by their high strain rate sensitivity. For the isotropic hardening, the rate equation has the following form:

$$\dot{R} = H\dot{\bar{\epsilon}} - C_D\dot{\bar{\epsilon}}R - C_S R^a \quad (3.14)$$

where $\dot{\bar{\epsilon}}$ is the effective strain rate, H is the hardening coefficient, C_D is the dynamic recovery coefficient, C_S and a are the static recovery coefficient and exponent, respectively.

The rate equation for kinematic hardening has a slightly different form:

$$\dot{\alpha} = HD - C_D D\alpha - C_S \alpha(h(\alpha))^{a-1} \quad (3.15)$$

where \mathbf{D} is the rate of deformation tensor defined by equation (3.2), and $\dot{\boldsymbol{\alpha}}$ is the corotational rate of the back stress tensor, related to the rate of change by:

$$\dot{\boldsymbol{\alpha}} = \dot{\boldsymbol{\alpha}} - \boldsymbol{\omega}\boldsymbol{\alpha} + \boldsymbol{\alpha}\boldsymbol{\omega} \quad (3.16a)$$

$$\boldsymbol{\omega} = \mathbf{W} - \xi(\boldsymbol{\alpha}\mathbf{D} - \mathbf{D}\boldsymbol{\alpha}) \quad (3.16b)$$

where $\boldsymbol{\omega}$ is the spin tensor, \mathbf{W} is the rotation tensor, and ξ is a material parameter measuring the magnitude of plastic spin. The corotational rate of $\boldsymbol{\alpha}$ is taken with respect to the plastic spin as was used by many investigators [Zbib and Aifantis 1988, Dafalias 1990].

$h(\boldsymbol{\alpha})$ in equation (3.15) is a scalar function of the internal stress tensor, which has the form of the yield function J , with \mathbf{S} set to zero:

$$h(\boldsymbol{\alpha}) = J(\boldsymbol{\alpha}) = \boldsymbol{\alpha} \left[\frac{3}{2} + c_1 \mathbf{M}^2 + c_2 \mathbf{N}_1^2 + c_3 \mathbf{N}_2^2 \right]^{\frac{1}{2}} \quad (3.17)$$

R in equation (3.14) is a scalar quantity, and the effective strain rate appears instead of the rate of deformation tensor \mathbf{D} , as it is the case for $\boldsymbol{\alpha}$ in equation (3.15). Also, for a given state of deformation (*effective strain rate*), R is merely a function of a set of material parameters (H , C_S , C_D & \mathbf{a}), and is not affected by the state of anisotropy in the material. On the other hand, $h(\boldsymbol{\alpha})$ term is a function of both the anisotropic angle ϕ and the anisotropic constants c_1 , c_2 & c_3 . This means that $\boldsymbol{\alpha}$ is not only influenced by the initial state of anisotropy, but also by its evolution through the evolution of ϕ .

3.3.5 Anisotropic Angle

In an early work, the anisotropic angle ϕ was assumed constant during superplastic deformation, and the model was able to capture the experimental data obtained in simple tension to a very good extent [Khraisheh and Abu-Farha 2003]. However, for the pure shear loading case, assuming a constant value of ϕ would not predict the induced axial stresses, observed and measured experimentally during fixed-end torsion tests [Khraisheh et al. 1997, Khraisheh 2000-b]. Therefore, the direction of anisotropy is assumed to evolve during superplastic deformation.

Motivated by the work of Dafalias [1990], the evolution of the anisotropic angle ϕ is considered initially with respect to the Eulerian plastic spin, and as deformation continues, it shifts towards an orthotropic spin. The following form for the evolution equation is proposed:

$$\dot{\phi} = -\frac{\sqrt{3}\dot{\varepsilon}}{2} [x(1 - \xi(\alpha_{11} - \alpha_{22})) + (1-x)(1 - \eta \cos(2\phi))] \quad (3.18a)$$

$$x = e^{-\beta\dot{\varepsilon}} \quad (3.18b)$$

where β & η are material parameters.

Giving a closer look at the simple shear loading case, equation (3.16b) reduces to:

$$\boldsymbol{\omega} = \frac{\dot{\gamma}}{2} (1 - \xi(\alpha_{11} - \alpha_{22})) \begin{bmatrix} 0 & 1 \\ -1 & 0 \end{bmatrix} \quad (3.19)$$

At the onset of deformation, $x = 1$ by equation (3.18b), and the evolution of ϕ becomes identical to the $\boldsymbol{\omega}_{12}$, which represents the spin of the substructure with respect to the plastic strain. As deformation continues, x approaches zero (*depending on the value of β*), so does the first term in equation (3.18a), and so the effect of plastic spin becomes insignificant.

3.4 Model Reduction to Various Loading Cases

3.4.1 Uniaxial Simple Tension

The uniaxial tensile loading condition is the simplest loading case, as it involves only one stress, and therefore strain rate, component; that is:

$$\boldsymbol{\sigma} = \begin{bmatrix} \sigma_{11} & 0 & 0 \\ 0 & 0 & 0 \\ 0 & 0 & 0 \end{bmatrix} \quad \mathbf{D} = \begin{bmatrix} \dot{\varepsilon}_{11} & 0 & 0 \\ 0 & \frac{-\dot{\varepsilon}_{11}}{2} & 0 \\ 0 & 0 & \frac{-\dot{\varepsilon}_{11}}{2} \end{bmatrix} \quad (3.20)$$

From which the deviatoric and the back stress tensors reduce to:

$$\mathbf{S} = \begin{bmatrix} \frac{2\sigma_{11}}{3} & 0 & 0 \\ 0 & -\frac{\sigma_{11}}{3} & 0 \\ 0 & 0 & -\frac{\sigma_{11}}{3} \end{bmatrix} \quad \boldsymbol{\alpha} = \begin{bmatrix} \alpha_{11} & 0 & 0 \\ 0 & -\frac{\alpha_{11}}{2} & 0 \\ 0 & 0 & -\frac{\alpha_{11}}{2} \end{bmatrix} \quad (3.21)$$

As a result, the tensorial constitutive equation (3.4) reduces to the following one-dimensional form:

$$\dot{\epsilon}_{11} = \left[\frac{C_I [J - (K_o + R)]^{\frac{1}{m}}}{d^p} + C_{II} J^n \right] \frac{\partial J}{\partial \sigma_{11}} \quad (3.22)$$

To evaluate the differential term $(\partial J / \partial \sigma_{11})$, stress and strain rate components are first fed into equation (3.5), to reduce J to the following form:

$$J^2 = K_I \sigma_{11}^2 + K_{II} \sigma_{11} \alpha_{11} + K_{III} \alpha_{11}^2 \quad (3.23)$$

where:

$$K_I = \left[\begin{array}{l} 1 + c_1 \cos^2 \phi \sin^2 \phi + c_2 \left(\frac{2}{3} \cos^2 \phi - \frac{1}{3} \sin^2 \phi \right)^2 \\ + c_3 \left(\frac{2}{3} \sin^2 \phi - \frac{1}{3} \cos^2 \phi \right)^2 \end{array} \right] \quad (3.24a)$$

$$K_{II} = \left[\begin{array}{l} -3(1 + c_1 \cos^2 \phi \sin^2 \phi) + \frac{c_2}{3} \left(\begin{array}{l} -4 \cos^4 \phi - \sin^4 \phi \\ + 4 \cos^2 \phi \sin^2 \phi \end{array} \right) \\ + \frac{c_3}{3} \left(\begin{array}{l} -4 \sin^4 \phi + 4 \cos^2 \phi \sin^2 \phi - \cos^4 \phi \end{array} \right) \end{array} \right] \quad (3.24b)$$

$$K_{III} = \left[\begin{array}{l} \frac{9}{4} (1 + c_1 \cos^2 \phi \sin^2 \phi) + c_2 \left(\cos^2 \phi - \frac{1}{2} \sin^2 \phi \right)^2 \\ + c_3 \left(\sin^2 \phi - \frac{1}{2} \cos^2 \phi \right)^2 \end{array} \right] \quad (3.24c)$$

Evaluating and then substituting $(\partial J / \partial \sigma_{11})$ in equation (3.22), the constitutive equation for the uniaxial loading case will have the form:

$$\dot{\epsilon}_{11} = \left[\frac{C_I (J - (K_o + R))^{\frac{1}{m}}}{d^p} + C_{II} J^n \right] \frac{2K_I \sigma_{11} + K_{II} \alpha_{11}}{2[K_I \sigma_{11}^2 + K_{II} \sigma_{11} \alpha_{11} + K_{III} \alpha_{11}^2]^{\frac{1}{2}}} \quad (3.25)$$

The evolution tensor equation for the kinematic hardening, On the other hand, is also reduced for the uniaxial loading case to a single equation:

$$\dot{\alpha}_{11} = H \dot{\epsilon}_{11} - C_D \dot{\epsilon}_{11} \alpha_{11} - C_S \alpha_{11} (h(\alpha))^{a-1} \quad (3.26)$$

where $h(\alpha)$ becomes simply:

$$h(\alpha) = \alpha_{11} [K_{III}]^{\frac{1}{2}} \quad (3.27)$$

Since $\dot{\varepsilon} = \dot{\varepsilon}_{11}$, the evolution equations for grain size, cavitation, isotropic hardening and anisotropic angle remain the same, except that each $\dot{\varepsilon}$ is replaced by $\dot{\varepsilon}_{11}$. Note that there is no need to use the index (11) for stresses and strain rates (σ_{11} for instance), since there is only one component for each.

3.4.2 Simple Shear

A simple shear loading case simulates a pure torsion test. But since anisotropy is taken into account, induced axial stresses or strains are expected depending on the type of test performed. Considering the fixed-end torsion test, (since the data obtained from such tests by Khraisheh et al. [1995 & 1997] will be used in a later section to calibrate and validate the model) induced axial stresses appear in the stress tensor as additional axial stress components, without affecting the rate of deformation tensor, that is:

$$\mathbf{S}_{ij} = \begin{bmatrix} S_{11} & \tau_{12} \\ \tau_{12} & S_{22} \end{bmatrix} \quad \mathbf{D}_{ij} = \frac{\dot{\gamma}_{12}}{2} \begin{bmatrix} 0 & 1 \\ 1 & 0 \end{bmatrix} \quad \boldsymbol{\alpha}_{ij} = \begin{bmatrix} \alpha_{11} & \alpha_{12} \\ \alpha_{12} & \alpha_{22} \end{bmatrix} \quad (3.28)$$

Where S_{11} and S_{22} represent the deviatoric induced axial stresses, τ_{12} is the deviatoric shear stress, and $\dot{\gamma}_{12}$ is the surface shear strain. Substituting these into equation (3.4) yields three independent equations in the 11, 12 & 22 directions as follows:

$$D_{11} = 0 = \left[\frac{C_I (J - (K_o + R))^{\frac{1}{m}}}{d^p} + C_{II} J^n \right] \frac{\partial J}{\partial \sigma_{11}} \quad (3.29a)$$

$$D_{12} = \frac{\dot{\gamma}_{12}}{2} = \left[\frac{C_I (J - (K_o + R))^{\frac{1}{m}}}{d^p} + C_{II} J^n \right] \frac{\partial J}{\partial \tau_{12}} \quad (3.29b)$$

$$D_{22} = 0 = \left[\frac{C_I (J - (K_o + R))^{\frac{1}{m}}}{d^p} + C_{II} J^n \right] \frac{\partial J}{\partial \sigma_{22}} \quad (3.29c)$$

Similarly, for the kinematic hardening, equation (3.15) reduces to:

$$\dot{\alpha}_{11} = \alpha_{12} \dot{\gamma}_{12} (1 - \xi(\alpha_{11} - \alpha_{22})) - \alpha_{11} \left(C_D \frac{\dot{\gamma}_{12}}{\sqrt{3}} + C_S (h(\alpha))^{a-1} \right) \quad (3.30a)$$

$$\dot{\alpha}_{12} = \left[\begin{array}{l} \frac{\dot{\gamma}_{12}}{2} (\alpha_{22} - \alpha_{11}) (1 - \xi(\alpha_{11} - \alpha_{22})) + H \frac{\dot{\gamma}_{12}}{2} - \\ \alpha_{12} \left(C_D \frac{\dot{\gamma}_{12}}{\sqrt{3}} + C_S (h(\alpha))^{a-1} \right) \end{array} \right] \quad (3.30b)$$

$$\dot{\alpha}_{22} = -\alpha_{12} \dot{\gamma}_{12} (1 - \xi(\alpha_{11} - \alpha_{22})) - \alpha_{22} \left(C_D \frac{\dot{\gamma}_{12}}{\sqrt{3}} + C_S (h(\alpha))^{a-1} \right) \quad (3.30c)$$

By definition, the effective strain rate for any loading case is given in terms of the corresponding tensorial components by:

$$\dot{\varepsilon} = \sqrt{\frac{2}{3} \dot{\boldsymbol{\varepsilon}}_{ij} \dot{\boldsymbol{\varepsilon}}_{ij}} \quad (3.31)$$

For this loading case, substituting the values of \mathbf{D}_{ij} from equation (3.28) yields:

$$\dot{\varepsilon} = \frac{\dot{\gamma}_{12}}{\sqrt{3}} \quad (3.32)$$

Again, the evolution equations for grain size, cavitation, isotropic hardening and anisotropic angle remain the same, except that each $\sqrt{3}\dot{\varepsilon}$ is replaced by $\dot{\gamma}_{12}$.

3.4.3 Combined Tension-Torsion

This loading case is very similar to the simple shear case; and despite the slight differences in the stress and strain rate tensors, the analysis is very much the same. Yet an important feature, which will be further analysed here, is the derivation of an analytical form for the yield surface, experimentally construct using tension-torsion tests. Since the elastic part of deformation is assumed negligible in superplasticity, the material yields at the onset of deformation, where the back stress is zero, and the angle of anisotropy has not yet evolved ($\phi = \phi_0$).

To start with, the loading case is represented by the following tensors:

$$\boldsymbol{\sigma}_{ij} = \begin{bmatrix} \sigma_{11} & \tau_{12} & 0 \\ \tau_{12} & 0 & 0 \\ 0 & 0 & 0 \end{bmatrix} \quad \mathbf{S}_{ij} = \begin{bmatrix} \frac{2\sigma_{11}}{3} & \tau_{12} & 0 \\ \tau_{12} & -\frac{\sigma_{11}}{3} & 0 \\ 0 & 0 & -\frac{\sigma_{11}}{3} \end{bmatrix} \quad (3.33a)$$

$$\mathbf{D}_{ij} = \begin{bmatrix} \dot{\epsilon}_{11} & \dot{\gamma}_{12} & 0 \\ \dot{\gamma}_{12} & \frac{-\dot{\epsilon}_{11}}{2} & 0 \\ 0 & 0 & \frac{-\dot{\epsilon}_{11}}{2} \end{bmatrix} \quad \boldsymbol{\alpha}_{ij} = \begin{bmatrix} \alpha_{11} & \alpha_{12} & 0 \\ \alpha_{12} & \alpha_{22} & 0 \\ 0 & 0 & 0 \end{bmatrix} \quad (3.33b)$$

By substituting in equation (3.5), the following expression for J is obtained:

$$J^2 = \left[\begin{aligned} & \left[(\sigma_{11} - \alpha_{11})^2 + 3(\tau - \alpha_{12})^2 \right] + \\ & c_1 \left[-\cos \phi \sin \phi (\sigma_{11} - \alpha_{11}) + (\cos^2 \phi - \sin^2 \phi) (\tau - \alpha_{12}) \right]^2 + \\ & c_2 \left[\frac{1}{3} (2 \cos^2 \phi - \sin^2 \phi) (\sigma_{11} - \alpha_{11}) + 2 \cos \phi \sin \phi (\tau - \alpha_{12}) \right]^2 + \\ & c_3 \left[\frac{1}{3} (2 \sin^2 \phi - \cos^2 \phi) (\sigma_{11} - \alpha_{11}) - 2 \cos \phi \sin \phi (\tau - \alpha_{12}) \right]^2 \end{aligned} \right] \quad (3.34)$$

This equation represents the general form of the flow potential for the tension-torsion loading case. However, the equation shall be normalised such that $J = \sigma_{11}$ when τ_{12} is equal to zero.

For a given strain rate value, at any point during deformation, the evolution equations can be solved for the values of α_{11} , α_{12} and ϕ . On the other hand, and since equation (3.34) is to be normalised with respect to the flow stress in uniaxial tension (σ_{11}), the flow stress value can be also normalised to unity, so that there is no need to solve the constitutive equations for any of the two stress components σ_{11} and τ_{12} .

To obtain an expression for the yield surface, we simply set $\alpha = 0$ and $\phi = \phi_0$, and rearrange the terms to get:

$$J^2 = A_I \sigma_{11}^2 + A_{II} \sigma_{11} \tau_{12} + A_{III} \tau_{12}^2 \quad (3.35)$$

Normalising with respect to σ_{11} , equation (3.35) becomes:

$$A_I J^2 = A_I \sigma_{11}^2 + A_{II} \sigma_{11} \tau_{12} + A_{III} \tau_{12}^2 \quad (3.36)$$

where:

$$A_I = \left(\begin{array}{l} c_1 \cos^2 \phi_0 \sin^2 \phi_0 + \frac{c_2}{9} (2 \cos^2 \phi_0 - \sin^2 \phi_0)^2 \\ + \frac{c_3}{9} (2 \sin^2 \phi_0 - \cos^2 \phi_0)^2 + 1 \end{array} \right) \quad (3.37a)$$

$$A_{II} = \cos \phi_0 \sin \phi_0 \left(\begin{array}{l} -2c_1 (\cos^2 \phi_0 - \sin^2 \phi_0) + \frac{4}{3} c_2 (2 \cos^2 \phi_0 - \sin^2 \phi_0) \\ - \frac{4}{3} c_3 (2 \sin^2 \phi_0 - \cos^2 \phi_0) \end{array} \right) \quad (3.37b)$$

$$A_{III} = 3 + c_1 (\cos^2 \phi_0 - \sin^2 \phi_0)^2 + 4(c_2 + c_3) \cos^2 \phi_0 \sin^2 \phi_0 \quad (3.37c)$$

Equation (3.36) is a quadratic equation in terms of both σ_{11} and τ_{12} ; so by varying the value of σ_{11} from zero (*pure shear case*) to the yield strength of the material (*pure tension case*), the equation is solved for the value of τ_{12} that corresponds to the state of yielding. Doing so, and plotting the pairs of the corresponding σ_{11} and τ_{12} , the first quadrant of the yield surface is constructed. The other three quadrants are plotted in a similar way, as it will be shown later.

3.4.4 Biaxial Stretching

For the biaxial stretching loading case, schematically interpreted by figure 3.2, proportional loading is assumed. And since strain rate is usually controlled, the relation between the applied strain rates (*and consequently strains*) in the two axial directions is assumed to be linear; that is:

$$\dot{\epsilon}_{22} = k \dot{\epsilon}_{11} \quad \epsilon_{22} = k \epsilon_{11} \quad (3.38)$$

where k is the biaxial strain rate ratio; $k = -0.5$ for the uniaxial loading case, and $k = 1.0$ for the balanced biaxial stretching case.

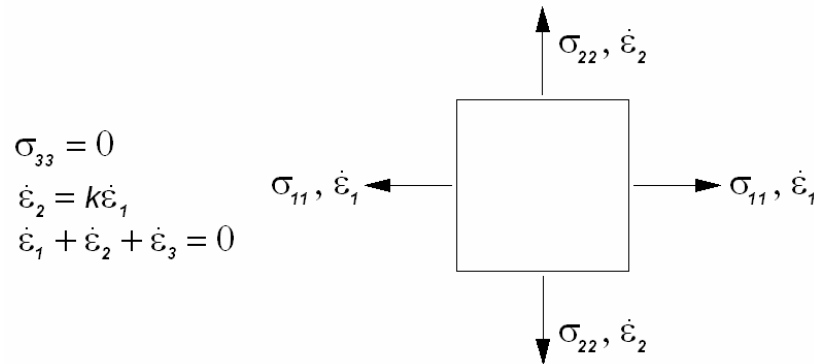


Figure 3.2: Stresses and strains in the biaxial stretching loading case

Since the stress component in the 33 direction is zero, plane-stress loading conditions apply, and can be represented by the following:

$$\boldsymbol{\sigma}_{ij} = \begin{bmatrix} \sigma_{11} & 0 & 0 \\ 0 & \sigma_{22} & 0 \\ 0 & 0 & 0 \end{bmatrix} \quad \mathbf{D}_{ij} = \dot{\boldsymbol{\varepsilon}} \begin{bmatrix} 1 & 0 & 0 \\ 0 & k & 0 \\ 0 & 0 & -(1+k) \end{bmatrix} \quad \boldsymbol{\alpha}_{ij} = \begin{bmatrix} \alpha_{11} & 0 & 0 \\ 0 & \alpha_{22} & 0 \\ 0 & 0 & 0 \end{bmatrix} \quad (3.39)$$

Substituting into the flow rule, two independent equations in the 11 and 22 directions are extracted:

$$D_{11} = \dot{\varepsilon}_{11} = \left[\frac{C_I (J - (K_o + R))^{\frac{1}{m}}}{d^p} + C_{II} J^n \right] \frac{\partial J}{\partial \sigma_{11}} \quad (3.40a)$$

$$D_{22} = k \dot{\varepsilon}_{11} = \left[\frac{C_I (J - (K_o + R))^{\frac{1}{m}}}{d^p} + C_{II} J^n \right] \frac{\partial J}{\partial \sigma_{22}} \quad (3.40b)$$

Similarly, two equations are extracted from equation (3.15) for the back stresses:

$$\dot{\alpha}_{11} = H \dot{\varepsilon}_{11} - \alpha_{11} (C_D \dot{\varepsilon}_{11} + C_S (h(\alpha))^{a-1}) \quad (3.41a)$$

$$\dot{\alpha}_{22} = H k \dot{\varepsilon}_{11} - \alpha_{22} (k C_D \dot{\varepsilon}_{11} + C_S (h(\alpha))^{a-1}) \quad (3.41b)$$

Using the definition of effective strain rate given by equation (3.31), an expression for the biaxial loading case in terms of k is obtained as:

$$\dot{\bar{\varepsilon}} = 2 \dot{\varepsilon}_{11} \sqrt{\frac{1+k+k^2}{3}} \quad (3.42)$$

Deriving an analytical form for the yield surface, experimentally construct by controlled biaxial tests, is similar to the tension-torsion case. Starting with equation (3.5), and feeding in the different tensor components from equation (3.39):

$$J = \left[\frac{3}{2} \left((S_{11} - \alpha_{11})^2 + (S_{22} - \alpha_{22})^2 \right) + c_1 \left[\frac{M_{11}(S_{11} - \alpha_{11}) + M_{22}(S_{22} - \alpha_{22})}{2} \right]^2 + c_2 \left[\frac{N_{111}(S_{11} - \alpha_{11}) + N_{122}(S_{22} - \alpha_{22})}{2} \right]^2 + c_3 \left[\frac{N_{211}(S_{11} - \alpha_{11}) + N_{222}(S_{22} - \alpha_{22})}{2} \right]^2 \right]^{\frac{1}{2}} \quad (3.43)$$

Setting $\alpha = 0$ and $\phi = \phi_0$, then rearranging the terms of σ_{11} and σ_{22} separately:

$$J^2 = A_{IV}\sigma_{11}^2 + A_V\sigma_{11}\sigma_{22} + A_{VI}\sigma_{22}^2 \quad (3.44)$$

Again, this equation is normalised such that $J = \sigma_{11}$ when σ_{22} is equal to zero:

$$A_{IV}J^2 = A_{IV}\sigma_{11}^2 + A_V\sigma_{11}\sigma_{22} + A_{VI}\sigma_{22}^2 \quad (3.45)$$

where:

$$A_{IV} = \frac{1}{3} \left(\begin{array}{l} c_1 \cos^2 \phi_0 \sin^2 \phi_0 + c_2 (2 \cos^2 \phi_0 - \sin^2 \phi_0)^2 \\ + c_3 (2 \sin^2 \phi_0 - \cos^2 \phi_0)^2 + 3 \end{array} \right) \quad (3.46a)$$

$$A_V = \frac{2}{3} \left(\begin{array}{l} -\frac{3}{2} - c_1 \cos^2 \phi_0 \sin^2 \phi_0 \\ (c_2 + c_3)(2 \cos^2 \phi_0 - \sin^2 \phi_0)(2 \sin^2 \phi_0 - \cos^2 \phi_0) \end{array} \right) \quad (3.46b)$$

$$A_{VI} = \frac{1}{3} \left(\begin{array}{l} c_1 \cos^2 \phi_0 \sin^2 \phi_0 + c_2 (2 \sin^2 \phi_0 - \cos^2 \phi_0)^2 \\ + c_3 (2 \cos^2 \phi_0 - \sin^2 \phi_0)^2 + 3 \end{array} \right) \quad (3.46c)$$

In plotting the first quadrant of the yield surface for the biaxial loading case, varying the value of σ_{11} from zero to the yield strength of the material and solving for σ_{22} might not be enough to cover the whole quadrant; because in many cases, there exist two values for σ_{22} that correspond to a single value of σ_{11} at yielding, and vice versa. For that, σ_{22} is solved for assuming σ_{11} , and for the remaining part of the quadrant, σ_{11} is solved for assuming σ_{22} . The same procedure applies for plotting the other parts of the yield surface in the other three quadrants.

3.5 Model Validation under Various Loading Cases

To calibrate the constitutive model, a large number of data points obtained from different tests is required, in order to evaluate the numerous material parameters. Thereafter, more versatile tests covering various loading condition will be needed to evaluate the capabilities of the proposed model. Therefore, data available in the literature on a specific superplastic material, the Pb-Sn eutectic alloy, is utilised here. Though this alloy has no significance in practical applications; the fact that it behaves superplastically at room temperature makes it very attractive for modelling purposes. As will be demonstrated in the subsequent chapters, testing materials at elevated temperatures is quite challenging, and it is always more favourable to acquire the demanded data by room temperature testing.

3.5.1 Material Parameters

Khraisheh et al. [1995, 1997] carried out a series of mechanical tests on the Pb-Sn eutectic alloy, including simple tension, stress relaxation, strain rate jump, fixed-end torsion and combined tension-torsion tests. Because of the comprehension and adequacy of the tests, in addition to material processing consistency, data extracted from these tests will be the main tool for calibration here.

Starting with strain rate jump tests, the strain rate sensitivity index m was evaluated by the investigators to be 0.5. Note that they are assuming a fixed value, which is quite common, yet not accurate, in superplastic studies. This critical issue will be investigated in details in chapter five, by experimentally highlighting the effects of temperature, strain and strain rate on the variability of this index for the AZ31 magnesium alloy.

Other parameters in the overstress function f given by equation (3.3) (K_0 , C_I and C_{II}) were determined by fitting the equation to the experimental stress/strain rate curve, after reducing it to the uniaxial loading case, and setting both R and α to zero [Khraisheh et al. 1997, Khraisheh and Abu-Farha 2003]. The logarithmic stress/strain rate sigmoidal-shaped curve is shown in figure 3.3; it is shown how the model closely fit the experimental data for the various strain rates.

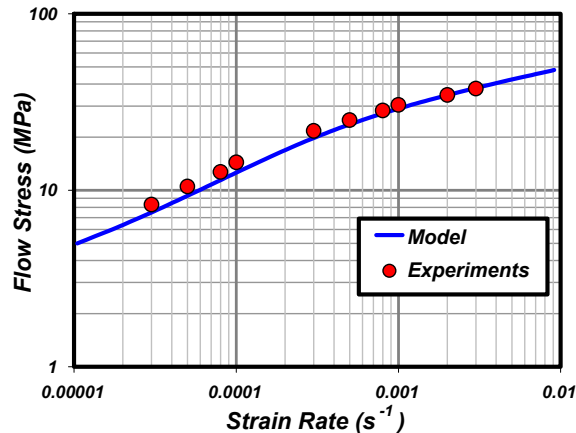


Figure 3.3: Model-generated versus experimentally-constructed stress/strain rate sigmoidal curve for the Pb-Sn Alloy

The anisotropic yield function parameters in equation (3.5) (c_1 , c_2 , c_3 , and ϕ_0) were determined from yield surfaces, constructed using combined tension-torsion tests at different effective strain rates [Khraisheh 2000a, Khraisheh and Abu-Farha 2003]. Other relevant anisotropic parameters, which appear in equation (3.18) describing the evolution of the anisotropic angle (ξ , β & η), were obtained by fitting the measured induced axial stresses in fixed-end torsion tests [Abu-Farha and Khraisheh 2004].

Parameters of the internal variables like static recovery coefficient and exponent, C_S & a , respectively, were extracted directly from the stress relaxation test. H & C_D , on the other hand, were determined later by fitting the experimental stress/strain data at different strain rates [Khraisheh and Abu-Farha 2003].

Grain growth parameters (k_S , g , k_D and τ) were determined by numerically integrating equations (3.10) and (3.11), and fitting them to experimental grain growth data (*some data were also obtained from [Zhang 1996]*). Based on a $5.0 \mu\text{m}$ initial grain size for the material used in these tests, model-generated grain growth curves at different strain rates are shown in figure 3.4 [Khraisheh and Abu-Farha 2003].

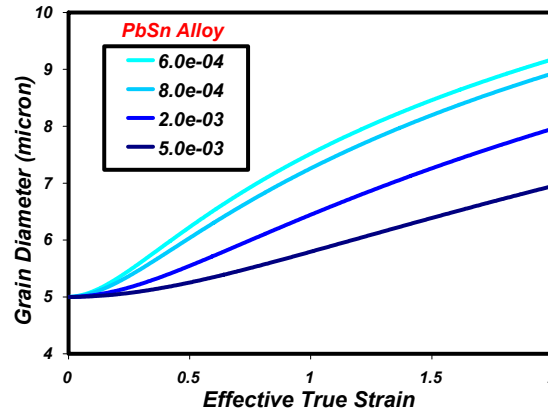


Figure 3.4: Modelled grain growth at different strain rates for the Pb-Sn alloy

The grain size exponent p in equation (3.4) is assumed to be strain rate dependent, in order to be able to accurately capture the stress strain behaviour at different strain rates. At higher strain rates, the superplastic flow stress experiences more significant softening (*more susceptible to necking*) and the grain size exponent is reduced to account for the softening behaviour. By varying the value of p for the different values of strain rate until a good fit is achieved, a relation between p and the strain rate can be obtained. For the Pb-Sn alloy, in the uniaxial and pure shear loading cases, the grain size exponent is approximated by the following expressions, respectively:

$$p = k_1 + k_2 \dot{\epsilon}_{11} + k_3 \dot{\epsilon}_{11}^2 \quad (3.47a)$$

$$p = k_1 + k_4 \dot{\gamma}_{12} + k_5 \dot{\gamma}_{12}^2 \quad (3.47b)$$

where the five coefficients k_i ($i = 1, 2, 3, 4$ & 5) are material constants.

After evaluating the majority of the material parameters, the values of the remaining ones were determined by fitting the model in its reduced forms to the corresponding material behaviour for that loading case. The fitting process is a back and forth routine, and might involve some interaction between two different

loading cases to evaluate specific parameters. But generally speaking, evolution equations are first solved numerically using fourth order Runge Kutta, since some parameters (*like anisotropic angle and kinematic hardening*) are needed to solve the yield function, and therefore plot the yield surfaces. All those variables are then fed into the reduced constitutive equation to obtain the stress/strain curves at various constant strain rate values. The results of the whole fitting process; the different parameters, their values and the means to evaluate them, are all summarised in table 3.1.

A closer look on this modelling effort, and the results obtained by capturing the behaviour of the material at different loading cases, is presented next.

Table 3.1: A list of the material parameters for the modelled Pb-Sn alloy

No.	Parameter	Value	Test / Curve Fitting
Constitutive Equation			
1	m	0.5	Strain Rate Jump Test
2	n	5.5	Stress-Strain Rate Curve
3	K_0	$1.8K_I^{0.5}$	Stress-Strain Rate Curve
4	C_I	$d_o^p (890K_I^{0.75})^{-1/m}$	Stress-Strain Rate Curve
5	C_{II}	$4.408 * 10^{-12} K_I^{-3.25}$	Stress-Strain Rate Curve
6	k_1	0.269	Stress/Strain curves
7	k_2	-500	Stress/Strain curves
8	k_3	-3.0×10^6	Stress/Strain curves
9	k_4	-550	Stress/Strain curves
10	k_5	2.0×10^4	Stress/Strain curves
Yield Function			
11	c_1	1	Yield Surfaces
12	c_2	5	Yield Surfaces
13	c_3	4	Yield Surfaces
14	ϕ_0	30	Yield Surfaces
15	β	1.0	Fixed-End Torsion Tests
16	μ	20	Fixed-End Torsion Tests
17	ξ	-2.0	Fixed-End Torsion Tests
Grain Growth Equation			
18	d_0	5.0	-----
19	k_S	0.04	Grain Growth Curves
20	k_D	6.0	Grain Growth Curves
21	g	3.9	Grain Growth Curves
22	τ	1300	Grain Growth Curves
Evolution Equations for α, R & ϕ			
23	H	80	Stress/Strain curves
24	C_D	15	Stress/Strain curves
25	a	2.2	Relaxation Test
26	C_S	0.006	Relaxation Test

3.5.2 Simple Tension

Model-generated stress/strain curves at different values of strain rate are plotted against the experimental data, obtained from uniaxial tensile tests, in figure 3.5a. As it is clearly shown, a very good fit is achieved, and the proposed model successfully proves its ability to capture the actual behaviour of superplastic flow in the material. Though the model developed by Khraisheh et al. [1997] did successfully capture the same data, yet the modified model presented here introduced a significant improvement in one aspect (*at least for this loading case*). The ability to capture both hardening and softening behaviours at different strain rates, evident in figure 3.5a; this feature is not observed in their fit. It is believed that accounting for grain growth in the model is the main reason for this improvement.

To validate this, the effect of grain growth on the modelled superplastic flow stress was further investigated. A second set of stress/strain curves were model-generated, this time by fixing the value of grain size throughout deformation, and therefore hindering its effects. A comparison between the experimental data and the model-predicted behaviour for both scenarios, with and without grain growth, is shown in figure 3.5b. Clearly, incorporating grain growth into the constitutive model enables it to capture hardening and softening behaviours, hence improving its capabilities.

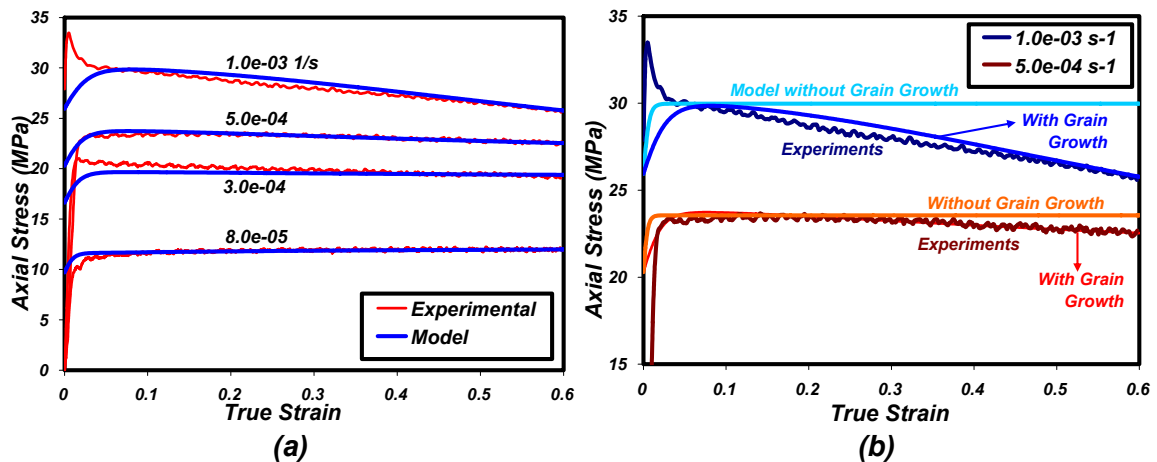


Figure 3.5: (a) Experimentally-obtained vs model-predicted stress/strain curves in simple tension (b) Effect of accounting for grain growth on the model capabilities

It should be mentioned here that the level of softening or hardening can be controlled by the grain size exponent p . And as mentioned earlier, such control would not be possible if p is assigned a constant value. That's why p is made strain rate dependent, as described by equation (3.47).

The second main aspect, after microstructural evolution, that was introduced to the model developed by Khraisheh et al. [1997] is anisotropy. The

influence of accounting for anisotropy in the model is hard to examine in the uniaxial tensile loading case, because simple tension tests do not provide a complete insight about the anisotropic behaviour of the material. All the same, an effort to do so was paid by examining the effect of the initial anisotropic direction ϕ_0 on the simulated stress/strain data, as illustrated in figure 3.6a. Expectedly, the effect is not quite significant, despite the large variation in the value of ϕ_0 . This effect is expected to be more significant for other loading conditions, as will be verified later. The potential for such effect is highlighted here, by turning the attention to the internal stress α (*kinematic hardening*). Figure 3.6b displays a clearer effect of ϕ_0 , for the same strain rate, on α compared to σ . This effect is introduced via $h(\alpha)$ in equation (3.17), which represents the effect of the dynamic yield surface on the internal stress.

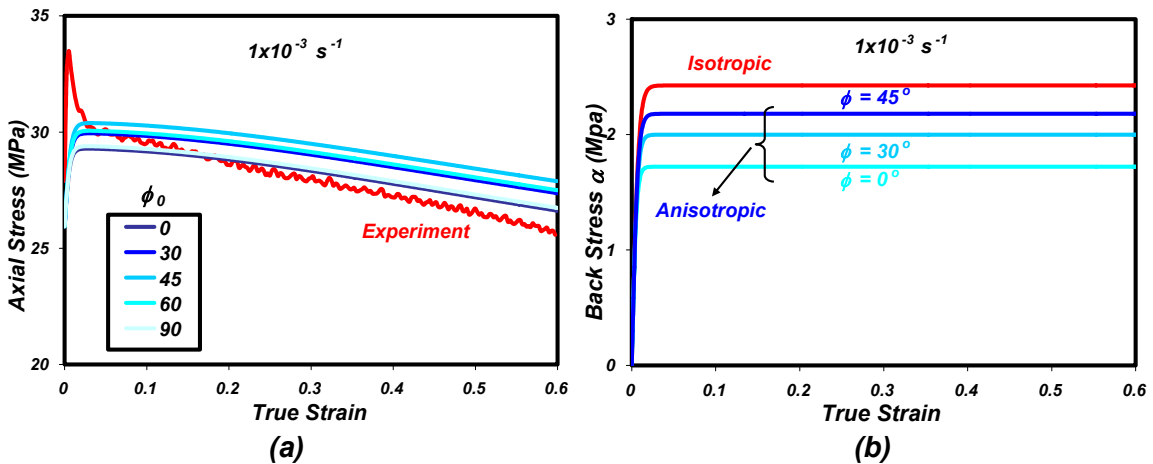


Figure 3.6: Effects of the initial anisotropic angle ϕ_0 on (a) Tensile stress (b) Back stress (kinematic hardening)

3.5.3 Simple Shear

For this loading case, practically embodied by the pure torsion test, the model is to target the behaviour of the Pb-Sn superplastic alloy in two modes. The first one, similar to the simple tension case, is to capture the shear stress/strain curves at various strain rates. The model demonstrates its capability in doing so to a good extent, as shown in figure 3.7. Moreover, accounting for grain growth proves again an enhanced performance, when compared to a previous modelling effort excluding this aspect [Khraisheh 2000b].

The second mode is to predict the induced axial stresses, measured in fixed-end torsion tests, reported by Khraisheh et al. [1995, 1997], and shown in figure 3.8a. Modelling efforts using the isotropic von-Mises yield function were unable to predict these stresses [Khraisheh et al. 1995, 1997]]. However, by using an anisotropic yield function instead, this anisotropy-driven behaviour was detected, as shown in figure 3.8b.

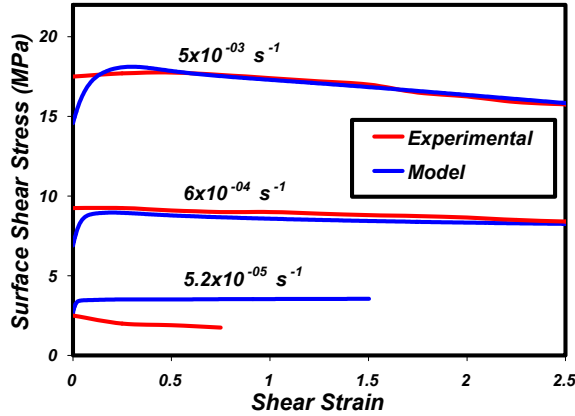


Figure 3.7: Experimentally-obtained versus model-predicted stress/strain curves in pure torsion tests

It can be seen that the model captured the actual trend of the induced axial stresses; they increase to a peak value, near a shear strain of 0.5, and then drop significantly. The model also predicted that for higher strain rates, the induced axial stresses became compressive.

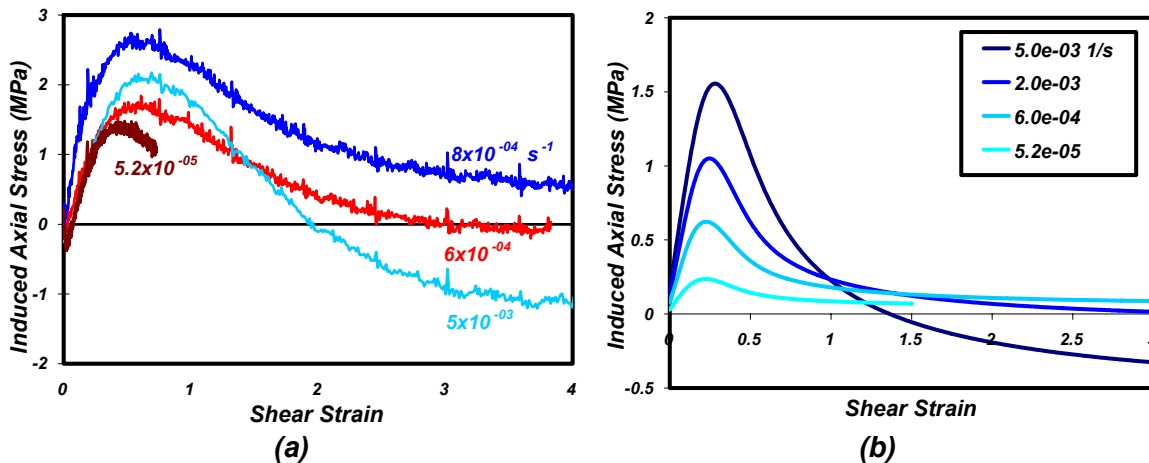


Figure 3.8: Induced axial stresses (a) Experimentally-measured in fixed-end torsion tests (b) Model-generated

Unlike axial stresses in simple tension, induced axial stresses are strongly influenced by the evolution of the anisotropic angle ϕ . Figure 3.9a shows the evolution of ϕ , modelled at different shear strain rates. Shall the anisotropic direction be taken constant (*i.e. ϕ_0 is constant*), the induced axial stresses become compressive, as shown in figure 3.9b. The same trend was reported when the isotropic von-Mises yield function was used in conjunction with the same model framework [Khraisheh et al. 1997, Khraisheh 2000b].

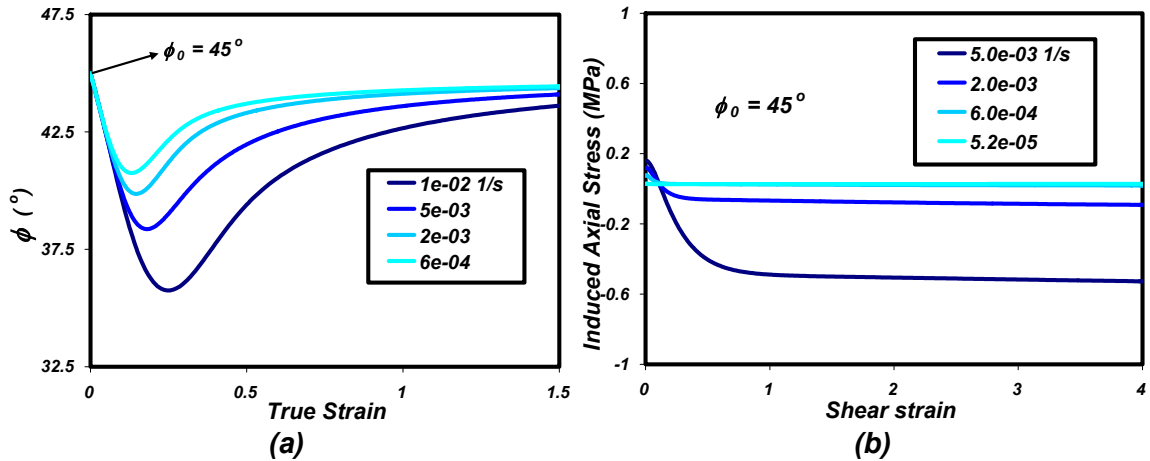


Figure 3.9: (a) Evolution of anisotropic angle ϕ (b) Model-generated induced axial stresses assuming a fixed anisotropic angle

By controlling the evolution of the anisotropic angle, which depends on the anisotropic parameters (ϕ_0 , β , μ & ξ) the shape of the induced axial stresses in figure 3.8b can be controlled. Figure 3.10 provides a closer look on the effect of each of these parameters on the evolution of the anisotropic angle ϕ .

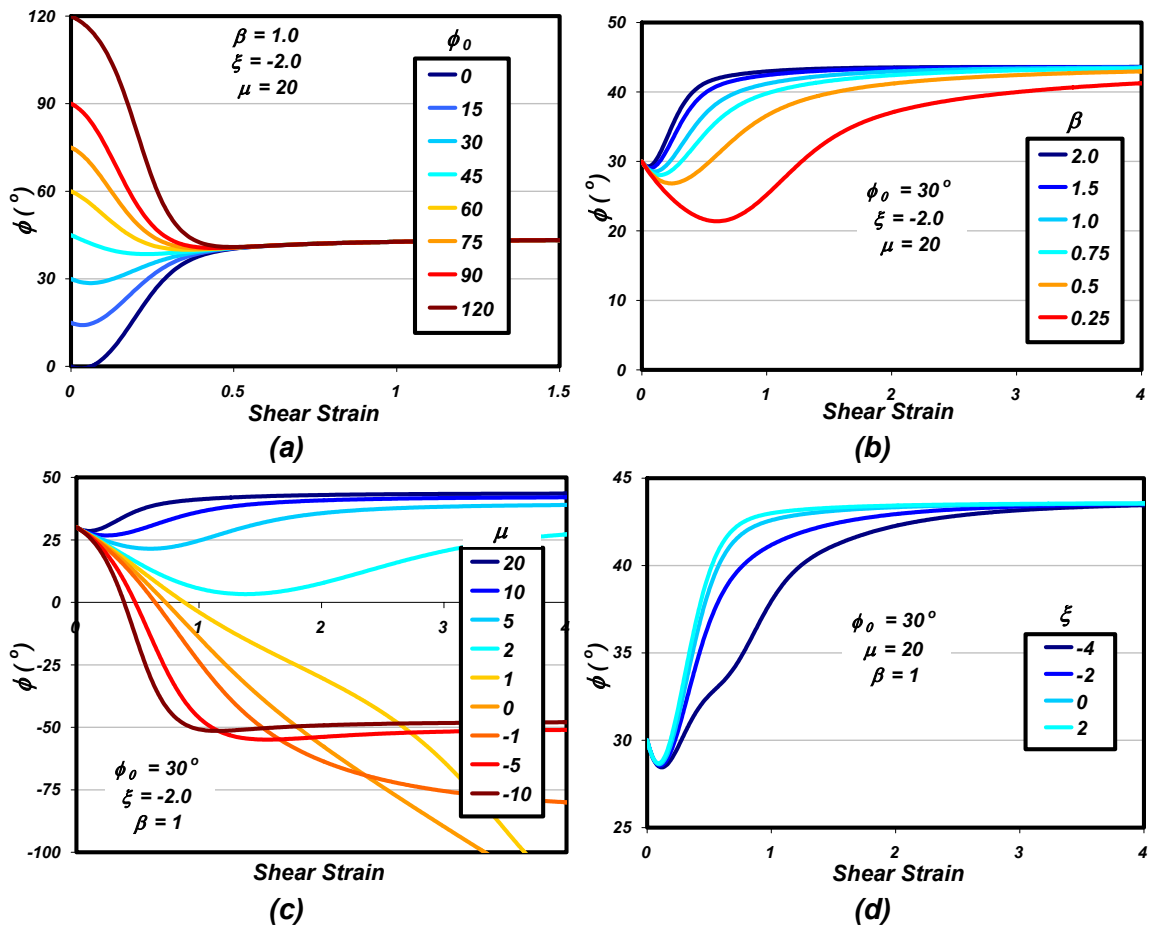


Figure 3.10: Effect of various parameters on the evolution of ϕ (a) ϕ_0 (b) β (c) μ (d) ξ

Consequently, the influences of these parameters on the applied shear stresses and induced axial stresses are shown in figures 3.11 and 3.12, respectively. All these results demonstrate the amount and complexity of the effort put into the fitting process; where the influence of each individual parameter was studied before the summary provided in table 3.1 was made!

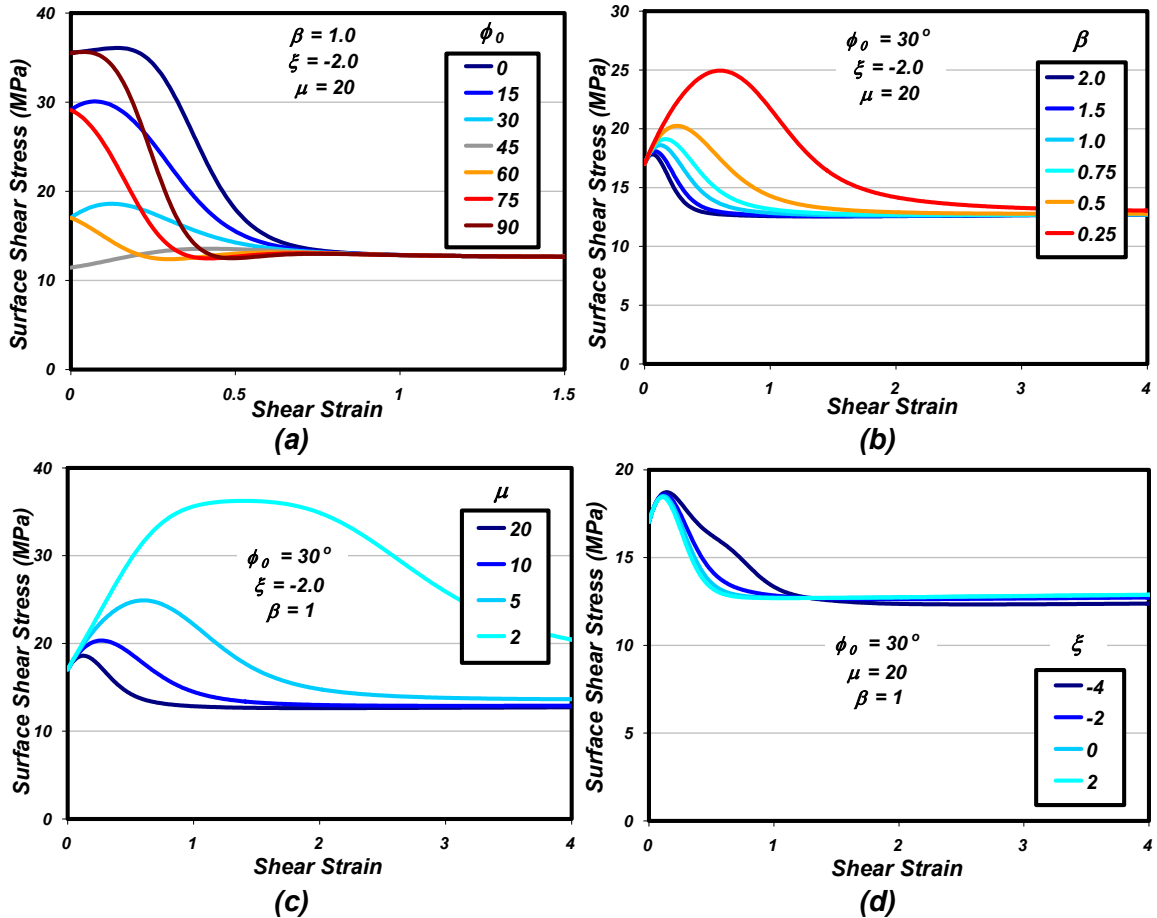
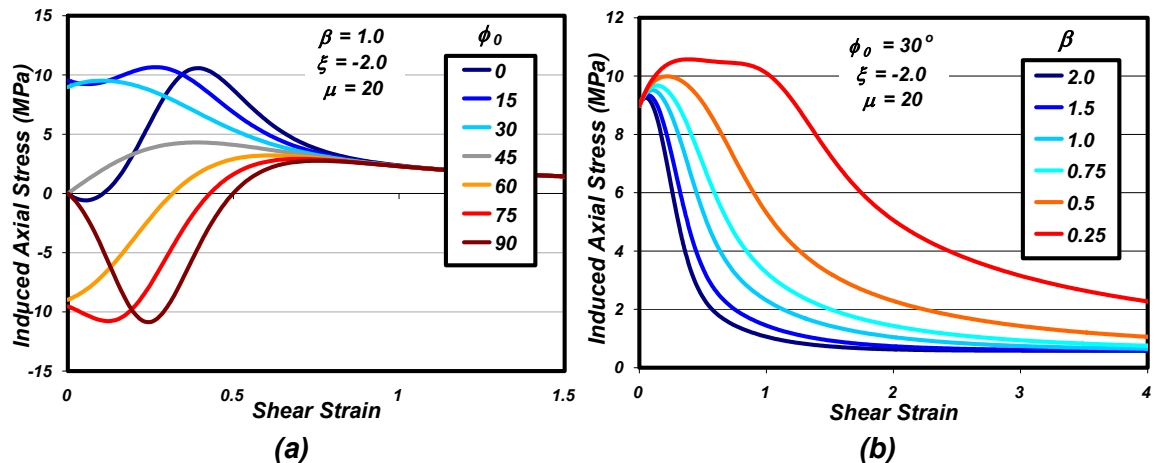


Figure 3.11: Effect of various parameters on shear stresses (a) ϕ_0 (b) β (c) μ (d) ξ



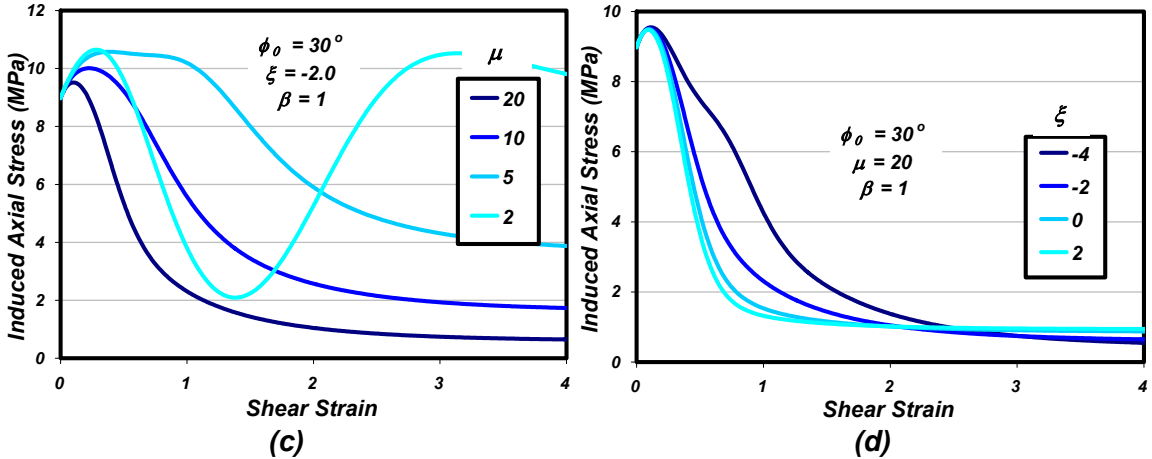


Figure 3.12: Effect of various parameters on induced axial stresses (a) ϕ_0 (b) β (c) μ (d) ξ

3.5.4 Combined Tension-Torsion

Because it involves two loading modes at the same time, tension-torsion test is ideal for constructing the yield surface, and hence test the capability of the proposed anisotropic yield function. To demonstrate that, the anisotropic yield surfaces for two different effective strain rates are plotted against both von-Mises isotropic yield surface and the experimental data in figure 3.13, using the material parameters listed in table 3.1. The divergence of experimental data points from the von-Mises curve is obvious in both cases, indicating the anisotropic nature of superplastic deformation in the model material. Clearly, the proposed anisotropic yield function is more capable (*than von-Mises*) of capturing this behaviour, for the combined tension-torsion loading case.

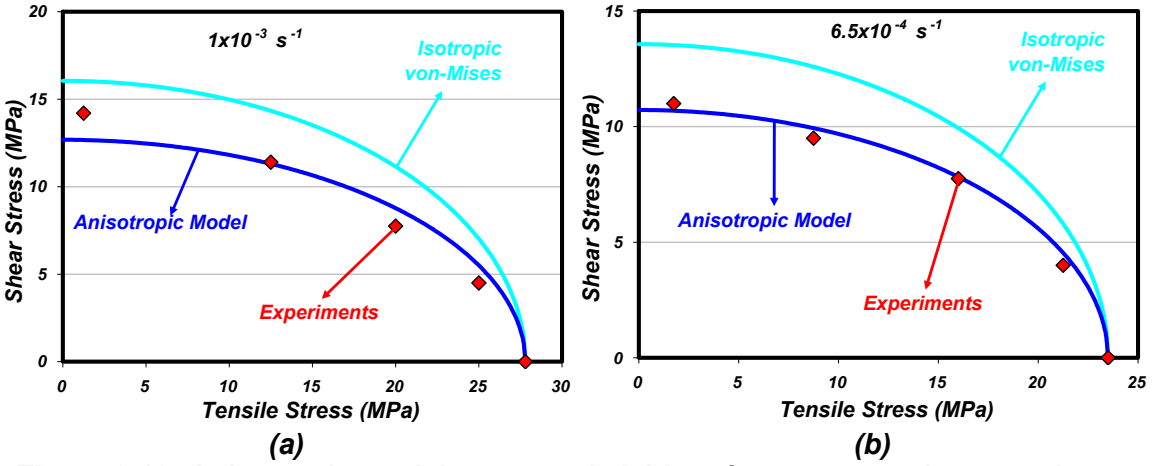


Figure 3.13: Anisotropic model-generated yield surface compared to experiments and isotropic von-Mises at (a) $1 \times 10^{-3} \text{ s}^{-1}$ (b) $6.5 \times 10^{-4} \text{ s}^{-1}$

Similar to anisotropy's influence on the shape of the induced axial stresses in pure torsion, anisotropy's influence in this case, embodied by the distortion of the yield surface and its deviation from the isotropic (*von-Mises*) shape, could be controlled by a combination of the anisotropic parameters, mainly ϕ_0 , c_1 , c_2 and c_3 . An investigation of the effect of each parameter on the shape of the yield surface was carried out; the results are summarised graphically in Figure 3.14.

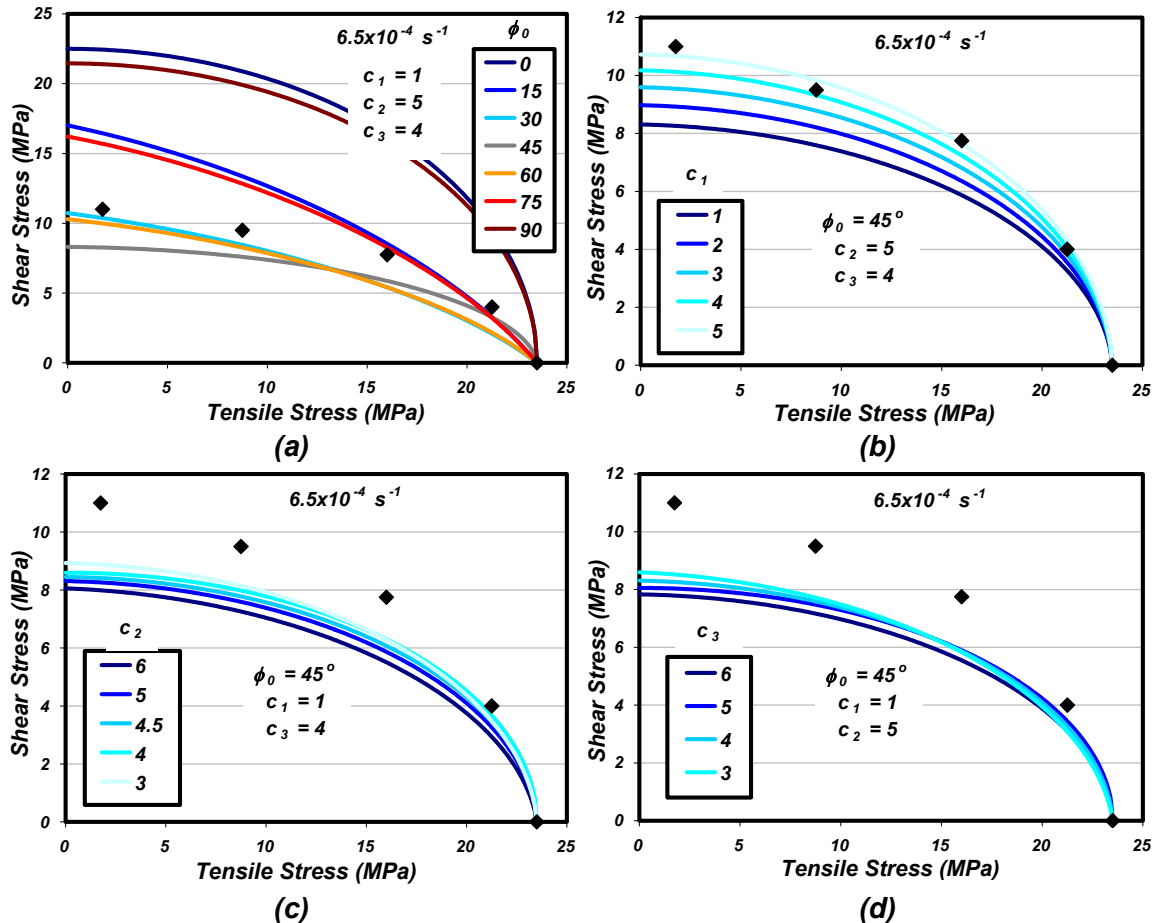


Figure 3.14: Effect of various parameters on yield surfaces (a) ϕ_0 (b) c_1 (c) c_2 (d) c_3

3.5.5 Biaxial Stretching

No experimental data is available in the literature on the biaxial superplastic deformation in the Pb-Sn alloy. In fact, there is no available data of such type for any other superplastic material. That's one of the main motivations behind designing and building a fixture to investigate the issue, as will be described in the next chapter. But at this point, and due to its importance and direct impact on actual superplastic forming practices, there is a need to investigate this loading case.

Luckily, the data available from the other three tests (*simple tension, pure torsion and combined tension-torsion*) were enough to evaluate all the material parameters needed to build the constitutive model. Therefore, and despite the lack of experimental data, the model which proved its capabilities in the previous loading cases, could be used to predict the material's behaviour in the biaxial loading case. In this section, the available tool (*the calibrated model*) is utilised to analyse the influence of both loading biaxiality and material's anisotropy on superplastic deformation. Thence, we go one extra step highlighting the importance, if not the necessity, of an accurate predictive model in the bulge forming process, the most common form of superplastic forming practices.

3.5.5.1 Stress/Strain Behaviour

Based on the analysis presented earlier in section 3.4.4, figure 3.15 shows the two stress components predicted by the model, for different biaxial strain ratios k . For $k = -0.5$, which represents the case of uniaxial simple tension, σ_{11} curve in figure 3.15a is identical to that obtained using the one dimensional form of the constitutive model, shown earlier in figure 3.5a. It agrees, therefore, with the experimental stress/strain curve, also shown in figure 3.15a.

For isotropic materials, one would expect a zero value for σ_{22} , since $k = -0.5$ implies no stress in the transverse direction (*the ϵ_{22} direction*). However, as shown in figure 3.15b, the value of σ_{22} is not zero, which is an indication of deformation-induced anisotropy. This observation is very similar to the induced axial stresses measured in fixed-end torsion tests, and predicted by the model in section 3.5.3 (*figure 3.8*). The model is capable of capturing this behaviour because of the anisotropic dynamic yield function. By setting the anisotropic parameters in equation (3.5) to zero, (*i.e. using the isotropic von-Mises yield function*) and solving the constitutive equations for σ_{22} , zero value was obtained.

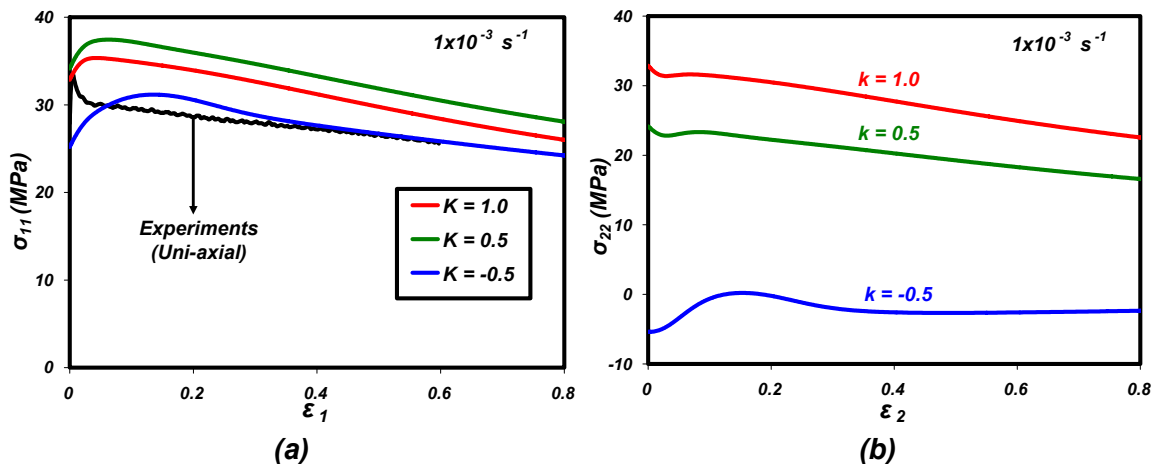


Figure 3.15: Model-predicted stress/strain curves for different biaxial strain ratios k (a) σ_{11} vs ϵ_{11} (b) σ_{22} vs ϵ_{22}

Another interesting result can be observed by considering both parts of figure 3.15; for the case of balanced biaxial stretching, which corresponds to $k = 1$, σ_{11} and σ_{22} are not equal. This can be also attributed to anisotropy, since the values of σ_{11} and σ_{22} were found to be identical when the anisotropic parameters were set to zero.

3.5.5.2 Yield Surface

J in equation (3.5) defines the effective stress, which reduces to the tensile flow stress of the material for uniaxial loading condition. Assuming that the flow stress is the same in the longitudinal and transverse directions, the yield surface in the $\sigma_{11} - \sigma_{22}$ plane can be constructed for a given effective strain rate. Figure 3.16 shows the normalised anisotropic yield surface for different initial anisotropic angles ϕ_0 , along with von-Mises yield surface. Only two quadrants are shown due to symmetry, third and fourth quadrants are mirror-images of first and second quadrants, respectively. It is clear that the yield surface is strongly affected by the anisotropic angle, and since the anisotropic direction may change during deformation, the von-Mises yield surface cannot accurately represent plastic flow during deformation.

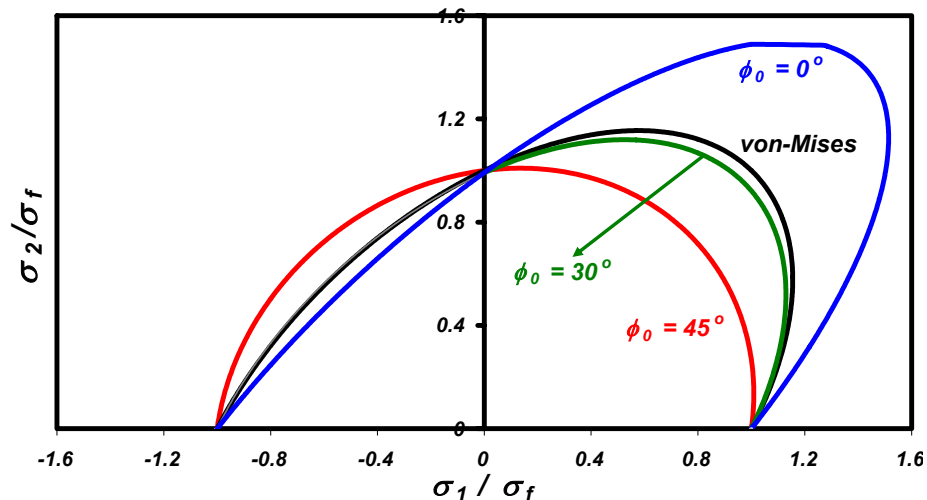


Figure 3.16: Anisotropic yield surfaces for different ϕ_0 values compared to von-Mises

Such changes in the anisotropic direction are strongly affected by various parameters; figure 3.10 showed the effects of some anisotropic parameters on it. For the biaxial loading case, another parameter arises; the biaxial strain ratio k . The evolution of the anisotropic angle for various values of k is shown in figure 3.17. The evolution of the anisotropic angle along with the evolution of the internal state variables can be used to predict the evolution of the yield surface during deformation.

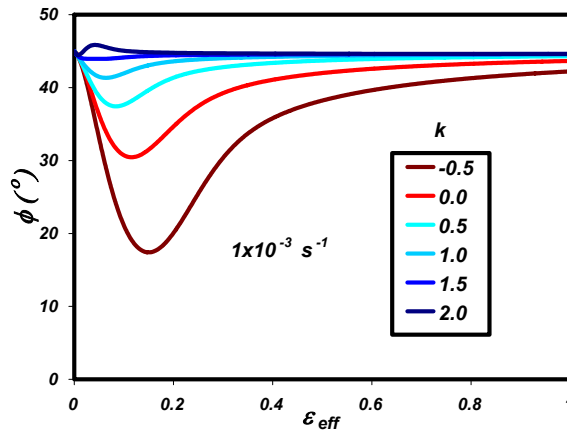


Figure 3.17: Effect of k on the evolution of ϕ

3.5.5.3 Bulge Forming

Since most superplastic materials are formed in bulge forming using pressurised gas, the selection of the forming pressure-time profile is very critical to achieve the maximum deformation without failure. Except for very few cases, where the geometry is simple and an analytical relation can be derived, forming pressure-time profile cannot be generated without finite element (FE) analysis. And because of the limited predictive capabilities of the available constitutive models, FE simulations cannot be expected to be accurate. That's why current industrial forming practices are often based on trial and error methods; and the advantages of FE simulation for optimisation purposes are not utilised. In chapter six this particular issue will be targeted, and the model presented throughout this chapter will be embedded, along with a stability criterion, in a FE code to optimise the process. Yet, in this last part of the chapter, the free bulge forming of circular superplastic sheets is considered, and the critical need for accurate modelling tools, even for such a simple geometry, is highlighted [Abu-Farha and Khraisheh 2005a].

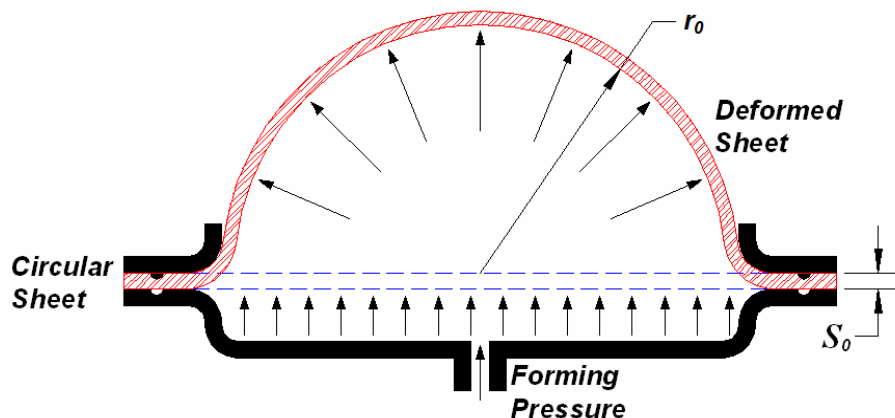


Figure 3.18: Schematic of the free bulge forming of circular sheets

A schematic of the free bulge forming process is shown in figure 3.18, where pressure P is applied at one side of the circular sheet, allowing the formation of a complete hemisphere of radius r_0 on the other side.

Due to its geometrical simplicity, many investigators studied and derived analytical expressions for the pressure-time forming profile [Jovane 1968, Dutta and Mukherjee 1992, Banabic et al. 2001]. Yet, these geometry-based models are still not quite accurate, because they are based on many assumptions concerning the material behaviour, mainly isotropic behaviour.

Most of the previous work on the free bulging of circular sheets assumes balanced biaxial plane-stress condition, and constant effective strain rate at the pole of the formed dome; implying the formation of a perfect hemisphere (*idealised case*) [Woo 1964, Holt 1970, Dutta and Mukherjee 1992, Carrino and Giuliano 1997, Ding et al. 1997, Dutta 2004]. However, it was shown in figure 3.15 that stresses in the two planar directions are not necessarily equal in the case of balanced biaxial stretching ($k = 1$), if anisotropy is taken into account. Therefore, it is possible that the unequal stresses will cause some sort of distortion, and instead of forming a perfect hemisphere, an ellipsoidal shape is generated. Yang and Mukherjee [1992] have shown that free bulging of circular sheets of superplastic materials with different strain rate sensitivities produces different shapes that deviate from the expected perfect hemispherical one.

As a result, for an anisotropic behaviour, it is not true to assume balanced biaxial stresses at the pole of the dome; also, it is not accurate to assume balanced biaxial strains and consequently a perfect hemisphere to be formed. In the following discussion, the two cases, of assuming balanced biaxial strains versus balanced biaxial stresses at the pole of the dome, are considered. The difference and hence the impact of the two approaches on the generated pressure-time profile is investigated.

Balanced Biaxial Strains at the pole

In the first scenario, the effective strain rate at the pole is kept constant at $2 \times 10^{-3} \text{ s}^{-1}$, and the strains (*and consequently strain rates*) in the two planar directions are assumed to be equal ($k = 1$). As a result, a perfect hemisphere of radius r_0 is expected to be formed. But, since we are accounting for anisotropy, the corresponding stresses will not be equal.

Siegert et al. [2003] used a theoretical model developed by Banabic et al. [2001] for the forming pressure-time profile in bulging magnesium sheets into elliptical dies. The same model, which has the form shown below, is used here since it includes both the biaxial stress ratio (*explicit*) and strain ratio (*implicit in the effective strain rate*):

$$P = 2 \frac{S_0 \sigma_{eff}}{b_0} \frac{1 + \rho \left(\frac{b_0}{a_0} \right)^2}{\sqrt{1 - \rho + \rho^2}} \left(e^{\frac{(2-\rho)}{2\sqrt{1-\rho+\rho^2}} \dot{\epsilon} t} - 1 \right)^{\frac{1}{2}} e^{\frac{-3}{2\sqrt{1-\rho+\rho^2}} \dot{\epsilon} t} \quad (3.48)$$

where P is the forming pressure, S_0 is the initial sheet thickness, a_0 & b_0 are the long and short semi-axes of the elliptical die, σ_{eff} is the effective stress, ρ is the biaxial stress ratio ($\sigma_{22} / \sigma_{11}$) and t is the forming time.

For the case of a perfect hemisphere ($k = 1$), a_0 & b_0 are equal ($a_0 = b_0 = r_0$), and ρ is obtained from the results of the previous analysis (figures 3.15). Substituting in equation (3.48) yields:

$$\frac{Pr_0}{2S_0} = \sigma_{eff} \frac{1 + \rho}{\sqrt{1 - \rho + \rho^2}} \left(e^{\frac{(2-\rho)}{2\sqrt{1-\rho+\rho^2}} \dot{\epsilon} t} - 1 \right)^{\frac{1}{2}} e^{\frac{-3}{2\sqrt{1-\rho+\rho^2}} \dot{\epsilon} t} \quad (3.49)$$

For comparison, equation (3.49) is plotted at three different conditions:

- (i) without anisotropy nor grain growth
- (ii) with anisotropy but without grain growth
- (iii) with both anisotropy and grain growth.

The three forming pressure-time profiles are shown in figure 3.19a. It is shown that to achieve the same deformation maintaining the same effective strain rate at the pole, less pressure is needed to form the part in the anisotropic case if compared with the amount calculated based on the isotropic von-Mises yield criterion. In addition, and because of its direct effect on stresses, grain growth causes additional drop in the pressure-time profile.

Balanced Biaxial Stresses at the Pole

In the second scenario, the effective strain rate at the pole is kept constant at $2 \times 10^{-3} \text{ s}^{-1}$, and the stresses in the two planar directions are assumed to be equal ($\rho = 1$). Since anisotropy is considered, the corresponding strains will not be equal ($k \neq 1$), and an ellipsoidal-shaped dome is expected to be formed.

For this case, b_0 is the radius of the bulged sheet in the transverse direction (along σ_{22} direction) and the ratio (a_0 / b_0) is the biaxial strain ratio k . Substituting in equation (3.48) again gives:

$$\frac{Pr_0}{2S_0} = \sigma_e \left(1 + \left(\frac{1}{k} \right)^2 \right) \left(e^{\frac{1}{2} \dot{\epsilon} t} - 1 \right)^{\frac{1}{2}} e^{\frac{-3}{2} \dot{\epsilon} t} \quad (3.50)$$

To evaluate k , the foregoing analysis (section 3.5.5.1) was carried out again by setting σ_{11} equal to σ_{22} , and making k the unknown. Since the effective strain rate is fixed, the two equations extracted from the constitutive model (3.40) were solved simultaneously with equation (3.42) to find the three unknowns; σ_{11} , $\dot{\epsilon}_{11}$ and k .

Similar to the first scenario, figure 3.19b shows the three corresponding pressure-time profiles, generated based on the balanced-biaxial stress state. Analogous behaviour is detected, with a more significant pressure drop in the second scenario. The Difference between the results of the two scenarios is highlighted in figure 3.19c, which shows the anisotropic pressure-time profiles of the two cases compared to the isotropic one. The three parts of figure 3.19 suggest that anisotropy causes a reduction in the required forming pressure; this might be attributed to the higher effective stress associated with the anisotropic yield function compared to the isotropic von-Mises one

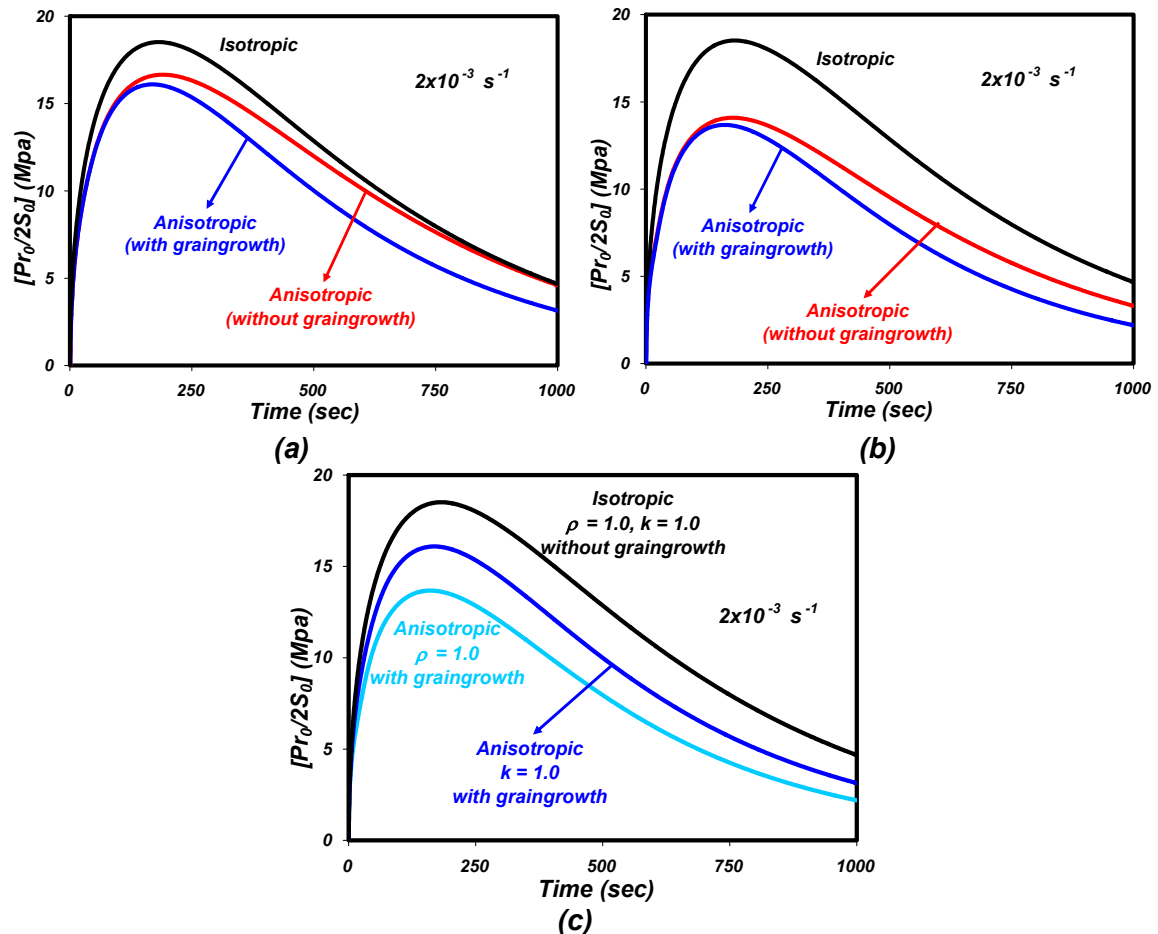


Figure 3.19: The effect of anisotropy and grain growth on the pressure–time profile for (a) Strain-balanced biaxial stretching [$k = 1$] (b) Stress-balanced biaxial stretching [$\rho = 1$] (c) Comparison between (a) and (b)

From equation (3.5), it is clear that for any given stress state (σ_{11} & σ_{22} in the *biaxial loading case*), the value of J (which is equivalent to the *effective stress*) is higher in the case of anisotropy, because of the additional three terms in the equation. These three terms vanish in the isotropic case. If the superplastic material is expected to plastically deform at a certain effective stress (*superplastic flow stress*), lower stresses are needed to achieve that effective stress in the anisotropic case compared to the isotropic one. And because of the direct proportionality between stress and pressure, the forming pressure is therefore lower in the anisotropic case [Abu-Farha and Khraisheh 2005a].

Finally, and to give a graphical representation to the second scenario (*the balanced-biaxial stress*); three different domes corresponding to three different conditions (*possibilities*) were constructed, as shown in figure 3.20. The three domes were formed starting with the same circular sheet, and all of them have identical semi-circular cross section in the *x-direction (the longitudinal axis)*, but they have different cross sections along the *y-axis (the transverse axis)*.

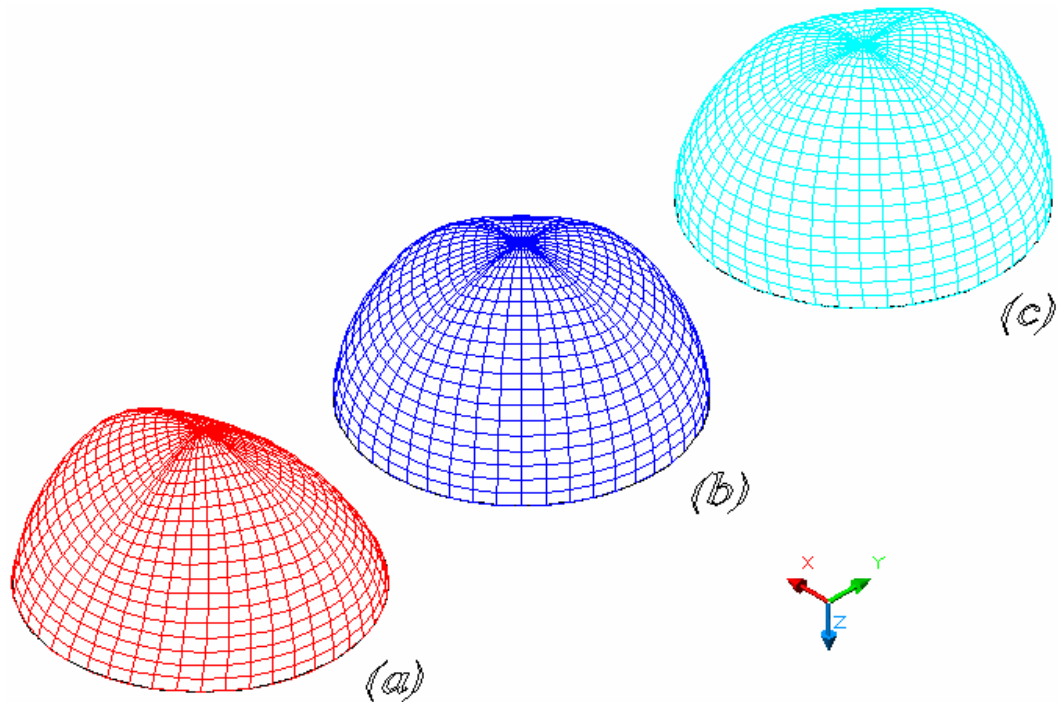
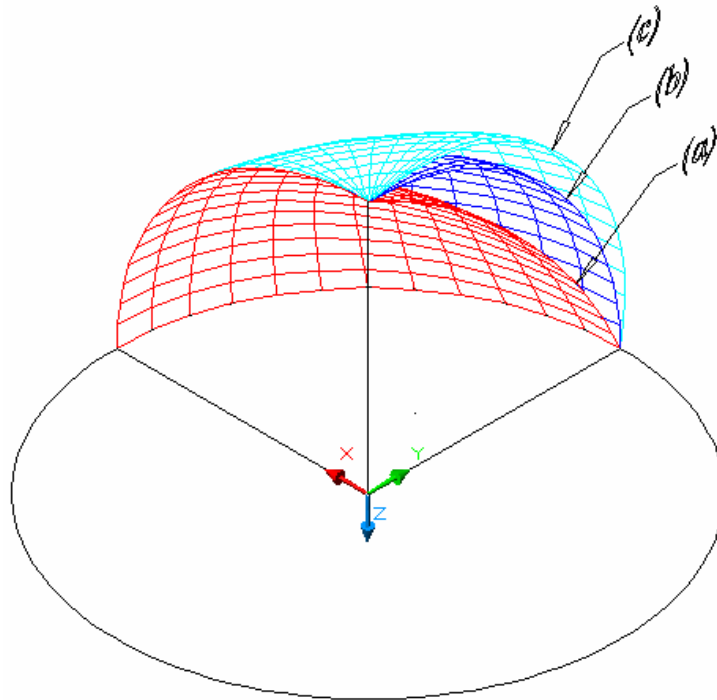


Figure 3.20: Expected shapes of a bulged circular sheet for different values of k
(a) Incomplete hemisphere [$k < 1$] (b) Perfect hemisphere [$k = 1$]
(c) Over-bulged hemisphere [$k > 1$]

A clearer view of the cross sections of all the domes is shown in figure 3.21. The transverse cross section of dome (b) is semi-circular as well, which means that dome (b) is a perfect hemisphere. This implies that strains in the two directions are equal, and k is equal to unity. And since the biaxial stresses were set to be equal ($\rho = 1$), this case embodies the isotropic deformation condition.

For dome (c), the transverse cross section exceeds the contour of a semi-circle, indicating a larger strain in the transverse direction ($k > 1$). On the other hand, the transverse cross section of dome (a) falls below the contour of a semi-circle, indicating a smaller strain in the transverse direction ($k < 1$). As a result, dome (a) might be described as an incomplete hemisphere, while (c) as an over-bulged one. These two cases mirror the anisotropic deformation at two different conditions, depending on the value of k .



**Figure 3.21: Longitudinal and transverse cross sections of the three domes
(a) $k < 1$ (b) $k = 1$ (c) $k > 1$**

4. CHAPTER FOUR: DESIGN AND BUILDING OF EXPERIMENTAL SETUPS

Three mechanical tests were selected to investigate the superplastic behaviour of the AZ31 magnesium alloy at elevated temperatures; uniaxial tensile test, controlled biaxial test and pneumatic bulge forming. This chapter presents the details of the experimental setups designed and built to carry out the abovementioned tests. Due to the lack of accurate guiding standards in the most common of all, the uniaxial tensile test, a closer look on the commonly-ignored testing issues in superplasticity is also given. The remarks made were in fact used in designing the setup employed throughout the majority of this work.

4.1 Uniaxial Tensile Testing at Elevated Temperatures

Uniaxial tensile testing is the most common and the easiest testing procedure for characterising the mechanical behaviour of different materials; that's why it is quite expected to be the first choice in studying the behaviour of superplastic materials. The simplicity in uniaxial tensile testing is reflected by the worldwide standardisation of its aspects; mainly specimen's geometry, gripping and stress/strain measurements. However, this is only true at room temperature; as this simplicity turns into a hard-to-ignore ambiguity when heat becomes involved. And since superplasticity in the majority of material is generally exhibited at elevated temperatures, such ambiguity must be cleared before any attempt to study these materials is made. Several issues which are not important in room temperature testing become unavoidably crucial in high-temperature testing; some of which are:

- i. Specimen's geometry
- ii. Grip's design and gripping method
- iii. Strain measurement
- iv. Load measurement
- v. Thermal expansion
- vi. Heating time

The available published studies do not provide any guidelines on how to account for these issues when testing superplastic material. Although some investigators may have used specialised and custom-made testing setups to account for (*some of*) these issues, the details of conducting those tests are generally not reported. In spite of the vast number of research activities directed towards studying the various aspects of superplastic deformation, there is a lack of a standardised testing procedure that can tackle the various issues associated with high temperature testing. In fact, this is also the reason for the

inconsistency of the published data, even in cases where the same material is used, and the same testing conditions are covered.

The ASTM E21 [2003] sets the standard method for high temperature tensile testing of metallic materials, offering some guidelines for testing superplastic materials. Testing apparatus, specimens, stress/strain measurements, temperature measurement, calibration and testing procedure are covered in the standard. Yet some of the procedure-related issues are not fully explained; to mention here: thermal expansion of the specimen, holding time before straining, and more crucially, the mechanism by which gripping/heating and then tensioning are combined. Above all, the ASTM E21 is a high temperature tensile testing standard, and simply cannot be expected to tackle the specific issues of superplastic testing.

The Japanese Industrial Standard (*JIS*) proposed a particular procedure for evaluating the tensile properties of metallic superplastic metals in the special report JIS H7501 [2002]. It is considered the first attempt to develop standards for testing superplastic materials. In spite of that, the report does indeed lack the comprehension needed to cover all the controversial issues associated with the nature of superplastic testing at elevated temperatures. Some issues including thermal expansion due to heating, gripping and load cell sensitivity were not addressed. Other important issues were discussed briefly without setting adequate guidelines to control them, as the case with the time required for heating prior to straining. Finally, some of the guidelines that were selected may be a subject of controversy, for example:

- i. Characterising the superplastic region by a minimum of 300% elongation!
- ii. Setting the constant cross-head velocity test as the standard way for the application of load!
- iii. Evaluating the strain rate sensitivity index from the logarithmic stress/strain rate curves, and not strain rate jump tests!

In this section, the issues of high temperature tensile testing are highlighted, accentuating on the need for developing standards for testing superplastic materials. As the main block for testing, and since available testing methods and grip designs fail to provide the required accuracy for high temperature tensile testing, a new set of grips were designed, built and then tested over several stages, in order to eliminate or minimise the associated problems to a very good extent. Moreover, the effects of various testing procedures and parameters on the accuracy of test results are investigated. The testing methodology proposed here aims at adequately covering the issues ignored in testing superplastic materials; from apparatus, grips and specimen geometry, to detailed experimental procedures and data recording.

4.1.1 Testing Machine and Heating Chamber

The equipment used to conduct the tensile tests throughout this study is the *INSTRON 5582* universal load frame, rated up to ± 100 KN load. An electrical resistance heating (*environmental*) chamber that provides a maximum temperature of 610 °C, maintaining a temperature variation of ± 1 °C, is mounted on the load frame to allow for elevated temperature testing. The chamber can be easily mounted on or taken off the load frame, depending on the type of test to be conducted. Two load cells are available for load measurement; a standard high capacity load cell rated to ± 100 KN, and another low capacity one with a maximum loading capacity of ± 5 KN. Generally speaking, and unless otherwise stated, the low capacity load cell was used throughout this work for elevated temperature testing to enhance the accuracy of load measurement, while the high capacity one was used for room temperature testing. A photo for the heating chamber mounted on the load frame is shown in figure 4.1.



Figure 4.1: Load frame equipped with a heating chamber

4.1.2 Standard Grips and Related Gripping Issues

The *INSTRON* testing machine is equipped with a set of grips designed to withstand elevated temperatures during testing. Each grip utilizes two sliding wedge-shaped grip inserts that apply pressure on the surface of the test specimen, causing the gripping action. The inner surface of each of the two matching grip inserts is knurled to guarantee firm gripping and eliminate slippage. Test specimens were first machined with a simple geometry, derived from those used in room temperature testing. The aforementioned grip and test specimen are shown in figure 4.2. Such a specimen's geometry is typically used by superplastic investigators, because of the short gauge length and small fillet radius, which suits the nature of superplastic testing. These grips were first used to perform a number of tensile tests under different combinations of temperature and strain rate. However, after a number of tests, a status was reached where some problems escalated to the point at which the grips had to be completely redesigned. The most critical problems are discussed in details next.

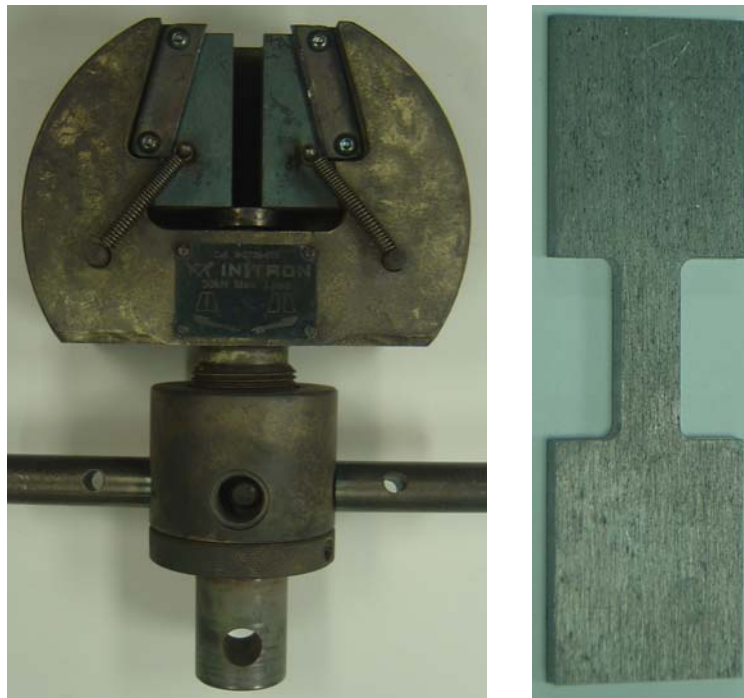


Figure 4.2: INSTRON grip and a simple-geometry test specimen

4.1.2.1 Slippage

The mechanism by which the sliding-action grip inserts work seems to be okay at room temperature. But when the testing temperature was raised, the test specimen was observed to lose contact with the grip inserts and slip out of the grip. This was reflected by an abrupt drop in the stress/strain curve, followed by slippage marks on the surface of the test specimen, as shown in figure 4.3. The

problem was observed to become more serious as the test temperature is raised, due to thermal softening of the test specimen, which caused the gripping pressure to decline down to the point where it is not enough to hold the specimen in place. In addition, material flow out of the grip area into the gauge section of the specimen makes the grip region thinner, and escalates the problem. To minimise the problem, excessive twisting force had to be applied when gripping the specimen, which did not help a lot, but rather caused the next problem.



Figure 4.3: Slippage marks on a test specimen

4.1.2.2 Imposed Twisting Torque

This problem is caused by the mechanism by which these grips work. The grip handle is twisted for the grip inserts to slide outwards, which consequently squeeze and hold the specimen tight in place. But this action imposes some twisting torque on the test specimen, which might affect the uniaxiality of the test. In some cases, and trying to avoid the slippage problem, high twisting caused a permanent distortion in the test specimen.

4.1.2.3 Material Flow

In addition to its effect in reducing the gripping pressure on the test specimen, as explained before; the fact that the material flows from the grip area into the gauge length area implies a sort of distortion in the strain measurements. This is simply referred to that an unaccounted-for material chunk is contributing to the total deformation measured during the test. This issue becomes more observable at higher temperatures, where the material is very soft and less resistive to flow in. Figure 4.4 illustrates how clear and un-ignorable this issue can be.



Figure 4.4: Material flow from the grip region into the gauge length region

4.1.2.4 Gauge Length Issues

This among all was the most serious problem; how to define the exact gauge length? The importance of defining the exact gauge length accurately is reflected directly on the strain measurement, and indirectly on the crosshead beam controlled speed during a constant strain rate test. Figure 4.5 explains the confusion in the gauge length determination, by showing the three possible positions for the test specimen with respect to the grip inserts. With these grips, it is almost impossible to guarantee that the edge of the grip insert matches the shoulder of the test specimen.

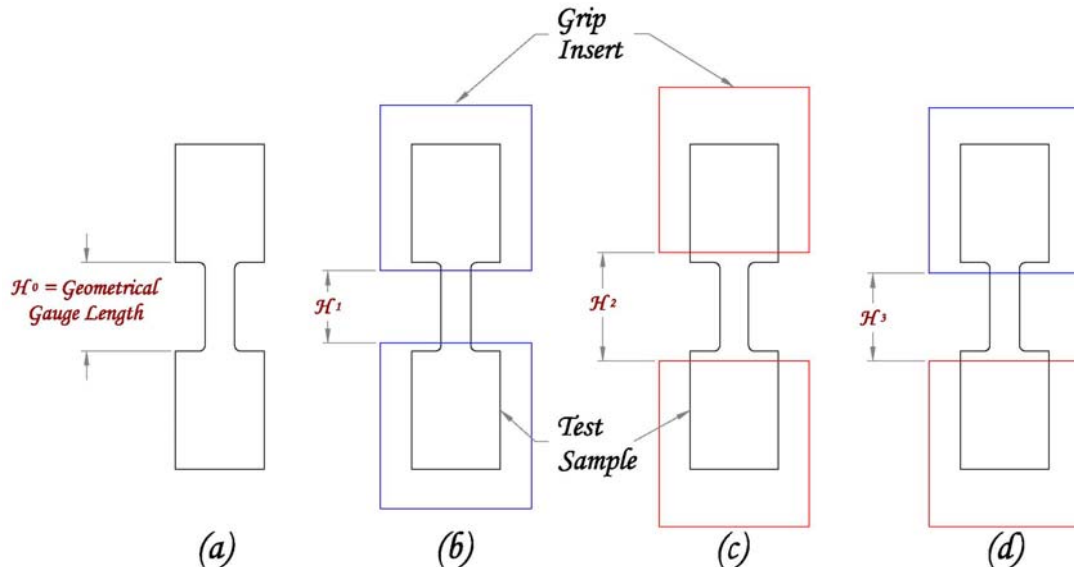


Figure 4.5: (a) Geometrically defined gauge length [H_0] (b) Grip inserts' edges inside the geometrical gauge length [$H_1 < H_0$] (c) Grip inserts' edges outside the geometrical gauge length [$H_2 > H_0$] (d) Combination of (b) and (c)

4.1.3 Modified Testing Grips

The aforementioned issues induced modifying the specimen geometry, in addition to designing & building a new set of grips that minimises or eliminates the highlighted problems. Therefore, by studying the design of the available grips, and the mechanism by which the uniaxial load is exerted on the specimen during the test, the following remarks were outlined:

- i. The tensile load has to be exerted on the shoulders of the specimen, and not applied through friction between the specimen's surface and the grips.
- ii. An alignment pin in the middle of the grip is essentially important.
- iii. The mechanism by which the specimen is gripped should eliminate or minimise any imposed non-uniaxial loads, like torsion or bending.
- iv. A restraint is to be provided at the threshold of the gauge length region to minimise material flow during the test.

Based on these remarks, a new set of grips were designed and built, as shown in figure 4.6. As the schematic drawings show, this design eliminates any possibility for slippage, and leaves no question marks about the actual gauge length, since the specimen is being pulled from its shoulders at both ends of the gauge length region. The cover part of each grip is made slide-able over a set of male/female type rails (*two side and two front*), to assure proper alignment. This also gives the grips the ability to take test specimens of any thickness up to 6.35 mm. With these grips, it is not necessary at all to tighten the grips firmly, because tension force is not applied through the grip/specimen interface. Bolts here act as alignment pins as well.

The presented set of grips has been used to conduct a series of different tests, in which they have proven to tackle the problems faced by the original grips, to a large extent.

The general outlook of the adopted test specimen was shown with the proposed grips in figure 4.6, yet selection of the actual proportions and dimensions was not random, or merely to fit the designed grips. In fact, it was also based on the observations and remarks made when testing the simple geometry shown in figure 4.2. Unfortunately, reviewing the literature was not very helpful in providing a clear guidance in this regard, as the reader would easily notice the numerous number of various specimens the different researchers use in their works, without explaining why that specific geometry was used. The case is still ambiguous, even when it comes to the available standards. The geometry of the specimen used in the JIS H7501 testing method is not justified and raise many questions, especially regarding the gauge length and the large fillet radius. The ASTM E21 [2003] specimen selection is more convincing, yet it does not offer a definite geometry where extensometers cannot be used, as it is the case in superplastic testing.

All the same, to select the proper proportions and dimensions for the test specimen to suit superplastic tensile testing, the following points were considered:

- i. Relatively short gauge length, to allow large deformation, due to the nature of superplastic tests.
- ii. Minimum corner fillet radius, since the gauge length is measured between the two shoulders of the test specimen.
- iii. Adequate shoulder width.

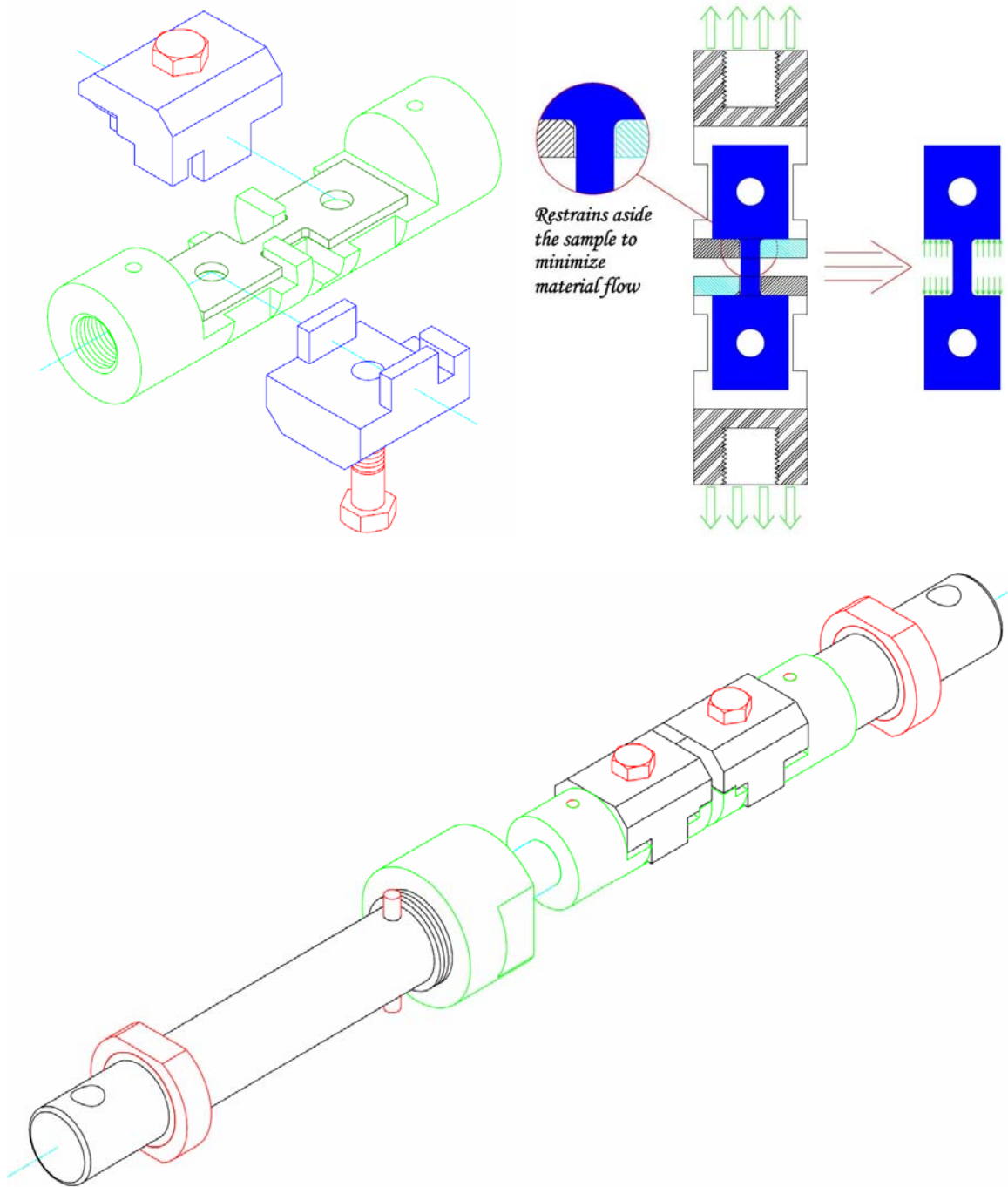


Figure 4.6: Type-I grips for high temperature tensile testing

Accordingly, the detailed type-I specimen geometry is shown with dimensions in figure 4.7.

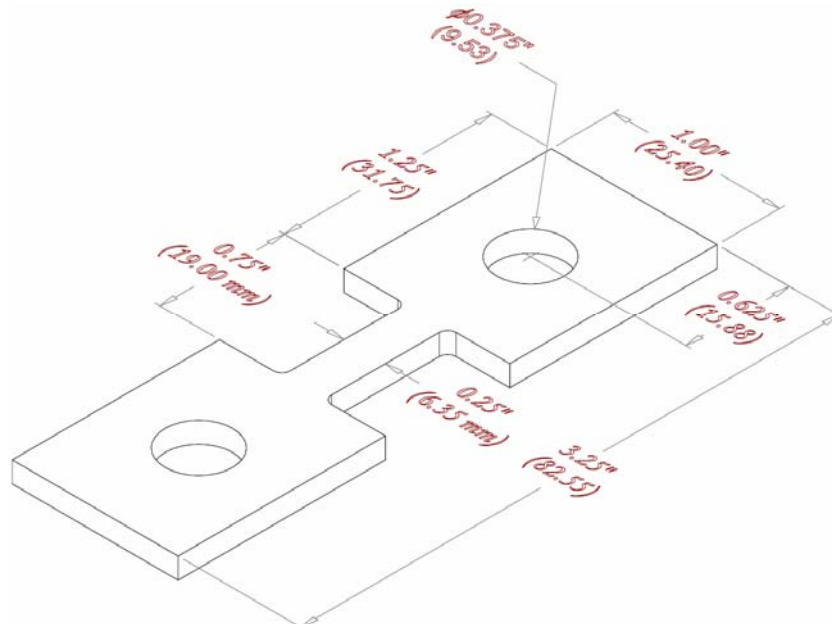


Figure 4.7: Dimensions of type-I tensile test specimen

The presented grips and specimen were utilised throughout the majority of tensile tests conducted in the work. Nevertheless, in the particular case of post-superplastic forming analysis, a need for adequately wide test specimens arose (*will be explained in chapter seven*). Therefore, a second set of grips and test specimen, having basically similar geometries but slightly different dimensions, were designed and build. To distinguish them, the first set is designated as type-I, as highlighted by figures 4.6 and 4.7, while the second is designated as type-II, which is shown in figures 4.8 and 4.9.

Test specimens will be machined at three different orientations, 0° , 45° and 90° , with respect to the rolling direction of the as-received sheet; and they will be designated by the corresponding angle. These orientations are illustrated in figure 6.10. Throughout the subsequent chapters, the 0° oriented specimens will be the default type for tensile testing, unless otherwise stated. The other two specimen orientations will be mainly used for investigating possible directional effects in the material.

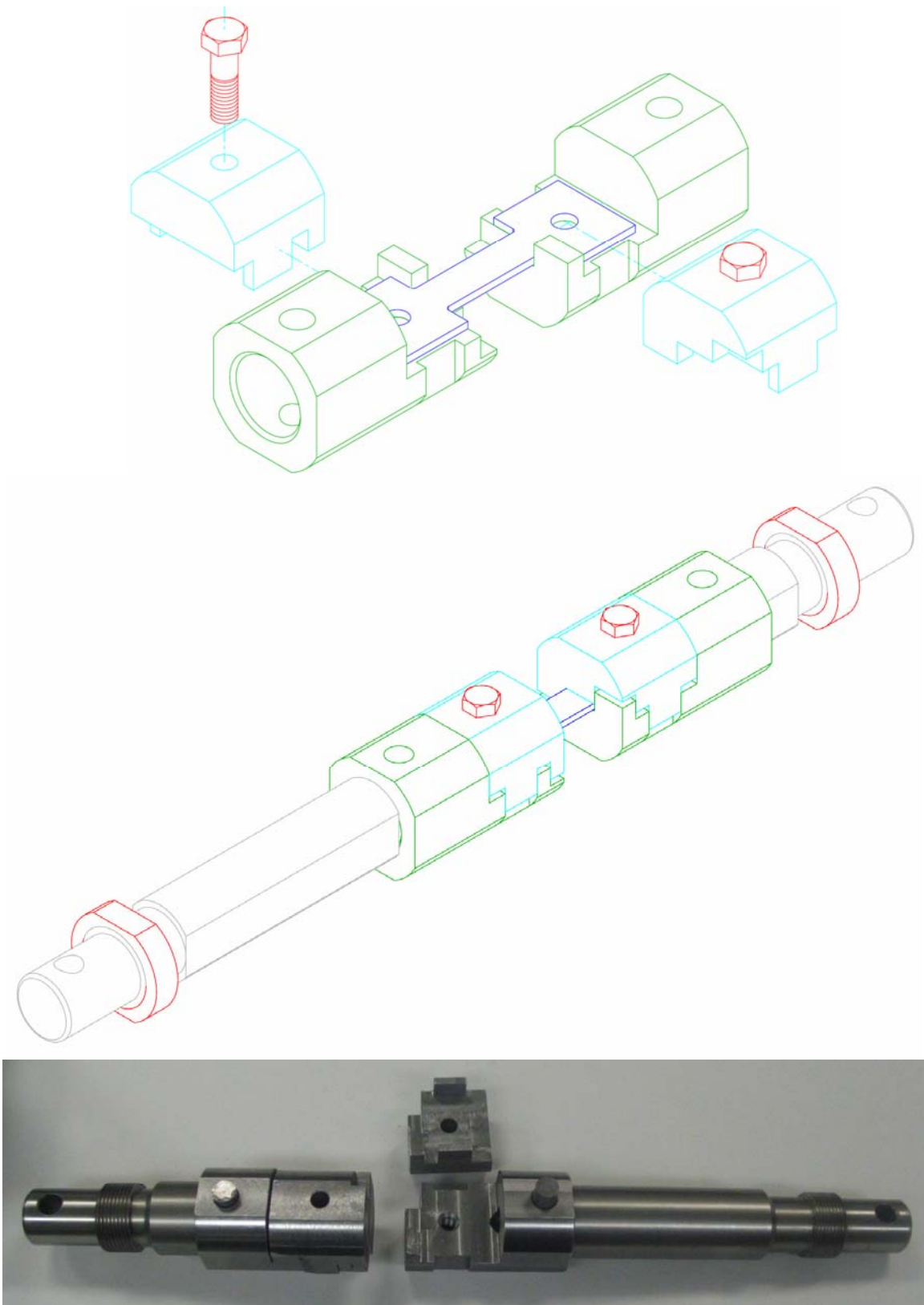


Figure 4.8: Type-II grips for high temperature tensile testing (for post-SPF in particular)

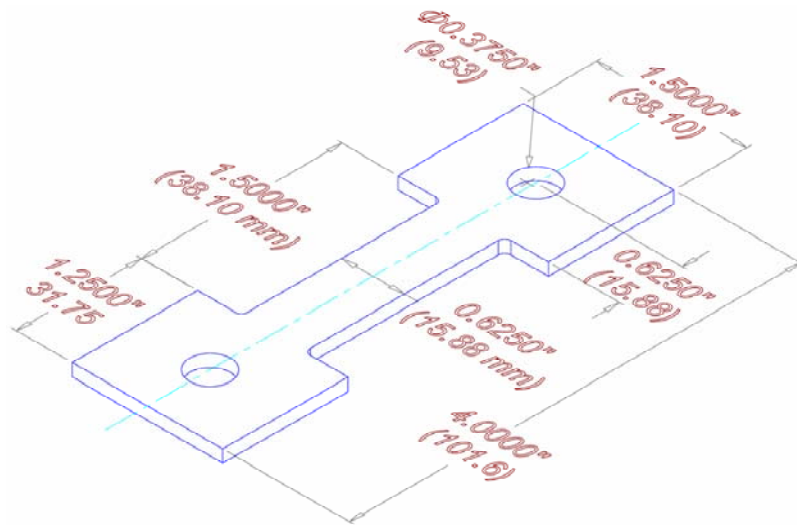


Figure 4.9: Dimensions of type-II tensile test specimen

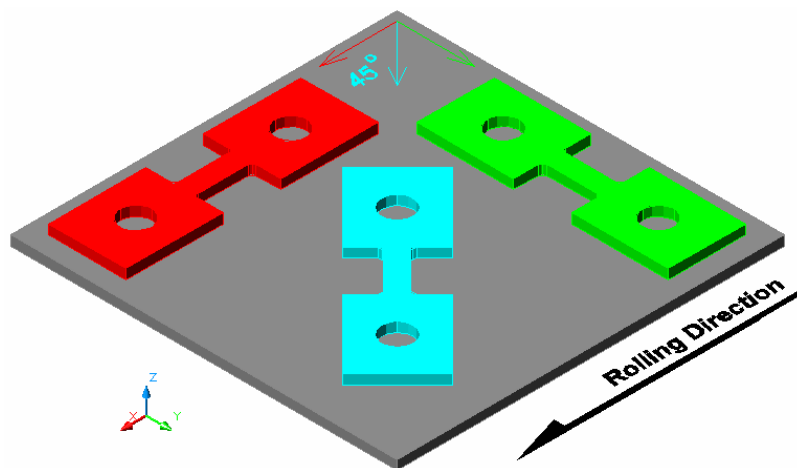


Figure 4.10: Different orientations for machining test specimens with respect to the rolling direction of the sheet

4.2 Effects of Testing Parameters on the Accuracy of Test Results

Before an attempt to set the proper procedure for tensile testing at elevated temperatures is made, an investigation of the effects of various testing parameters is required, which is covered next.

4.2.1 Heating Issues

4.2.1.1 Protecting the Specimen

The first step in high temperature testing would be to bring the test specimen to the desired temperature before straining. Few investigators heat the setup (*grips and adaptors inside the heating chamber*) first, and then insert and grip the specimen when the required test temperature is already established in the chamber. But due to its impracticality and the need to heat the specimen thereafter for sometime anyway, the majority of investigators grip the test specimen and prepare for straining before heating. The problem is, if heating is applied while the specimen is fixed between the lower and upper parts of the grips, thermal expansion of both the specimen and the grips would definitely impose severe compressive loads, which would lead to the buckling and distortion of the test specimen before the test starts. To avoid this, “protect specimen” control option, which is available on most recent universal testing machines, must be applied. This option controls the movement of the cross head beam, to maintain almost zero load on the specimen throughout the heating phase.

4.2.1.2 Thermal Expansion

As just mentioned, the test specimen is expected to expand during the heating phase, thus it is important to evaluate the change in its gauge length, and then, if large enough, account for it in both load application and strain measurements. For a constant cross-head beam speed test, the gauge length value does not affect the loading path during the test. But for a constant true strain rate test, the velocity of the cross-head beam is determined based on the initial gauge length value.

The mean coefficient of linear thermal expansion for polycrystalline magnesium is about $29.9 \mu\text{m}/\text{m}\cdot^{\circ}\text{C}$, for temperatures in the range from 20 to 500°C [ASM Handbook 1999, Tabellenbuch Metall 2001]. For a temperature of 375°C , the maximum thermal expansion the gauge length undergoes was estimated to be 0.19 mm , which is about 1.03% of the original gauge length. Similar estimates were made for some other temperatures, as listed in table 4.1. In order to determine if these values are small enough to be ignored, two tests were conducted at 375°C and $5 \times 10^{-4} \text{ s}^{-1}$; thermal expansion was taken into account in one, and was ignored in the other. The true stress/strain rate curves were almost identical and the variation in the gauge length of the specimen due to thermal expansion did not reveal any significant impact.

Table 4.1: Percentage change in gauge length due to the thermal expansion

Temperature (°C)	Gauge Length Change (%)
250	0.64
300	0.78
350	0.96
400	1.10
450	1.29
500	1.44

It should be mentioned here that the total distance the cross-head beam moved during the heating phase before reaching the thermal equilibrium point (*to be explained later*) was recorded and averaged about 3.25 mm for a number of subsequent tests conducted at 375 °C. This value is much higher than the abovementioned estimate of 0.19 mm, which is quite expected since it accounts for the expansion of the steel components (*grips and adaptors*) too. The mean coefficient of linear thermal expansion for steel is about 0.625 that of that of magnesium [Tabellenbuch Metall 2001], and the ratio of the total length of steel components inside the furnace to the magnesium specimen's length is about 30 to 1. Consequently, the ratio of total thermal expansion in steel to that of the magnesium specimen is about 19 to 1, which leaves the specimen with about 0.17 mm out of the total 3.25 mm. This value is close to the 0.19 mm estimated based on the values listed in table 4.1.

Moreover, for each test thereafter, the actual length of the specimen at fracture was measured and compared to the reading that corresponds to the cross-head beam's movement. The difference was always less than 2%.

In conclusion, the thermal expansion of the specimen was found small enough and can be ignored. In fact, the slight extra length the specimen gains as a result of heating is considered a sort of compensation for the reduced effective gauge length due to the small fillets at both ends.

4.2.2 Effect of heating time on Stress/strain curves

It was described earlier that the test specimen is gripped and then heated till the desired temperature in the chamber is reached, yet this does not guarantee that thermal equilibrium is established in the test specimen. Therefore, a certain period of time must be allowed to reach equilibrium before straining. Interestingly, investigators seem to agree on the necessity of allowing some time for thermal equilibrium, yet they do not agree on the amount, nor provide an explanation of how to identify when it occurs.

In the following discussion, the total heating time is defined as the period from the point when heating starts, until straining is started. The holding time is defined as the time from reaching the desired test temperature until straining is started. The total heating time is the sum of the time it takes the heating chamber to reach the desired test temperature and the holding time.

Some investigators alluded to this issue in different ways. Tan and Tan [2002] heated the specimen to the desired test temperature, followed by 20 minutes holding time to ensure thermal equilibrium, for tests in the range of 250 to 400 °C. Wu et al. [2001] tested the material between 150 to 500 °C, and mentioned the allowance of 20 minutes for stabilising prior to testing. Mohri et al. [2000] carried out their tests at 300 °C, where the specimens required 30 minutes to equilibrate prior to the initiation of straining. Chino et al. [2004] also equilibrated specimens for 30 minutes, yet they tested the material between 300 and 450 °C. For the tests conducted by Jäger et al. [2004] at temperatures ranging between *RT* and 400 °C, each specimen was tempered for 30 minutes. Lee et al. [2005] specified a short period of 60 seconds holding-time before straining, for tests ranging between 250 and 500 °C. Kim et al. [2001] on the other hand, followed a different heating route in their tests between 300 and 410 °C, where the tensile jig was heated first inside the furnace, and then the test sample was inserted into the heated jig and held for 10 minutes before starting the test. Finally, cope et al. [1987] adopted a period of 2 hours of holding time for thermal equilibrium before straining!

From the above review, the following is noted:

- i. The different researchers allowed different holding times to achieve thermal equilibrium in the test specimen.
- ii. Investigators who conducted their tests at different temperatures allowed the same holding time for all temperatures to reach thermal equilibrium.
- iii. None of the available studies provided an explanation on how to determine the necessary holding time, how to practically define thermal equilibrium and why it is important to reach thermal equilibrium before straining.

Unfortunately, and in addition to the previous discussion, neither the ASTM E21 [2003] nor the JIS H7501 [2002] fully tackle this issue. ASTM E21 requires a holding time of no less than 20 minutes as a necessity for thermal equilibrium, without any reference to the material or the test temperature. On the other hand, JIS H7501 left the selection of heating and holding times for the interested parties to agree on, provided that uniform temperature distribution is assured.

In an approach to tackle this critical issue, several uniaxial tensile tests at different combinations of temperatures and strain rates were repeated at the exact conditions, except for the holding time. The effects of holding time on the true stress-strain curves for two strain rates at 400 °C are shown in figure 4.11.

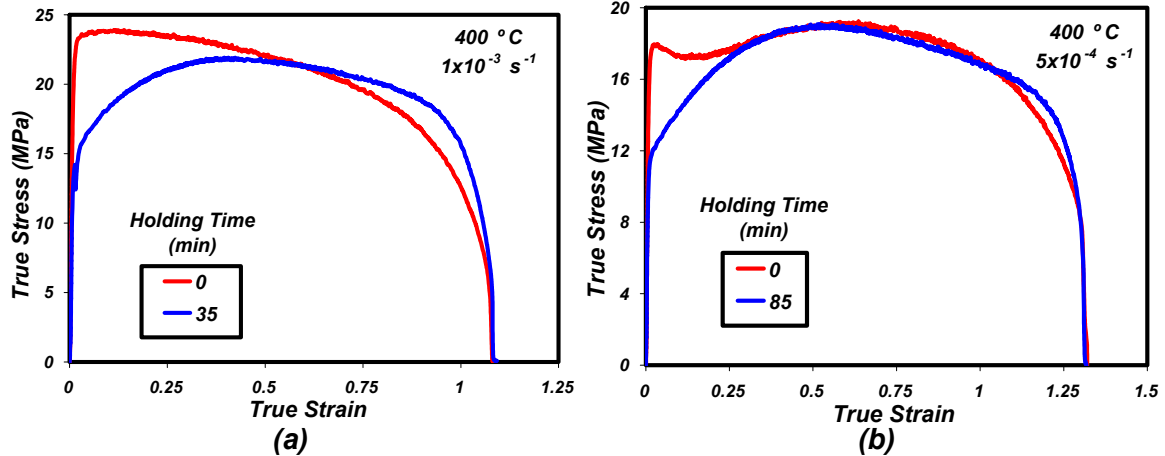


Figure 4.11: Effect of holding time on stress/strain curves at 400 °C and (a) $1 \times 10^{-3} \text{ s}^{-1}$ (b) $5 \times 10^{-4} \text{ s}^{-1}$

Holding time has obviously a significant effect on the flow stress, and similar behaviour was also observed at other temperatures. The differences are particularly clear during the early stages of deformation, where flow stress measurement (*for a particular strain rate*) is usually used to construct the sigmoidal-shaped stress/strain rate curve. In fact, non-realistic strain rate sensitivity values were obtained from a stress/strain rate curve constructed at 400 °C based on tests conducted with no holding time. The effect highlighted by figure 4.11 can be mainly attributed to the static grain growth in the material as a result of maintaining high temperature for long durations. Static grain growth in the AZ31 magnesium alloy was found to increase with holding time (*chapter six*), and hence reduce the flow stress of the material (*chapter seven*).

The heating chamber shown in figure 4.1 provides a maximum heating rate of about 25 °C/min, which decreases gradually to about 2 °C/min at the end of the heating stage. Such a heating rate should guarantee a homogenous temperature distribution in few minutes after reaching the desired test's temperature, due to the small size of the test specimen. On the other hand, the steel components inside the furnace are bulky and hence require longer time to acquire temperature homogeneity. And until that state is reached, the cross-head beam will keep moving to accommodate the ongoing thermal expansion of the steel components, and protect the test specimen.

The seriousness of this issue was detected in tests conducted at very low strain rates. When such tests were started with no (*or not enough*) holding time, the load cell reading indicated compressive loads on the test specimen, simply because the imposed cross-head speed is smaller than the rate at which the steel bulk is expanding.

In conclusion, and based on the previous observations and remarks, the necessary holding time to reach thermal equilibrium was defined as the time

needed for the cross-head beam to stop moving, indicating that thermal expansion is almost ceased. Following this definition, the required total heating time to reach thermal equilibrium for different test temperatures were measured and summarised in table 4.2.

Table 4.2: Holding and heating times corresponding to various temperatures

Temperature (°C)	Holding Time (min)	Total Heating Time (min)
325	23	48
350	25	52
375	27	58
400	30	65
425	34	72
450	38	80
475	43	90

4.2.3 Effect of Heat on Load Cell Measurements

Though it might not seem relevant, the effect of heat on the load cell readings was a serious problem simply because it was unexpected, since the heating chamber is made by the same manufacturer, and built to fit the load frame. The problem was noticed during the low strain rate tests, where it was observed that after fracture takes place, and the two parts of the broken specimen are entirely apart, the load cell reading was not zero. In fact, the load cell reading after fracture exceeded 10 N in many occasions, and reached 29 N in one case. For a test conducted at 10^{-4} s^{-1} and 400 °C , a 10 N force is equivalent to a 0.5 MPa true stress in the early stage of deformation ($\approx 18\%$ of the flow stress), and about 2.65 MPa true stress in the very last stage of deformation ($\approx 48\%$ of the flow stress at that point). Figure 4.12 shows the stress/strain curve obtained from a uniaxial tensile test at 375 °C and $1 \times 10^{-5}\text{ s}^{-1}$. When the specimen fractured, the load cell reading was still 6.2 N , equivalent to 4.3 MPa , or approximately 45% of the flow stress just before fracture.

To further investigate this problem, a tensile test was prepared as usual, with the exception that no test specimen was used; only grips were in position inside the heating chamber. Testing temperature was set to 500 °C , and the applied strain rate was set to zero. Since there is no specimen between the grips, one should expect the load cell reading to stay zero during the test. Surprisingly, the load reading kept increasing gradually, and a maximum value of 58 N was recorded! It became clear that the load cell is experiencing some heat that alters its reading.

To solve the problem, the gap between the shaft and the hole on the upper surface of the heating chamber was minimised by using an insulating material. In addition, a fan was installed next to the load cell, in order to blow any

hot air away from it, and cool the steel shaft where it is connected to the load cell. These modifications minimised the heat effect on the accuracy of load cell readings as illustrated by figure 4.13. Tests were later conducted at temperatures between 325 and 500 °C, and in all cases the reading of the load cell after fracture was never high to indicate 10% of the flow stress before failure.

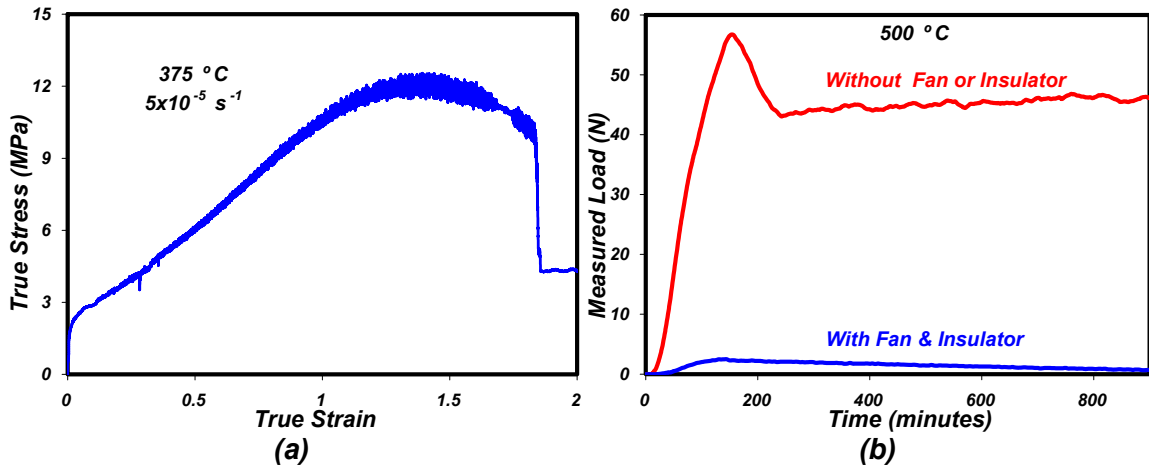


Figure 4.12: Effect of heat on load cell reading (a) Detected by the stress/strain curve at 375 °C and $1 \times 10^{-5} \text{ s}^{-1}$ (b) Measured directly in a zero-load test at 500 °C

4.2.4 Straining Mode; Constant Strain Rate vs Constant Speed

The JIS H7501 [2002] sets the standard way for testing superplastic materials by maintaining constant crosshead speed during deformation, rather than constant true strain rate! Yet, superplastic materials are essentially characterised by their flow stress sensitivity to strain rate, expressed by the sigmoidal-shaped stress/strain rate curve. Figure 4.13 shows the results of two tests conducted at 375 °C and initial true strain rate of $5 \times 10^{-4} \text{ s}^{-1}$. This strain rate value was kept constant during one of the two tests, while the corresponding crosshead speed was maintained constant in the second. The difference between the results is clear and becomes more significant as the deformation progresses.

Furthermore, in order to achieve maximum uniform deformation during SPF, forming pressure cycle is usually designed based on a target strain rate selected from tensile tests. Only constant true strain rate tests must be used in this regard for accurate description of deformation. This will become more important if an optimum loading path based on variable strain rates is used (*chapter six*). Constant cross head speed tests will lead to underestimation of the desired strain rate and will shift the location of the desired strain rate jumps.

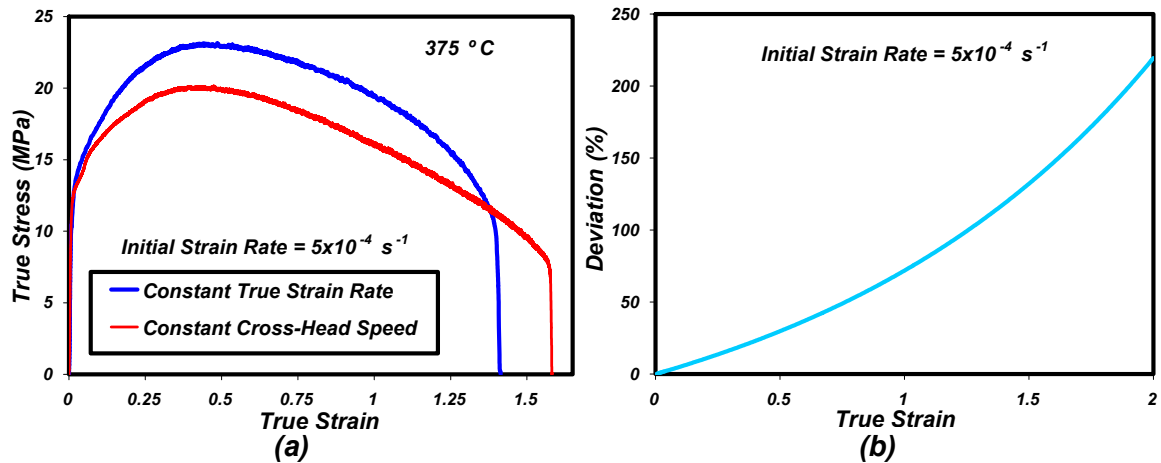


Figure 4.13: (a) Difference between constant strain rate and constant cross-head speed tests (b) Deviation from constant strain rate when applying constant cross-head speed

4.2.5 Testing Procedure

The last step in building a methodology for uniaxial tensile testing of superplastic material is to establish a testing procedure, taking all the aforementioned issues into account. The first step would be fitting the test specimen between the grips inside the heating chamber. Before heating is started, the “specimen protect” controller is set to 2.5 N, and thence activated to allow for thermal expansion without distorting the test specimen. When the desired temperature is reached, some additional holding time is allowed according to table 4.2, thereafter, the test is started by applying the desired strain rate. Stress measurement is directly obtained from the load cell reading. Due to the large superplastic deformation, the lack of high temperature extensometers, and the relatively short gauge length, strain measurement is established from the direct displacement of the cross-head beam.

4.3 Pneumatic Bulge Forming at Elevated Temperatures

As uniaxial tensile testing is essential for studying the behaviour of the material, bulge forming is important for simulating the actual material behaviour during superplastic forming operations. To have this capability, a complete pneumatic operated bulge forming setup was designed and built. The setup consists of two main parts; the controlled pressurised gas line and the forming die assembly.

4.3.1 Controlled Pressurised Gas Line

This part of the setup represents the line stretching from the pressurised gas tank to the forming die assembly. High pressure argon gas is supplied from a 6000 *psi* gas tank to the tubing line after passing a manually-operated pressure regulator, which sets the upper pressure limit. The gas travels through a set of stainless steel tubes to an electronically-controlled pressure regulator, which delivers the desired down stream pressure according to a selected pressure profile. This pressure profile is fed to the regulator by a DAS through a specialised software. To enhance the accuracy of the setup, a closed-loop feedback system is employed with the aid of a pressure transducer placed after the regulator. As the transducer continuously monitors the down stream pressure, the controller compares the feedback signal with the input signal to impose any required corrections. Several pressure gauges are placed at different locations along the tubing line to monitor the pressure. Finally, a two-way ball valve acts as the gate to the forming die, to control when to start and stop the forming operation.

To increase the flexibility of the setup, a sensor inside the regulator can be easily changed to alter the capacity, and hence improve the accuracy, of the regulator based on the application. Therefore, the same line can be operated up to six different pressure limits; 500, 800, 1500, 2500, 4000 and 6000 *psi*. On the other hand, another low pressure line of 120 *psi* maximum pressure was installed, in order to actuate the regulator of the high pressure line. This line is also used in specific forming operations where high pressures are not needed. The two lines are included in a photo for this part of the bulge forming setup, shown in figure 4.14.

4.3.2 Forming Die Assembly

To achieve forming at elevated temperatures, the easiest solution was to design the forming die assembly to fit in whole inside the heating chamber shown earlier in figure 4.1, rather than implementing heating elements inside the die, and then controlling the temperature of the sheet to be formed. A schematic of the forming die assembly is shown, for a particular die geometry, in figure 4.15. The whole assembly is supported by and anchored to the *INSTRON* load frame by means of a custom made adaptor. The die represents the main part of the assembly that defines the shape to be formed. Several dies of various geometries were designed, including square and cylindrical dies with various heights; few samples are shown in figure 4.16. The one shown in figure 4.15 is an open die with a circular cavity, used to free from sheets into hemispherical domes. The pressurised argon gas enters the die cover, which is secured against leak by a simple screw-type clamp, with the aid of a graphite gasket (*sealant*). This configuration creates a chamber on top of the sheet, allowing pressure build-up throughout the forming process.

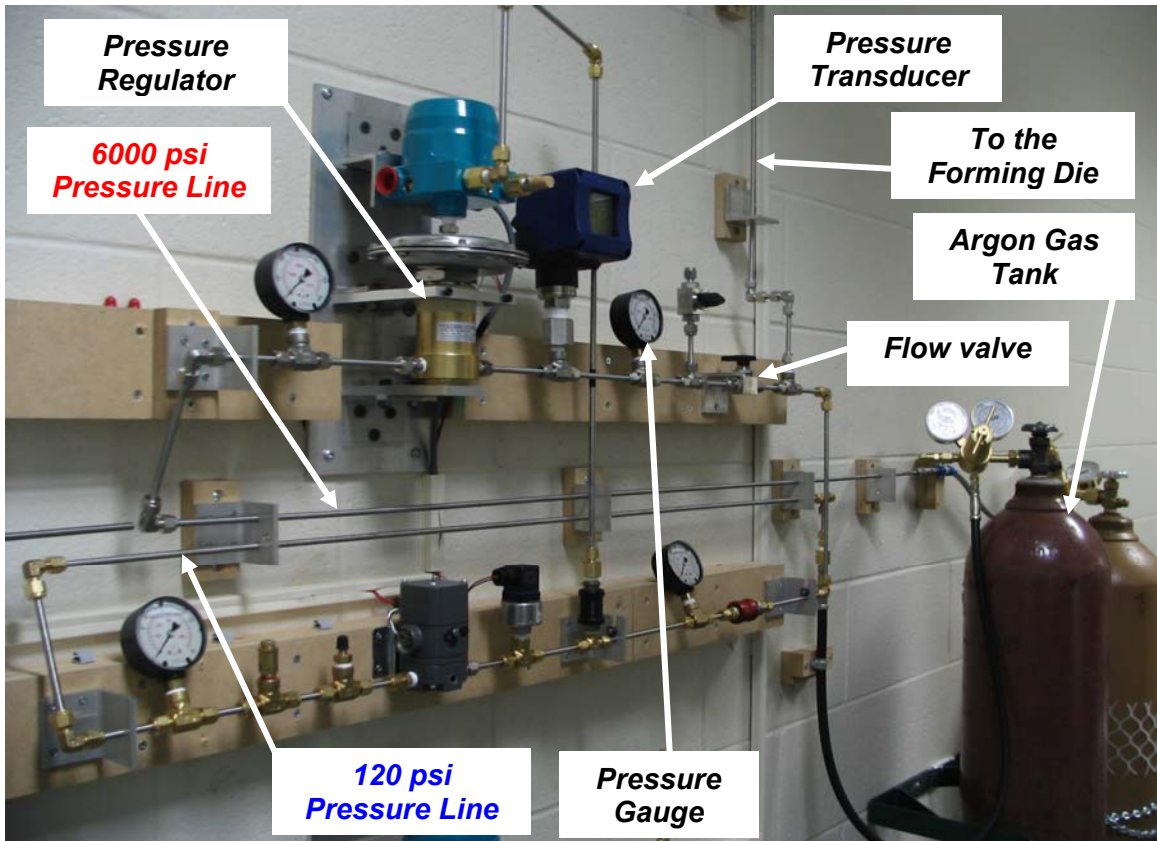


Figure 4.14: Controlled pressurised gas lines with 120 & 6000 psi capacities

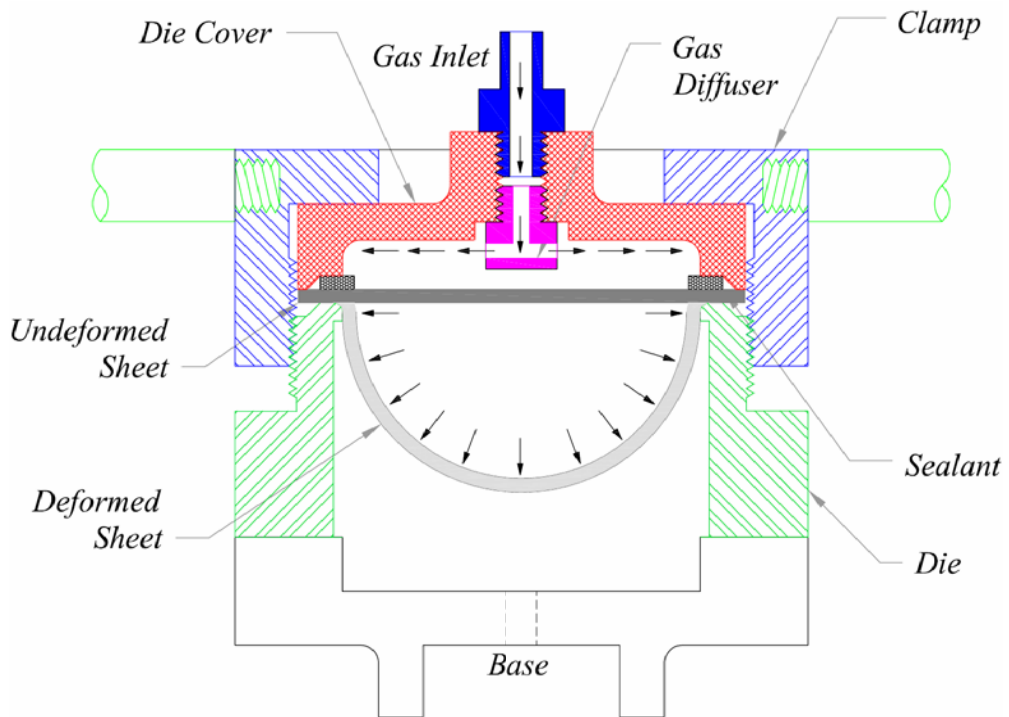


Figure 4.15: Schematic of type-I forming die assembly

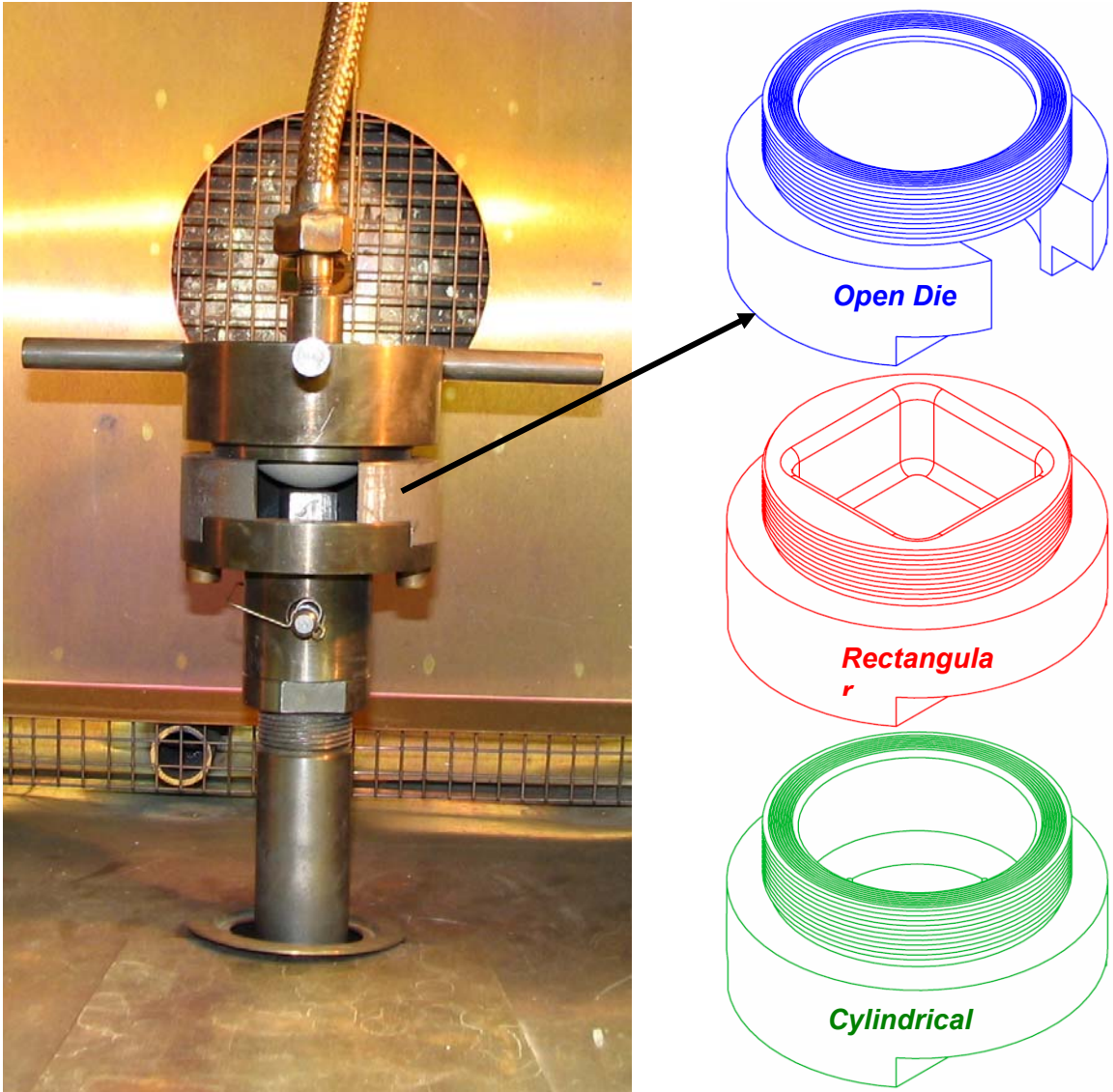


Figure 4.16: Type-I forming die assembly with different die geometries



Figure 4.17: Examples for magnesium sheets formed into different shapes using type-I forming dies

The forming process starts by selecting the appropriate die with the desired geometry, and cutting a circular disk out of the desired sheet material. After securing the sheet in place, the whole forming die assembly is heated till the desired forming temperature is reached. Meanwhile, the upstream pressure is built-up in the line to a limiting pressure just higher than the maximum value to be reached during forming. In addition, the pressure profile to be employed is uploaded through the software to make sure that the regulator is ready as soon as the forming temperature is established. Thereat, the flow valve is opened, and gas flow is started. The forming process is stopped either as soon as the pressure profile is entirely covered, or earlier in case the sheet perforated (*because the pressure is high or the sheet is stretched to a large strain limit*). Examples of successfully formed sheets into three different geometries are shown in figure 4.17.

The mechanism by which the die cover is sealed against the sheet has proved to be effective for low forming pressures; yet for pressures higher than 250 *psi*, the clamping mechanism could not provide enough force, hence gas leak used to take place. In order to overcome this limitation, another forming die assembly, schematically shown in figure 4.18, was designed and built.

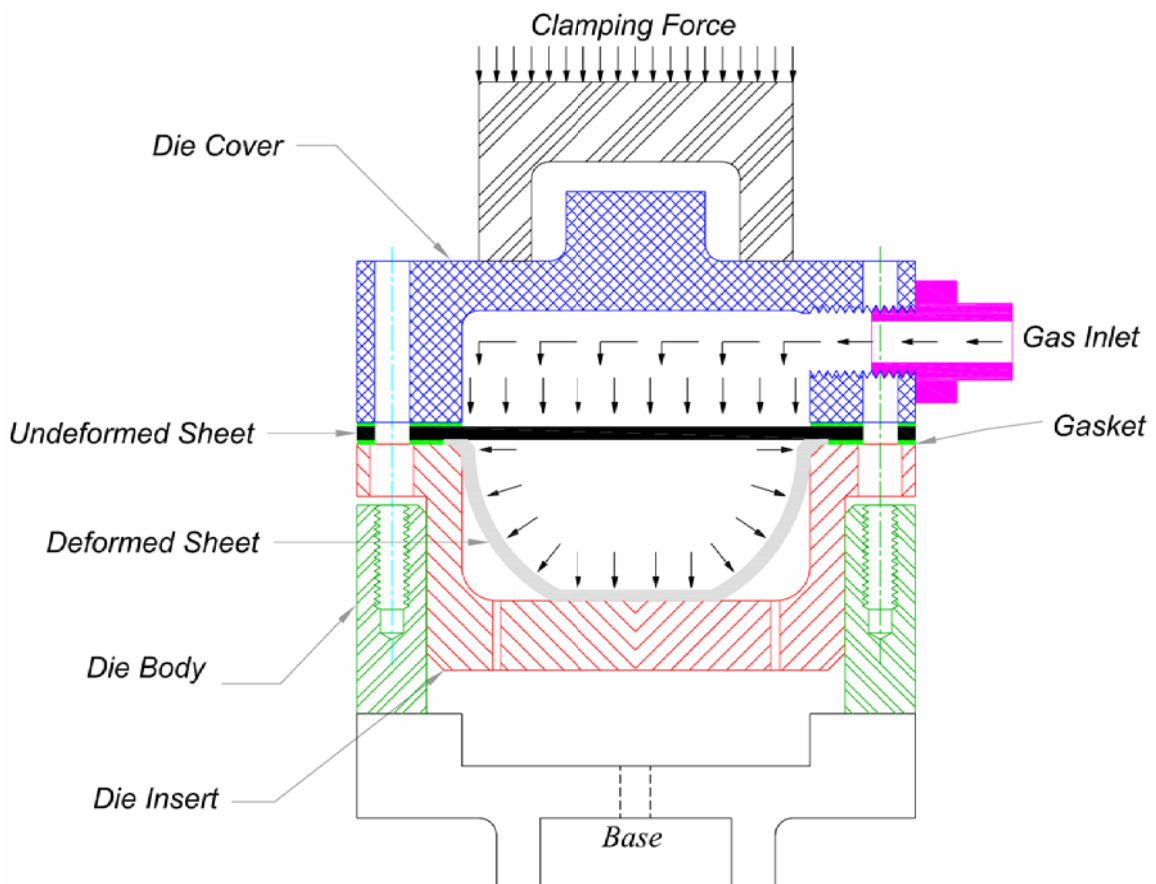


Figure 4.18: Schematic of type-II forming die assembly

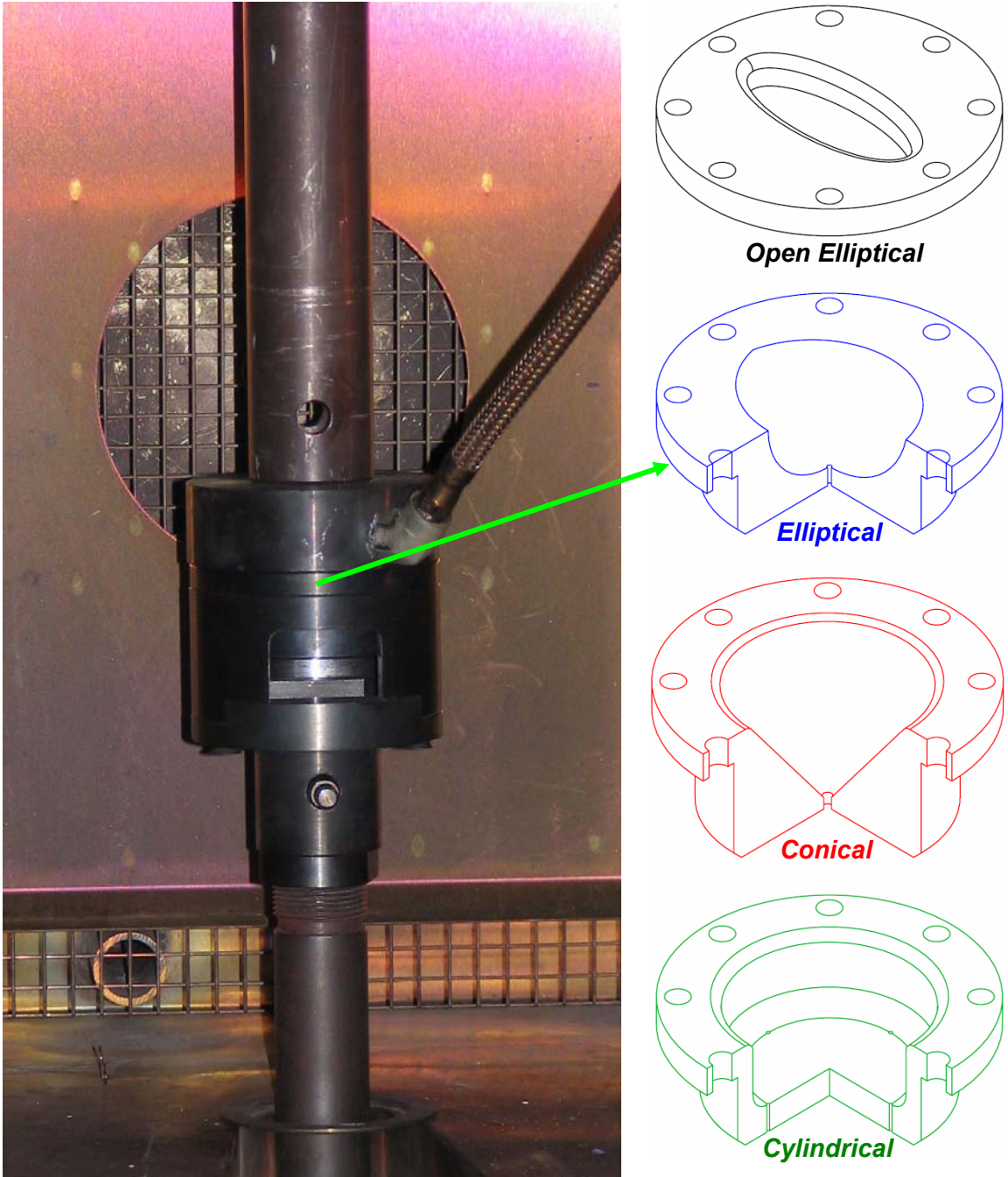


Figure 4.19: Type-II forming die assembly with different die geometries



Figure 4.20: Examples for magnesium sheets formed into different shapes using type-II open elliptical forming dies

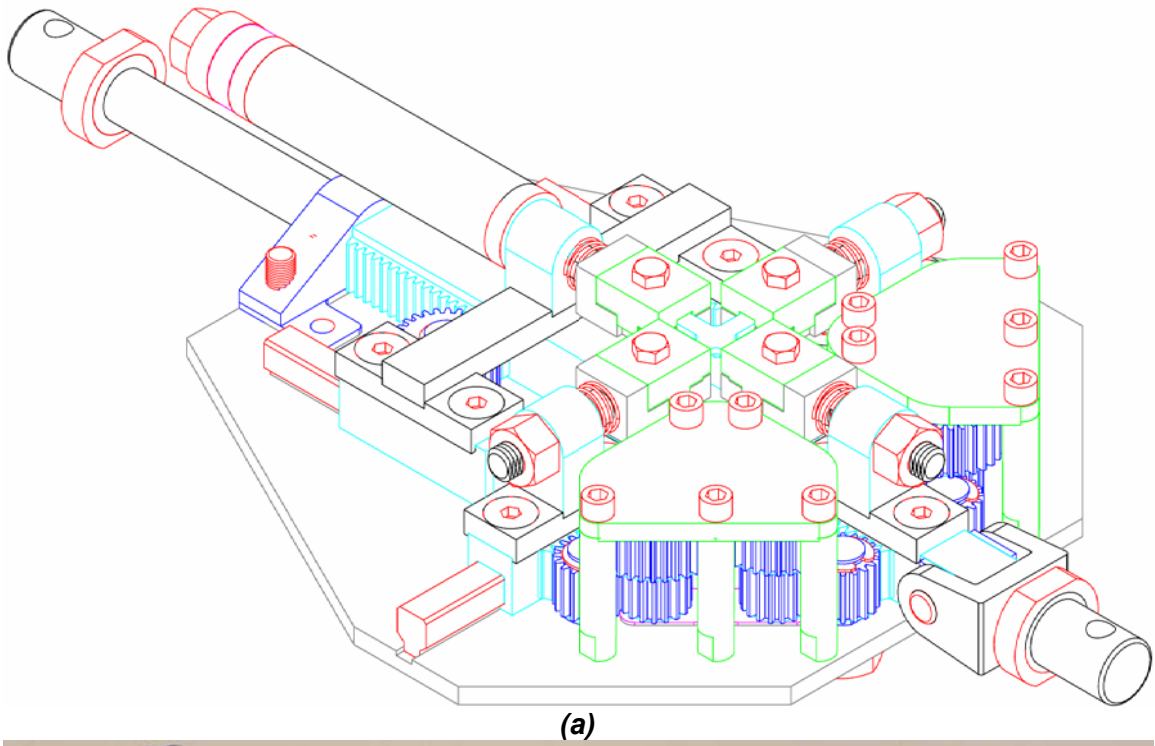
The clamping force in this type is acquired from the INSTRON load frame, which can sustain large loads up to *100 KN*, as highlighted earlier in section 4.1. A shaft is dropped down from the cross head beam, and used to transfer a compressive load to the die cover of the forming assembly. Using this large force, gas leak problems were eliminated, even without using a gasket. Since the load has to be applied from top, the gas inlet was moved to the side of the die cover, and the use of a braided metallic hose ensured enough flexibility during operation. Another feature introduced to the second design is the use of a single die body with multiple interchangeable die inserts. And similar to the previous case, die inserts were prepared with different geometries and proportions, as shown by the few examples in figure 4.19 and 20.

Both forming die assemblies were used for testing throughout this work, and so, to distinguish between them in later chapters, they are designated by type-I and type-II, respectively. The designations are highlighted in figures 15-20.

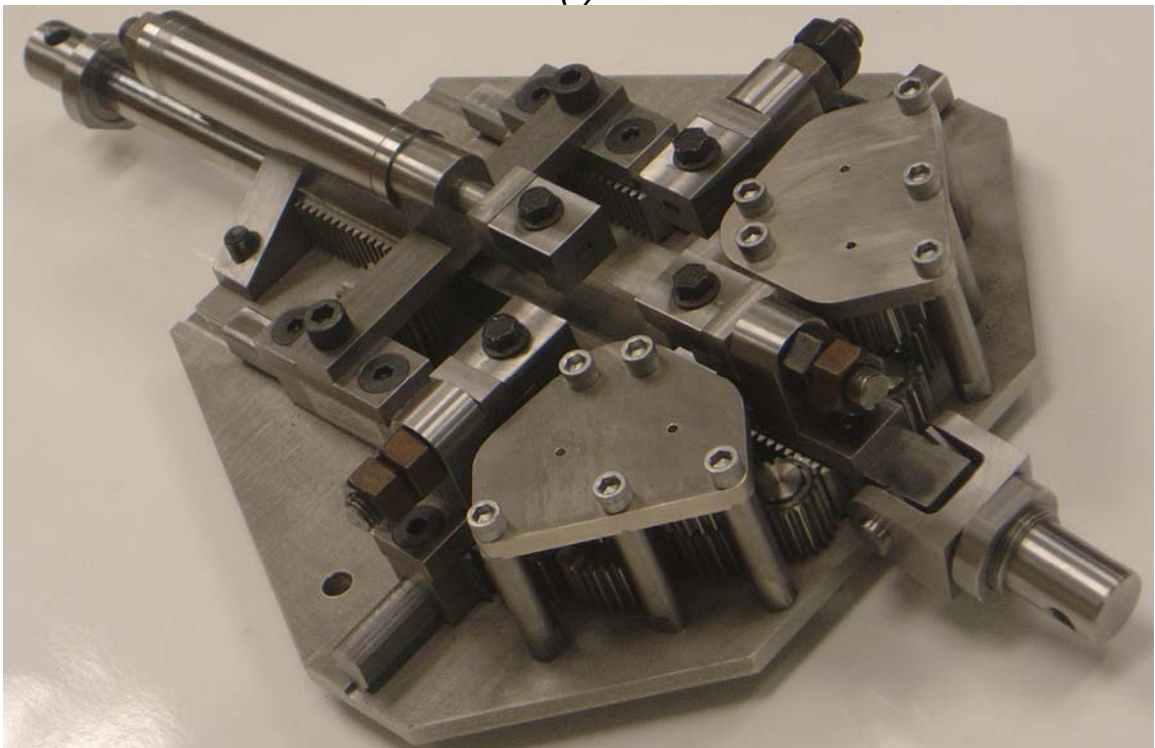
4.4 Controlled Biaxial Testing at Elevated Temperatures

By following the data that have been obtained in the field of testing the strength of materials, one could observe that almost all those data are based on the uni-axial loading case, and that not so much work has been done regarding the other miscellaneous loading conditions. Uniaxial tensile testing might be satisfactory in some cases, for instance, to obtain the stress/strain curves of a material, from which the mechanical properties are extracted. Yet in some other cases, there is a need for more expansion in the considered loading case, either because the uni-axial loading case is not satisfactory (*anisotropy, yield surface and flow potentials*), or because it is not the correct representation for the actual case. It is well known that almost all manufacturing processes involve combined loading conditions, and so if we are to conduct some experimental tests to simulate the response of a certain material's work-piece to that process, then it is important to conduct such tests on the basis of the same loading conditions presented in any of the selected manufacturing processes.

For the superplastic forming process in particular, the metallic sheet is blown into a specific die geometry, imposing multiaxial stresses on the material, mainly biaxial. Therefore, if we are to evaluate and assess the formability of superplastic materials, then the biaxial loading case would be more representative than the uniaxial loading case, and so more reliable data would be expected. Motivated by this, an effort to investigate the effects of loading biaxiality on the deformation of superplastic materials has been attempted. To be able to do that, a special fixture that enables testing under the biaxial stretching loading condition has been designed and built; a 3D view of the fixture is shown in figure 4.21.



(a)



(b)

Figure 4.21: Biaxial testing fixture (a) CAD model (b) A photo

The fixture is made to fit the *INSTRON-5582* load frame, as shown in figure 4.22, and transform any vertical displacement by the crosshead beam into biaxial stretching of the test specimen. The test specimen is chosen to have a general cruciform shape, similar to the one shown in figure 4.23, which helps localising the biaxial deformation into the centre region. The details of the specimen geometry will be discussed later in section 5.3. The fixture can provide different ratios between the transverse and longitudinal strains (ϵ_Y and ϵ_X) imposed on the test specimen; 1, 0.8, 0.6667, 0.5 and 0.3. Switching from one ratio to the other is made possible by changing a set of gears already designated for each specific straining ratio. Two load cells, one mounted along each axis, are used for force measurement. Displacement, on the other hand, is derived from the crosshead beam's, where the one along the horizontal axis is considered a linear multiplication of the vertical one, based on the straining ratio.

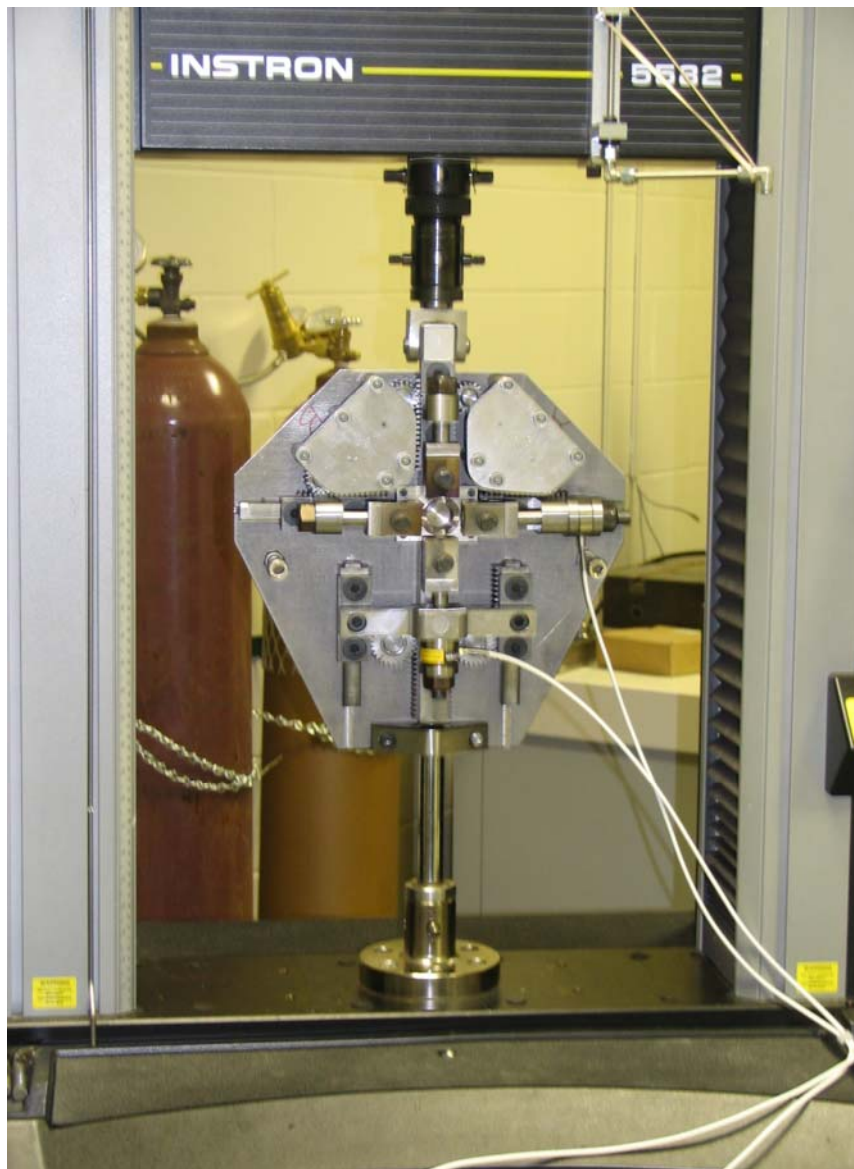


Figure 4.22: Biaxial testing fixture fitted to the INSTRON load frame

The main plate of the fixture carries all the other components, and it is fixed to the testing load frame from its lower side. The input vertical displacement is transferred directly from the cross-head beam to the middle slider, which has a rack on both sides to drive the gear trains of each side, and over which the upper grip is fitted. In addition, the middle rack drives two gears in the lower part of the fixtures, which in turn move the lower grip in the opposite direction of the middle slider's movement. Each one of the side gear trains ends with a horizontal rack that carries one of the two horizontal grips; the amount by which each horizontal rack moves depends on the train value of the gear trains. For a train value of 1, the net effect of any positive vertical displacement (y) of the middle rack is a positive (y) for the upper grip, a negative (y) for the lower grip, a positive (y) of the right grip and a negative (y) of the left grip. In other words, the four grips will move the same distance in four directions, away from the centre of the test specimen.

More details about the fixture, and the preliminary results obtained using it are all presented in section 5.3.

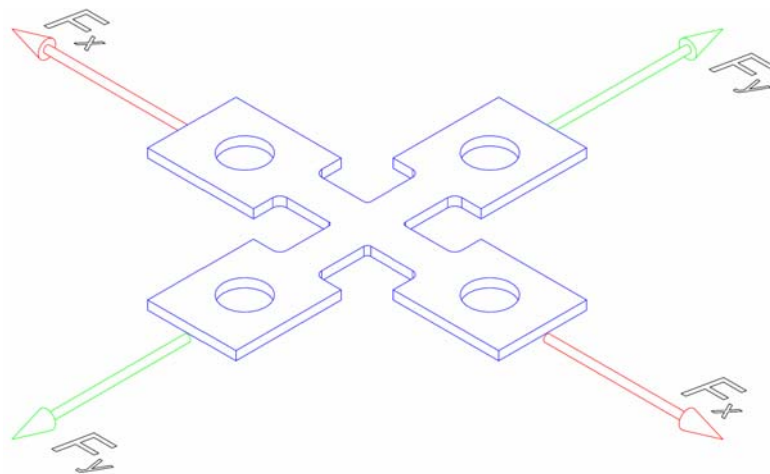


Figure 4.23: A cruciform-shaped test specimen for biaxial testing

5. CHAPTER FIVE: TESTING AND CHARACTERISATION OF THE SUPERPLASTIC BEHAVIOUR IN THE AZ31 MAGNESIUM ALLOY

The promising weight-saving potentials offered by the lightest constructional metal on earth, magnesium, are usually dampened by the metal's limited room temperature tensile ductility. However, several magnesium alloys exhibit superplasticity at elevated temperatures, yielding extraordinarily enhanced ductility. AZ31 is one such magnesium alloy possessing good mechanical properties, that makes it particularly attractive for automotive applications [Abu-Farha and Khraisheh 2006]. Yet, in order to advance the utilisation of this alloy, a broad database of its deformation behaviour, the superplastic in particular, is needed. To establish such a database requires a large number of diverse tests (*both mechanical and microstructural*), covering wide ranges of forming conditions. Unfortunately, investigators' efforts, and consequently, the available experimental data on this alloy are scattered.

Recently, a large number of studies investigated the formability and deformation aspects of the AZ31 magnesium alloy at various temperatures. The different researchers targeted different aspects in their respective studies, including warm formability, high temperature deformation and superplasticity, cavitation and microstructural evolution, and anisotropy.

Doerge and K. Dröder [1997 & 2001], Dröder and Janssen [1999], Doerge et al. [2000 & 2001b], Siegert et al. [2003] and Kurtz [2004] have done significant amount of work on the warm forming of the AZ31 mg alloy, under uniaxial and biaxial loading conditions. Uniaxial tensile tests, deep drawing, hydro forming and gas bulge forming were carried out at various strain rates, covering temperatures up to 250 °C. Their practices proved that the AZ31 mg alloy is warm-formable, producing some components for potential automotive applications. Despite the formability enhancement, warm forming of the alloy at such temperatures yields a behaviour (*formability*) similar to that of steel or aluminium at room temperature! For this reason, many other investigators studied the behaviour of the alloy at higher temperatures, highlighting the effect of various parameters, mainly temperature, strain rate and texture, on the enhanced ductility of the alloy [Tsao et al. 2001, Agnew and Duygulu 2003, Jäger et al. 2004, Lee et al. 2005, Watanabe et al. 2005, Abu-Farha and Khraisheh 2005b].

Superplastic behaviour in the AZ31 mg alloy was observed in many studies, and was given special attention by a number of researchers. However, the majority of those studies covered limited forming temperatures [Watanabe et al. 2000, Mabuchi et al. 2000, Bussiba et al. 2001, Kim et al. 2001, Tan and Tan 2002, Ben Artzy et al. 2003, Chino and Iwasaki 2004] and/or strain rates [Kim et al. 2001, Wu and Liu 2002, Tan and Tan 2002]. Lee et al. [2005] covered in their tests temperatures between 250 and 500 °C over a wide range of strain rates,

$10^{-4} - 100 \text{ s}^{-1}$. Yet, their experiments aimed at studying the deformation mechanisms and establishing the processing map of the alloy, and their published data does not cover the response of the material in terms of flow stress, fracture strain and strain rate sensitivity. There is no single comprehensive study that covers all the mechanical aspects of deformation of AZ31 mg alloy (*flow stress, elongation-to-fracture and strain rate sensitivity*) over a wide range of temperatures and strain rates. In addition, it is difficult to compile the results of different researchers who covered various aspects of the alloy's deformation due to the variation in testing procedures, loading paths and initial microstructure of the alloy [Bussiba et al. 2001, Tan and Tan 2002, Ben-Artzy et al. 2003, Yin et al. 2004 & 2005].

Microstructural evolution in terms of grain growth and cavitation has been also studied, due to its strong influence on the limiting fracture strain, and the post-forming attributes of the alloy [Wu et al. 2001, Chino and Iwasaki 2004, Lee and Huang 2004, Yin et al. 2005]. Wu et al. [2001] investigated the static grain growth in the AZ31 mg alloy at elevated temperatures up to $500 \text{ }^\circ\text{C}$, but did not model or show the variations of grain size over the different temperatures. Lee and Huang [2004], on the other hand, showed the effects of time, temperature and strain rate on the grain growth of the alloy, yet for limited temperatures and strain rates. Similarly, cavitation studies [Lee and Huang 2004, Chino and Iwasaki 2004, Yin et al. 2005] covered limited temperatures and strain rates.

Kaiser et al. [2003a & b] was one of few to highlight the issue of planar (*initial*) anisotropy exhibited by the AZ31 mg alloy, both at room temperature and temperatures up to $250 \text{ }^\circ\text{C}$. No comprehensive data has been published on the initial state of anisotropy, and more importantly, the deformation-induced anisotropy in the alloy at elevated temperatures.

So, in spite of the numerous and diverse available studies on the AZ31 mg alloy, there is still a need for a systematic work, in order to establish a comprehensive quantitative database of the alloy's superplastic behaviour. In an effort to tackle this issue, this chapter presents an experimental study on the various deformation characteristics of the AZ31 magnesium alloy. Its elevated-temperature deformation aspects are first investigated through a set of uniaxial tensile tests; where flow stress, fracture strain and strain sensitivity index maps are to be constructed over a wide range of strain rates, covering temperatures between 325 and $450 \text{ }^\circ\text{C}$. Finally, the last section of the chapter presents the preliminary results on the biaxial testing of the alloy.

The results of some of these mechanical tests, combined with microstructural examinations later in chapter six, will be used to calibrate the developed constitutive model (*chapter three*), in order to capture the superplastic behaviour of the AZ31 magnesium alloy.

5.1 Properties of the As-Received Material

Thought, the area of interest is its high-temperature deformation, it is essential to start with a background testing of the AZ31 magnesium alloy's room temperature characteristics. Three aspects are primarily needed for later reference; the alloy's as-received microstructural status, room-temperature mechanical behaviour, and planar (*initial*) anisotropy.

5.1.1 Initial Grain Size

The magnesium alloy studied throughout this work is the commercial AZ31B-H24 mg alloy, with the chemical composition given in table 5.1. The material is received in the form of sheets of various thicknesses; 1.04, 1.65 and 3.22 mm. Unless otherwise stated, mechanical tests are generally carried out using specimens machined out of the 3.22mm thick sheets, while bulge forming practices are performed on discs cut out from the other two sheets (1.04 and 1.65 mm).

Table 5.1: Chemical composition of the AZ31B-H24 magnesium alloy

Element	Mg	Al	Zn	Mn	Si	Fe	Cu	Ni
Percentage (%)	95.27	3.29	0.991	0.412	0.028	0.0041	0.004	0.0007

Different samples were taken from the three sheets, and then hot mounted in two different orientations; looking at the cross section **C**, or the top view **T** of the sheet. Sample preparation for microstructural examination was carried out according to the ASM standard procedures [ASM Handbook 1999]. After several grinding thence polishing steps, acetic picral was used to etch the samples, in order to reveal its microstructure. An example of the of the observed grain structures is given in figure 5.1, which shows two pictures taken for samples cut out of the 1.65mm thick sheets, in both the **C** and **T** orientations.

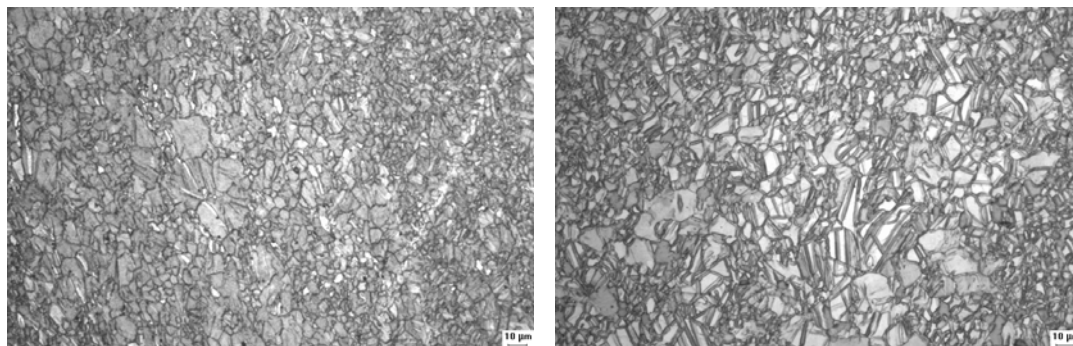


Figure 5.1: Pictures of the grain structure for samples taken from the 1.65mm thick sheets (a) Cross section view (b) Top view

Though the grain boundaries are not very clear, remarkably fine grain-structure is observed in both cases. It could be said that the microstructure is generally homogeneous, despite the few localised areas of very fine or very coarse grains. Twinning bands are observed all over, perhaps clearer in the *T* oriented sample, which is quite expected since the alloy is cold rolled. Twinning is a major deformation mechanism in hexagonal close-packed crystal structure metals; and magnesium is one of them. After examining the various samples from the three different sheets, no distinguishable differences were observed.

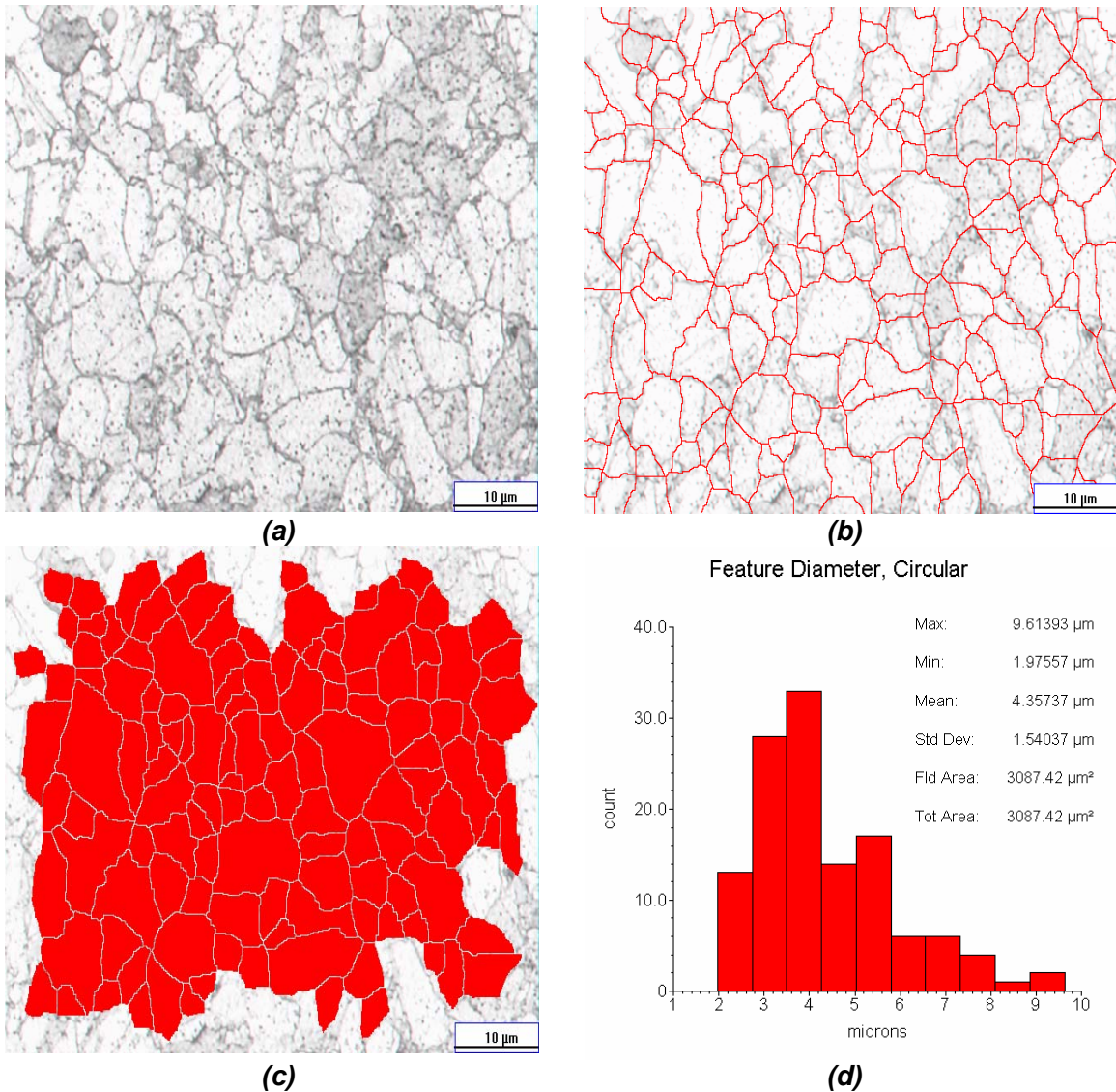


Figure 5.2: Software used for grain size measurement in a *T*-oriented sample taken from the 3.22 mm thick sheet (a) Photo of the microstructure (b) Captured grain boundaries (c) Captured grains (d) Results

In order to estimate the average grain size of the material, two methods were adopted:

- 1) **Using a specialised software:** While capturing a picture for the microstructure, a software (*Omni, supported by Buehler*) was used to estimate the average grain size, based on that specific exposure. The software first scans the picture, highlighting the captured grain boundaries. The accuracy of this step depends mainly on the quality of the picture and lighting level, and it is repeated till a good mesh (*that decently fits the actual grain boundary mesh*) is obtained. The number of grains and the total occupied area are then used to estimate the average grain size (*either area, or diameter assuming a circular shape*) of the material. Figure 5.2 shows an example of the steps by which an estimate for the average grain size using this software is obtained.
- 2) **The line method:** This lengthy and quite tedious method was carried out on few specimens, merely to validate the estimates obtained from the grain size measurement software. Pictures taken from samples were printed, and 26 lines were drawn horizontally (10), vertically (10) and diagonally (6). The average grain size along each line was estimated by dividing its length over the total number of grains it crosses. Finally, the values obtained from all the lines were averaged, to yield the average grain size of the material.

Regardless of the sheet thickness, estimates using different samples and based on both methods yielded an average value in the vicinity of $4.5 \mu\text{m}$; and therefore this value is assigned as the average grain size (*diameter*) of the as-received material throughout this work.

5.1.2 Room Temperature Mechanical Properties

All the uniaxial tensile tests covered in this chapter are conducted using type-I grips and specimen geometry, presented in the previous chapter; please refer to figures 4.6 and 4.7, respectively. In this section, room temperature tensile tests were carried out using 0° oriented specimens, at a constant speed of 1.5 mm/s . The objective is to determine the material's mechanical properties; mainly fracture strain, yield and tensile strengths. The same test was repeated six times for repeatability, and the obtained stress/strain curves are plotted in figure 5.3a. It is clear that all the curves match almost perfectly, until failure point, where we start to see some variations. Such variations are considered normal in *RT* testing, particularly with such a small gauge length and fillet radius. The values of mechanical properties were estimated by averaging the results from the six tests, and they are also shown in the figure.

The resulting fracture strain value is quite intriguing, and makes it hard to decide whether to consider this alloy ductile or brittle? An average fracture strain of 16.11% is hardly indicative of brittleness in the material; in fact, this value is higher than that for some aluminium alloys, which is generally considered more ductile than magnesium!

By focusing on the last part of the six curves in figure 5.3a, it is hard to observe any softening before failure takes place, which implies some degree of brittleness. A closer look is provided by figure 5.3b, which shows one of the specimens before and after testing. At the fracture location, there is hardly any indication of necking before failure; in addition, failure takes place at 45° across the section of the specimen. These observations make it more likely to consider the behaviour of the AZ31 mg alloy as brittle-like at room temperature.

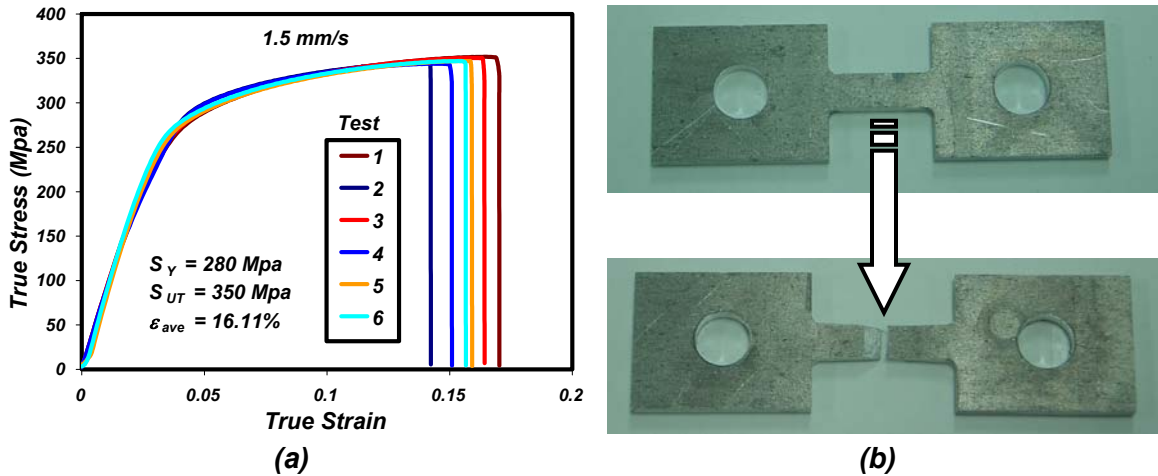


Figure 5.3: Stress/strain curves for six 0° oriented specimens tested at RT and 1.5 mm/s (a) A test specimen before and after failure

5.1.3 Initial (Planar) Anisotropy

To investigate *RT* initial anisotropy in the material, tensile tests were carried out using specimens cut at three different orientations with respect to the rolling direction of the sheet; 0° , 45° & 90° oriented specimens (*figure 4.10*). In addition, to examine the deformation rate sensitivity of the material, tests were conducted at different strain rates, instead of the constant speed mode used before. Figure 5.4 shows the stress/strain curves for every family of specimens (*by orientation*), where each curve was selected as the average of three trials. It is observed that for each set of curves, both yield and tensile strengths are strain rate insensitive, while fracture strain is more observably sensitive. Lowering the imposed strain rate enhances the tensile ductility of the material, but still insignificantly.

By comparing the three sets of curves, it is noticed that the 0° specimens exhibit the lowest tensile ductility, regardless what the strain rate value is. This can be clearly depicted from figure 5.5, which shows the stress/strain curves for the three differently-oriented specimens at both 5×10^{-4} and $2 \times 10^{-4} \text{ s}^{-1}$, separately. In both cases, 45° oriented specimens exhibit a slightly higher tensile ductility compared to the 90° specimens, but both clearly exceed that exhibited by the 0° specimens.

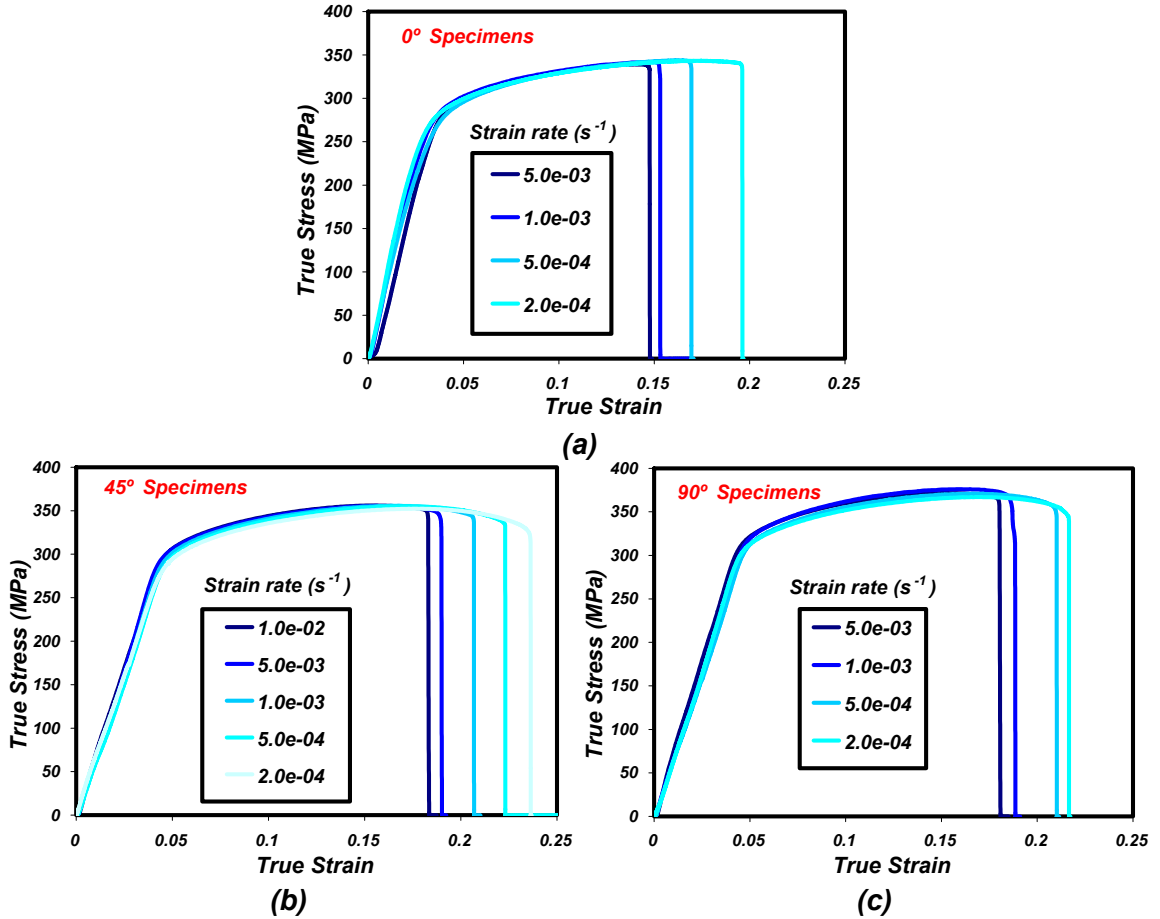


Figure 5.4: Stress/strain curves at room temperature and various strain rates for (a) 0° (b) 45° (c) 90° oriented specimens

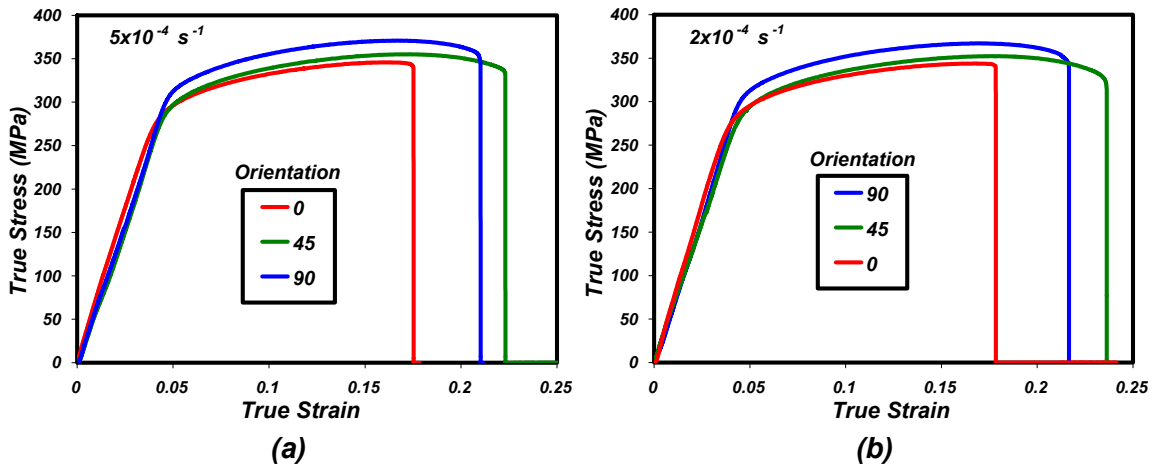


Figure 5.5: Stress/strain curves for 0°, 45° and 90° oriented specimens indicating RT initial anisotropy at (a) 5x10⁻⁴ s⁻¹ (b) 2x10⁻⁴ s⁻¹

On the other hand, yield strengths for the three different specimens are not equal, and the variation does not follow the same trend. The 90° specimens have the highest yield strength, followed by the 45° specimens, and again 0° specimens have the lowest of all. The same applies to the ultimate tensile strength; that is $\sigma_{UTS,90^\circ} > \sigma_{UTS,45^\circ} > \sigma_{UTS,0^\circ}$.

Kaiser et al. [2003a] conducted a more detailed investigation, by considering specimens cut at various orientations with respect to the rolling direction, ranging between 0° and 90° , at 10° increments. A plot for yield strength as a function of specimen's orientation (*angle*) clearly shows a direct proportionality, which supports the conclusion presented here. Moreover, in a plot for fracture strain versus the same angle, a behaviour similar to the one observed here was noticed, but with smaller differences. One of the reasons might be that the investigators considered only one strain rate value in their tests.

5.2 High Temperature Tensile Testing and Superplastic Behaviour

In this section, uniaxial tensile tests are carried out in two main forms to characterise the superplastic behaviour of the AZ31 magnesium alloy, in terms of three main quantities; flow stress, fracture strain and strain rate sensitivity index [Abu-Farha and Khraisheh 2000c & 2000d]. In its first form, constant strain rate tensile tests are conducted to extract both flow stress and fracture strain. Thereafter, strain rate sensitivity index is evaluated through another set of strain rate jump tests, which is the second form. Each family of tests is conducted at temperatures between 325 and 450 °C, in 25 °C increments. And for each one of these temperatures, a wide band of strain rates stretching between 2×10^{-5} and 10^{-2} s^{-1} is covered. The effects of temperature and strain rate on the behaviour of the material are emphasised, and the region in which the material exhibits optimum superplasticity is highlighted for further testing (*Chapter six*). As a typical warm forming temperature, 225 °C is also covered in both of the aforementioned test forms, for comparison and assessment of the material's superplastic behaviour.

5.2.1 High Temperature Anisotropy

Before conducting such wide-ranging test matrix, it was essential to decide on the orientation of test specimens to be used, especially that different orientations revealed different behaviours in room temperature testing. This issue was raised at an early stage, because it has a significant impact on the number of tests to be conducted. Should the material behave anisotropic-ally at high temperatures, means that the aforementioned tests proposed to cover all the combinations of temperatures and strain rates are to be carried out using the

three differently-oriented specimens (0° , 45° & 90°). Otherwise, the characterisation process could be carried out using only 0° oriented specimens, reducing the total number of tests by two thirds. For that, a preliminary investigation of high temperature anisotropy in the AZ31 magnesium alloy was carried out first.

Two temperatures, 375 and 400 °C, and a strain rate of $2 \times 10^{-4} \text{ s}^{-1}$ were selected for a preliminary study on any possible effects for test specimen's orientation on the mechanical properties of the material during high temperature testing. For each temperature, three specimens with 0° , 45° & 90° orientations, respectively, were tested individually at the designated strain rate. The stress/strain curves for the three specimens are shown in figure 5.6a & b. For both temperatures, small differences between the three curves, corresponding to the three specimens, are observed. Flow stresses in particular are quite the same, throughout the entire deformation. The effect on the maximum failure strain, on the other hand, might be more observable; yet the differences are not strong enough to draw a conclusion in this regard. A third set of tests was then conducted at 400 °C, but at $5 \times 10^{-5} \text{ s}^{-1}$ this time. The same behaviour was observed, despite the smaller strain rate value, as shown in figure 5.6c.

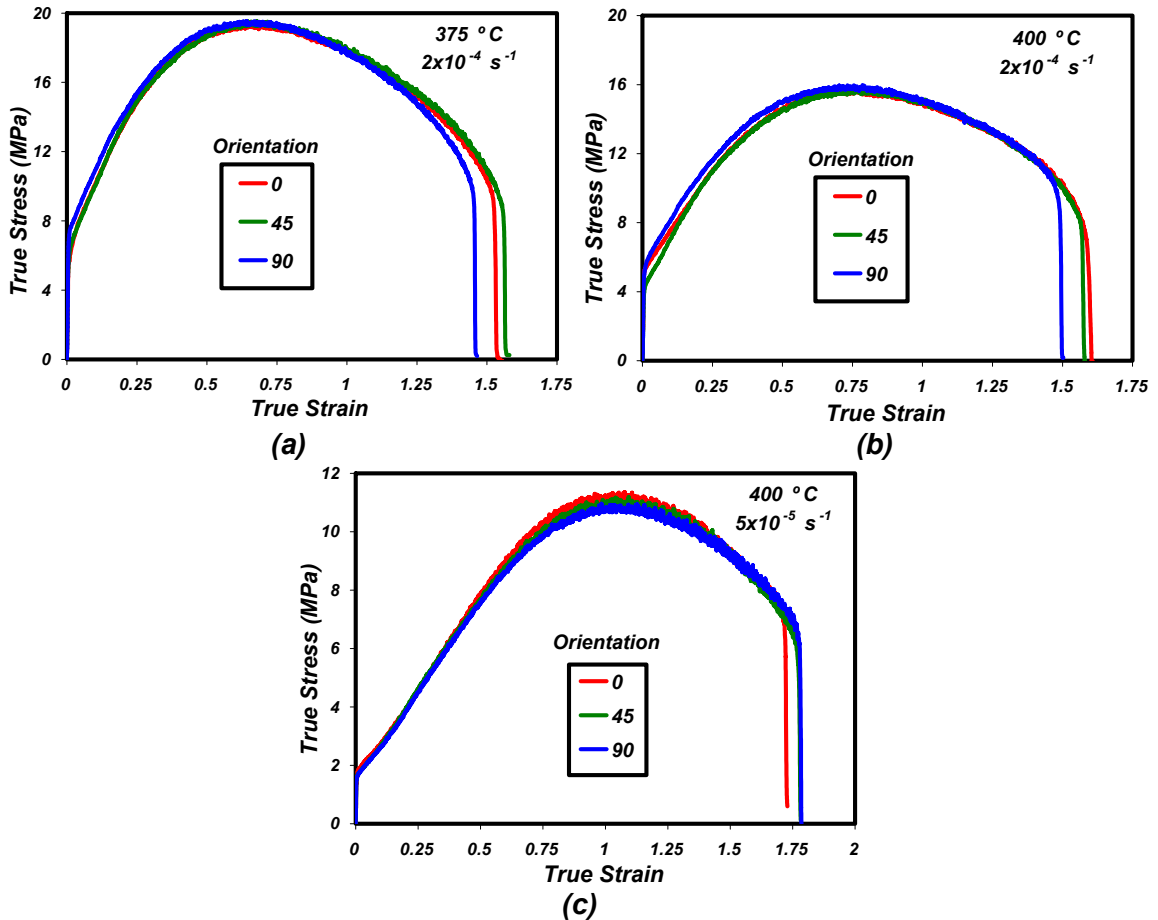


Figure 5.6: Stress/strain curves for 0° , 45° and 90° oriented specimens at (a) 375 °C and $2 \times 10^{-4} \text{ s}^{-1}$ (b) 400 °C and $2 \times 10^{-4} \text{ s}^{-1}$ (c) 400 °C and $5 \times 10^{-5} \text{ s}^{-1}$

Based on these results, it can be said that the initial anisotropy is less significant at higher temperatures, than it is at room temperature. Reasoning for this might be heating for relatively long time; recall that the test specimen is heated for more than an hour before the test (*straining*) actually starts. All the same, this conclusion is still in agreement with Kaiser et al. [2003a] who examined the effect of temperature on initial anisotropy and observed that anisotropy decreases constantly with rising temperature, to become almost unobservable at 250 °C!

Anisotropy is one of the highly-influential, yet seldom-covered, parameters in high temperature testing. It is important to note that the uniaxial tensile tests can only provide information on the initial state of anisotropy and can not provide information on possible deformation-induced anisotropy. Other tests that involve multiaxial loading are required for better characterisation of the anisotropic behaviour of the material (*section 5.4*).

5.2.2 Constant Strain Rate Uniaxial Tensile Tests

5.2.2.1 Mechanical Behaviour

With no significant influence for sheet orientation in high temperature tensile testing, only one type of specimens was used here, the 0° oriented specimens. Tensile tests were carried out at combinations of strain rates between 2×10^{-5} and 10^{-2} s^{-1} , and temperatures between 225 and 450 °C, following the procedures detailed in the previous chapter. After thermal equilibration at a selected temperature, the test specimen was stretched at a constant strain rate value up to failure; thereat, quenched in water for possible microstructural examination (*chapter 6*). For consistency assurance, each combination of temperature and strain rate was tested twice, and the generated stress/strain curves were compared. In few cases where large deviation between the two curves was observed, a third test was added.

An example of a good pair of stress/strain curves, obtained at 400 °C and $5 \times 10^{-5} \text{ s}^{-1}$, is shown in figure 5.7a. The good match between the two curves mirrors the overall control of the setup and testing procedure. Moreover, the small noise in stresses indicates the stability of the load cell, provided that the maximum load measured in this test is 100 N, which is within the 2% of the full capacity of the load cell (5 KN). A test specimen corresponding to one of the curves is shown before and after testing in figure 5.7b. Superplasticity is highly evident, not only by the large plastic strain, but also by the remarkably uniform deformation up to fracture, which could be described as neck-free.

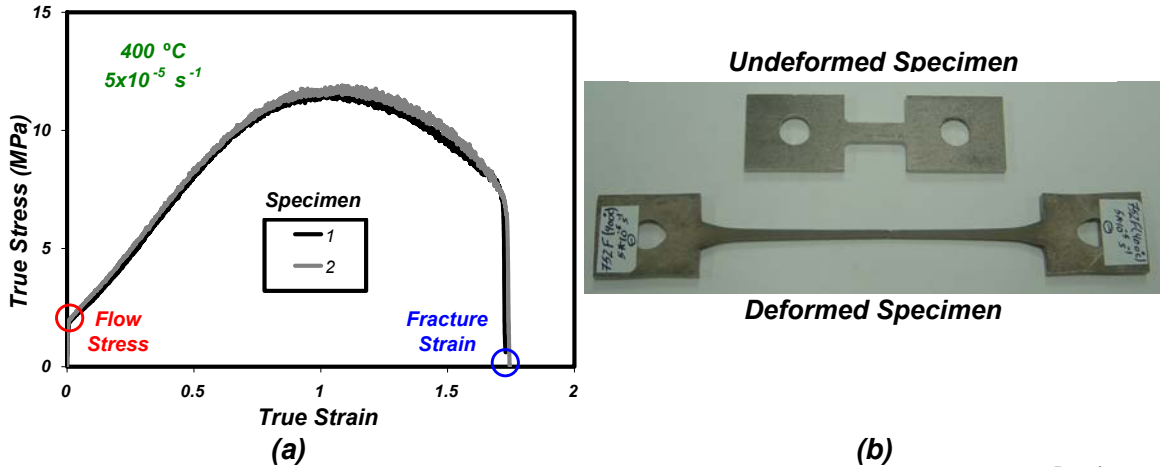


Figure 5.7: (a) Stress/strain curves for two tensile tests at 400 °C and $5 \times 10^{-5} \text{ s}^{-1}$ (b) A test specimen before and after testing

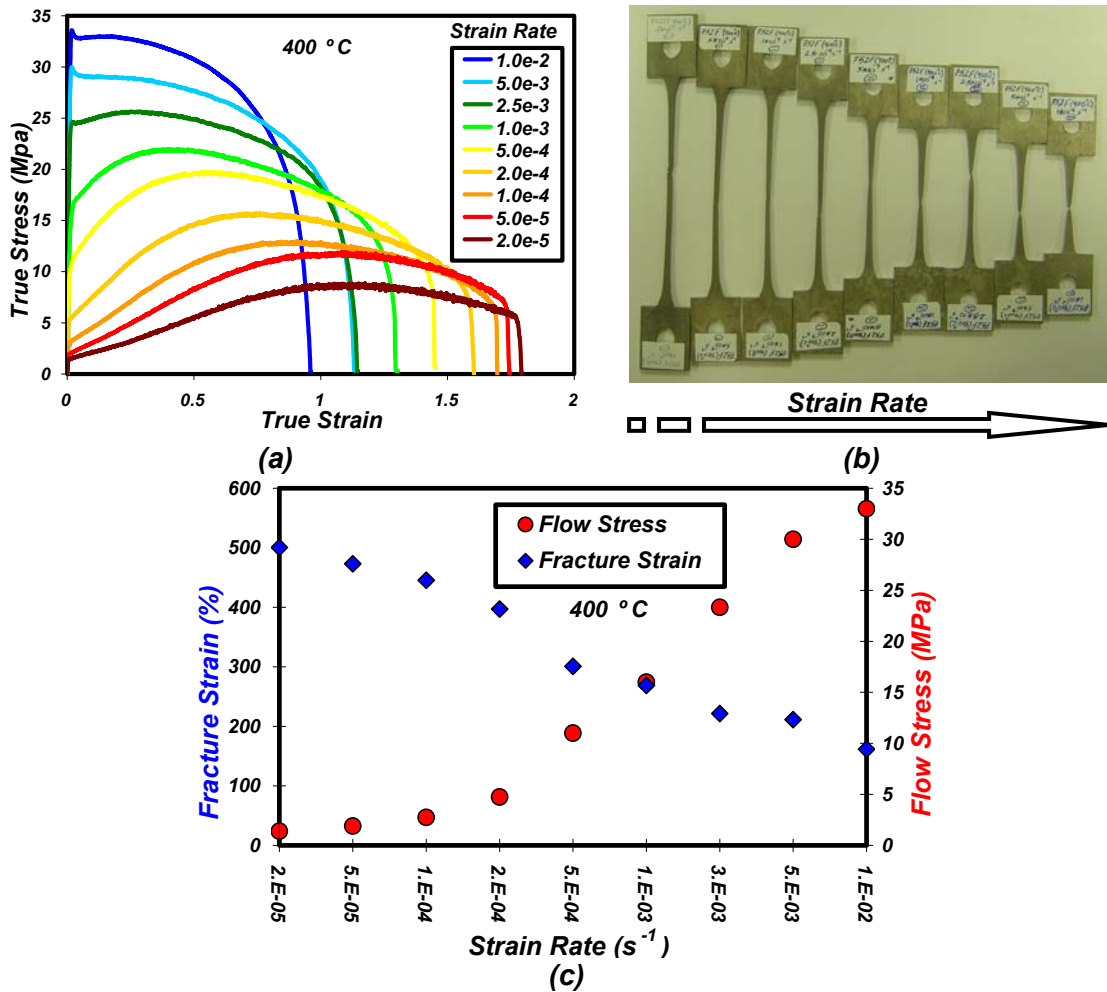


Figure 5.8: (a) Stress/strain curves for various strain rates at 400 °C (b) Corresponding deformed specimens (c) Extracted flow stress and fracture strain curves

By considering the tests conducted at all the strain rates for a single temperature, a band of stress/strain curves, like the ones corresponding to 400 °C and shown in figure 5.8a, was obtained. The corresponding deformed specimens are shown in figure 5.8b. Out of each stress/strain curve, two main quantities that characterise the superplastic behaviour of the materials were extracted; flow stress and fracture strain. By plotting them versus strain rate as shown in figure 5.8c, the general trend shows that, opposite to flow stress, fracture strain increases as strain rate decreases. These two quantities, and therefore these two curves, are commonly considered satisfactory in describing the superplastic behaviour of the material. However, the long plastic deformation history in superplasticity makes this inaccurate from two perspectives:

- 1) The flow stress/strain rate curve in figure 5.8c is constructed using the threshold stresses in figure 5.8a, in other words, at strain almost equal to zero. Nevertheless, as deformation progresses, the behaviour of the various stress/strain curves is totally different at different strain rates. The strong softening observed at high strain rates fades away and turns into strong hardening, as strain rate decreases. The significance of this issue arises in many forming pressure-time expressions, where a single effective stress value is assigned for a certain strain rate [Dutta and Mukherjee 1992, Banabic et al. 2001]. Using such expressions leads to over estimated pressures at high strain rates (*due to softening*), and under estimated pressures at low strain rates (*due to hardening*). This issue has been alluded to earlier in section 3.5.5.3, and will be further demonstrated for the AZ31 mg alloy in later sections.
- 2) The deformed specimens shown in figure 5.8b not only highlight ductility improvement, but also draw the attention to clear enhancement in deformation uniformity, as strain rate drops. And though might seem similar, these two closely-related terms (*fracture strain and deformation uniformity*) are quite distinct, and should be considered equally important in superplastic forming operations. In fact, in many cases where a part is superplastically-formed, the failure criterion is often set as the thinning factor (*which mirrors deformation uniformity*) and not the actual rupture of the part (*i.e. fracture strain*). A closer look on the distinction between the two terms, and the implementation of deformation uniformity as an important individual quantity in assessing superplasticity, is given later in chapter seven.

Stress/strain curves for all the other temperatures are shown separately in figure 5.9.

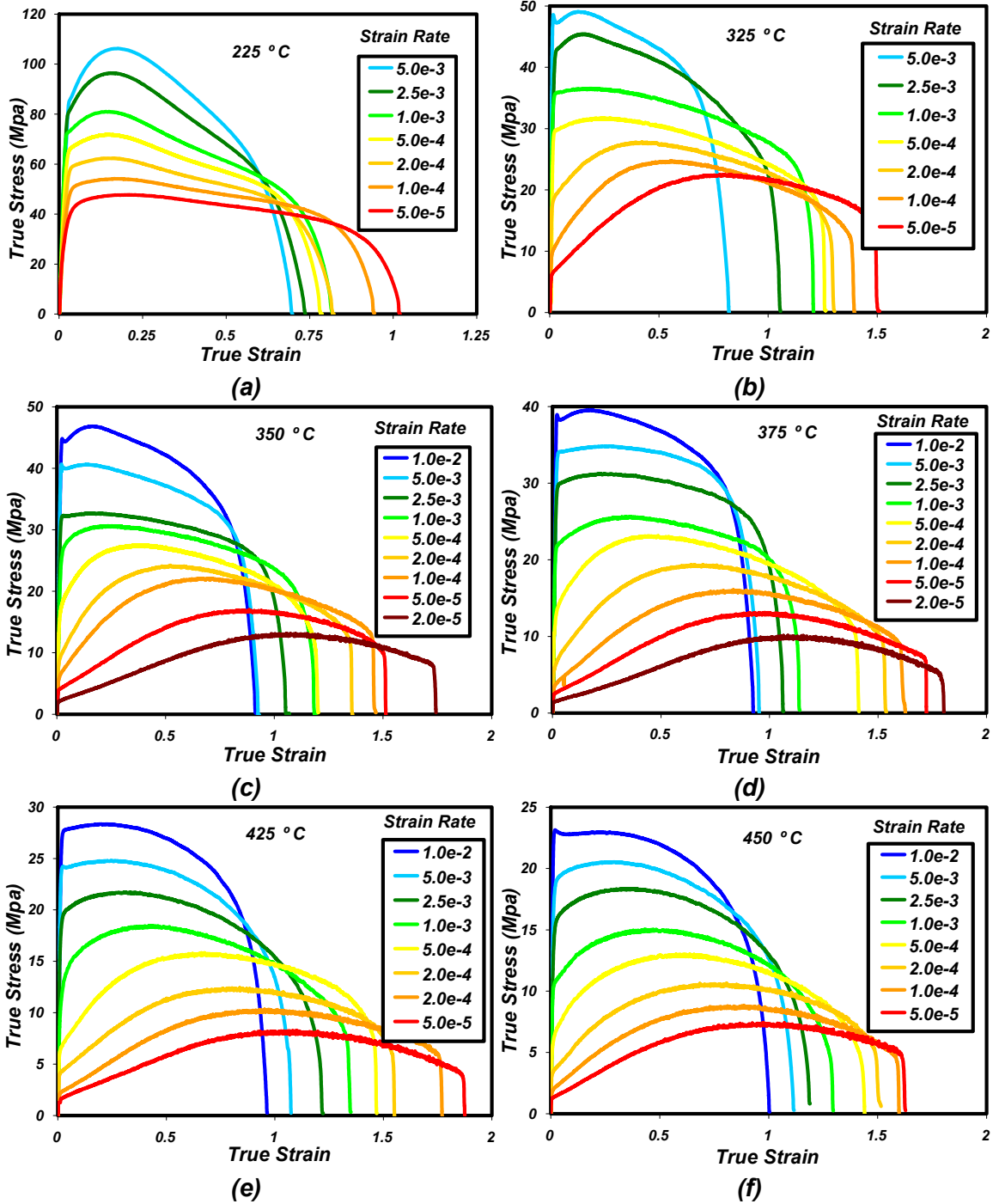


Figure 5.9: Stress/strain curves for various strain rates at (a) 225 °C (b) 325 °C (c) 350 °C (d) 375 °C (e) 425 °C (f) and 450 °C

5.2.2.2 Flow Stress

Similarly, by extracting flow stress and fracture strain data point from these curves, and combining the results, the effects of forming temperature and strain rate on the superplastic behaviour of the AZ31 magnesium alloy can be quantitatively assessed. Figure 5.10a presents all the flow stress/strain rate curves corresponding to the various forming temperatures, where the well-known sigmoidal-shaped behaviour is clearly observed. At each specific temperature, flow stress sensitivity to strain rate is strongly depicted; in other words, the higher the strain rate, the higher the flow stress of the material.

A quick assessment of this sensitivity can be made by considering the slope of each curve at any specific strain rate. It is observed that for all the temperatures but 225 °C, significant increase in the curve's slope takes place as strain rates decreases below 10^{-3} s^{-1} . Such behaviour is indicative of superplasticity in that region, and the quite distinctively lower slope in the case of 225 °C excludes it of the superplastic region. Yet, a more accurate assessment in this regard requires a quantitative evaluation of the index m by means of the strain rate jump test, which is covered in the next section.

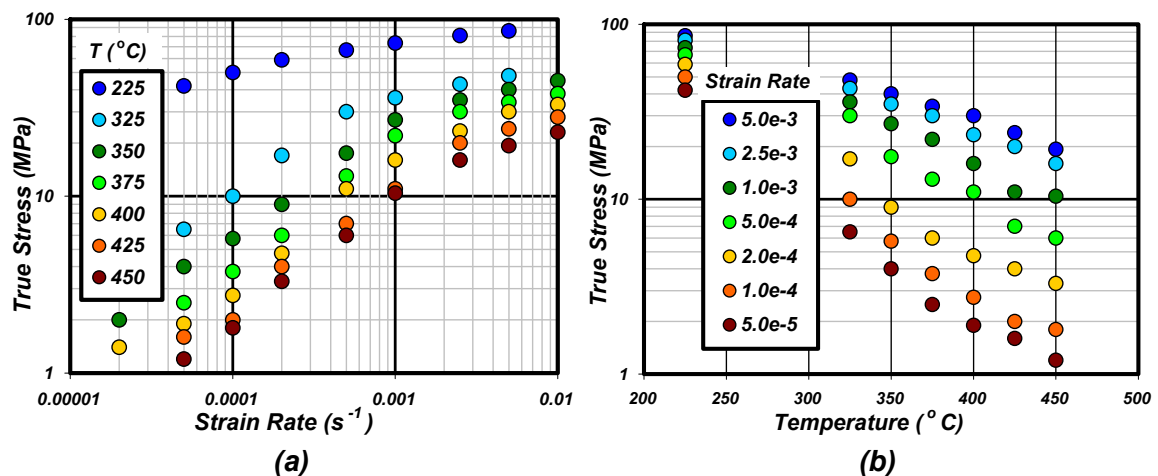


Figure 5.10: (a) Sigmoidal-shaped stress/strain rate curves at different temperatures (b) Flow stress versus temperature for various strain rates

A different way of representing the same data points is shown in figure 5.10b. Such representation makes it easier to depict the nearly-linear inverse relationship between flow stress and forming temperature. Moreover, one can observe the stronger influence of strain rate on flow stress, compared to that caused by temperature.

5.2.2.3 Fracture Strain

The second quantity assessing the superplastic behaviour of the alloy, fracture strain, is plotted against strain rate for all the temperatures in figure 5.11a. At any temperature, an inverse relationship is observed. And since 200% elongation is usually considered the threshold of superplasticity, it can be inferred that forming at any strain rate lower than 10^{-3} s^{-1} yields superplastic behaviour in the alloy at all the considered elevated temperatures ($> 325 \text{ }^\circ\text{C}$). On the other hand, from temperature point of view, superplasticity cannot be achieved by warm forming at $225 \text{ }^\circ\text{C}$, even at the lowest strain rate considered. These observations represent preliminary guidelines for drawing the boundaries of the superplastic region for the AZ31 magnesium alloy.

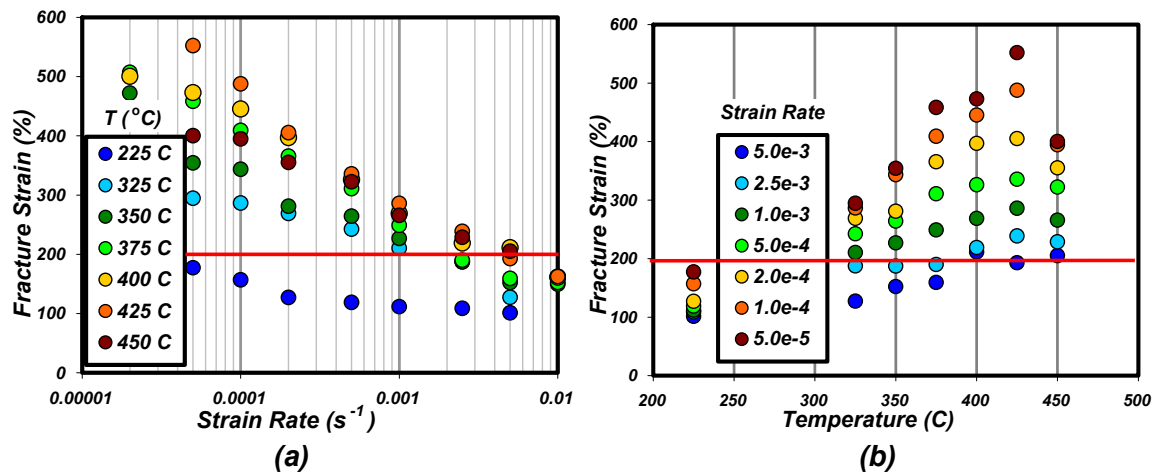


Figure 5.11: (a) Fracture strain versus strain rate at different temperatures (b) Fracture strain versus temperature for various strain rates

The effect of temperature on fracture strain seems to follow some trend, with the exception in the case of $450 \text{ }^\circ\text{C}$. For a clearer view, data points are re-plotted against temperature for the various strain rates, as shown in figure 5.11b. By comparing the two sets of curves, two main observations are highlighted. First; for a fixed temperature, varying strain rate has more effect on fracture-strain, compared to the case when strain rate is held fixed and the temperature is varied. Second; for any strain rate, there is a limiting temperature beyond which no further ductility enhancement can be achieved. Figure 5.11b in particular demonstrates the conclusion that forming the AZ31 Mg alloy at temperatures higher than $425 \text{ }^\circ\text{C}$ brings no benefit when ductility is concerned.

At this point, it is worth mentioning that the bands of temperature and strain rate covered in this study were not randomly chosen, but rather based on the results of preliminary investigations (*insignificant superplastic behaviour at temperatures lower than $325 \text{ }^\circ\text{C}$ and strain rates higher than 10^{-2} s^{-1}*), combined with practical limitations imposed by the process itself (*heating to temperatures higher than $450 \text{ }^\circ\text{C}$, and applying strain rates lower than $2 \times 10^{-5} \text{ s}^{-1}$*).

5.2.3 Strain Rate Jump Tests

5.2.3.1 Strain Rate Sensitivity Index m

Strain rate jump testing is a special form of constant strain rate tensile testing, specifically carried out for accurate determination of the strain rate sensitivity index of the material (m). The test is conducted at an initial constant strain rate $\dot{\epsilon}_1$ up to a certain strain value; thereat, the strain rate is suddenly increased to $\dot{\epsilon}_2$. Doing so, the material flow stress will accordingly change from σ_{f1} to σ_{f2} . By definition, the strain rate sensitivity index mirrors flow stress' sensitivity to strain rate, and therefore it is given by the expression:

$$m = \frac{\log \sigma_{f2} - \log \sigma_{f1}}{\log \dot{\epsilon}_2 - \log \dot{\epsilon}_1} \quad (5.1)$$

And since m is evaluated between two strain rates, its value is assigned to the average of the two strain rates between which the jump took place. The smaller the jump in strain rate, the more accurate the assessment of m is. The jump could be either upwards (*towards a higher strain rate*) or downwards (*towards a lower strain rate*). Nonetheless, in many cases, two successive jumps (*upwards followed by downward*) are carried out in the same test, in order to get two estimates for m .

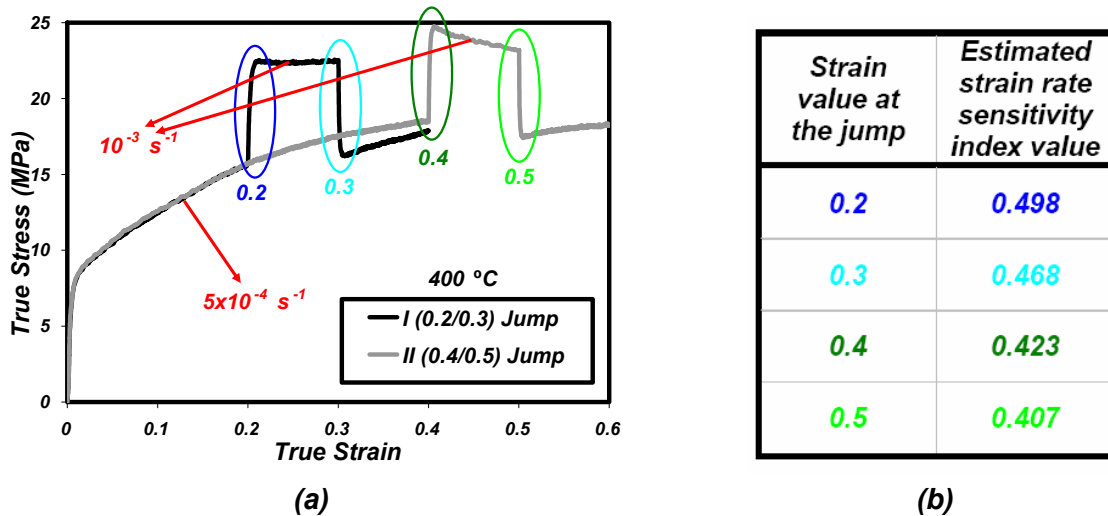


Figure 5.12: (a) Stress/strain curves for two strain rate jump tests between 5×10^{-4} and 10^{-3} s^{-1} at $400 \text{ }^\circ\text{C}$ (b) Estimated strain rate sensitivity index values

In this effort to evaluate m for the AZ31 mg alloy, jump tests were conducted at temperatures between 225 and $450 \text{ }^\circ\text{C}$, covering a band of strain rates between 1×10^{-5} and $2.5 \times 10^{-2} \text{ s}^{-1}$ at each temperature [Abu-Farha and Khraisheh 2007d & 2007c]. To enhance the accuracy of our evaluation, and for later investigation of the effect of plastic strain on m , the jump between every two

successive strain rates was carried out by two tests at four plastic strain values; upward jumps at 0.2 & 0.4, and downward jumps at 0.3 & 0.5. An example is given in figure 5.12a, which shows the stress/strain curves of two strain rate jump tests carried out at 400 °C, between 5×10^{-4} and 10^{-3} s^{-1} . Using equation (5.1), four values for the sensitivity index m were obtained; the evaluations are listed in figure 5.12b.

By combining all the jump tests conducted at a specific temperature, a band of stress/strain curves, like the one corresponding to 400 °C and shown in figure 5.13a, is obtained. For each strain rate couple, four values of m are extracted, which if plotted against the average strain rate, yield a set of curves as shown in figure 5.13b. By averaging the four m values, the effect of strain rate could be summarised for that specific temperature by one of the curves shown in figure 5.13c.

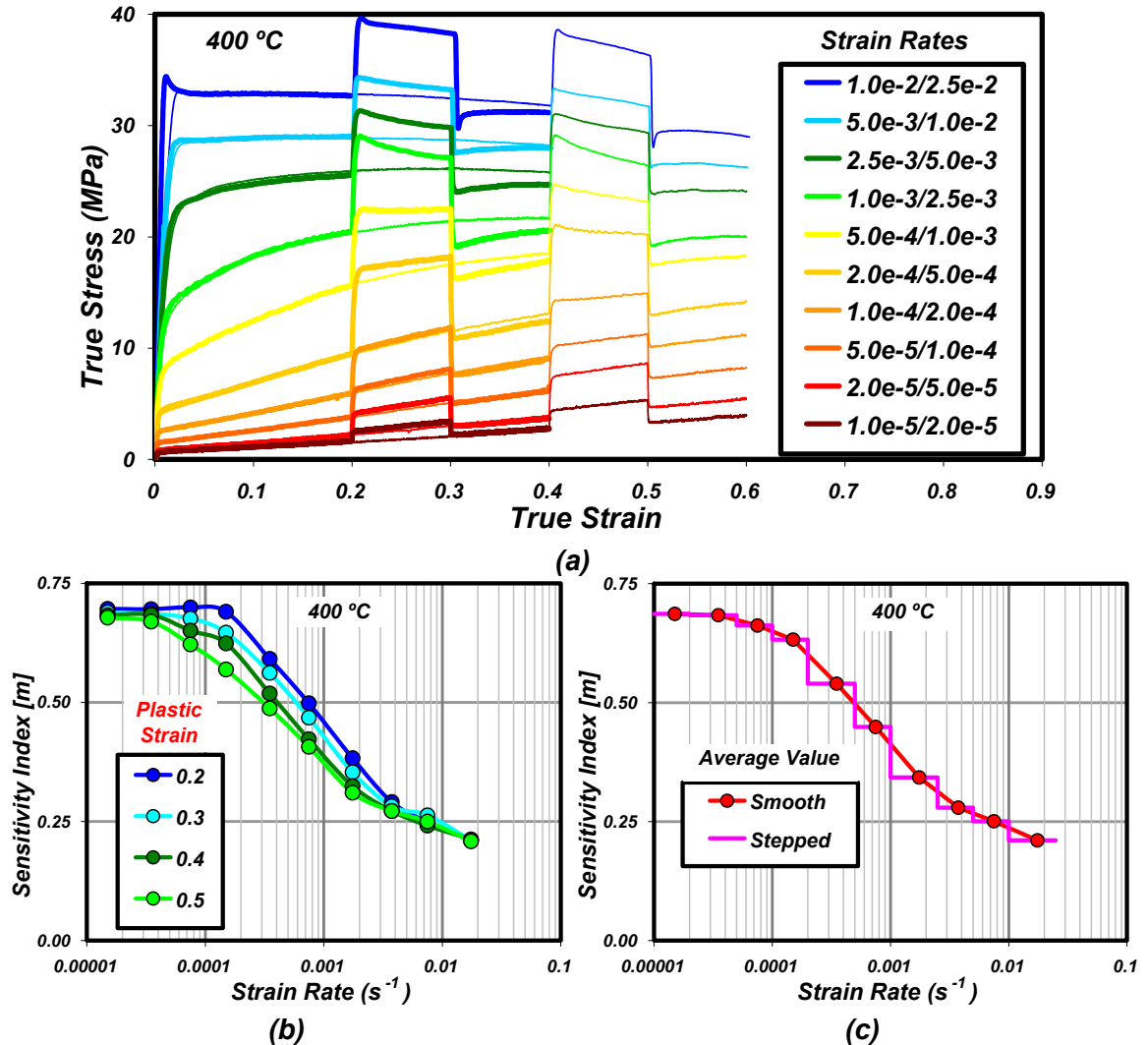


Figure 5.13: (a) A complete set of strain rate jump tests at 400 °C (b) Corresponding strain rate sensitivity index curves for four different strains (c) Continuous and stepped averaged curves for m

Part c of figure 5.13 clearly demonstrates the influence of strain rate on the strain rate sensitivity index m , highlighting the inaccuracy of assuming a fixed value, which is commonly observed in most superplastic studies. The significance of this issue arises particularly in the modelling and finite element simulation efforts. Since flow stress sensitivity to strain rate is the main characteristic of superplastic materials, m is always present in these constitutive and FE models, regardless of their different forms. Many investigators evaluate m and show its variation with strain rate, in the form of a well-known bell-shaped curve. Despite that, it is commonly practiced to assume a fixed value for m , usually the maximum one, at each forming temperature. Doing so leads to overestimates in the material's ductility, particularly at higher strain rates where the sensitivity index is way lower than the maximum assumed value, often corresponding to low strain rates.

In an effort to highlight the impact of such a practice, Nazzal et al. [2007] simulated the superplastic forming of a rectangular box, assuming both a constant and a variable sensitivity index m . It was shown how the two different approaches yield significant differences in terms of the generated pressure-time profile and the resulting sheet thickness distribution of the formed part.

Results from all jump tests at the other covered temperatures were combined together; the average m value for each combination of temperature and strain rate is presented graphically in figure 5.14.

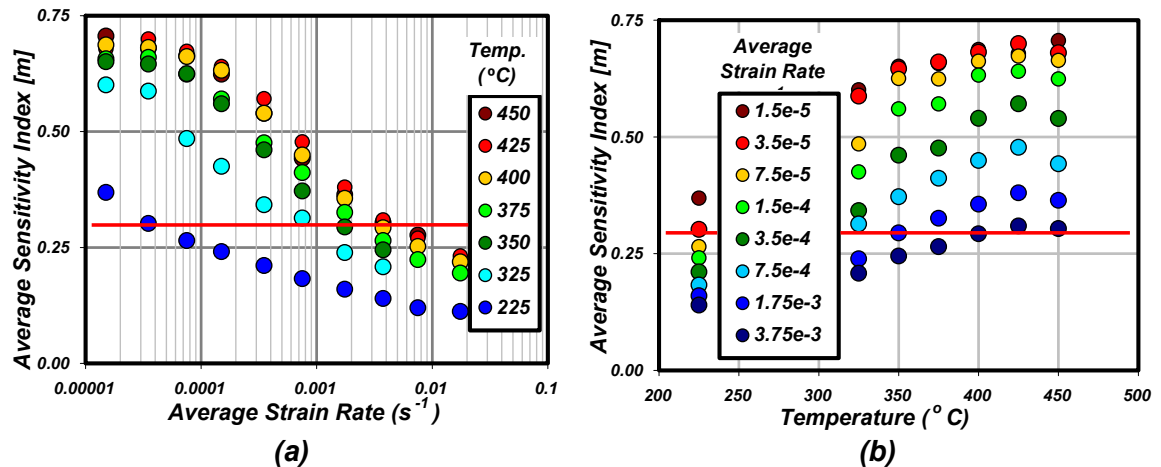


Figure 5.14: Average strain rate sensitivity index m versus (a) Average strain rate (b) Temperature

Figure 5.14a shows that for any fixed temperature, m generally increases as strain rate decreases. But at some point within the low strain rate region, m achieves a maximum value, and thence starts to decrease again. Yet, this drop is not as significant as might be depicted from the slope of the stress/strain rate curves, shown earlier in figure 5.10a. Quantitatively and as generally outlined in chapter two, superplastic behaviour is characterised by a strain rate sensitivity

index value between 0.3 and 0.7. So by considering the horizontal line corresponding to 0.3 m value, it is obvious that 225 °C does not provide enough strain rate sensitivity for superplastic behaviour to take place, except for extremely low strain rates. Moreover, any strain rate below 10^{-3} s^{-1} guarantees superplastic behaviour at all the other higher temperatures. These two conclusions highly agree with the previous discussion in which the boundaries of the superplastic region of the alloy were set based on the fracture strain values.

Though temperature's increase seems to improve the alloy's sensitivity, a clearer look on its effect may be gained by considering figure 5.14b. It is shown that raising the temperature beyond 425 °C adversely affects m , regardless of strain rate. This also coincides with the conclusion regarding the effect of temperature on the maximum attainable fracture-strain, presented earlier in figure 5.11b. Another interesting conclusion also supporting the previous one related to ductility; varying strain rate significantly affects the m value at a fixed temperature, while holding a fixed strain rate value yields less effect on m when temperature is varied.

5.2.3.2 Effect of Plastic Strain on m

By looking back at figure 5.14b, it is inferred that the effect of plastic strain at which the sensitivity index m is evaluated on the value of m , varies between insignificant at very high and low strain rates, to quite observables at middle-ranged ones. Recall that this middle region is the optimum region at which superplastic forming operations are more likely (*desired*) to take place.

In the previous section, we highlighted the inaccuracy of assuming a fixed value for m , despite the fact that its variability with strain rate is a common knowledge. Plastic strain, on the other hand, has been virtually ignored, and no single study investigates or highlights its effect on m . Therefore, in order to further emphasise its influence, additional jump tests were conducted at a selected temperature (400 °C), by which four more jumps were added covering plastic strains up to 0.9. The new m values corresponding to the higher strains were added to those presented in figure 5.13b, generating an expanded set of curves, as shown in figure 5.15a. It is evident that the shape of the m /strain rate curve is affected by the jump strain at which m is evaluated. The higher the strain value, the more it deviates from the bell-shaped curve. At its peak, the difference in the m value evaluated at 0.2 and 0.9 jump strains is about 0.25, which represents more than 35% of the higher value!

Data points in figure 5.15a were plotted again with plastic strain as the x-axis in figure 5.15b. This representation makes it easier to depict the inverse influence of plastic strain on m , which is strongest at the centre of the superplastic region, and diminishes as we move away.

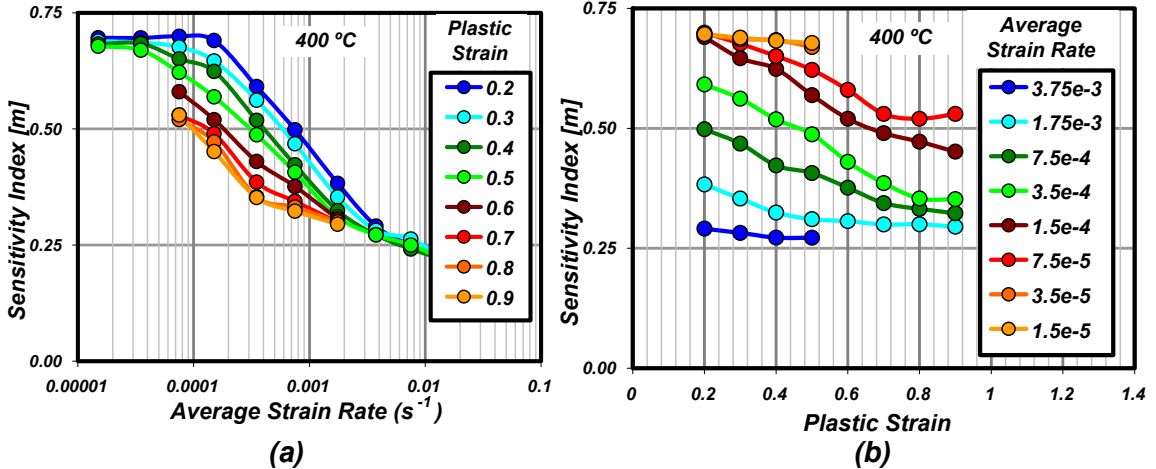


Figure 5.15: Strain rate sensitivity index m at 400 °C versus (a) Average strain rate at different strains (b) Plastic strain at different strain rates

5.2.3.3 Jump Test versus Slope of the Stress/Strain Rate Curve

In many superplastic studies, the strain rate sensitivity index m is still estimated by taking the slope of the sigmoidal-shaped stress/strain rate curve. However, such estimates are inaccurate and very misleading, particularly if incorporated in constitutive models, FE simulations or actual superplastic forming practices. To demonstrate that, the stress/strain rate curve corresponding to 400 °C, presented earlier in figure 5.8c, was reconsidered. By taking the slope of the curve at different strain rates, an m /strain rate curve as the one shown in figure 5.16a, was constructed. The curve exhibits the well-known bell shape, but the values of m are very high around the apex. For a superplastic material, m value should not exceed 0.7 under any circumstances, which is not the case here.

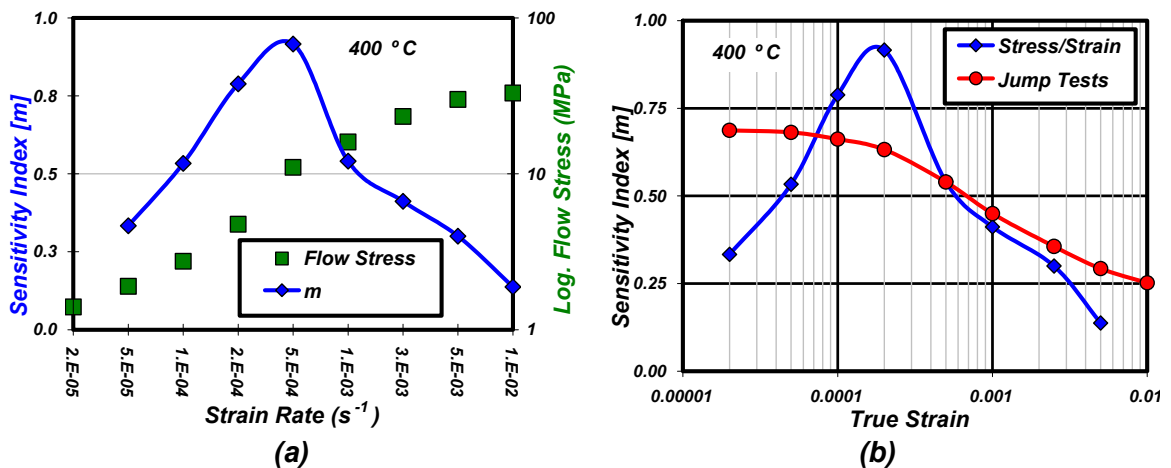


Figure 5.16: (a) Sensitivity index m derived from the slope of the stress/strain rate curve at 400 °C (b) Comparison with the curve generated by strain rate jump tests

Figure 5.16b shows the same curve plotted on top of the one obtained from the series of strain rate jump tests, presented earlier in figure 5.13c. Evidently, slope-derived m values are either overestimated or underestimated, almost all over the entire superplastic region for the material (*strain rates lower than 10^{-3} s^{-1}*). Quantitatively, slope-derived m values fluctuate between -52% to +45% of the corresponding values obtained from strain rate jump tests. Strain rate jump test is not only the accurate mean for evaluating m , but it also offers the flexibility to investigate the effects of the various process parameters (*strain and strain rate*) on it.

5.3 High Temperature Biaxial Testing at Controlled Rates

To conduct biaxial tensile tests at elevated temperatures, the fixture presented in chapter four (*figure 4.21*) was first considered to be fitted inside the heating chamber. However, to avoid causing any damage to the various parts of the fixture (*particularly the sliding parts*), the fixture was modified by adding a heating capsule that encloses only the centre part of the test specimen. Heating was then achieved by using a high performance multi-setting heat gun, as shown in figure 5.17. The temperature inside the chamber can be controlled by both the blower speed and exit temperature of the heat gun. For temperature measurement and monitoring during testing, two thermocouples were installed at fixed positions inside the capsule. On the other hand, two additional thermocouples were attached to a test specimen, and the obtained temperature was assigned to that specific heat gun setting (*blower speed and output temperature*), as shown in figure 5.18.

Testing procedure starts by fitting the test specimen (*discussed next*) between the four grips, and then enclosing the heat gun's nozzle to the open side of the heating capsule. Thereafter, heating phase is started till the desired forming temperature is reached. And because the size of the capsule is small, reaching the set temperature was found to take less than 15 minutes. Similar to the uniaxial loading case, some holding time is allowed before straining; in this case, a 10 minute holding time is adopted.

The test is then started in a way similar to the uniaxial loading case, by setting the desired strain rate and initial specimen dimensions; the gear trains transmit the vertically applied strain rate to a combined horizontal-vertical strain rate, defined linearly by the gear train ratio. Simultaneously, data acquisition in the two mounted load cells is started, to measure forces while straining. The two load cells are synchronised together, yet they are not synchronised with the INSTRON's displacement measurements, this is done after testing, by combining the two lines of data. Time lag between the two sources of data is very small that it should not affect the results, especially that testing takes often a long time.

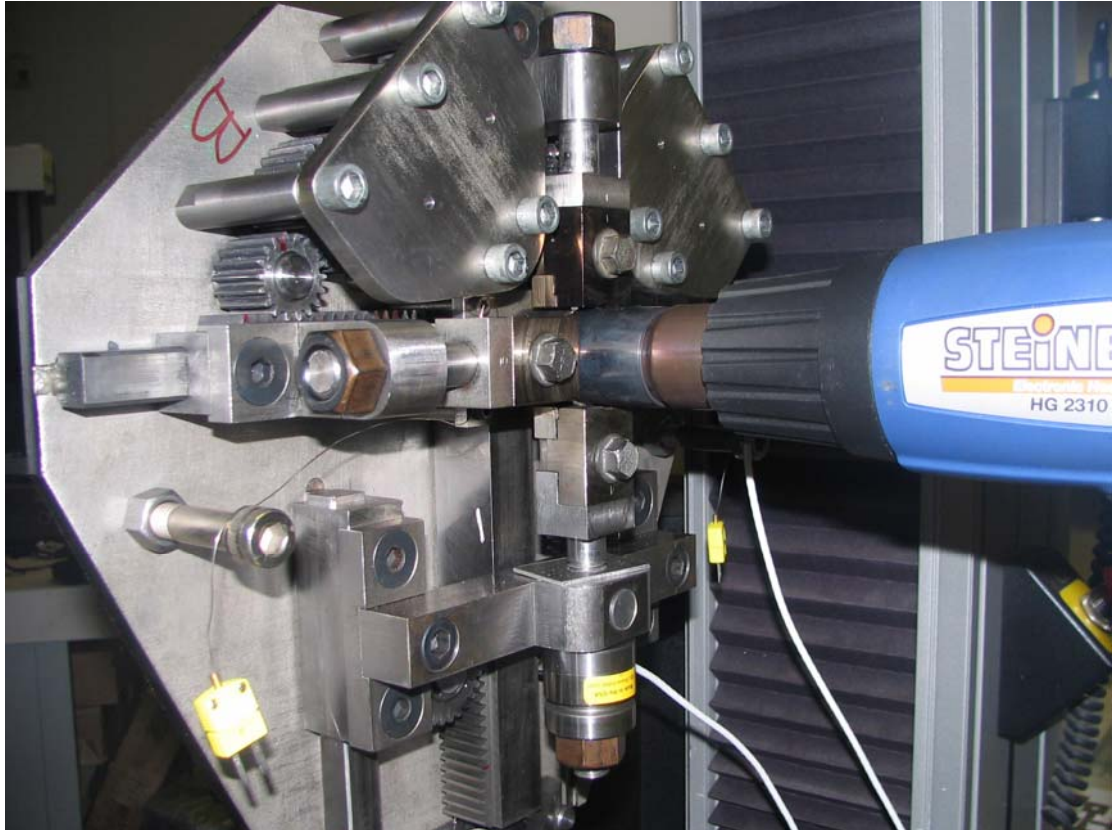


Figure 5.17: A heat gun used to produce localised heating inside the heating capsule

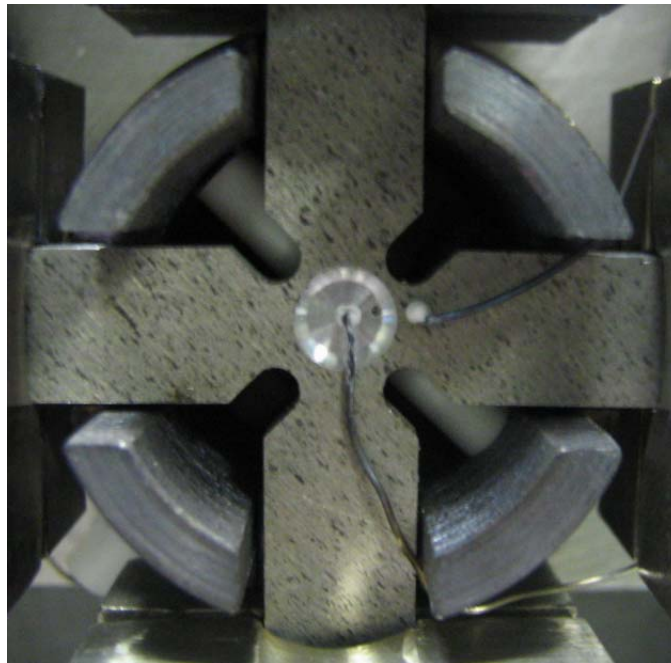


Figure 5.18: A calibration test specimen with two thermocouples for temperature measurement

After testing the new specimen geometry, improvement was observed with regard to that the deformation was shifted more towards the centre point of the specimen. Yet, the outcome was not as good as hoped for. By deforming the material to higher strain limits, deformation becomes highly localised in the neck region between the centre and one of the four arms, as illustrated by figure 5.20.

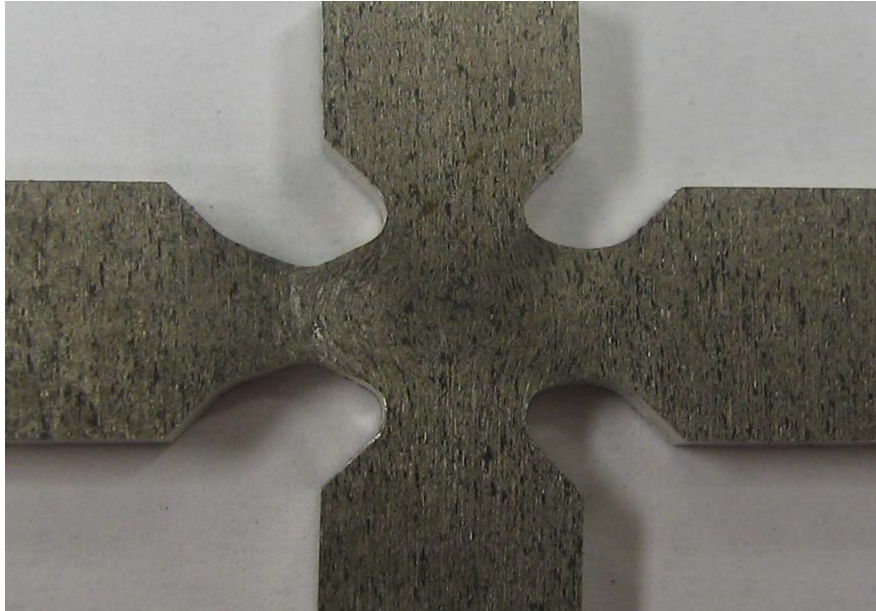


Figure 5.20: localised deformation in the neck region between the centre region and one of the four specimen arms

To further improve the outcome, the second major modification was to machine a small recess on both sides of the centre region, such that the cross sectional area is smaller than the neck region. This is schematically shown in figure 5.21.

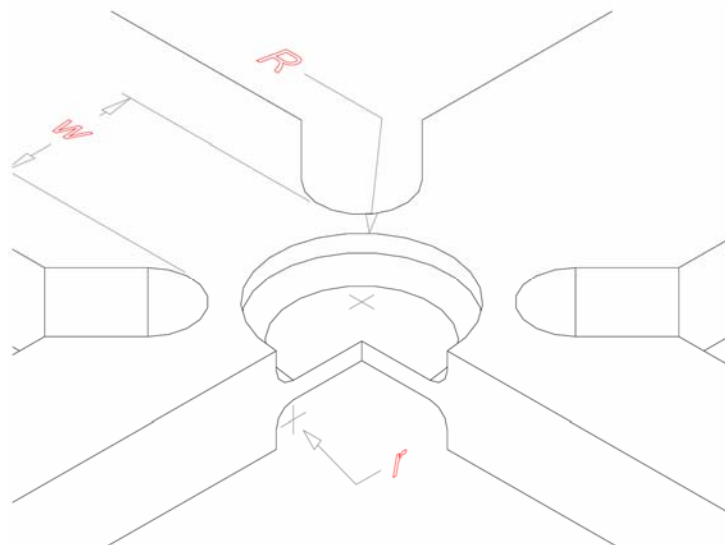
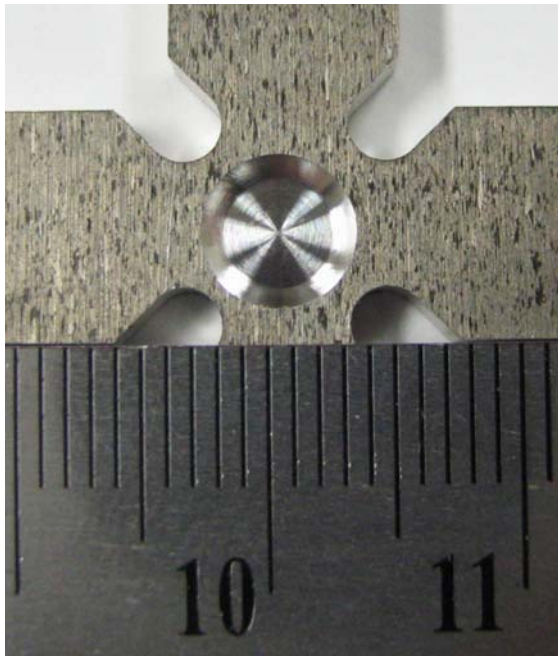


Figure 5.21: A recess introduced to the centre region of the specimen

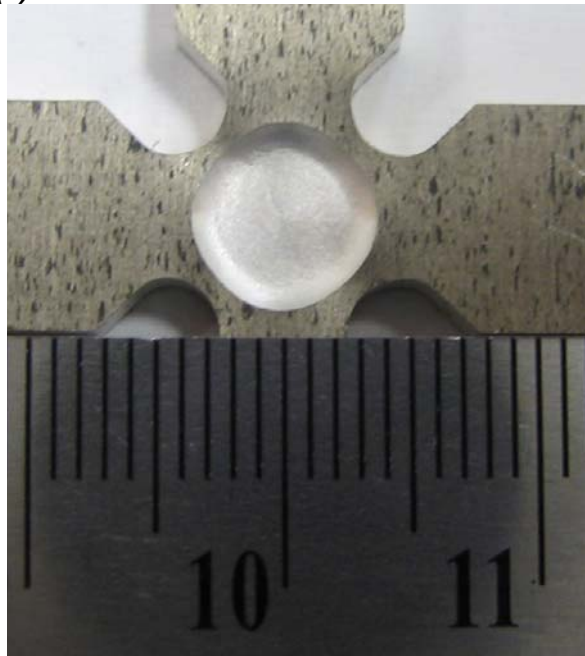
Though the size of the recess was still arbitrarily-chosen, the results were significantly improved, indicating the effectiveness of the approach. An example is shown in figure 5.22, which shows a specimen deformed at 275 °C and strain rate of $2 \times 10^{-3} \text{ s}^{-1}$.



(a)



(b)



(c)

Figure 5.22: An example of a uniform biaxial deformation localised at the centre part of the test specimen (a) Before and after (b) Zoomed before (c) Zoomed after

Interestingly, by repeating the same testing conditions and stretching the specimen to higher strain limits, fracture took place right at the centre of the test specimen, as depicted from the two cases shown in figure 5.23. Such fracture implies that the biaxiality of deformation was maintained throughout the test, up to the point where the specimen failed.

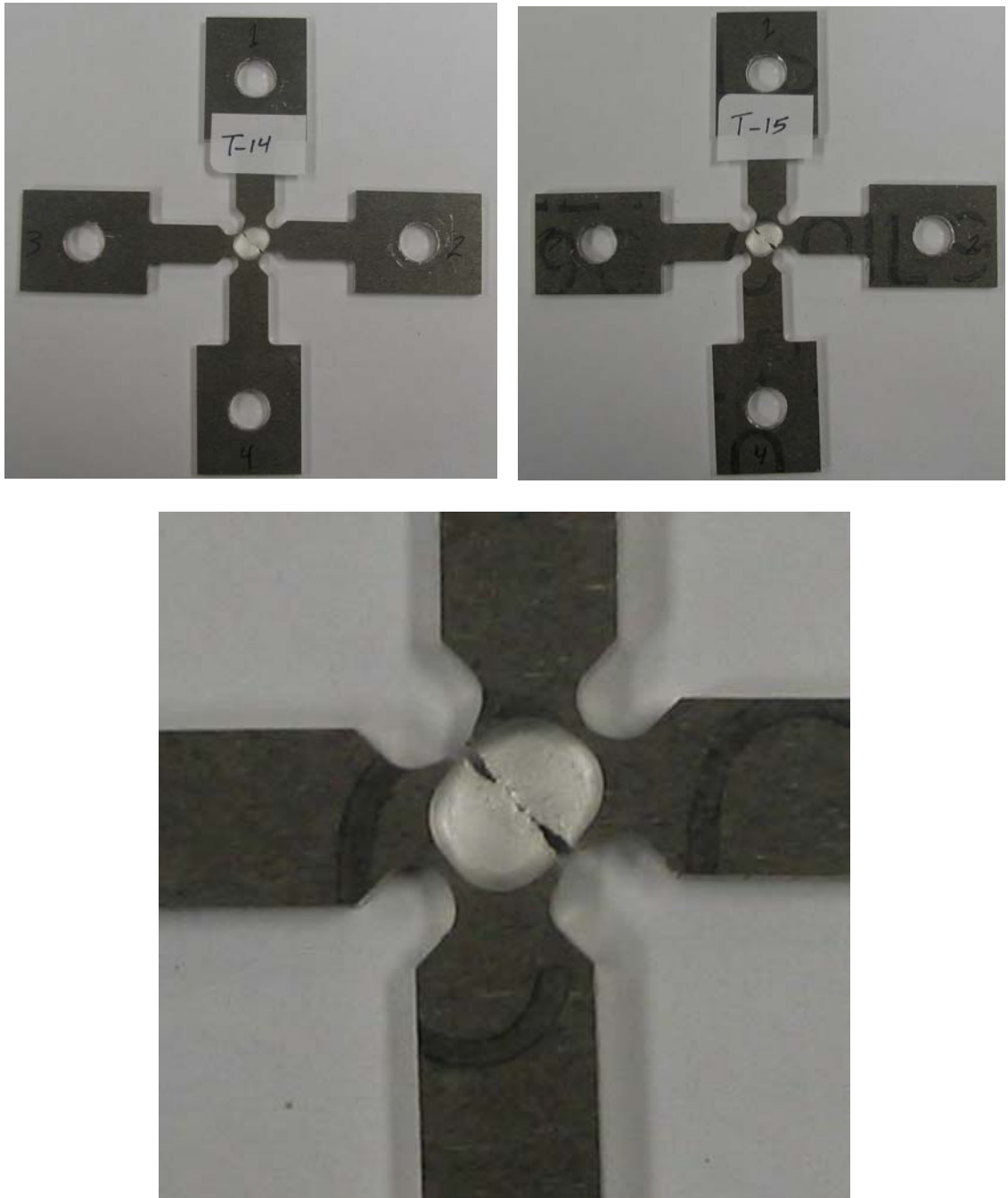


Figure 5.23: Fracture taking place at the centre of the test specimen

This significant result represents a big step in our effort to test superplastic materials in biaxial tension at elevated temperatures. Despite that, one more step might be still needed regarding the issue of specimen design, which is to optimise the selection of the various parameters defining the deformation zone. That is, the diameter of the recess D , its depth d , its fillet radius r , and the ratio between the recess diameter and neck width D/w (figure 5.21). It is hoped to accomplish this task with the aid of finite element analysis.

Finally, it is important to mention one of the major problems that still need to be resolved; which is the issue of compliancy and its effects on the accuracy of stress and strain measurements. Figure 5.24 shows the forces measured along both the x and y axes of the test specimen, during a balanced biaxial tensile test at $2 \times 10^{-3} \text{ s}^{-1}$ and $290 \text{ }^\circ\text{C}$. Two problems can be noticed from the curves in the figure; the horizontal shift (*time lag*) and the difference in slope between the two curves.

The horizontal shift implies that deformation started in the y direction before it was actually transmitted by the fixture to the x direction. This problem is caused by some pre-loading exerted on the specimen in one of the two directions (*usually vertical*) before the test starts. On the other hand, the lower slope in the case of the x -force curve implies some compliancy, caused mainly by the number of moving parts in the gear trains that transmit the vertical displacement into a horizontal one. These two problems make it hard to get accurate evaluations of stress and strain in both directions during deformation. Refinements in the fixture's mechanism are needed to eliminate or at least minimise these problems.

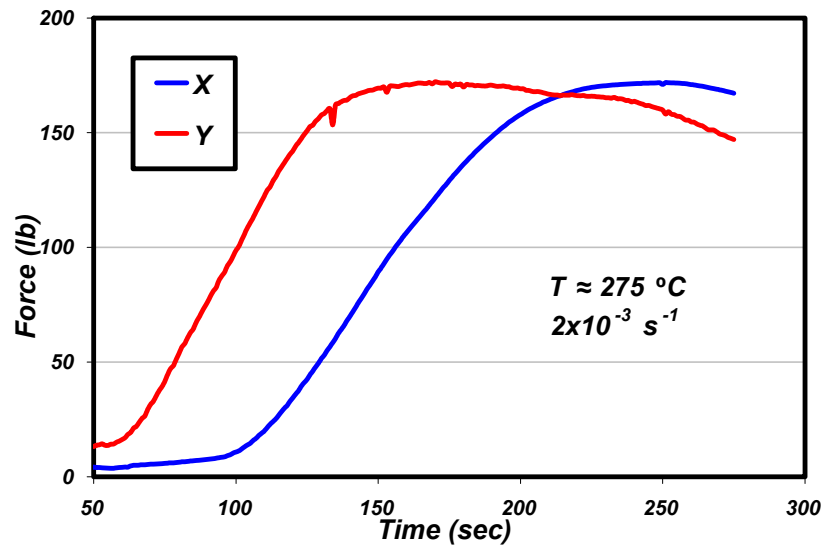


Figure 5.24: Measured forces along the x and y axes of the test specimen

6. CHAPTER SIX: MODELLING, SIMULATING AND OPTIMISING THE SUPERPLASTIC FORMING OF THE AZ31 MAGNESIUM ALLOY

Superplastic Forming (*SPF*) is an innovative process that stretches the boundaries of ductility in conventional forming operations, offering a great potential for successful sheet metal forming of hard-to-form materials, such as magnesium alloys. However, the success the process has been living is still very limited, even with other alloys. And in spite of the several titanium and aluminium parts that have been superplastically-formed and used in various aerospace applications, the widespread industrial utilisation of the process is hindered by many issues. The majority of these issues are mirrored practically by the lack of control in forming practices, which are directly related to the limited predictive capabilities of deformation and failure.

Blow forming is considered the most common practice employed in forming superplastic materials, where the sheet is formed onto the die using pressurised gas. The selection of forming pressure profile (*or forming pressure-time profile*) is very critical, as it ultimately determines the integrity of the formed part and the production time; in other words, it controls the whole forming process. But with the current lack of predictive capabilities, forming pressure profiles used in the industry are still based on trial and error routines. And since superplastic deformation is rate-dependent, it is a common practice to employ a low “safe” pressure to prevent excessive thinning and premature failure.

Controlling deformation during the superplastic forming processes is a necessity, if *SPF* is expected to be the process of choice, for future magnesium sheet metal applications. Such control would mean, as a first step, having the ability to generate the right forming pressure profile, that maintains a constant strain rate during deformation, within the range where maximum ductility is achieved. By doing so, thinning and failure could be prevented, regardless how complicated the shape to be formed is. Unfortunately, maximum superplastic ductility is usually achieved at relatively low strain rates, leading to prolonged forming times. Therefore, the challenge is to go an extra step, and optimise the process by generating an optimum forming pressure profile.

Several investigators have reported that using variable strain rate schemes may reduce the forming time, and yet maintain the integrity of the formed component [Johnson et al. 1993, Ding et al. 1995, Akkus et al. 1997, Khraisheh and Zbib 1999]. Others reported increased thickness strain at failure by applying pulsating strain rate schemes [Vulcan et al. 2004, Banabic et al. 2005]. Generally, these studies are based on limited experimental observations and/or simple models that cannot be generalised to optimise *SPF* of the various materials. To develop accurate optimum forming paths, deformation behaviour of superplastic materials must be accurately described, and thence, a failure criterion that takes different failure mechanisms into account must be used.

Recently, a new multiscale failure criterion, that takes both geometrical and microstructural features into account, has been developed [Thuramalla and Khraisheh 2004]. The criterion was combined with a simplified constitutive model, the *1D* form of the constitutive model presented in chapter three, to optimise the superplastic deformation of the Ti6Al4V alloy [Thuramalla et al. 2004] and the Pb-Sn eutectic alloy [Deshmukh et al. 2004].

In this chapter, we present a systematic integrated approach, which combines previous modelling and testing efforts with a selected failure criterion, to optimise the superplastic behaviour of the AZ31 magnesium alloy. First, the general constitutive model presented earlier in chapter three is reduced to the uniaxial loading case, accounting for both grain growth and cavitation. The focus is then directed to the behaviour of the alloy at 400 °C, where microstructural examination is carried out. These results are combined with those obtained from mechanical testing (*chapter five*), and thereafter used to calibrate the constitutive model. In a collaborative effort with a fellow student (*M. Nazzal*), the calibrated model is fed along with a stability criterion (*developed by N. Thuramallah*) into a FE code to generate optimum variable strain rate loading paths for the AZ31 magnesium alloy. The FE code employs user-defined subroutines developed by M. Nazzal to combine the model with the stability criterion [Nazzal et al. 2004 & 2007]. Uniaxial tensile tests and free bulge forming experiments are finally conducted to evaluate the effectiveness of the proposed optimisation technique [Khraisheh et al. 2006].

Though the approach presented in this chapter is directed towards one temperature, yet it could be generalised to any other temperature in the same manner.

6.1 Modelling the Material's Tensile Behaviour at 400 °C

One temperature was considered in the upcoming analysis for two main reasons. First, the large number of tests needed (*mechanical and microstructural*), in addition to the added effort in fitting the behaviour of the material at each temperature. Second, the main objective is to provide and validate the proposed optimisation approach, and not to compare its outcome at various temperatures. 400 °C was selected based on the investigation of the material's superplastic behaviour, conducted and presented in chapter five. The results in terms of fracture strain and strain rate sensitivity index indicate that 400 °C falls within the optimum forming range of the AZ31 magnesium alloy (*but not necessarily the most optimum*).

6.1.1 Reduced Model

Only the uniaxial loading case is considered, because of the lack of data under any other loading condition. Anisotropy was dropped, since the material did not show any strong indications of such behaviour under simple tension at elevated temperatures, as shown in figure 5.6, presented earlier in section 5.2.1. And since preliminary investigations indicated so, grain growth and cavitation were both included.

Starting with the generalised $1D$ form of the constitutive equation, given by equation (3.22), and dropping the $_{11}$ index, since there is only one stress and strain rate components, we get:

$$\dot{\varepsilon} = \left[\frac{C_I [J - (K_0 + R)]^{\frac{1}{m}}}{d^p} + C_{II} J^n \right] \frac{\partial J}{\partial \sigma} \quad (6.1)$$

By substituting zero values for the anisotropic parameters (c_1 , c_2 and c_3) in the yield function given in equation (3.5), it reduces to the von-Mises isotropic yield function, which is equal to the axial stress in simple tension, that is:

$$J = \sigma \quad (6.2)$$

Therefore, the differential term ($\partial J / \partial \sigma$) in equation (6.1) reduces to unity. Substituting back in equation (6.1) gives:

$$\dot{\varepsilon} = \frac{C_I [\sigma - (K_0 + R)]^{\frac{1}{m}}}{d^p} + C_{II} \sigma^n \quad (6.3)$$

The creep region (*region I in figure 2.2*) is not clearly identified in the stress/strain rate curve corresponding to $400\text{ }^\circ\text{C}$, shown in figure 5.10a. And since this region is represented by the hardening term (*raised to the n power*) on the right hand side of the equation, this term can be dropped. Also, with no evolution for the internal variables, the remaining constants can be combined in one to get:

$$\dot{\varepsilon} = \frac{C_{III}}{d^p} \sigma^{\frac{1}{m}} \quad (6.4)$$

where C_{III} is a new material constant.

Finally, to account for cavitation, the stress term is altered by compensating for the reduction in the effective area, using the area fraction of voids f_a , to yield:

$$\dot{\varepsilon} = \frac{C_{III}}{d^p} \left[\frac{\sigma}{1-f_a} \right]^{\frac{1}{m}} \quad (6.5)$$

The forms of the evolution equations for grain growth and cavitation will be selected based on the experimental results, as discussed next.

6.1.2 Grain Growth

Due to large plastic strains and heat application for prolonged periods of time, microstructural changes during superplastic deformation could be very significant, and therefore need to be quantified. Grain growth is generally dependent on both heat and strain, yet this dependence is different for different superplastic materials. For the AZ31 magnesium alloy, Lee and Huang [2004] showed that the alloy's grain-structure evolves due to both heat and strain, indicating both static and dynamic grain growths. Therefore, both terms were investigated in this work, and to distinguish between them, test specimens were prepared in two different ways before microstructural examination; heat cycling and interrupted tensile tests.

6.1.2.1 Static Grain Growth

Small pieces, about 1 cm^2 each, were cut from the 3.22 mm thick AZ31 magnesium alloy sheet. These pieces were heated to $400 \text{ }^\circ\text{C}$ then left for different times before taken out, and immediately quenched in water. Each piece was then mounted, grinded, polished and etched, as previously described in section 5.1.1, and several photos at different locations across the polished surface were taken. An example from two samples heated to different times is shown in figure 6.1. In general, all the heated samples revealed clearer microstructures, because of the larger grains and the reduced twinning.

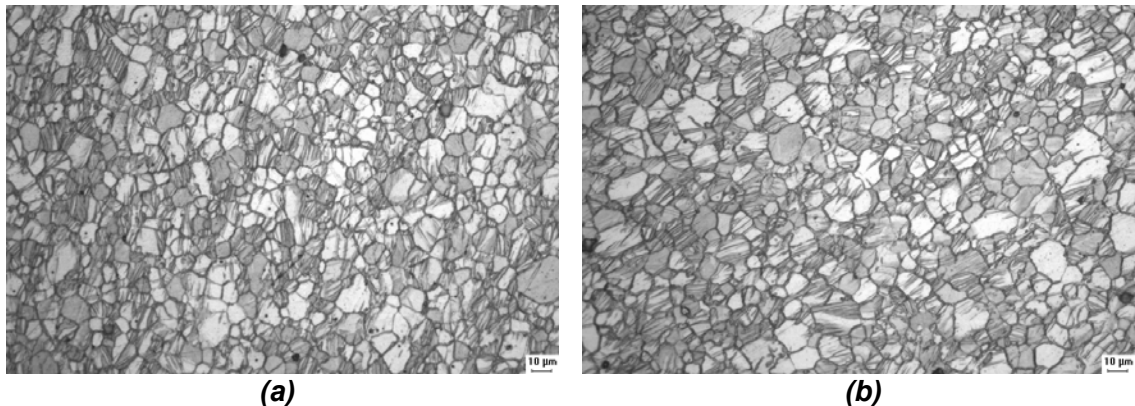


Figure 6.1: Selected photos for the grain-structure of the AZ31 mg alloy taken after heating at $400 \text{ }^\circ\text{C}$ for (a) 75 (b) and 252 minutes

Average grain size estimates were all made using the software described in section 5.1.1. The line method was not used for time-saving purposes; besides, the photos were all clear enough to capture the grain boundaries to a very good extent using the software. At least five measurements were made, and the average of all was assigned to each sample; the results are summarised graphically in figure 6.2.

Figure 6.2a shows that heating effect is most significant in the early stage, where grain size increases from 4.5 to about 8 μm within the first 65 minutes of heating. And since this is equal to the total heating time prior to straining in tensile testing at 400 °C, the figure indicates that the initial grain size at the threshold of plastic deformation should be considered 8 μm , and not 4.5 μm . In fact, this is the most important result extracted from static grain growth analysis, since it defines the starting point for the dynamic grain growth curves. On the other hand, the curve also indicates a generally logarithmic static grain growth behaviour, which could be better observed by plotting the same data points against a logarithmic heating time axis, as shown in figure 6.2b.

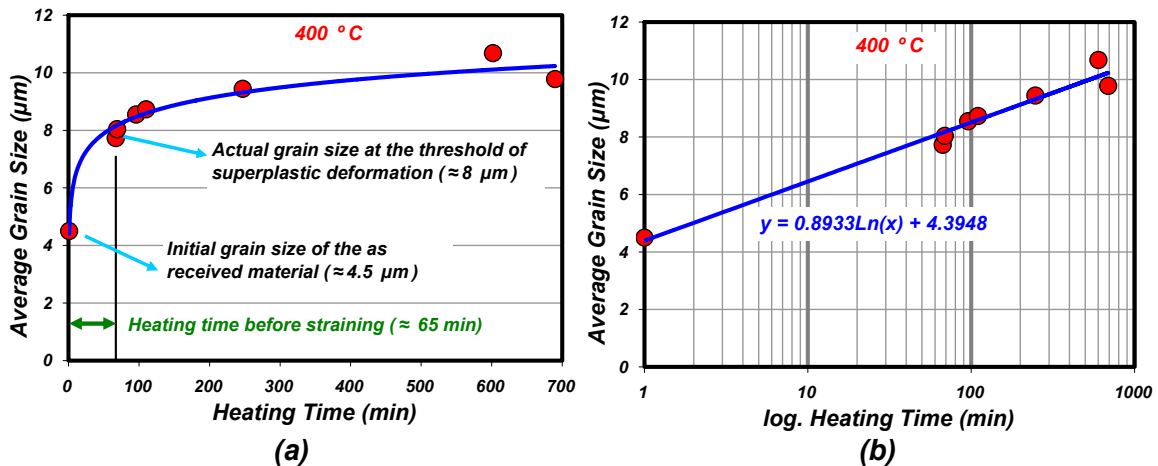


Figure 6.2: Static grain growth curve at 400 °C (a) Normal time scale (b) Logarithmic time scale

6.1.2.2 Dynamic Grain Growth

Interrupted tensile tests were carried out at different strain rates up to certain strain values, thereafter, the test would be stopped, and the specimen is quenched in water. Specimens strained to higher strains were simply taken from the tensile tests, which, as was highlighted in chapter five, were quenched in water immediately after failure took place. A small sample was taken out of each specimen; close to the failure point, or somewhere at the middle of the gauge length. Each sample was then prepared for microstructural examination as described before; and again, several photos at different locations across the sample were taken. An example from three samples corresponding to a certain strain level is shown in figure 6.3.

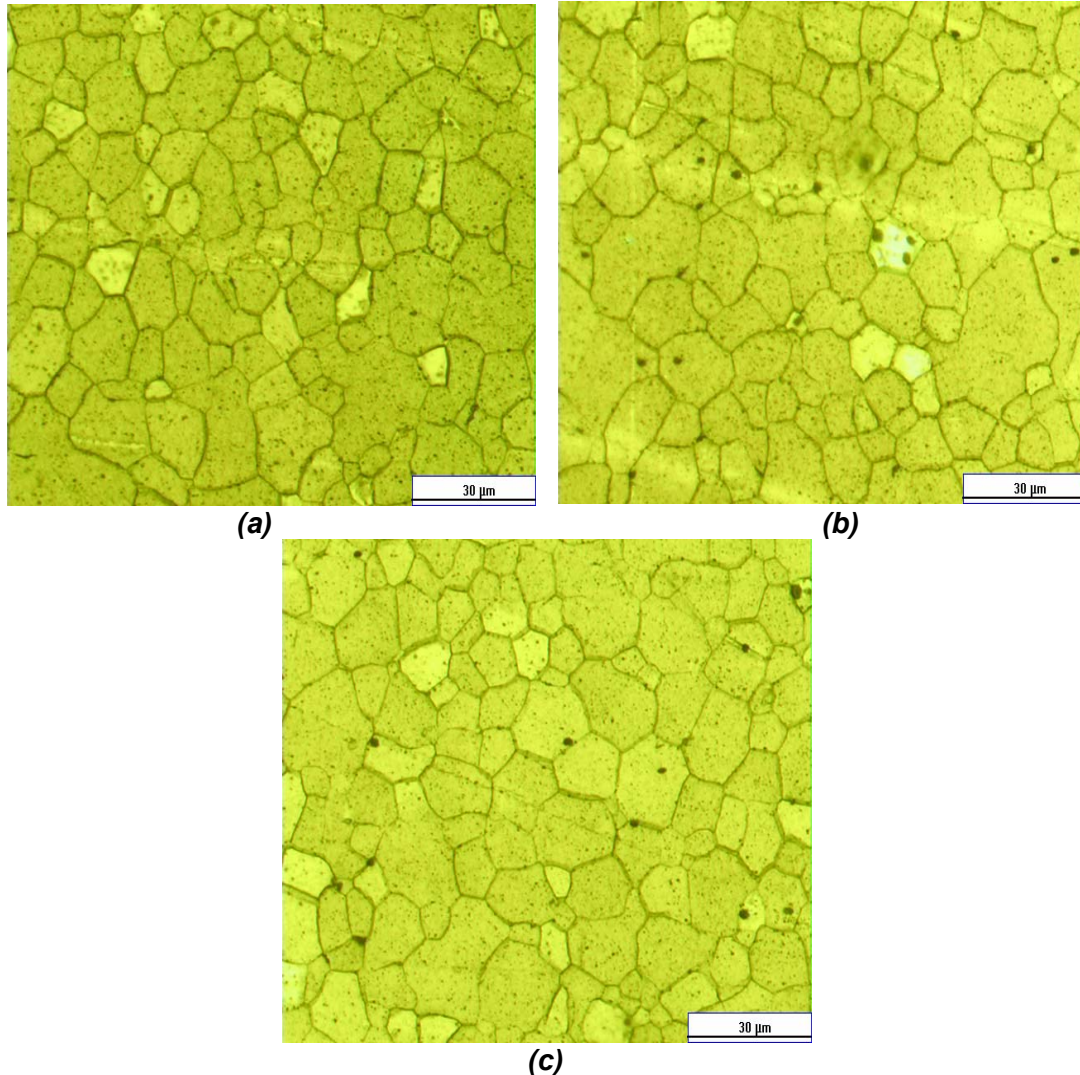


Figure 6.3: Selected photos for the grain-structure of the material taken after straining at $1 \times 10^{-4} \text{ s}^{-1}$ and $400 \text{ }^\circ\text{C}$ to different strains (a) 0.3 (b) 0.7 (c) 1.1

Average grain size estimates were made as described in the static grain growth part, and the results were plotted against strain, as shown in figure 6.4. As explained earlier, the dynamic grain growth curve starts at about $8 \mu\text{m}$. The remaining data points follow a decently linear behaviour with respect to strain. By fitting all the data points to the closest straight line, the equation shown inside the figure was obtained. This equation is the basis for selecting the appropriate grain growth model, which will be fed into the constitutive model, given by equation (6.5). Therefore, instead of using a complex form like the one we used for the Pb-Sn alloy, a simple linear grain growth model similar to the one used by Wilkinson and Caceres [1984] is used here:

$$d = d_0 + C_{IV} \varepsilon \quad (6.6)$$

Where the values of d_0 and C_{IV} are extracted from the figure.

Strain rate did not show any significant effect on dynamic grain growth, and therefore the results in figure 6.4 are assumed to be strain rate independent.

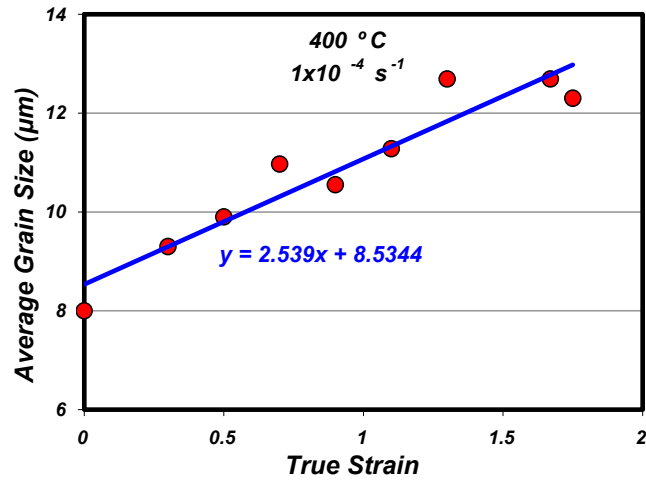


Figure 6.4: Dynamic grain growth curve at 400 °C

6.1.3 Cavitation

Cavitation was observed in the AZ31 magnesium alloy during the tensile testing stage, even without microstructural examination. Figure 6.5 shows the visually-clear evidence of cavitation, observed on one end of a tensile specimen, after straining at 400 °C and 1×10^{-4} . And as it is strongly strain-dependent, microstructural examination for cavitation was carried out in a similar manner to the dynamic grain growth; i.e., by analysing samples taken from tensile specimens after interrupted tensile tests. In fact, the same samples used in evaluating the dynamic grain growth, were used for cavitation examination, just before the etching stage, since all what's needed is a flat polished surface.



Figure 6.5: Evident cavitation in a specimen deformed at 400 °C and $5 \times 10^{-5} \text{ s}^{-1}$

Several photos at different locations across the sample were taken, and few examples from samples corresponding to different strain levels are shown in figure 6.6.

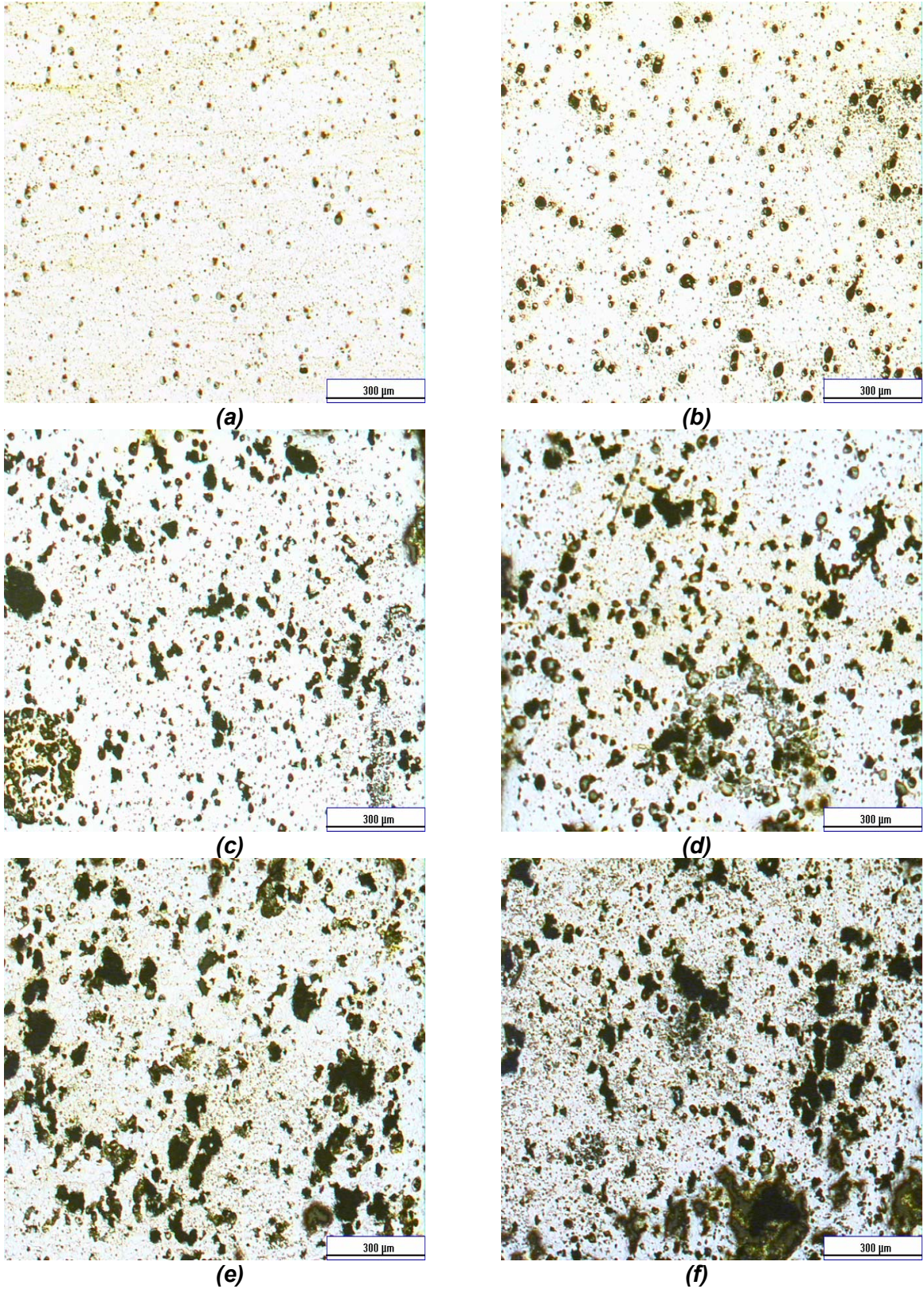


Figure 6.6: Selected photos for cavitation in the material taken after straining at 400 °C to different strains (a) 0.5 (b) 1.15 (c) 1.45 (d) 1.6 (e) 1.68 (f) 1.75

To quantify cavitation, the area fraction of voids needs to be evaluated. To do so, a different module of the software utilised before for grain size measurement, was used. This module mechanism evaluates voids' area fraction in a slightly different way, as illustrated by figure 6.7. The microstructural photo is first scanned, and two areas are highlighted; a bright main substrate (*orange*) and a collection of dark spots representing voids (*blue*). The total blue area is divided by the overall area, yielding an estimate for the area fraction of voids.

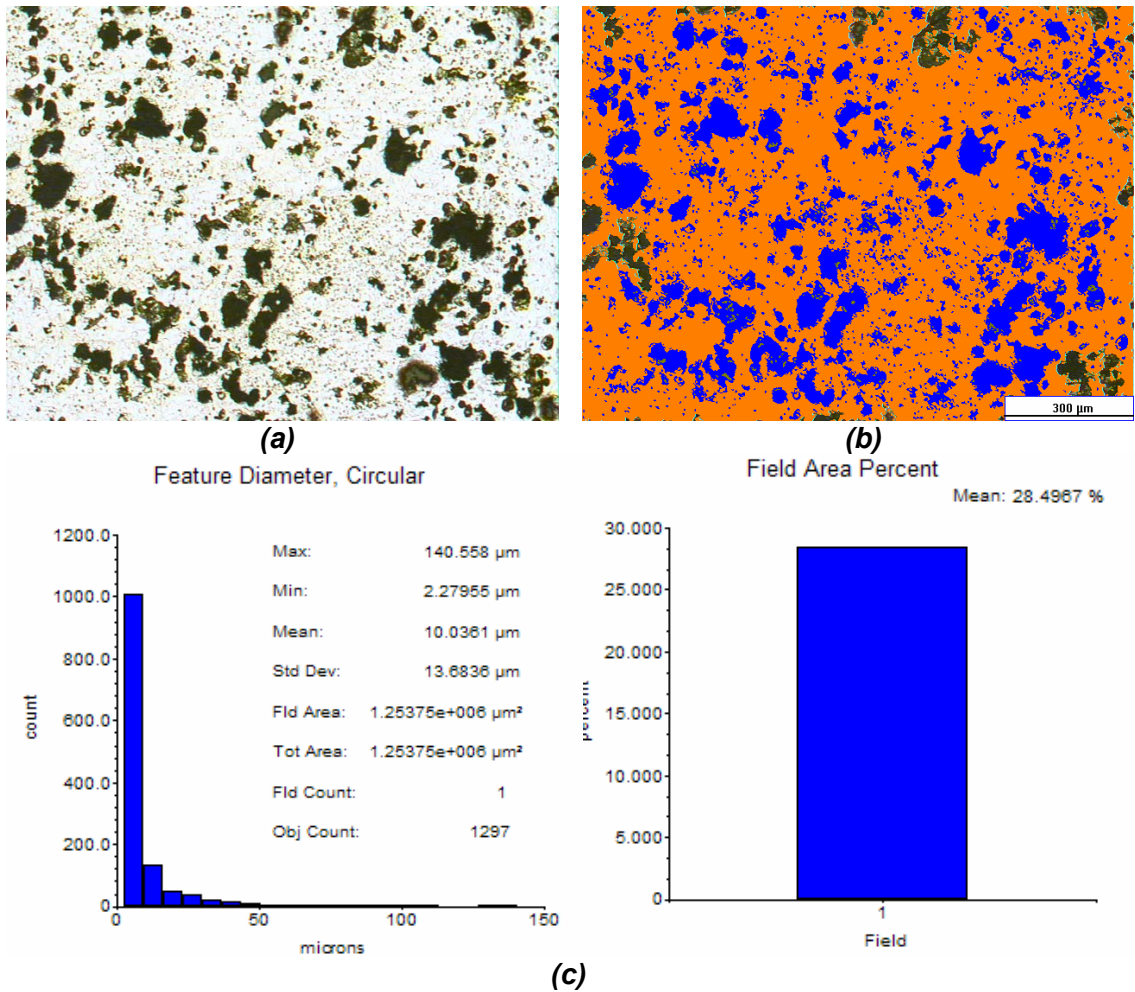


Figure 6.7: Software used for area fraction of voids' measurement in a sample taken from a specimen strained at $1 \times 10^{-4} \text{ s}^{-1}$ and $400 \text{ }^\circ\text{C}$ (a) Photo of the microstructure (b) Captured voids (c) Results

The results of those estimates were plotted against strain, as shown in figure 6.8. Note that cavitation increases slowly at first, up to strains in the vicinity of 0.9; and thereafter, clear escalation of cavitation level takes place. This overall exponential behaviour is similarly observed in other superplastic materials [Chino and Iwasaki 2004]. The data points in figure 6.8 were then fitted to an exponential curve, yielding the equation shown inside the figure.

This equation has the exact form given by equation (3.12) earlier in chapter three, and therefore the same cavitation model is used here for the AZ31 mg alloy, that is:

$$f_a = f_{a0} \exp(\psi \varepsilon) \quad (6.7)$$

Where the values of f_{a0} and ψ are extracted directly from the figure. Similar to the dynamic grain growth case, strain rate did not show strong influence on cavitation, and therefore it is also assumed to be strain rate independent.

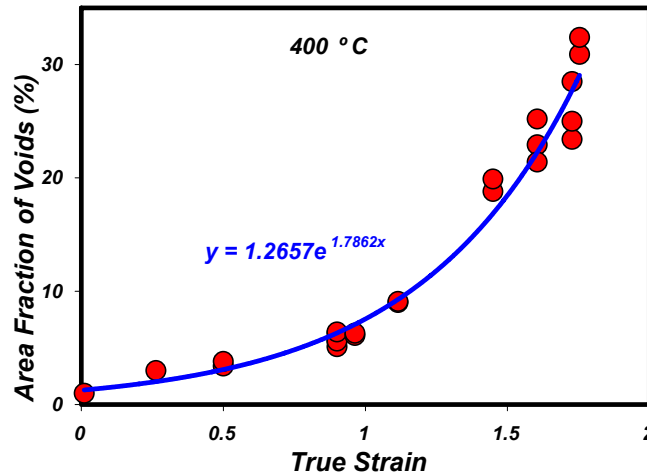


Figure 6.8: Area fraction of voids versus strain at 400 °C

6.1.4 Model Calibration

The evolution equations of grain size and area fraction of voids were calibrated first using the data presented in figures 6.4 and 6.8, respectively. Note that evaluating all the parameters in both equations is quite straightforward. Moreover, since we are not using rate equations (*like the ones used in chapter three*), their implementation in the constitutive equation is made easier. Strain rate sensitivity index m was considered strain rate dependent, and an expression for its variation with strain rate was extracted from the curve corresponding to 400 °C in figure 5.14a. Finally, equation (6.5) was solved numerically for given strain rate values, to generate the corresponding stress/strain curves. The remaining parameters in the constitutive equation were obtained as functions of strain and strain rate by fitting the generated stress/strain curves to those shown in figure 5.8a. The results of the fitting process are shown in figure 6.9, with a summary of the material parameters given in table 6.1.

Figure 6.9 demonstrates how the calibrated model provides an excellent fit to the experimental data, at various strain rates. Strain rates higher than 10^{-3} s^{-1} were excluded since the alloy's superplastic behaviour diminishes beyond that

limit. Recall that the constitutive model is supposed to describe the superplastic behaviour of the material, and therefore it is not accurate to use it for capturing the behaviour of the material outside the superplastic region.

In the same analogy, all the analysis that has been presented so far (*including chapter three*) applies only to the stable deformation region; any unstable deformation is not accounted for. In fact, unstable deformation is undesirable and out of the scope of this work, since we usually try to avoid it by maintaining stable uniform deformation during any forming process. Account for unstable deformation requires the integration of a stability criterion that defines the onset of instability point, in addition to another model, based on totally different deformation mechanisms, to take over and describe the material flow within the unstable region.

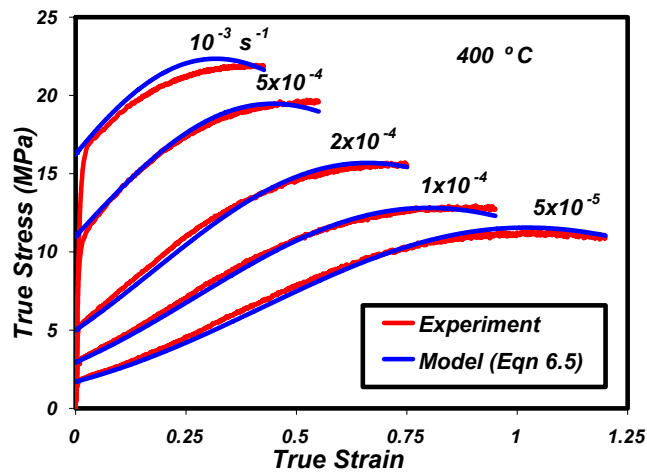


Figure 6.9: Model-predicted versus experimentally-obtained stress/strain curves at 400 °C

Table 6.1: A summary of the calibration material parameters for the AZ31 magnesium alloy

Parameter	Value [Figure]
Grain Growth (Equation 6.6)	
d_0	8.0 [6.4]
C_{IV}	2.5 [6.4]
Cavitation (Equation 6.7)	
f_{a0}	1.25 [6.8]
ψ	1.8 [6.8]
Constitutive Equation (6.5)	
m	func. ($\dot{\epsilon}$) [5.14a]
C_{III}	func. ($\dot{\epsilon}, \epsilon$) [5.8a]
p	func. ($\dot{\epsilon}, \epsilon$) [5.8a]

6.2 Simulation of Superplastic Forming Using the Calibrated Model

Before attempting to optimise the process, the developed and calibrated model needs to be validated experimentally in actual superplastic forming practices. And being the most common of all, it is natural to test the capabilities of the model in bulge forming operations. And as was mentioned earlier, the most important and critical input in any of these operations is the applied forming pressure profile. Therefore, for the model to enhance the way the process is currently carried out, its foremost task would be to improve the prediction of such forming profiles, and hence the overall control of the process.

This section details how such a prime task is carried out, in two steps. The first one focuses on a simple geometry, where available analytical models can be used for comparison. In the second step, other more complex geometries are considered, and the model's capabilities are widely tested. This task is carried out with the aid of finite element analysis. Unfortunately, available FE packages are far away from being suitable for simulating the behaviour of superplastic materials, simply because they employ very simple constitutive models that do not fit such unique class of materials. However, by implementing an accurate predictive model, the FE powerful tools can be exploited.

6.2.1 Model Capabilities in Superplastic Forming of Simple Geometries

6.2.1.1 Analytical Expressions

In chapter three, the free bulge forming of circular superplastic sheets was analytically analysed, and the critical need for accurate modelling tools, even for such a simple geometry, was highlighted [Abu-Farha and Khraisheh 2005a]. In this section, the issue is further emphasised experimentally, by employing the calibrated model in forming the AZ31 magnesium alloy at 400 °C. For the convenience, a schematic of the forming geometry, similar to figure 3.18, is shown again in figure 6.10. P is the time-variable applied gas pressure, r_0 is the radius of the die cavity (*and therefore the radius of the deformed sheet when it forms a full hemisphere*), and S_0 is the initial thickness of the undeformed sheet. Since it is the simplest forming geometry, several analytical expressions for the pressure-time forming profile have been derived for the free bulge forming, the most commonly used is the one introduced by Dutta and Mukherjee [1992]. For a fixed strain rate at the pole of the formed sheet, and assuming uniaxial isotropic behaviour obeying the von Mises effective stress criterion, Dutta and Mukherjee [1992] derived a conveniently simple pressure-time relationship having the following form:

$$P = \frac{4 S_0 \sigma_{eff}}{r_0} e^{\frac{-3\dot{\epsilon}t}{2}} \left(1 - e^{-\dot{\epsilon}t}\right)^{\frac{1}{2}} \quad (6.8)$$

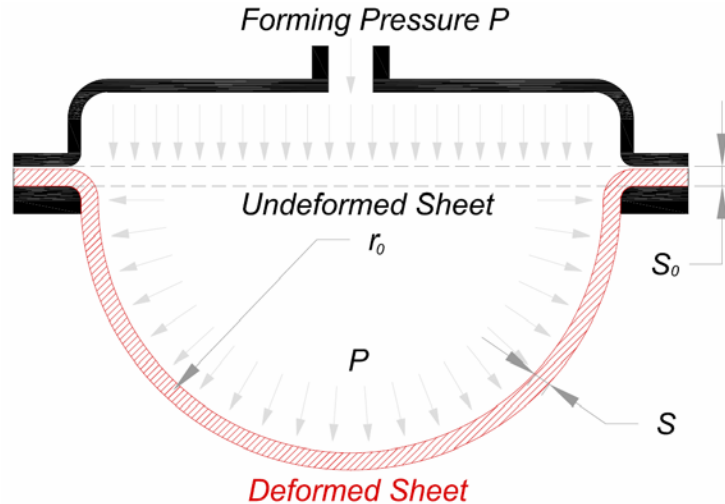


Figure 6.10: Schematic of the free bulge forming of circular sheets

The effective stress σ_{eff} in this equation is assumed a fixed value so long the strain rate is kept constant during the process, and it is given by the simple stress/strain rate constitutive relationship (*presented earlier in chapter two*):

$$\sigma_{eff} = K\dot{\epsilon}^m \quad (6.9)$$

Equation (6.9) is widely-used in modelling elevated temperature deformation in different (*not superplastic*) materials, with available tabulated values for K and m for each of those materials, even at different forming temperatures. In fact, it is even used as the standard built-in constitutive equation in many FE packages (*Abaqus, LS Dyna, Ansys*). However, this equation cannot describe the sigmoidal-shaped stress/strain rate curve particularly associated with the class of superplastic materials. And even if we ignore this fact, by no means such a simple constitutive model would be able to capture the variations of stress with strain, embodied by the diverse hardening and softening behaviours, also observed in superplastic materials. Consequently, regardless how accurate the pressure-time relationship given by equation (6.8) is, using a fixed stress value will definitely yield inaccurate predictions.

To demonstrate this for the AZ31 magnesium alloy, equation (6.8) is used to derive the forming pressure-time profile, for an effective strain rate of $5 \times 10^{-4} \text{ s}^{-1}$, in two different ways:

- 1) **Assuming a fixed stress value:** which is the value corresponding to $5 \times 10^{-4} \text{ s}^{-1}$ in the stress/strain rate curve in figure 5.8c, and is equal to 11.4 MPa .
- 2) **Using time-variable stress values:** by feeding the equation with stress data points from the stress/strain curve corresponding to $5 \times 10^{-4} \text{ s}^{-1}$ in figure 5.8a.

The generated pressure-time profiles for both cases are shown together in figure 6.11. The difference between them is so large, which is quite expected based on the strong hardening (*and consequently large stress variations*) at that strain rate, depicted from figure 5.8a. Forming using these two profiles will definitely yield different results, but for comparison with our calibrated model (*later in this section*), the curve based on the variable stresses is adopted, because it is more accurate (*in terms of representing the material's behaviour*) and replicates how the calibrated model captures the actual behaviour of the material.

Moreover, another analytical expression derived by Banabic et al. [2001], and based on the deformation theory and the classical Hill yield criterion, is also considered here. The extras of this expression, which was previously used in chapter three, is that it represents the anisotropic bulging through elliptical die, of which free circular bulging is a special case. Therefore, for an isotropic forming through a circular cavity, the general expression given by equation (3.48) reduces to the following forming pressure-time formula:

$$P = \frac{4S_0\sigma_{eff}}{r_0} \left(e^{\frac{1}{2}\dot{\epsilon}t} - 1 \right)^{\frac{1}{2}} e^{-\frac{3}{2}\dot{\epsilon}t} \quad (6.10)$$

Similarly, the effective stress σ_{eff} in this equation is assumed a fixed value when forming at a constant strain rate; and it is also given by equation (6.8). For the same conditions at which figure 6.11a was generated, this formula was used to generate two forming pressure-time profiles, as shown in figure 6.11b. In addition to the clear difference between the curves based on constant versus variable flow stresses, the two analytical expressions yield noticeably two different predictions, and the best way to test the accuracy of both would be an experimental validation by actual forming.

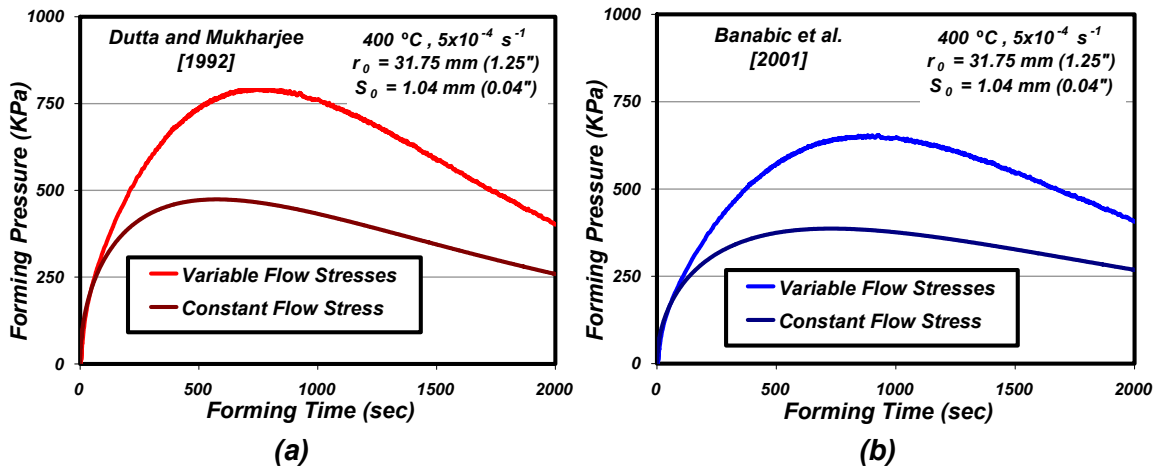


Figure 6.11: Forming pressure-time profiles for the AZ31 mg alloy based on (a) Dutta and Mukherjee [1992] (b) Banabic et al. [2001]

6.2.1.2 Calibrated Model Combined with FE

Alternative to deriving an analytical expression for the desired forming pressure-time profile, a rather flexible approach of combining the calibrated constitutive model with finite element analysis has been employed. This approach will prove effective not only in this simple case, but also in simulating more complicated forming operations, and then more importantly, in optimising the superplastic forming process.

FE simulation of the process has been performed by M. Nazzal using the commercial finite element solver ABAQUS. User defined subroutines were compiled to implement the constitutive model into the FE code. A built-in pressure control algorithm aimed at obtaining a practical load curve at low computational cost was used in the analysis to generate the forming pressure profiles. For more details about the FE model, the subroutines and the pressure control algorithm, please see Nazzal et al. [2004, 2007].

For the aforementioned forming conditions, the generated pressure-time profile based on the calibrated model is plotted against the previously-obtained profiles based on the two analytical models, and they are all shown in figure 6.12. For almost half the time-span, the pressure profile predicted by the calibrated model ascends gradually, thereabout, follow the other two curves predicted by the theoretical models. However, after assuming their peak points, the calibrated model's predicted profile dwells at a constant pressure, while the other two curves start descending, and therefore diverging from it. The differences between the three curves, clearer in the second half of the plot, would probably lead to different outcomes; yet without experimental validation, it is hard to tell which one is more accurate. But at this point, figure 6.12 gives the first positive signs of the model's ability, represented by the proximity of its prediction to the theoretical models.

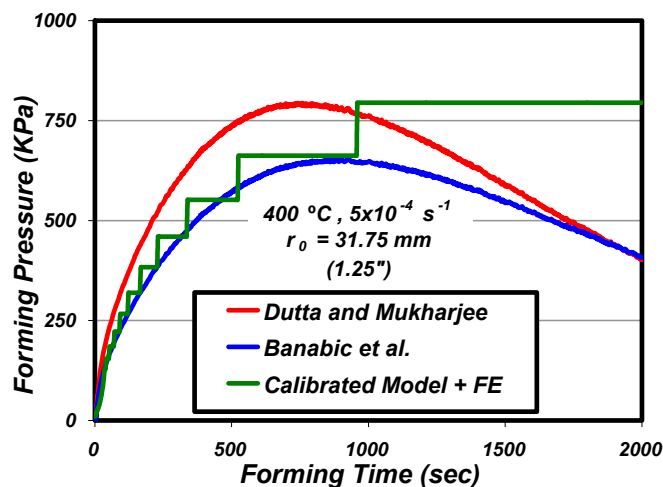


Figure 6.12: Forming pressure-time profile generated by the calibrated model in comparison with two analytical models

For the designated strain rate of $5 \times 10^{-4} \text{ s}^{-1}$, the time theoretically needed to form a full hemisphere of 31.75 mm in height is about 1800 seconds. Therefore, following each one of these profiles, 1.04 mm thick circular sheets were bulged for about 1800 seconds; the formed parts are shown in figure 6.13. The bulge forming setup (section 4.3) was used with the type-I open die shown earlier in figures 4.15 & 16.



Figure 6.13: Formed domes using the three different forming pressure profiles

Table 6.2 summarises the obtained results, and as also depicted from figure 6.13, none of the three profiles was able to deliver the full bulge height in the specified forming time. Still, despite the small differences, forming using the FE-generated pressure scheme produced the best result; a dome 29.5 mm in height. Also recall that the two analytical models were fed by time-varying stresses, directly extracted from the stress/strain curve of the material. Evidently, and by referring to figure 6.11, having used these models assuming a constant stress value would have certainly underestimated the forming process by far.

Table 6.2: Forming time versus achieved bulge height following the three different forming pressure profiles

Pressure-Time Profile	Forming Time (seconds)	Bulge Height (mm) [%]
Calibrated Model + FE	1805	29.5 [92.9]
	1888	31.5
Dutta and Mukherjee [1992]	1800	28 [88.2]
	2045	31.8
Banabic et al. [2001]	1798	26.5 [83.5]
	2151	31.6

In a second set of trials, forming times were extended to the values also shown in table 6.2 to be able to get (*as close as possible*) an approximate hemispherical dome. For the calibrated model, it took about 88 extra seconds,

which is almost 5% of the expected total forming time, to deliver a full hemisphere, as also shown in table 6.2. Combined with finite element, the calibrated model proposed here already shows promising results in improved predictions during superplastic forming; other cases will further accentuate that. Note that using the open die facilitated monitoring the forming process, as illustrated by figure 6.14. And by using a measuring gauge block, the required forming height was set, and forming trials were all stopped at almost the same point.

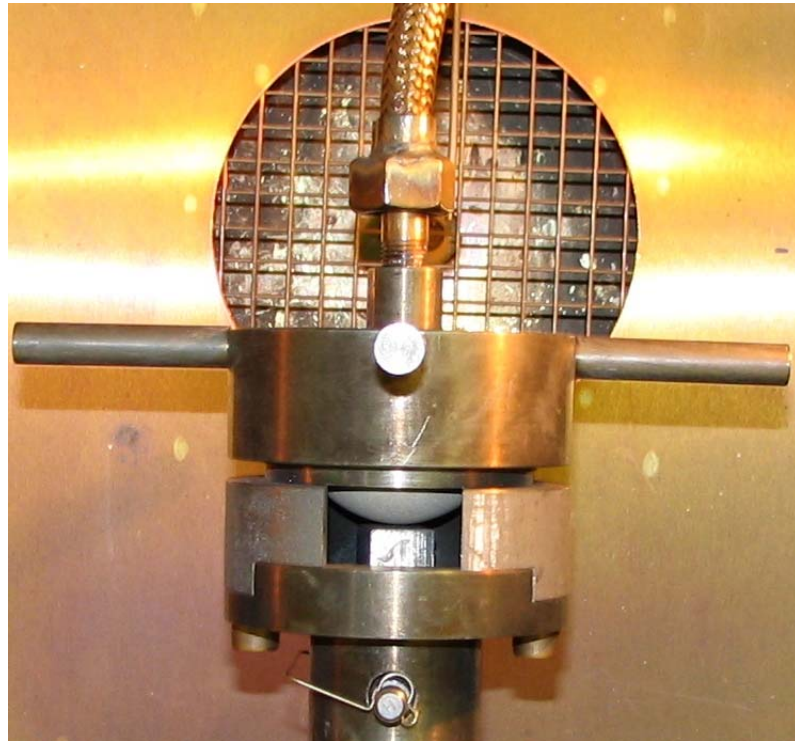


Figure 6.14: Formed domes using the three different forming pressure profiles

6.2.2 Model Predictions in Superplastic Forming of Complex Geometries

The vast majority of superplastic bulge forming investigations are based on very simple geometries, particularly the free bulge forming of circular sheets. Very small number of efforts goes the extra step and involves more complex geometries. Even those, are either simulation efforts which lack accuracy, or actual parts' forming efforts which are carried out by trial and error routines. And where analytical models fail to provide any assistance, the powers of an accurate modelling tool combined with a FE code can approach any geometry, regardless how complicated it is.

Already, proximity to two available theoretical models followed by experimental validation, were used to test the model's capability to predict the

forming path of a simple geometry. However, only experimental validation can test the capabilities of the model for more complicated forming cases.

An example is presented here, where the bulge forming through a cylindrical die cavity is considered; there is no analytical form for the pressure-time profile for such a geometry. Four different cylindrical dies of the same diameter but various heights were considered, and the pressure-time profiles corresponding to a constant strain rate forming at $2 \times 10^{-4} \text{ s}^{-1}$ were generated using the FE model, as shown in figure 6.15a. The actual forming of 1.65 mm thick sheets was carried out using the type-II forming dies, shown earlier in figures 4.18 and 4.19. The formed parts are shown in figure 6.15b.

The calibrated model's ability to capture the material behaviour, and the effectiveness of incorporating it into FE, is highlighted by the fact that all the cups except the first were fully-formed. The 12.70 mm in height cup did not take all the details of the die, the corners in particular.

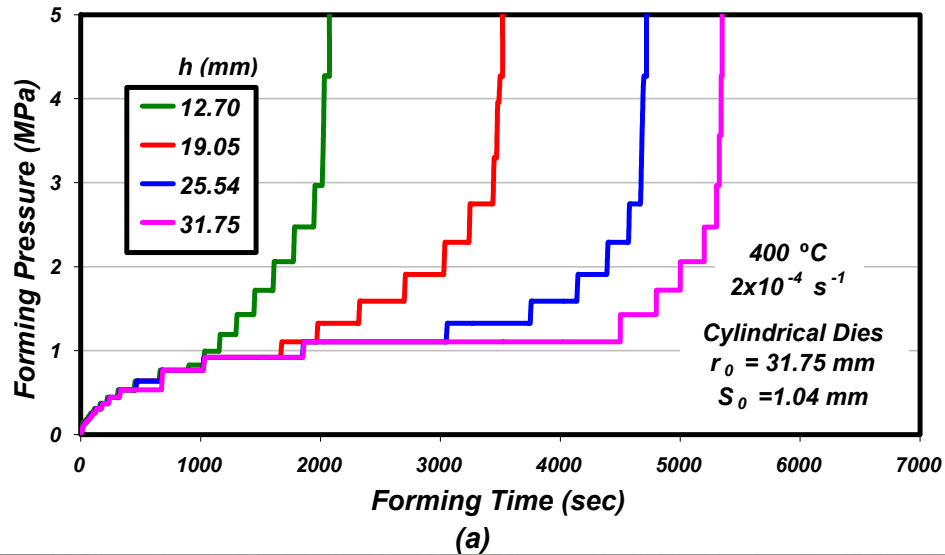


Figure 6.15: Pressure-time profiles for forming at $2 \times 10^{-4} \text{ s}^{-1}$ into multi-deep cylindrical dies (b) The corresponding formed parts

6.3 Optimising the Superplastic Forming Process.

In the opening of this chapter, two main steps were highlighted in order to considerably enhance the way the superplastic forming process is currently carried out; controlling and thence optimising the process. The first step was tackled in the foregoing section, and provided the basic ground on which the second step could be realised. And just like controlling the process is all about generating the right forming pressure profile; optimisation is all about generating an optimum forming pressure profile.

The fact that maximum ductility is often associated with the low strain rate part of the superplastic region, has been the main motivation for many investigators to follow a variable strain rate approach, instead of the conventional constant strain rate ones [Johnson et al. 1993, Ding et al. 1995, Khraisheh and Zbib 1999, Deshmukh et al. 2004]. The overall concept of this approach translates into constructing a forming path that starts at a high strain rate value; and as deformation progresses and stability is hindered, strain rate is gradually dropped, maintaining deformation uniformity and therefore preserving the part's integrity. However, the selection of such a variable strain rate forming path should not be arbitrary, but rather based on the behaviour of the material for optimum results. To do so, and in addition to the accurate constitutive model, a stability criterion that defines the onset of non-uniform deformation is needed. This was demonstrated earlier by Johnson et al. [1993] and Khaleel et al. [1995], where optimised forming paths were generated after combining a constitutive model with Hart's stability criterion.

In this work, the collaborative effort to control the process is expanded to optimise it. The presented calibrated constitutive model was combined by M. Nazzal with a modified multiscale stability criterion (*which takes both geometrical and microstructural features into account*) developed by N. Thuramalla. Then they were both fed into a FE code, to generate the optimum variable strain rate forming path for the AZ31 magnesium alloy at 400 °C. To do that, the calibrated model was solved numerically alongside the stability criterion for a given strain rate, to yield the limiting strain at which the onset of unstable deformation is expected to occur for that specific strain rate. This process was repeated for other strain rates, and by connecting the resulting points, an optimum forming path, as shown in figure 6.16, was generated. For more details about the stability criterion, please refer to Thuramalla et al. [2004] and Nazzal et al. [2004 & 2007].

Uniaxial tensile tests and free bulge forming experiments were carried out to evaluate the effectiveness of the proposed optimisation scheme; the results are detailed next [Khraisheh et al. 2006].

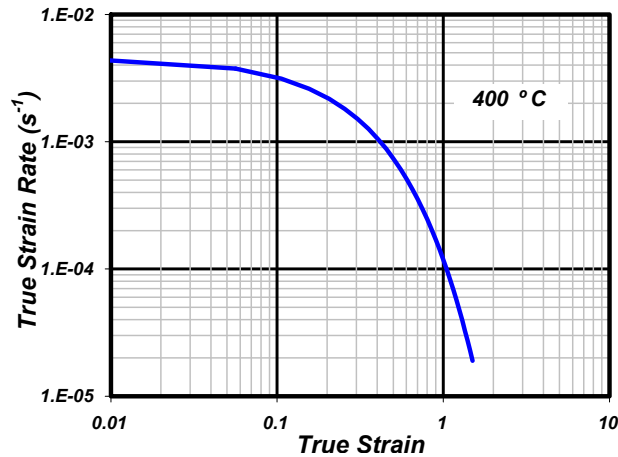


Figure 6.16: Optimum forming path for the AZ31 magnesium alloy at 400 °C

6.3.1 Optimisation in 1D

The 5582-INSTRON load frame cannot perform a variable strain rate test following the smooth continuous optimum curve shown in figure 6.16. To overcome this limitation, the curve had to be converted into a multi-step variable speed forming path. This was carried out in two stages. In the first, the continuous curve was divided into equally spaced strips of constant strain rates, to generate an approximated stepwise profile. Approximated by multi-steps of constant strain rates starting at $3 \times 10^{-3} \text{ s}^{-1}$, and ending at $5 \times 10^{-5} \text{ s}^{-1}$, the two profiles are shown in figure 6.17a. The more segments used, the finer the approximation process would be. Yet, this issue is not of high significance, and beyond a certain point, the effort becomes redundant. The continuous curve in figure 6.17a was in fact approximated by almost twenty steps. The second stage was to convert each constant strain rate segment into its equivalent constant speed segment(s). And because constant strain rate is not equal to constant speed, each segment was further divided into several sub-segments, such that the conversion error did not exceed $\pm 2.5\%$. Doing so, the final variable speed loading path, according to the optimum scheme in figure 6.16, is shown in figure 6.17b.

Type-I grips and 0° oriented tensile test specimens (figures 4.6 and 4.7) were used for conducting the uniaxial tensile tests at 400 °C. And by following the generated optimum loading path in figure 6.17b, several specimens were stretched to strain values of 250%, 300% and 350% elongation, respectively. Thereat, each test was stopped, and the corresponding specimen was cooled down to room temperature, preserved for following dimensional measurements. Since the actual strain rate is changing from a high to a low value throughout each of these tests, the stress/strain curve is expected to resemble such a change. Figure 6.18 shows how the stress/strain curve for the optimum loading path compares to those corresponding to the band of constant strain rates,

shown earlier in figure 5.8a. Instead of a smooth curve, it is noticed that each drop in speed (or equally strain rate) in figure 6.17b results in an abrupt drop in flow stress in figure 6.18, and vice versa. Yet, it is more interesting to observe that the optimised stress/strain curve is, more or less, confined within a region bounded by a line connecting the peak points of all the other stress/strain curves. This in fact embodies the very nature of the optimum forming path of the material in figure 6.16, where the limiting stable strain at each strain rate is approximately the strain corresponding to the peak point of each curve.

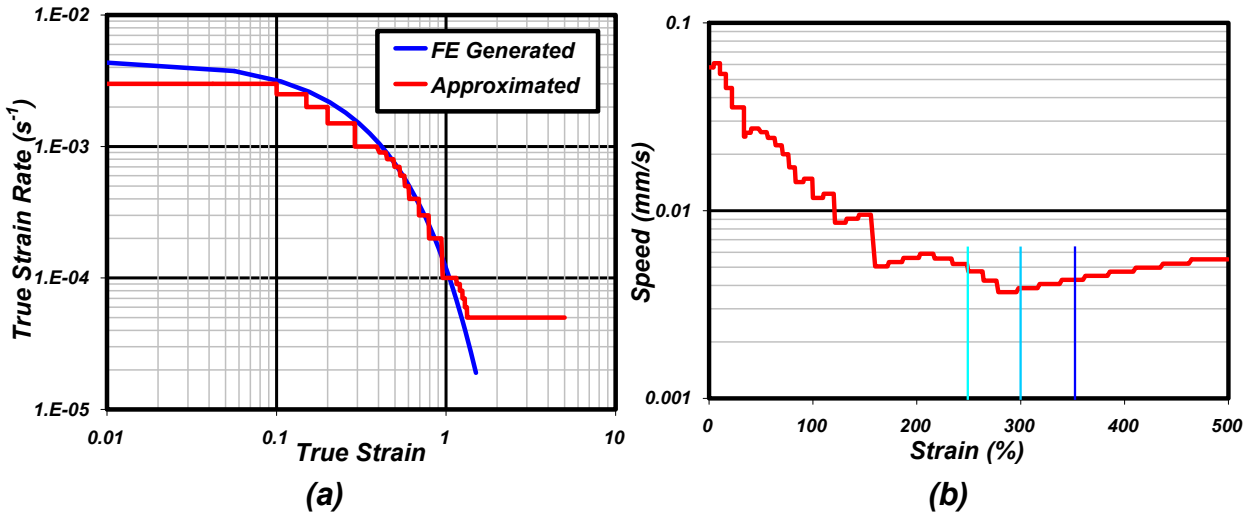


Figure 6.17: (a) Continuous versus approximated variable strain rate loading (forming) path (b) Corresponding variable speed loading path

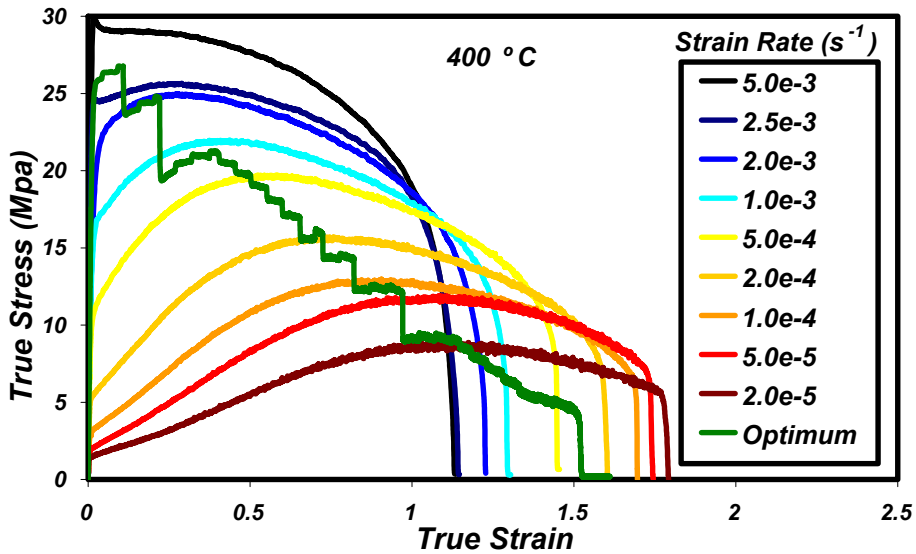


Figure 6.18: Stress/strain curve based on the optimum loading path compared to those corresponding to constant strain rates

Moreover, additional tensile specimens were stretched to the same strain values (250, 300 and 350%) at selected constant true strain rates for comparison: $2 \times 10^{-3} \text{ s}^{-1}$ as a fast forming rate and $5 \times 10^{-5} \text{ s}^{-1}$ as a slow forming rate. Width and thickness were measured along the gauge length of all the specimens; thickness data points in particular were used to evaluate the thinning factor for each case. Thinning factor is a parameter used to quantitatively express the level of deformation non-uniformity, by the ratio between the minimum and average thickness in the specimen. It assumes values between 0 and 1, where 1.0 corresponds to an ideally uniform deformation. The results of all the abovementioned tests are summarised in table 6.3 below.

Table 6.3: Summary of the tensile tests at constant versus optimum variable strain rate loading paths

Strain Rate (s^{-1})	Forming Time [min]		
	Thinning Factor ($t_{\text{Min}} / t_{\text{Ave}}$)		
	Thinning $\{t_{\text{Min}} / t_0\}$		
	250 %	300 %	350 %
2×10^{-3}	[10.44]		
	(0.339)	Failed	Failed
	{0.205}		
5×10^{-5}	[417.6]	[462.1]	[501.4]
	(0.856)	(0.805)	(0.751)
	{0.553}	{0.478}	{0.438}
Optimum	[84.2]	[125]	[160.8]
	(0.738)	(0.687)	(0.624)
	{0.453}	{0.407}	{0.350}

For the specimen stretched to 250% elongation at the highest constant strain rate of $2 \times 10^{-3} \text{ s}^{-1}$, forming time was quite short at 10.44 minutes, yet the resulting thinning factor value was remarkably low at 0.339, indicating highly localised necking. In fact, the specimen actually failed at that strain, as shown in figure 6.19a. To improve deformation uniformity and avoid such failure, a lower strain rate must be used. For the lowest constant strain rate of $5 \times 10^{-5} \text{ s}^{-1}$, uniformity is considerably improved to a 0.856 thinning factor; however, forming time drastically increased to 417.6 minutes. The challenge is to go in between these two extremes, and the results corresponding to the specimen formed according to the proposed optimum profile clearly show the effectiveness of the optimisation scheme. Forming time was reduced from 417.6 minutes to only 84.2 minutes, while maintaining almost the same deformation uniformity, mirrored by the 0.738 thinning factor. In other words, forming time was reduced by astonishing 80%, at the cost of only 13.8% drop in deformation uniformity. Figure 6.19a further illustrates how decently uniform the optimised deformation is, compared to the one achieved at the low strain rate.

Another look at deformation uniformity is given in figure 6.19b & c, which shows plots of both width and thickness distributions for the three specimens. If we consider the best case corresponding to $5 \times 10^{-5} \text{ s}^{-1}$ as the reference line here, the optimum case shows fairly uniform distributions, with no signs of necking initiation in either direction; width or thickness. On the contrary, the high strain rate case shows spikes in both thickness and width plots, indicating severe localised neck formation. Thinning (t_{Min} / t_0) values listed in table 6.3 also emphasise that; and since all the specimens had the same initial thickness, these values directly show how close the optimum case is to the low strain rate one, despite the huge forming time savings.

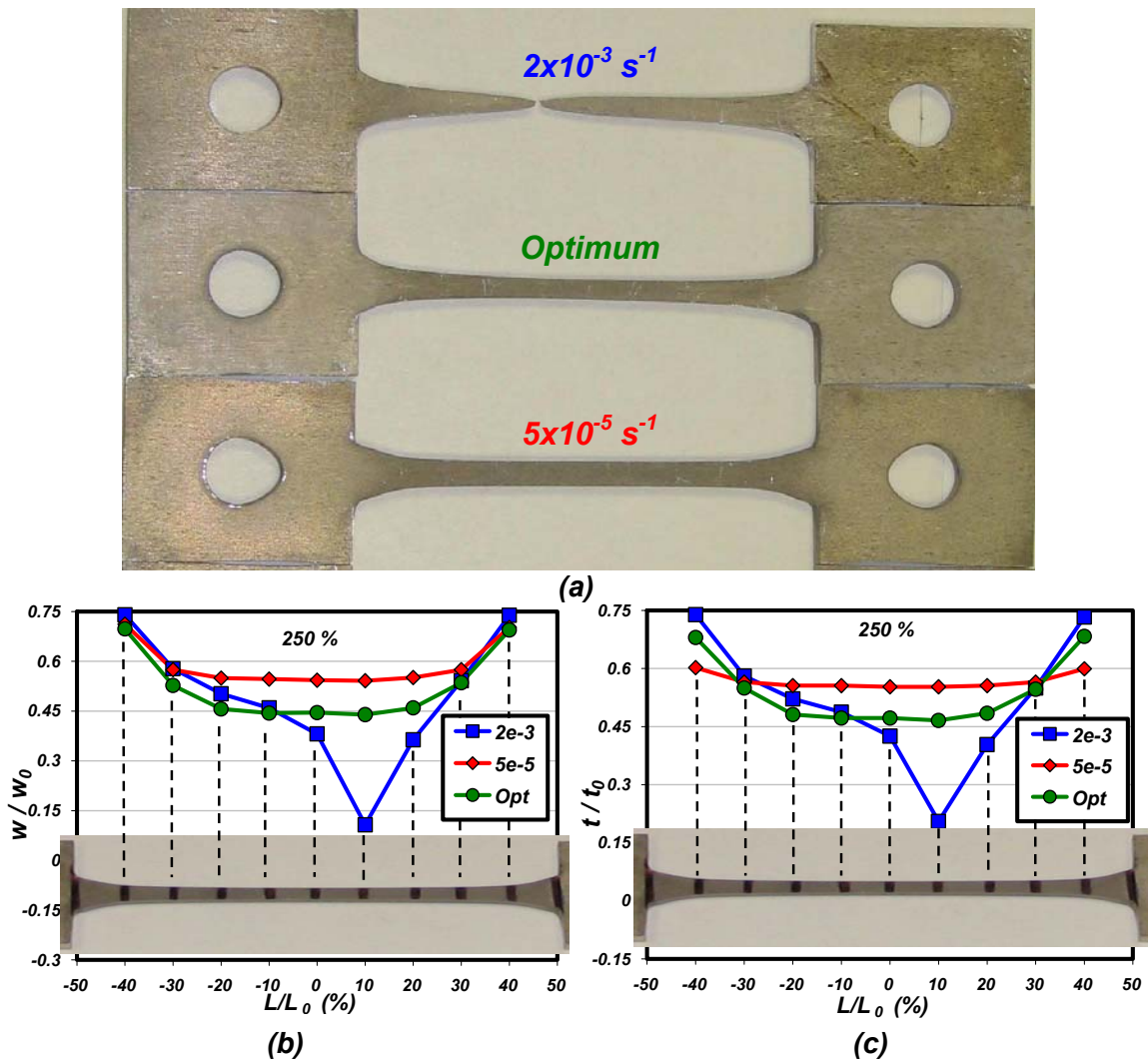


Figure 6.19: (a) Specimens deformed to 250% at various strain rates (b) Width distribution (c) Thickness distribution along each specimen

Similar results were achieved for the 300% and 350% elongation strain limits, except that specimens strained at $2 \times 10^{-3} \text{ s}^{-1}$ could not even reach these limits, as they failed at about 250% due to severe localised necking. The

Specimens formed according to the optimum profiles still exhibit uniform deformation with significant reduction in forming time, as shown in table 6.3.

Figure 6.20 shows the deformed specimens, their width and thickness distributions for the 300% elongation strain. The very initial signs of localised deformation start to appear in the optimum case compared to the low strain rate case, as shown in figure 6.20a. This might be clearly depicted from the width and thickness distributions, where both curves show slight deviation from the uniform distribution at specific points, as shown in figure 6.20b&c. Despite that, the optimum approach still proves its effectiveness in cutting the forming time, at an affordable deformation uniformity loss.

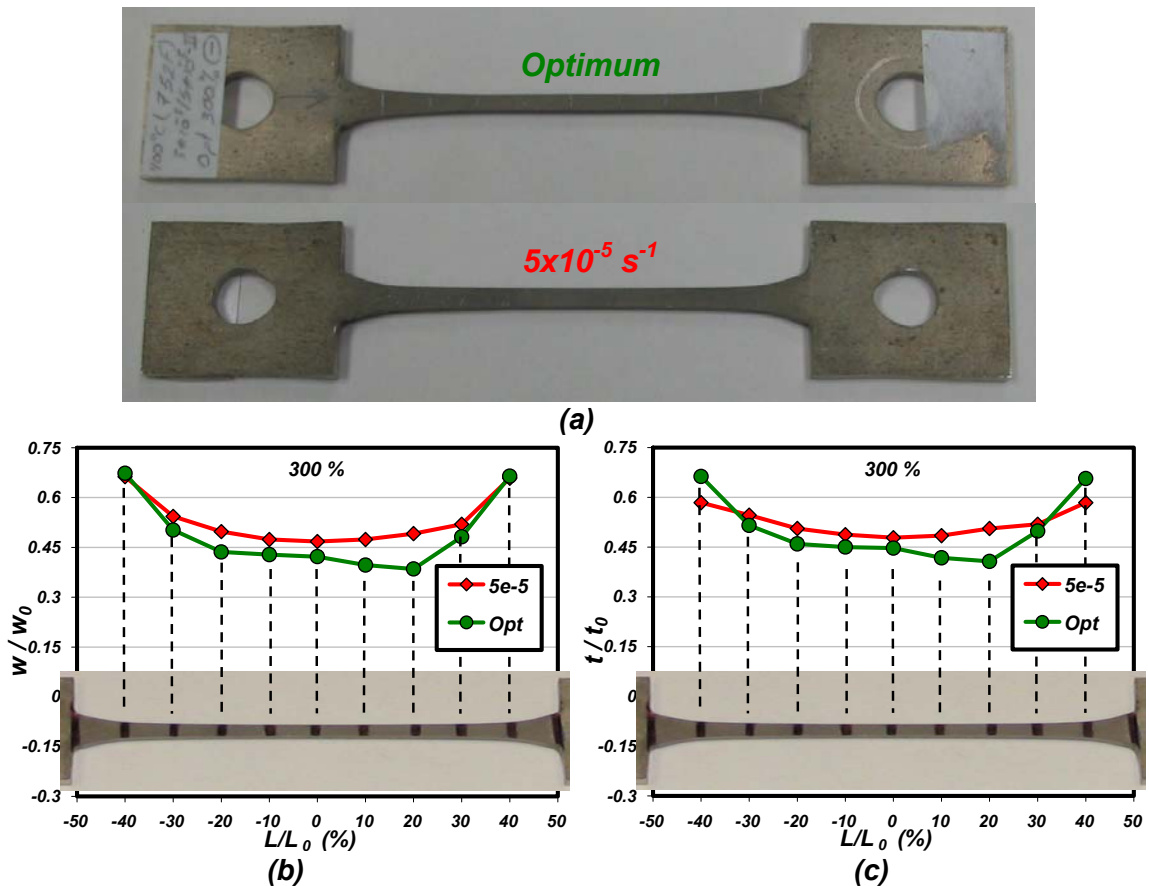


Figure 6.20: (a) Specimens deformed to 300% at various strain rates (b) Width distribution (c) Thickness distribution along each specimen

For the third strain limit of 350% elongation, though table 6.3 still indicates a decent thinning factor, the specimen deformed following the optimum loading path failed, as shown in figure 6.21a. However, even by considering both width and thickness distributions in figure 6.21b&c, one cannot see any abrupt changes indicating localised necking, like those previously observed in the 10^{-3} s⁻¹ case in figure 3.21.

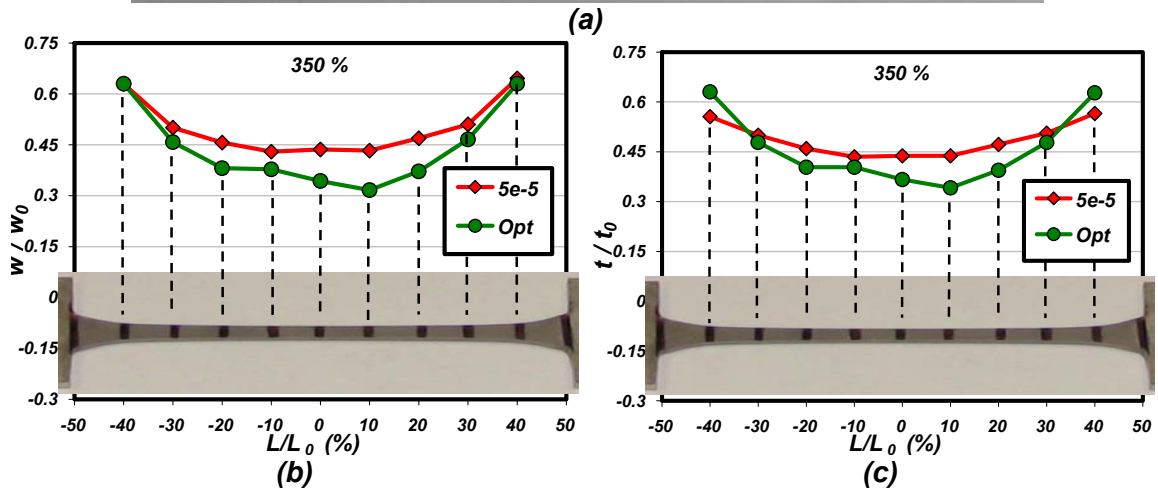


Figure 6.21: (a) Specimens deformed to 350% at various strain rates (b) Width distribution (c) Thickness distribution along each specimen

The last observation further emphasises on the effectiveness of the proposed optimisation scheme; not only forming time is significantly reduced without compromising deformation uniformity, but also uniform deformation is maintained until the thresholds of failure. The importance of this conclusion is derived from actual forming practices, in which deformation uniformity is as important as ductility limits. In other words, achieving high ductility is virtually impractical, unless it is coupled with good deformation uniformity.

6.3.2 Optimisation in 2D

The previous analysis was expanded to the 2D loading case by considering the free bulge forming of circular sheets. Just like the FE simulations discussed earlier in section 6.2, user-defined subroutines were compiled to implement the constitutive model into the FE code. Moreover, the variable strain rate optimum loading path shown in figure 6.16 was also incorporated into the FE code. Doing so, the FE model was able to generate an optimum forming pressure-time profile that maintains the desired variable strain rate path at the pole of the formed sheet.

Similar to the 1D loading case, two other constant strain rates were considered, in order to evaluate the results of the optimum profile; $1 \times 10^{-3} \text{ s}^{-1}$ as a fast forming rate, and $5 \times 10^{-5} \text{ s}^{-1}$ as a slow forming rate. The forming pressure-time profiles corresponding to these strain rates were also generated, and they are shown against the optimised one in figure 6.22.

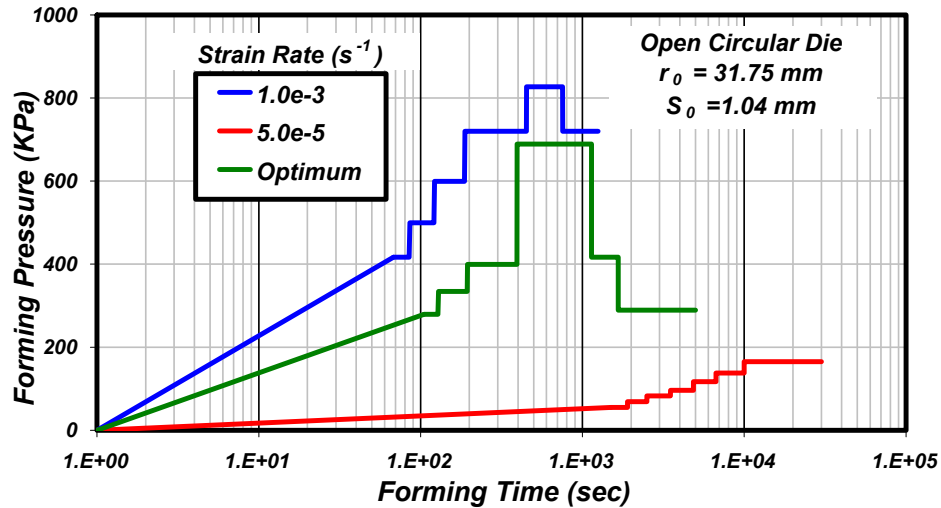


Figure 6.22: Forming pressure-time profiles generated for constant versus optimum variable strain rate loading paths

Following each one of these profiles, bulge forming of 1.04 mm thick AZ31 magnesium circular sheets at 400 °C were carried out, using the bulge forming setup (section 4.3) with the open die shown in figures 4.15 and 4.16. Unlike tensile testing where deformation can be stopped at a certain strain limit (250%, 300%, 350% ...); bulge forming can be controlled either by forming time or dome height. And since these three strain rate paths have different time spans, dome height was set as a measure of strain limit. In this case, two heights were targeted for establishing the comparison. The first is the full circular dome height of 31.75 mm, which is equal to the radius of the circular die. The second is the maximum height at which the sheet formed at the high strain rate would perforate. The results of all the bulge forming tests are summarised in table 6.4.

For the first dome height of 31.75 mm, the sheet formed at the fast strain rate of $1 \times 10^{-3} \text{ s}^{-1}$ took less than 15 minutes, with the lowest thinning of 0.311 and thinning factor of 0.594. On the other hand, the sheet formed at the slow strain rate of $5 \times 10^{-5} \text{ s}^{-1}$ had the highest thinning and thinning factor of 0.423 and 0.819, respectively. Yet, it took about 398 minutes to achieve the same height. The sheet formed according to the optimum profile took about 58 minutes, reducing the forming time by 85.5% (compared to the $5 \times 10^{-5} \text{ s}^{-1}$), sacrificing only 11.4% deformation uniformity. These numbers signify the effectiveness of the optimisation scheme in actual superplastic bulge forming, similar to the uniaxial tensile tests presented earlier.

Table 6.4: Summary of the bulge forming experiments at constant versus optimum variable strain rate loading paths

Parameter	Strain Rate (s^{-1})					
	Dome Height \approx 31.75 mm			Dome Height \approx 35.5 mm		
	1×10^{-3}	5×10^{-5}	Optimum	1×10^{-3}	5×10^{-5}	Optimum
Status	Ok	Ok	Ok	Fail	Ok	Ok
Forming Time (min)	14.68	398.07	58.33	17.33	500	67.5
Arc Length (mm)	99	100	99.5	105.5	106	105.5
Circumferential Strain	0.444	0.454	0.449	0.524	0.528	0.524
Thickness Strain	1.169	0.883	0.973	1.586	0.918	1.075
t_{Min} (mm)	0.323	0.440	0.393	0.213	0.415	0.355
t_{Ave} (mm)	0.544	0.537	0.541	0.525	0.525	0.522
Thinning t_{Min} / t_0	0.311	0.423	0.378	0.205	0.399	0.341
Thinning Factor t_{Min} / t_{Ave}	0.594	0.819	0.726	0.406	0.791	0.680

An interesting measure of how uniform the deformation is, following the three different strain rate paths (*constant fast, variable optimum and constant slow*), was extracted from the shape of the formed domes, which are shown in figure 6.23a. These profiles were traced by slicing each dome in half, and taking the impression of either section. Though the difference is slight, yet it is noticed that the faster the forming process is, the more the shape deviates from its perfect circular profile into an elliptical one. This behaviour could be generally associated with the variation of strain rate sensitivity of the material with strain rate. As it was experimentally proven earlier, sensitivity index was shown to be highest at low strain rates, and decrease as strain rate increases, as shown in figure 5.13a. As a result, the low strain rate sensitivity hinders uniform deformation and localises it more in the centre of the deformed sheet, causing such deviation. This behaviour was similarly observed by Yang and Mukherjee [1992], who have shown that free bulging of circular sheets of superplastic materials with different strain-rate sensitivities produces different shapes that deviate from the expected perfect spherical one.

By measuring the thickness at different points along the perimeter of each sectioned dome, plots for thickness distributions for all the three formed domes are shown in figure 6.23b. It is shown that forming at the highest strain rate not only causes the highest thinning, but also the greatest variation of thickness along the deformed dome. The graph testifies the fairly uniform distribution corresponding to the optimum forming case, and shows how close it is to the low strain rate case, provided that huge forming time savings are achieved.

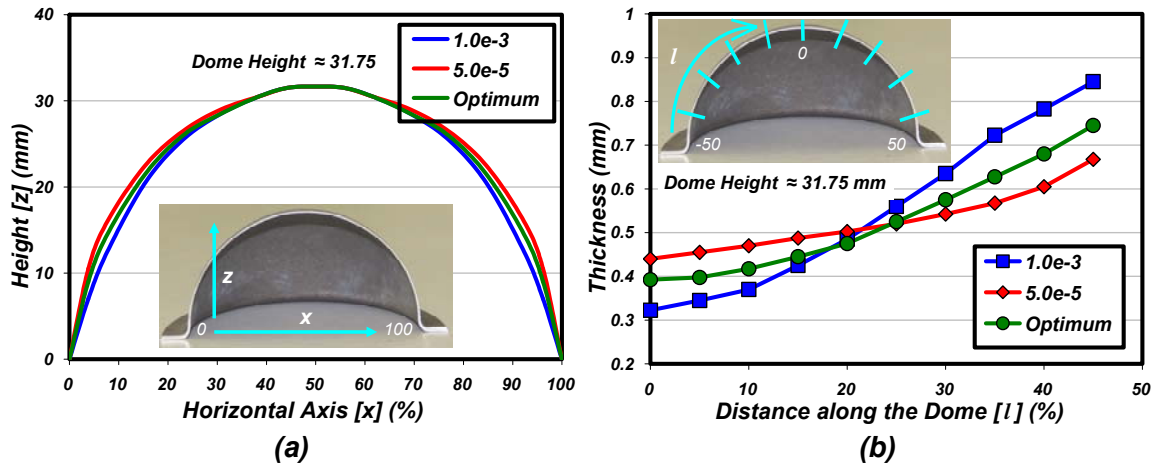


Figure 6.23: (a) Dome profile (b) Thickness distribution along the perimeter of sheets formed following constant versus optimum strain rate paths to 31.75 mm height

To set the second dome height, and consequently limiting strain, a sheet was formed at the fastest strain rate of $1 \times 10^{-3} \text{ s}^{-1}$ unto fracture, which took place at about 35.5 mm dome height. Therefore, other sheets were formed at both $5 \times 10^{-5} \text{ s}^{-1}$ and the optimum variable strain rate forming path up to the aforementioned height for comparison. The results shown also in table 6.4 follow the same trend of the previous case, and the optimum forming scheme continues to demonstrate significant reduction in the forming time, without compromising the uniformity of the form part. Just like the previous case, each dome was sliced in half, taking the impression of the dome profile, and recording the thickness along each section. The results are shown in figure 6.24.

Because of the larger strain limit, the significant differences, in terms of deviation from the ideal circular profile, between the three curves in figure 6.24a, could be easily observed in the formed domes shown in figure 6.25a. Likewise, the curves quantifying thickness distribution in figure 6.24b could be visually assessed by looking at sections in the formed domes, shown in figure 6.25b. The photo clearly shows the localised thinning in the dome formed at the high strain rate of $1 \times 10^{-3} \text{ s}^{-1}$, which ultimately led to its failure near its apex. On the other hand, thickness variation along the section is observed to decline as strain rate is dropped. The figure reveals how uniform the section of the dome formed using the optimum profile is, when compared to the one formed at $5 \times 10^{-5} \text{ s}^{-1}$.

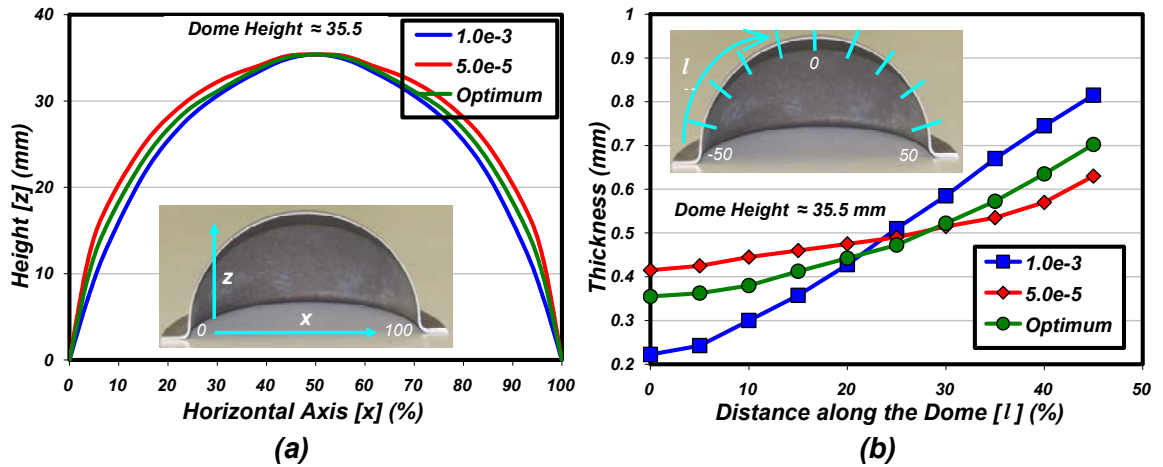


Figure 6.24: (a) Dome profile (b) Thickness distribution along the perimeter of sheets formed following constant vs optimum strain rate paths to 35.5 mm height

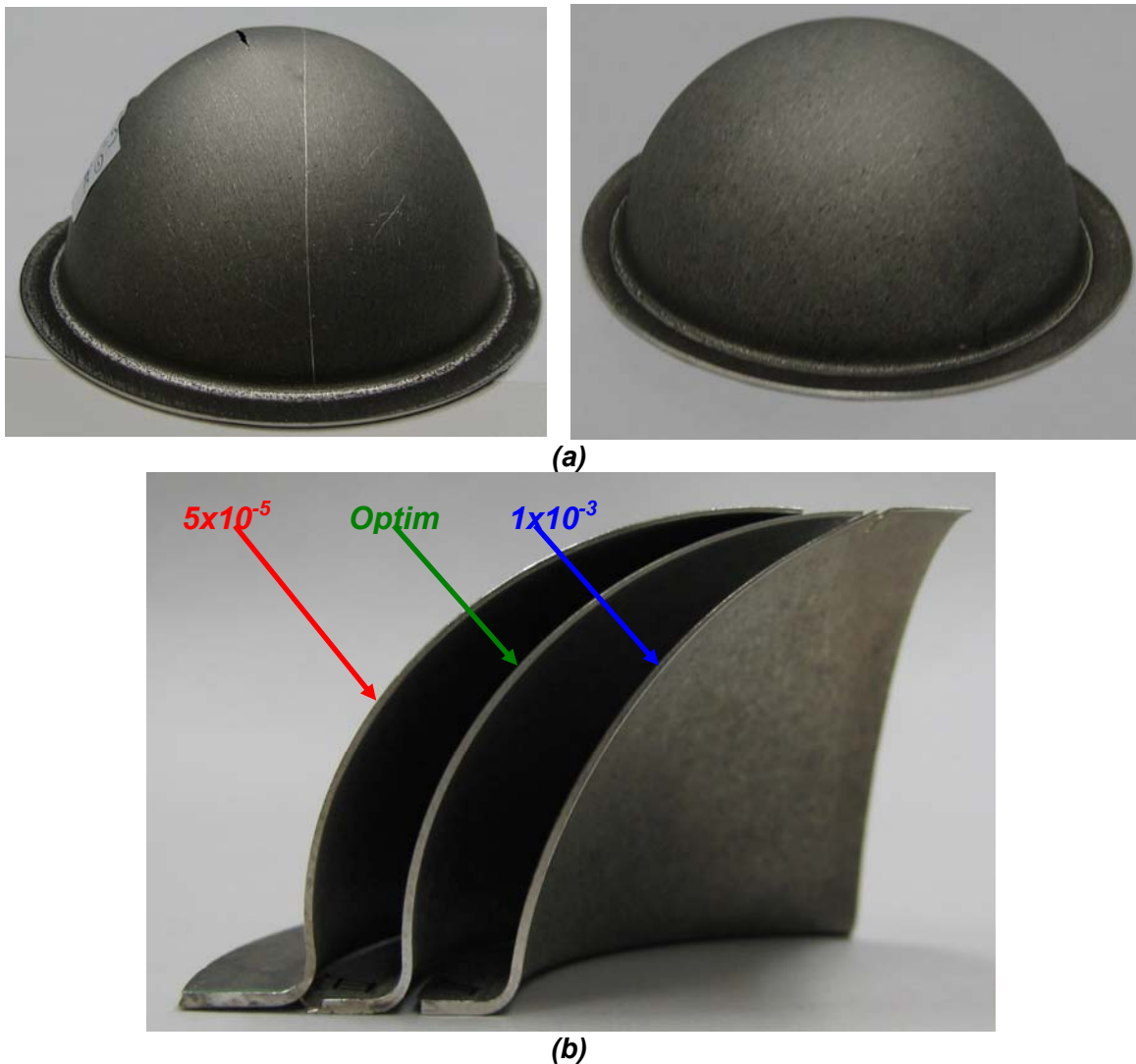


Figure 6.25: (a) Domes formed at different strain rate paths to 35.5 mm height (b) A section showing thickness variation along each dome

It is very important to emphasise on the issue of how hard it is to control the strain in bulge forming at different strain rate paths, despite the fact that almost the same dome height is achieved. This can be inferred from table 6.4, which shows different thickness strains corresponding to the different strain rates, despite that dome height is the same for all. In fact, and though it is not as quite significant, the same problem is also observed in uniaxial testing, if we are to compare the thickness strains instead of the axial strains. These variations are direct consequence of the differences in deformation uniformity associated with each strain rate, and cannot be eliminated. Therefore, and in order to have a meaningful comparison, the limiting strain was set as the average circumferential strain (*an arc line passing through the pole of the dome*), which justifies using dome height as a mean of comparison.

7. CHAPTER SEVEN: POST-SUPERPLASTIC FORMING ANALYSIS

Superplasticity and the superplastic forming technique are becoming more familiar terms in both the academic research arena and the metal forming industry; a fact embodied by the mounting number of studies in the field, and the increasing number of parts formed using the technique. Furthermore, the escalating demand for lightweight alloys along with conventional forming techniques' limited capabilities to successfully form such alloys (*Aluminium, Titanium and Magnesium*) increases the chances for SPF to secure a good position among advanced future forming techniques. Yet, just like other currently-utilised sheet metal forming processes, most of the activities in the field of superplasticity are focused on the material/process level, with very scarce attention paid to the process on the post-forming level (*i.e. post-superplastic forming properties*). The importance of this specific issue in superplasticity is inherited by the very nature of the process itself, which makes it even a necessity.

Superplastic studies generally target achieving maximum plastic strain, which is very often set as the mere basis for selecting optimum forming parameters, mainly strain rate and temperature. Similarly, higher strain limits and better deformation-uniformity are often the criteria for evaluating the various proposed optimisation practices. Such approach could be very misleading, since the conditions for optimum superplasticity in terms of maximum ductility may not necessarily result in optimum values for the mechanical properties, such as tensile strength, ductility, creep or fatigue resistance in a formed component. Exposure to elevated temperatures for prolonged periods of time ($> 0.5T_m$), very large plastic strains ($> 200\%$) and the corresponding microstructural changes (*grain growth and severe cavitation*), are all factors that might deteriorate the mechanical properties of superplastically-formed materials, and therefore need to be studied and quantified in details.

There are very few available studies on post-superplastic forming, all of which focus on specific aluminium or titanium alloys, since these alloys have been the main market and attraction of the superplastic forming technique. Besides, the majority of these studies not only lack the systematic approach in investigating this important subject, but they are also limited to narrow ranges of operating conditions, such as loading types, forming temperatures, strain rates and strain limits. [Bampton and Edington 1982 & 1983, McMarmid 1985, Shakesheff 1985, McDarmid and Shakesheff 1985, Agrawal and Tuss 1985, Ahmed Pearce 1985, Miyagi et al. 1987, Dunford et al. 1991, Hales and Wagner 1992, Hales and Lippard 1994, Moore et al. 1995, Bradley and Carsley 2004, Chen and Thomson 2004]. To mention here few exceptions that surpassed the others in comprehension, despite some limitations. Wisbey et al. [1993] investigated the post-form tensile properties of the IMI 834 titanium alloy at both *RT* and $600\text{ }^\circ\text{C}$ using tensile specimens formed at $900, 940$ and $990\text{ }^\circ\text{C}$, yet the tensile specimens were strained to 300% at 1×10^{-4} and $3 \times 10^{-4}\text{ s}^{-1}$. Duffy et al.

[1988] studied the effects of biaxial superplastic deformation at 900 °C on the ambient temperature tensile properties and texture of IMI 550 titanium sheets, covering different strain rates and strain limits. Cope et al. [1987] performed perhaps the most comprehensive study on the influence of uniaxial superplastic deformation on the ambient temperature tensile properties of Ti6Al4V sheets. They covered temperatures between 850 and 970 °C, strain rates between 1.1×10^{-4} and $1.8 \times 10^{-3} \text{ s}^{-1}$, and strains up to 200%. Tests were also performed on statically annealed material to separate the effects of high temperature exposure and superplastic deformation. Unfortunately, the aforementioned ranges of temperature, strain and strain rate were not all covered together. Instead, the authors varied one of the three parameters over its full range, keeping the other two parameters at fixed values. Table 7.1 summarises these and other efforts, highlighting the investigated alloys, testing conditions and targeted post-SPF properties.

Table 7.1: Summary of several studies on the post-superplastic forming properties of various superplastic alloys

Reference	SP Deformation [Material]	T (°C)	Strain Rate (s^{-1})	Strain Limit (%)	Post-SPF properties
McMarmid 1985	1D [Ti IMI 550]	880 & 928	1.05×10^{-4} & 4.2×10^{-3}	Up to 537	Mechanical
Shakesheff 1985	2D [Supral 100 & 220]	500	---	100, 200 & 250	Mechanical Fatigue Cavitation
Agrawal and Tuss 1985	2D [AA 7475]	850-970	---	50, 100 & 150	Mechanical fatigue
Cope et al. 1987	1D [Ti4V6Al]	850-970	$1.1-18 \times 10^{-4}$	Up to 200	Mechanical Grain growth
Miyagi et al. 1987	1D & 2D [AA7475]	515	2×10^{-4}	Up to 200	Mechanical Cavitation
Duffy et al. 1988	2D [Ti IMI 550]	900	1.3, 2.5 & 4.4×10^{-3}	80, 130, 230 & 320	Mechanical Texture
Dunford et al. 1991	1D [Ti4V6Al]	925	6×10^{-4}	300	Mechanical
Wisbey et al. 1993	1D [Ti IMI 834]	900, 940 & 990	1×10^{-4} & 3×10^{-4}	300	RT and 600 °C Mechanical
Bradley and Carsley 2004	2D [AA5083]	500	1×10^{-3}	Two values	Mechanical Fatigue Cavitation

There are no available studies on the issue of post-superplastic forming in magnesium alloys, which is quite expected since the SPF/Magnesium partnership has evolved recently. But with the increasingly growing interest in magnesium alloys, this issue needs to be investigated in details, for such a partnership to succeed and produce components for practical applications.

In chapter five, a set of comprehensive curves that describe the effects of the various forming parameters (*temperature, strain and strain rate*) on the behaviour of the model material during superplastic deformation, in terms of flow stress fracture strain and strain rate sensitivity index, was established. Yet, to complete the picture, the material's behaviour following superplastic deformation needs to be quantified. To do so, this chapter presents a systematic approach for evaluating the mechanical post-superplastic forming properties of the AZ31 magnesium alloy [Khraisheh et al. 2007]. The goal is to construct a set of maps that assess the effects of the same forming parameters on the outcome of the superplastic forming process, in terms of the level of deformation-uniformity and the percentage changes in RT mechanical properties (*strength and ductility*).

The focus is first directed towards the specific temperature of 400 °C, to investigate the effects of both strain and strain rate on post-SPF mechanical properties. These properties are compared to those of the as-received material, and their changes are thereafter correlated to the microstructural evolution in the material. Because of the large number of tests required, the influence of forming temperature is investigated at a fixed strain rate, yet still at various strain limits. Finally, some light is shed on how to expand the proposed approach, and therefore the analysis, to the biaxial loading case, which is the closer simulation for loading in actual superplastic forming practices.

The results obtained from this study accentuate on the necessity of a combined forming/post-forming analysis in designing and forming various components, and ultimately optimising the process of superplastic forming. The presented maps provide a unique tool for process designers to select forming parameters based directly and solely on the desired properties of the formed part. Such approach is quite unique and flexible, unlike most current optimisation practices which target specific process or material parameters.

7.1 General Approach

The general approach for studying post-SPF properties is simply derived by simulating the response of the material during and after it has been formed into a certain part, and it is best described by the schematic flow chart shown in figure 7.1. This approach represents an expansion to the efforts of many investigators, like McMarmid [1985], Cope et al. [1987] and Duffy et al. [1988], and it is not confined to a specific loading case. The basic steps presented in the figure are self-explanatory, and will not be listed here. Instead, and since the mainstream of our investigation is carried out in *1D*, the details of how it is conducted are laid out as follows:

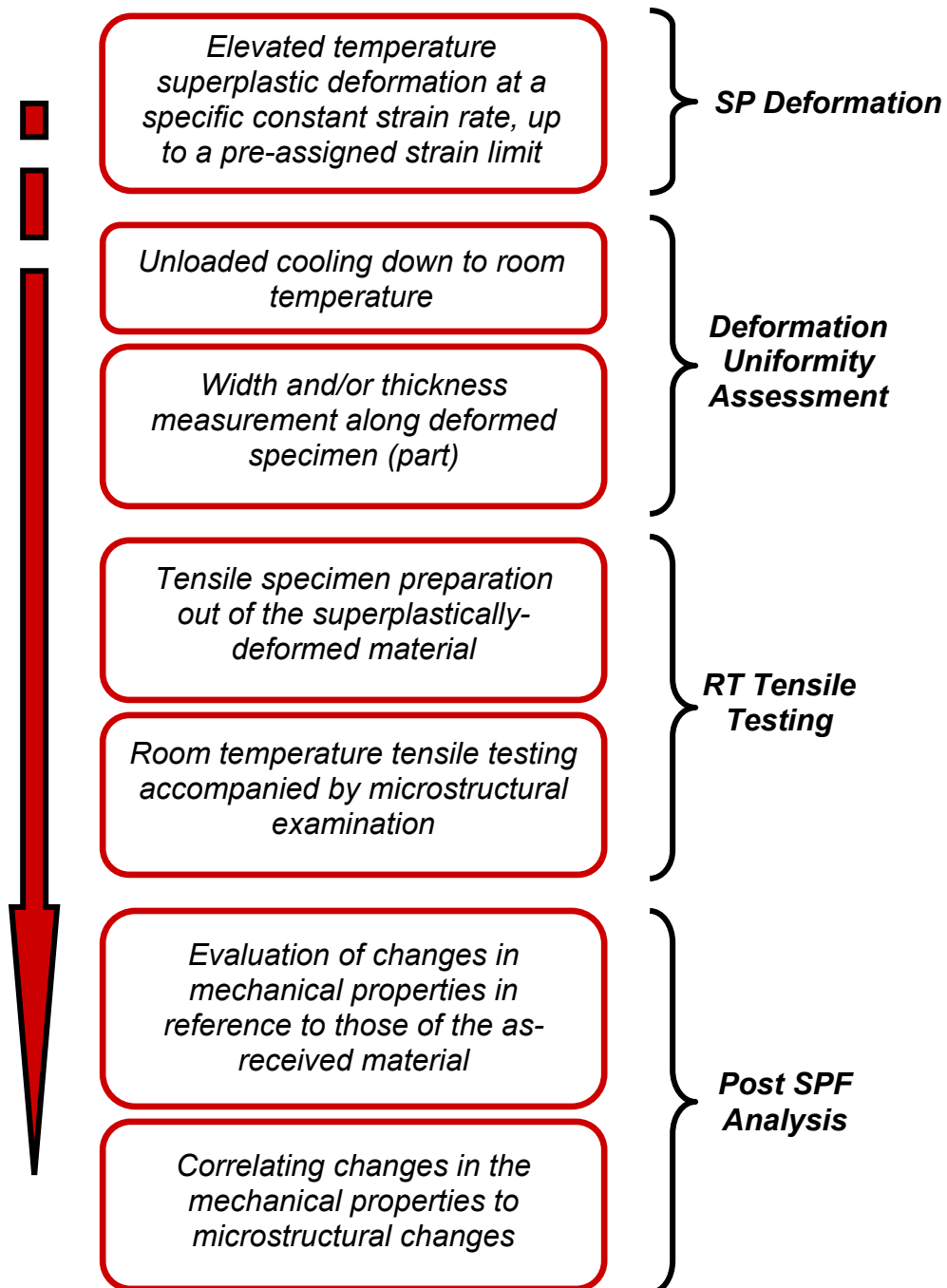


Figure 7.1: Schematic approach to investigating the post superplastic forming properties

- i. For a selected forming temperature and strain rate, a set of interrupted uniaxial tensile tests are carried out, up to various pre-assigned strain limits.
- ii. In each test, once the tensile specimen reaches the desired strain, cooling starts to bring its temperature to the ambient temperature, maintaining an almost zero load all along.
- iii. Each specimen is then divided into equally spaced points along the gauge length, where both thickness and width are measured and recorded.

- iv. These interrupted tensile tests are repeated covering several temperatures and strain rates.
- v. Thickness and width measurement are combined to generate the deformation uniformity maps.
- vi. After that, each specimen is machined along the sides to produce a uniform section, and eliminate any width variations caused by superplastic deformation.
- vii. The new specimen is then uniaxially tested at room temperature, to evaluate the mechanical properties, namely; yield strength, tensile strength and ductility (*fracture strain*).
- viii. Instead of their absolute values, the ratios between those properties and the corresponding values for the as-received material are evaluated. These ratios represent the changes in mechanical properties due to superplastic deformation at a certain combination of forming parameters.
- ix. The results obtained from all the tests are combined to generate the maps of post-superplastic forming mechanical properties.
- x. The changes in mechanical properties are finally correlated to the microstructural changes in the material, mainly cavitation and grain growth.

Following these steps, the remaining details including the selected forming conditions and testing parameters, in addition to the results of this investigation, are all covered in the subsequent sections of the chapter.

7.2 Detailed Investigation of Post-SPF in 1D at 400 °C

7.2.1 Superplastic deformation at 400C

To allow for material removal when machining, type-II grips and 0° oriented tensile test specimens (*figures 4.8*) were used for conducting the uniaxial tensile tests at 400 °C. As detailed earlier in chapter four, type-II specimens are 19 mm wide and 38 mm long (*figures 4.9*). The specimens were all machined from the 3.22 mm thick AZ31 magnesium sheets. Interrupted uniaxial tensile tests were carried out, covering four different strain rates (1×10^{-3} , 5×10^{-4} , 2×10^{-4} and 10^{-4} s^{-1}) and six true strain values (0.3, 0.5, 0.7, 0.9, 1.1 and 1.3). As the strain is reached and the test is stopped, the test specimen was cooled down to room temperature, and preserved for further dimensional measurements. Each combination of strain and strain rate was repeated at least twice for repeatability assurance. Stress/strain curves of the specimens strained at $2 \times 10^{-4} \text{ s}^{-1}$ to different strain values are shown, as an example, in figure 7.2a. The curves clearly indicate that the tests are repeatable and that the experimental setup and forming conditions are well-controlled. The corresponding deformed specimens are shown in figure 7.2b, demonstrating how deformation slowly deteriorates as strain limit is increased.

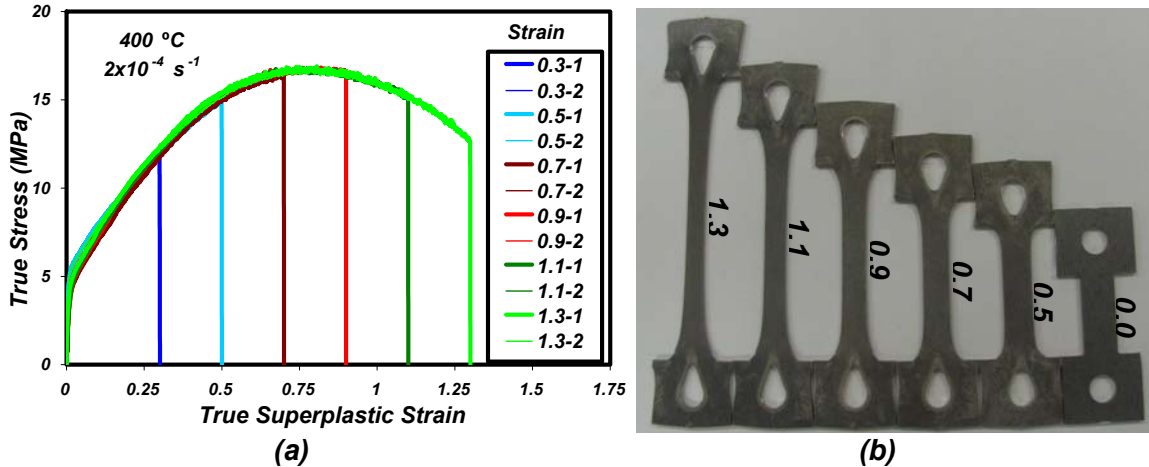


Figure 7.2: (a) Interrupted stress-strain curves of specimens strained at $2 \times 10^{-4} \text{ s}^{-1}$ to different strain values (b) The corresponding deformed specimens

The intriguing distortion in the grip area, particularly observed at higher strains, implies significant material flow into the gauge length region. A look back at figure 5.9b does not show such distortion in type-I specimens, despite the fact that some specimens in the recalled figure were strained to higher strains. Despite that, the clear difference between both specimen geometries is mainly caused by the different grip-to-gauge area ratio, which is higher for type-I specimens. This, nonetheless, does not mean that type-II exhibits higher material flow; it is just that the lower grip-to-gauge area ratio makes it more observable. All the same, it was quite necessary to use type-II, as it would be rather hard to machine type-I specimens after large superplastic deformation.

7.2.2 Deformation Uniformity

In order to evaluate deformation uniformity, width and thickness distributions along the gauge section of each specimen were measured and recorded, and plotted for every combination of strain rate and strain limit. The “evolution” in terms of both width and thickness can be traced as deformation progresses at any fixed strain rate. An example is shown in figure 7.3, where the percentage thickness and width drops are plotted along the gauge length for specimens deformed at $5 \times 10^{-4} \text{ s}^{-1}$. Percentage width/thickness drop is simply the ratio between width/thickness after deformation and the initial specimen’s width/thickness; such normalisation is more representative, and eliminates the dependency on the initial dimensions of the specimen. Parts (b) and (c) of the figure show how significant the drop in both thickness and width are, in addition to their variation along the specimen, as deformation progresses. The maximum drop in the middle of the specimen after a strain of 1.3 (equivalent to 267% elongation) exceeds 50% in both cases. And the large variation at this high strain limit indicates how fast the deformation non-uniformity is taking place at the given strain rate.

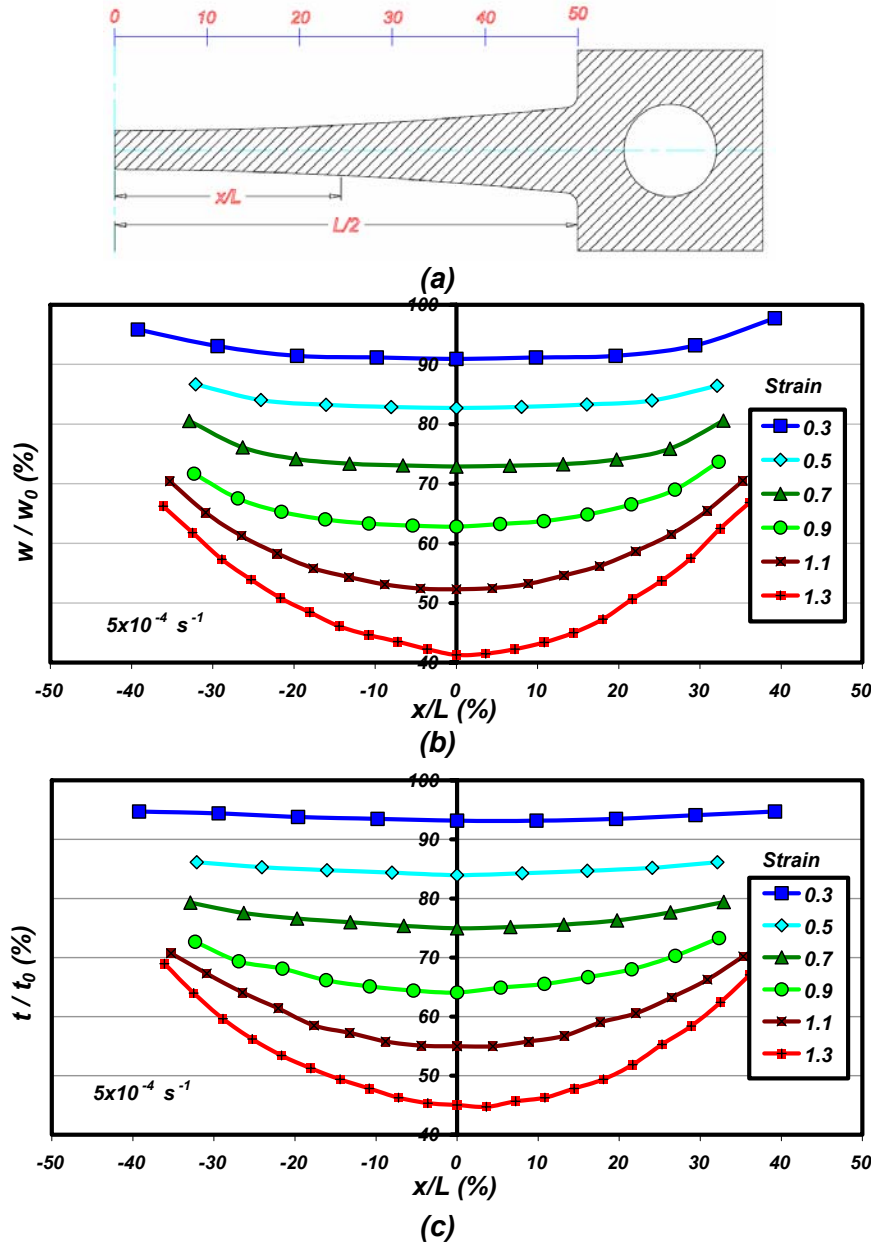


Figure 7.3: (a) Schematic of the deformed specimen (b) Normalised width and (c) Thickness distributions along specimens strained at $5 \times 10^{-4} \text{ s}^{-1}$ to various strains

Naturally, such drop and variation are also strain rate dependent, and expected to escalate at higher strain rates, or decline at lower strain rates. A look at the effect of strain rate is given in figure 7.4, where both percentage width and thickness drops are plotted for specimens deformed to the same strain limit of 1.1, at the four different strain rates investigated here. It is shown how forming at the high strain rate of 10^{-3} s^{-1} not only resulted in severest thinning, but also yielded the largest thickness variation along the deformed specimen at about 25%. This variation drops to less than 5% for the strain rate of 10^{-4} s^{-1} .

The curves presented in figures 7.3 & 7.4, might seem redundant, since the trend is quite expected; in other words, deformation uniformity is known to deteriorate at higher strain rates and larger strains. Yet it is the quantitative assessment that is very critical for the ultimate goal of understanding the combined effects of both strain and strain rate on deformation uniformity.

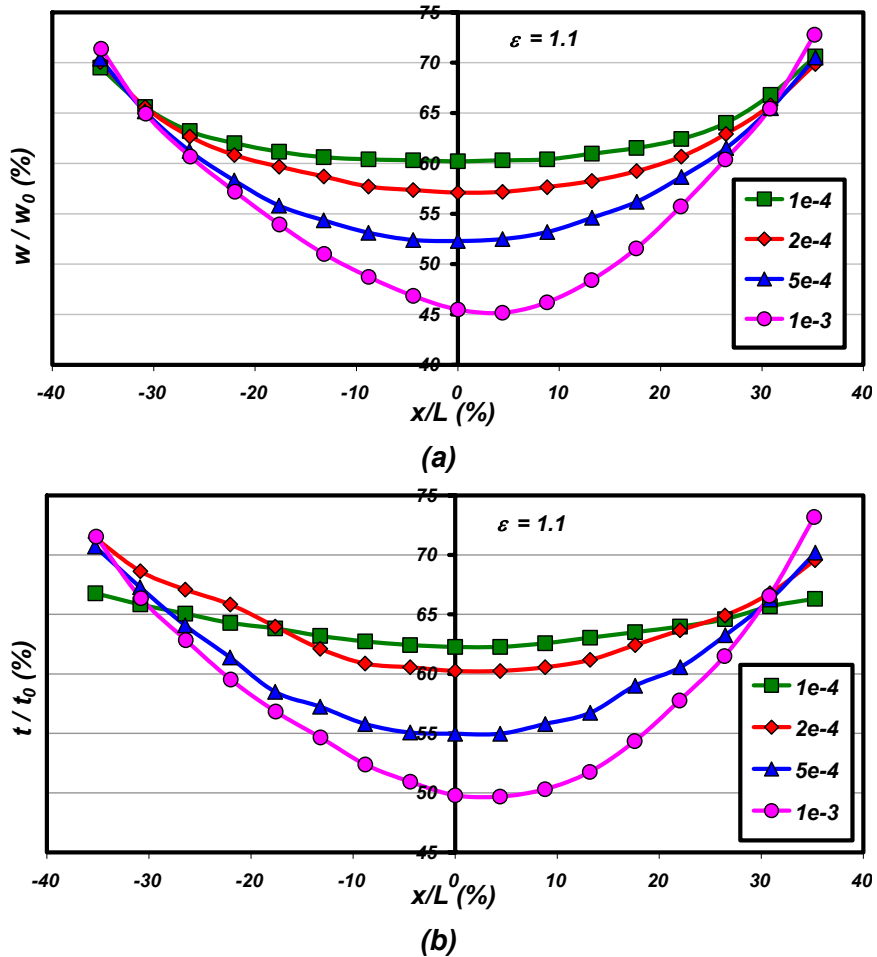


Figure 7.4: (a) Normalised width and (b) Thickness distributions along specimens strained to 110% at various strain rates

Out of each curve corresponding to a certain combination of strain and strain rate, the point of maximum percentage drop is extracted, and the numerous normalised width and thickness distribution curves (*some of which are shown in figures 7.3 & 7.4*) are replaced by the two graphs shown in figure 7.5. These plots summarise the mutual influence of the two forming parameters (*strain and strain rate*) on the uniformity of superplastic deformation achieved at 400 °C. It should be emphasised that the plots do not imply using the lowest strain rate for the best deformation uniformity results, but rather give the freedom to choose the fastest “satisfactory” strain rate to achieve the desired uniformity level for a particular strain limit.

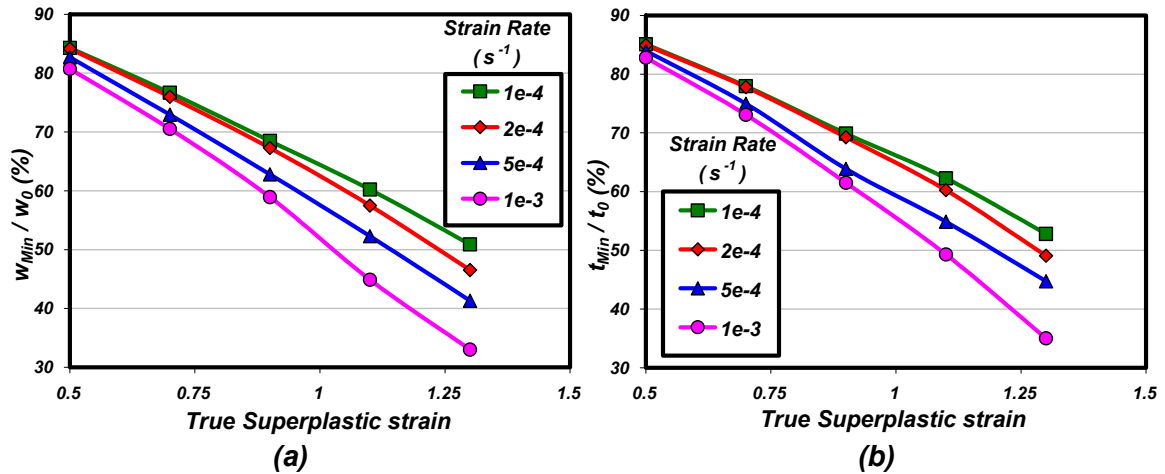
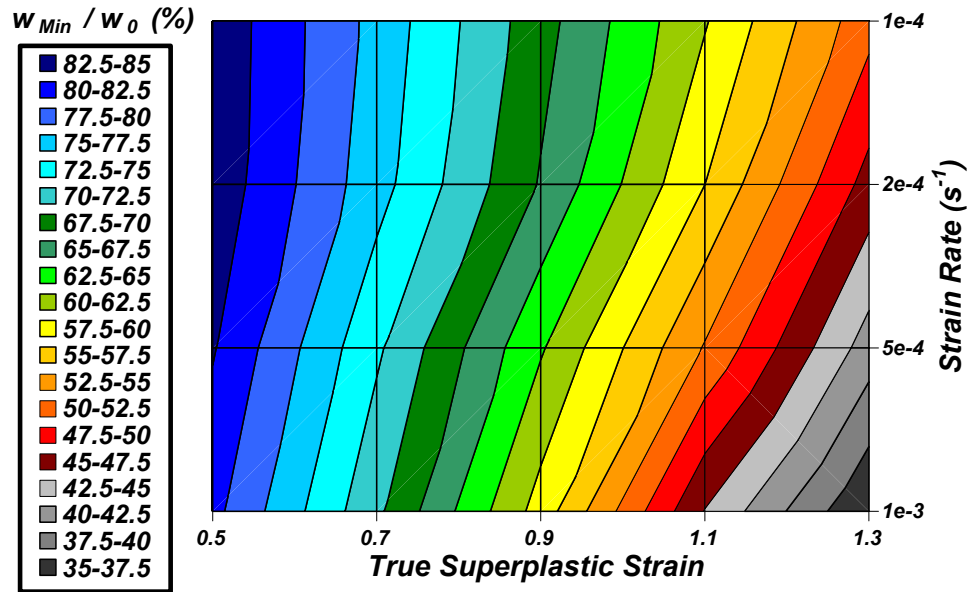


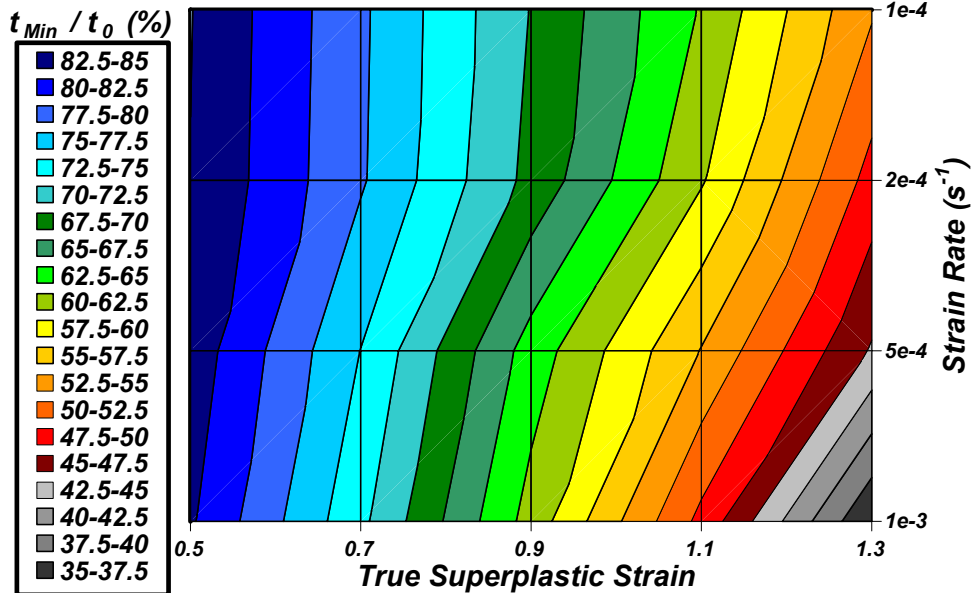
Figure 7.5: Maximum thinning at various combinations of strain and strain rate in terms of (a) Width (b) Thickness

The curves in figure 7.5 were re-plotted in a different way, to provide practical easy-to-use deformation maps, as the ones shown in figure 7.6. Each colour in these maps corresponds to a certain band of width/thickness percentage drop, which is set to a narrow range of only 2.5%. Such a unique way of presentation provides, not points but, continuous zones of strain and strain rate combinations that yield the same influence on deformation uniformity. By making use of that, trial and error forming practices could be eliminated, if forming parameters are selected based on the desired outcome (*deformation uniformity for instance*). A similar case was presented earlier in chapter five, where figure 5.11a provided a mean for selecting the appropriate forming parameters based on the maximum fracture strain. Deformation maps shown here are complimentary to the fracture strain curves given in figure 5.11a; as those curves sets the boundaries (*limits*) of superplastic deformation, these maps designate the level of deformation uniformity when forming within those boundaries.

To highlight the importance of such maps, consider for instance the true strain of 0.5. By referring to figure 7.6b for instance, it is noticed that all the strain rates share the same colour strip (*dark blue*), which means that up to that strain level, changing the rate of deformation would not yield any improvement in terms of deformation uniformity. Nevertheless, as the strain level increases, colour variation along any vertical line (*i.e. constant strain*) is noticed, always in favour of the lower strain rate. This colour variation keeps increasing with strain, giving a quantitative measure of deformation uniformity as a function of strain and strain rate. If a strain level of 1.3 is targeted instead, the map in figure 6.7b indicates that thickness drop percentage is around 55% when deformation takes place at a low strain rate of 10^{-4} s^{-1} and around 37.5% when deformation takes place at the high strain rate of 10^{-3} s^{-1} .



(a)



(b)

Figure 7.6: 2D Maps for maximum thinning at various combinations of strain and strain rate in terms of (a) Width (c) Thickness

Practically, such maps would be used in a reversed way by specifying the lowest acceptable thinning level, then selecting a strain rate for a target strain value. If a part, for example, is to be formed with no less than 60% thinning (*thickness percentage drop*) at the most critical region of 1.1 true strain; figure 7.6b indicates that forming at $2 \times 10^{-4} \text{ s}^{-1}$ or lower would guarantee that.

7.2.3 RT Tensile Tests and Post-SPF Mechanical Properties

Following the deformation uniformity assessment, all the specimens were machined (*by milling*) along the sides to produce a uniform section. Despite the various lengths of the specimens deformed to different strain limits, only *60 mm* of the gauge section was machined, in order to further localise deformation in the subsequent room temperature tensile testing. *60 mm* was not chosen randomly, but rather to guarantee enough room for a *50 mm* extensometer, which was used for more accurate strain measurements. Thickness, on the other hand, was not altered to avoid distorting the specimens. Besides, thickness variation was minimal around the centre of the deformed specimens within a *50 mm* circle, as might be depicted from figures 7.3 and 7.4. The machined specimens were then tested in simple tension at room temperature, at a constant speed of *1.5 mm/min* to evaluate the post-SPF mechanical properties. Figure 7.7 demonstrates the main changes each specimen undergoes in the presented post-superplastic forming analysis.

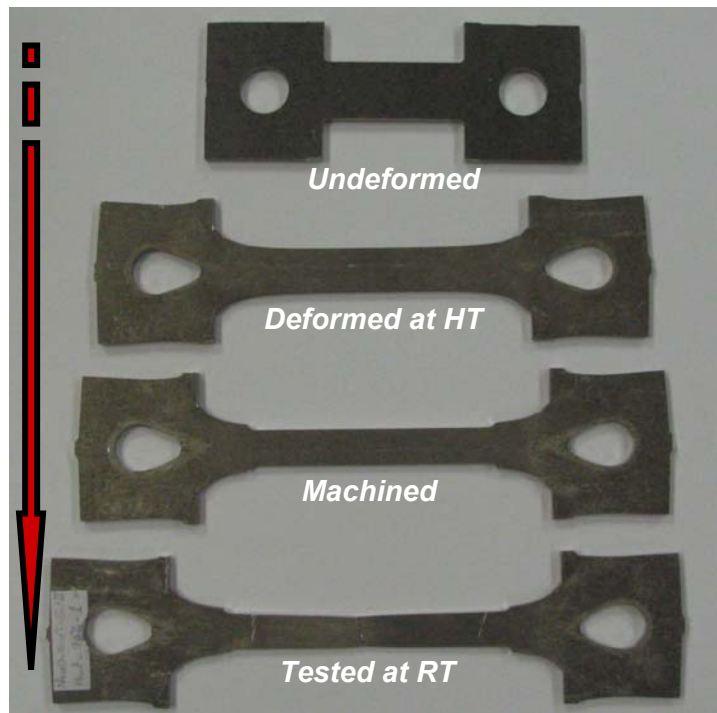


Figure 7.7: Post-SPF analysis mirrored by the changes underwent by test specimens

For each specimen superplastically-deformed at a certain combination of strain and strain rate, three main quantities were extracted from the subsequent RT tensile test; yield strength, ultimate tensile strength and fracture strain. Figure 7.8a shows the RT stress/strain curves for specimens superplastically-deformed at $5 \times 10^{-4} \text{ s}^{-1}$ to the aforementioned six strain limits. One can see the clear inverse effect of superplastic strain on both fracture strain and ultimate

tensile strength; in other words, the higher the superplastic strain, the lower these two quantities are. The same cannot be said about yield strength, which seems to be independent of superplastic strain, as the six different curves share almost the same yield point.

By focusing on one superplastic strain value, 1.1 for instance, figure 7.8b shows the effect of strain rate on these three mechanical properties. The trend is very similar; while yield strength is hardly affected, higher strain rate deteriorate both fracture strain and tensile strength of the material after such superplastic deformation.

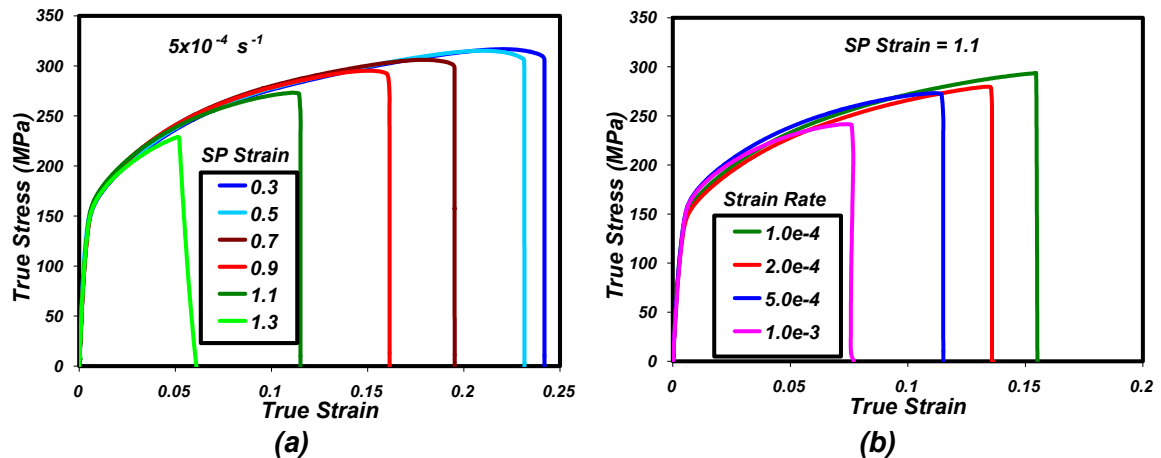


Figure 7.8: RT Stress/strain curves for specimens already superplastically deformed (a) At the same strain rate (b) To the same strain limit

The absolute values of the mechanical properties are not of prime interest, since the ultimate goal of this analysis is to arrive at a quantitative assessment of the “changes” in the yield strength, ultimate tensile strength and room temperature ductility caused by superplastic deformation at various strains and strain rates. Therefore, these quantities were normalised by comparing them to the corresponding mechanical properties of the as-received material, obtained by similar tensile tests using type-II specimens. The results are summarised in the three parts of figure 7.9.

As alluded before by figure 7.8, the post-SPF yield strength results were different from both ductility and ultimate tensile strength results, in regard to their insensitivity to strain and strain rate. Neither parameter shows any significant impact in figure 7.9a, where yield strength of the post-SPF material varies between 58% and 62% of that corresponding to the as-received material. Apart from that, the figure accentuates on the clear impact of superplastic deformation, embodied by the large drop of about 40% in yield strength. And since neither strain nor strain rate seem to be responsible for this, heat must be the cause. To verify that, a simplified heating cycle analysis was carried out, in which tensile specimens were heated to 400 °C and then cooled down to the ambient

temperature without straining. Room temperature tensile tests of those specimens revealed about 38% drop in yield strength, with respect to the as-received material. It is believed that this huge drop is associated with microstructural changes due to heating, as will be further discussed in the next section.

Post-SPF tensile strength in figure 7.9b is both strain and strain rate dependent, perhaps with more sensitivity to strain. The curves show a steady decline up to 1.1 superplastic strain, beyond which tensile strength drops drastically. In fact, the specimens superplastically-deformed at 10^{-3} s^{-1} failed at a true strain of about 1.3. At the lowest strain of 0.3, the material seems to have lost about 10% of its strength, which cannot have been caused by strain only. Again, and similar to the yield strength case, heating cycle analysis explained this initial, not quite as large, strength drop. Non-superplastically-deformed specimens exhibited about 7% drop in their tensile strength due to heating only.

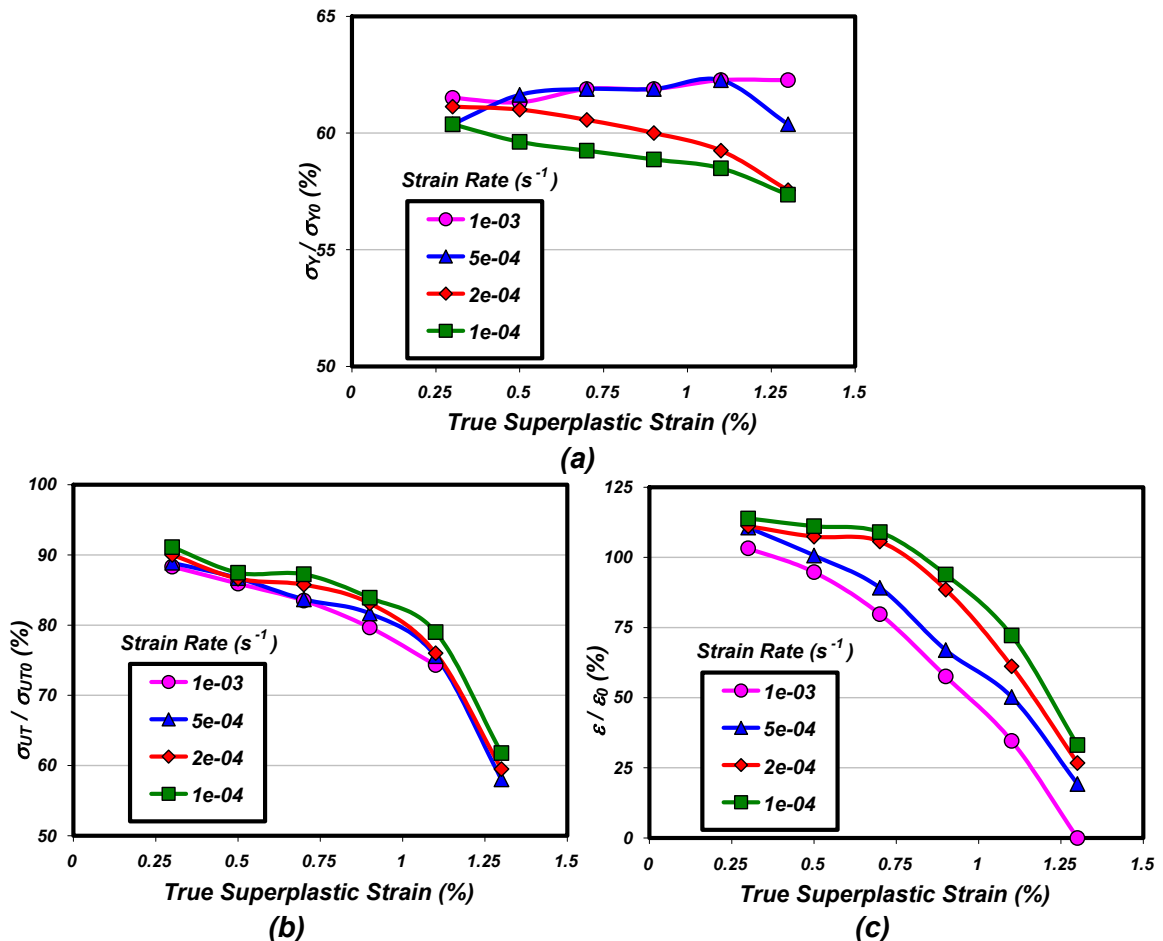


Figure 7.9: Normalised post-SPF mechanical properties for various strains and strain rates (a) Yield strength (b) Tensile strength (c) Fracture strain

The plot shown in figure 7.9c shows the clearest effect of both strain and strain rate on the post-SPF room temperature ductility. The trend is somewhat expected; the higher the superplastic strain and strain rate, the lower the post-SPF ductility is. Similar to the previous case of ultimate tensile strength, the adverse effect of these two parameters is initially small, but increases dramatically as superplastic deformation progresses to higher strain limits. Post-SPF fracture strain was set to zero at the last point on the 10^{-3} s^{-1} curve, since as mentioned before, specimens deformed at this strain rate failed at about 1.3. Quite opposite to strength, figure 7.9c shows an interesting observation of high fracture strain ratios (ϵ/ϵ_0) that exceed 100%, for all small strains, regardless of strain rate. These ratios imply that superplastic deformation up to certain limits causes some ductility enhancement, before it gradually decreases as higher strains are achieved. Heat cycling analysis indicated about 23% increase in room temperature ductility over the as-received material's.

All together, the three mechanical properties were shown to be affected, in different ways and by different levels, by superplastic deformation. On the other hand, heat was also shown to be responsible for those sharp changes in mechanical properties at the threshold of superplastic deformation. But in either case (*strain rate and strain on one side, and heat on the other*), no explanation to how they influence post-SPF mechanical properties was given. A trial to do so is presented in the next section.

Lastly, it is more convenient to present the data points of figure 7.9 in a form similar to the deformation maps represented earlier by figure 7.6. Therefore, 3D surface maps of the post-SPF room temperature tensile strength and fracture strain were generated, and they are shown in the two parts of figure 7.10. Yield strength was excluded, since its variation with superplastic deformation is slight. Just like the previous ones, these maps provide an easy and effective way for selecting the appropriate superplastic forming parameters that would yield the desired mechanical properties in the formed part.

The results presented so far testify the critical importance of the issue of post-forming analysis, particularly for the superplastic forming technique, and the need to combine it with a forming analysis, for proper selection of process parameters. It is quite clear how misleading it would be to select a certain material for a specific application, based only on its mechanical properties in the as-received condition, without accounting for the changes induced by the superplastic forming process itself.

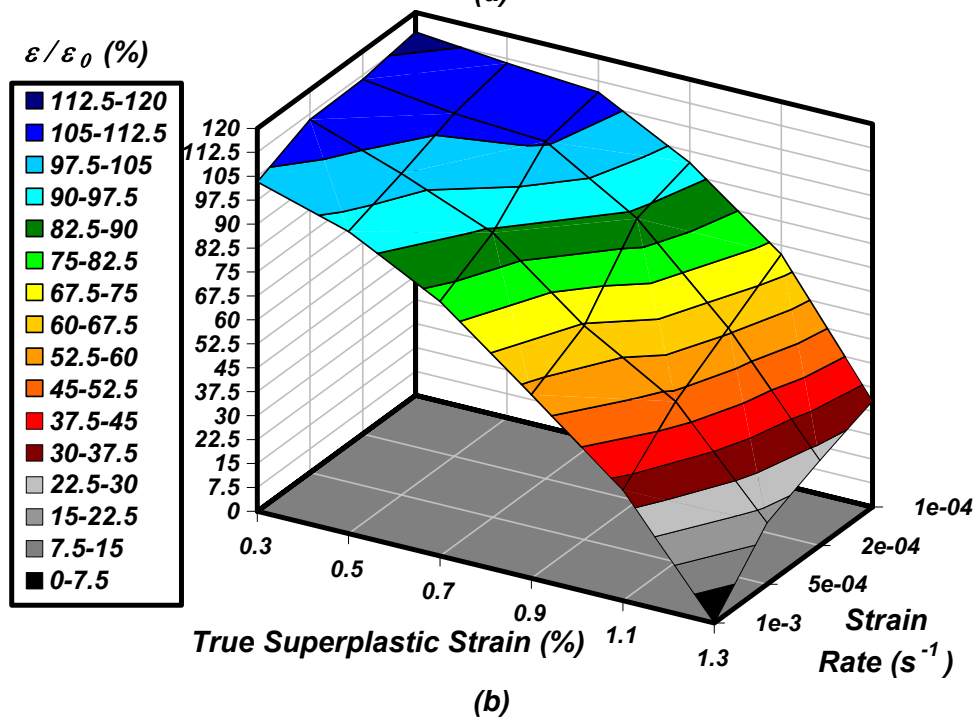
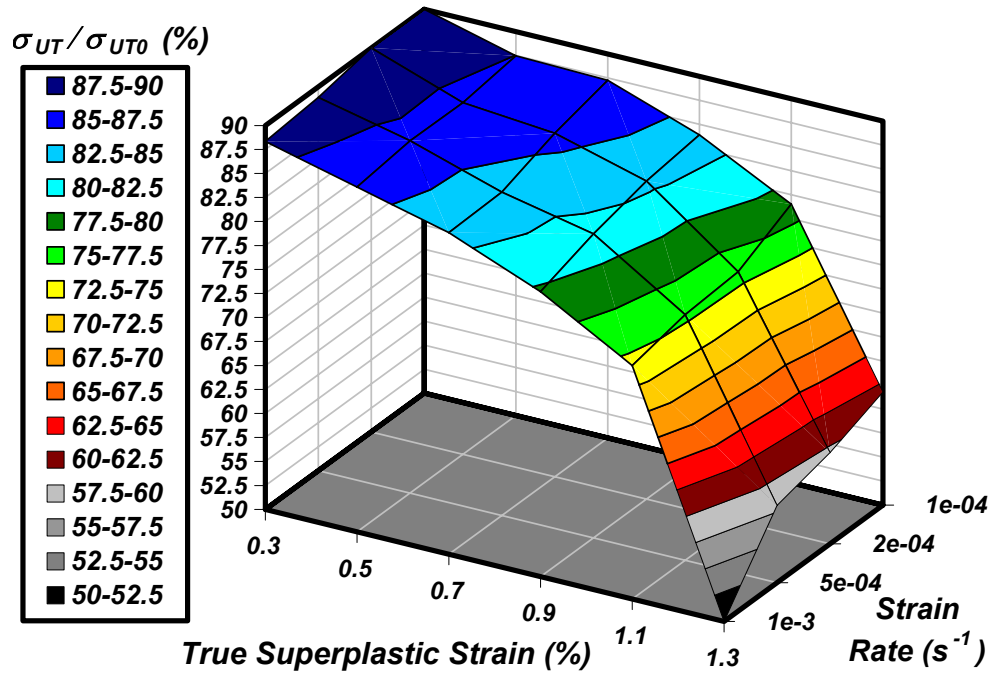


Figure 7.10: 3D post-SPF maps for various strains and strain rates (a) Ultimate tensile strength (b) Fracture strain

7.2.4 Post-SPF Mechanical Properties versus Microstructural Evolution

The key for understanding the effects of heating and straining on post-superplastic forming mechanical properties is to investigate the microstructural changes associated with these two factors separately.

A complete grain growth analysis during the superplastic forming of the AZ31 magnesium alloy at 400 °C, covering both the static and dynamic parts, was presented earlier in section 6.1.2. The analysis revealed strong static growth with a high rate of change during the heating phase, which slowly dampens with the subsequent dynamic growth as deformation progresses. By recalling figure 6.2a, the curve indicated that static grain growth takes place predominantly within the first 65 minutes of heating time, where grains grow from 4.5 to 8 μm . It was also highlighted that since this amount of time is equal to the total heating time prior to straining in tensile testing, then the initial grain size at the threshold of superplastic deformation is actually 8 μm , and not 4.5 μm .

Consequently, this large difference in initial grain size between the as received material and the superplastically deformed material is the main reason for the large, and thence steady, drop in yield strength, shown in figure 7.6a. In fact, it also explains why the thermally cycled specimens exhibited 38% drop in yield strength, even though no plastic deformation was imposed on the material. When those specimens were heated to 400 °C for about 65 minutes, then cooled down to room temperature; what actually happened is that the grain-structure was coarsened by about 175%, causing the yield strength of the material to drop significantly. Such behaviour is consistent with the well-known Hall-Petch relationship. To conclude, it is believed that post-SPF yield strength is solely affected by heating (*in terms of both temperature and time*), which is the driving mechanism for static grain growth. Figure 7.11a supports that by showing how infinitesimal the effect of straining is on the post-SPF yield strength, compared to that of heating.

The effect of grain growth extends to explain the initial drop in post-SPF ultimate tensile strength ($\approx 7\%$), and the initial boost in post-SPF tensile ductility ($\approx 23\%$). Just like yield strength, ultimate tensile strength is inversely proportional to the initial grain size, according to the Hall-Petch relationship, even if not to the same degree. Ductility on the other hand is directly proportional to it; and by heating, we can think of the material as getting closer to the O-temper, which is less strain hardened and therefore more ductile (*compared to the as-received material AZ31B-H24, which is half hardened*). However, grain growth does not explain the reduction in ductility and ultimate tensile strength as deformation progresses. Examining the cavitation behaviour of the material provided the explanation.

Cavitation in the material was investigated earlier in section 6.1.3, where it was presumed to be temperature and strain dependent, and independent of

heating time. Escalation of cavitation during superplastic deformation at 400 °C was plotted in figure 6.8. Interestingly, by plotting post-SPF tensile strength and fracture strain on the same graph, as shown in figure 7.11b for instance, one can clearly observe the correlation between cavitation and these two mechanical properties. Beyond a certain superplastic strain (≈ 0.7), cavitation in the material causes the deterioration of its post-SPF mechanical properties. In conclusion, these results indicate that cavitation is directly responsible for the deterioration of post-SPF mechanical properties that are strain dependent, namely ductility and tensile strength.

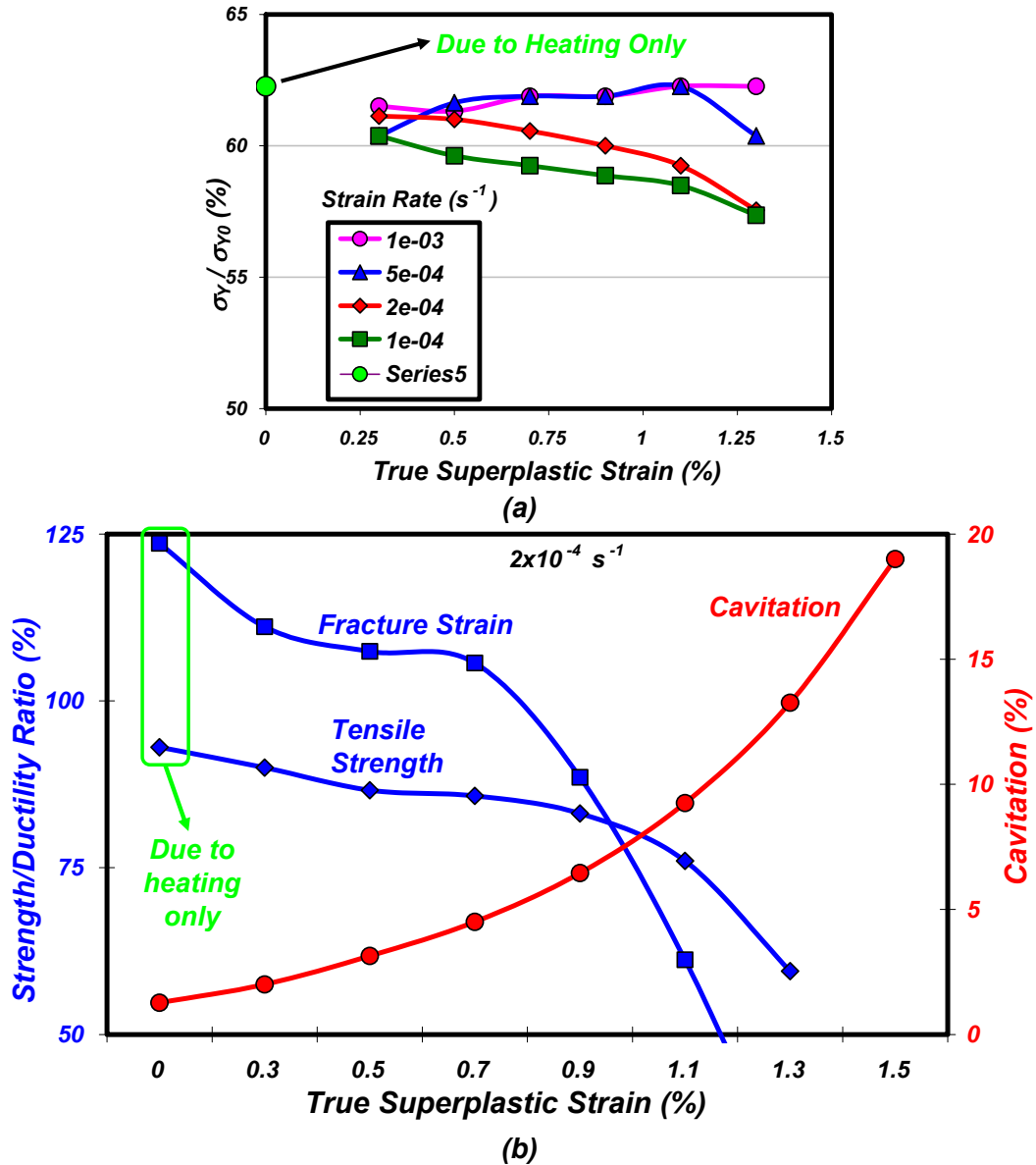


Figure 7.11: (a) Effect of heating on the post-SPF yield strength (b) Cavitation versus post-SPF tensile strength and fracture strain

7.3 Post-SPF Mechanical Properties in 1D at Various Temperatures

After a detailed investigation on the effects of strain and strain rate on the post-SPF properties of the AZ31 magnesium alloy at 400 °C, the influence of forming temperature was then investigated by focusing on a specific strain rate of $5 \times 10^{-4} \text{ s}^{-1}$. Interrupted tensile tests were carried out at this strain rate, covering six forming temperatures; 225, 325, 350, 375, 400, 425 and 450 °C. Type-I grips and 0° oriented tensile test specimens were used here instead of type-II. The reason for this, was that only four strain limits were covered; 0.3, 0.5, 0.7 and 0.9. And since the highest strain considered is 0.9, it was assumed that the deformation is uniform enough, that there is no need to machine the specimens for the subsequent room temperature tensile tests. Besides, the results from the previous section indicate that drastic drops in post-SPF properties take place at large strains. Figure 7.12 shows a set of test specimens superplastically-strained to the four strain limits at 350 °C. The figure shows how uniform the deformation is in terms of both width and thickness, justifying the use of type-I specimens here.

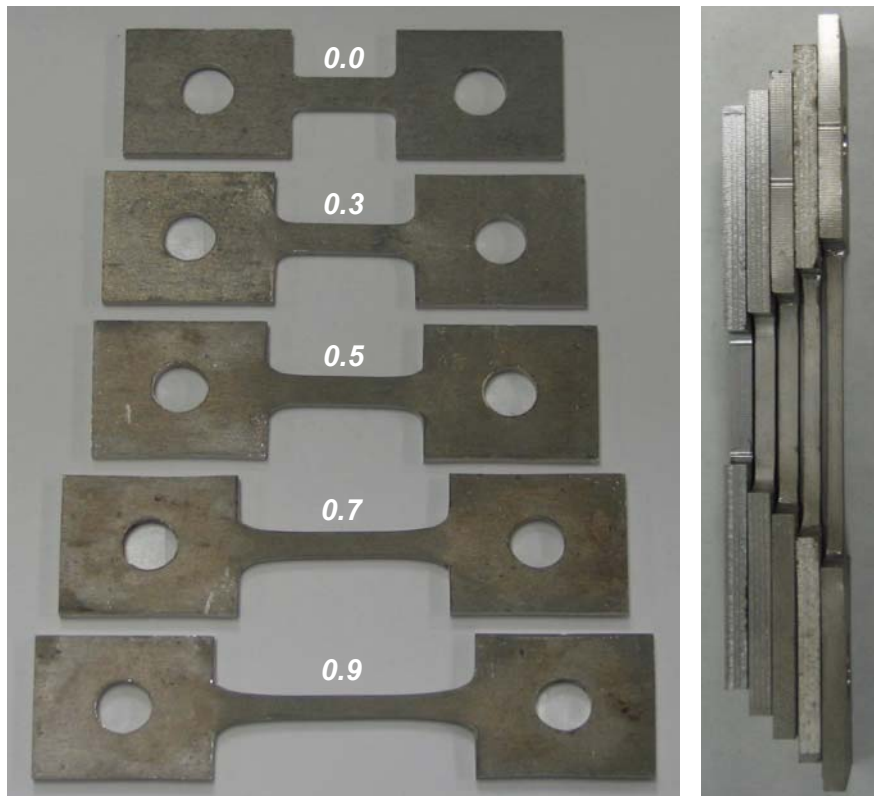


Figure 7.12: Specimens deformed at $5 \times 10^{-4} \text{ s}^{-1}$ to different strain values at 350 °C

After the interrupted tests at all the six different temperatures, the procedure followed in the previous section was imitated here, with the exception of the machining step. So, for deformation uniformity assessment, width and thickness distributions along the gauge section of each specimen were measured

and recorded, and plotted for every combination of strain and temperature. Then the point of maximum percentage drop was extracted out of each curve, and by combining all the points, the two graphs shown in figure 7.13 were generated. These plots demonstrate the effect of forming temperature on deformation uniformity at different strain limits. Interestingly, part a of the figure shows that width percentage drop is quite independent of forming temperature, except for the warm forming temperature of 225 °C. Even for thickness percentage drop in figure 7.13b, and though temperature's influence is more significant as its increase improves deformation uniformity, this improvement seems to dampen at higher temperatures. This implies that beyond some line, heating the material to very high temperatures becomes ineffective in yielding any significant deformation uniformity enhancement. Such curves assist in drawing the aforementioned limiting line.

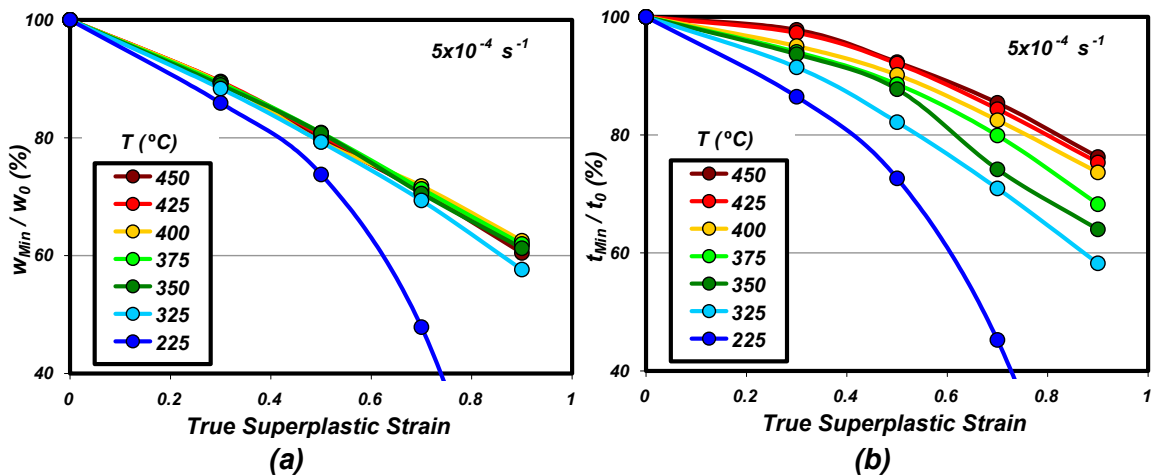


Figure 7.13: Maximum thinning at various combinations of strain and temperature in terms of (a) Width (b) Thickness

Since temperature does not show a strong effect on width percentage drop, only a thinning deformation map, combining the six different temperatures and the four strain limits, was generated, and it is presented in figure 7.14. Similar to the previously presented maps in figure 7.6, the use of this map is meant to help selecting the proper forming parameters in a way that optimises the desired outcome in terms of deformation uniformity. Moreover, this map is analogous and complimentary to the fracture strain curves presented earlier in figure 5.11b, as it specifies the level of deformation uniformity when forming within the limits drawn by those curves.

Following deformation uniformity assessment, uniaxial tensile tests were carried out at room temperature, at a constant speed of 1.5 mm/min , in order to evaluate the mechanical properties of all the specimens superplastically-deformed at the various combinations temperature and strain limits. The same three quantities were extracted from each RT tensile test; yield strength, ultimate tensile strength and fracture strain.

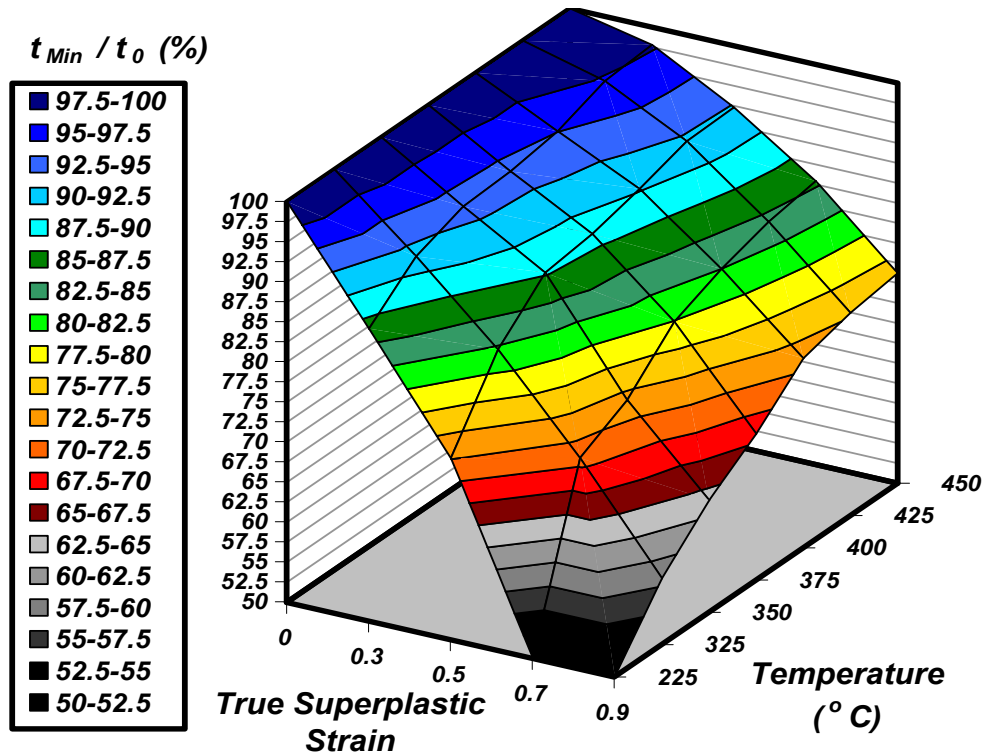


Figure 7.14: Maximum thinning map at various strains and temperatures

For the same purpose highlighted in the previous section, these quantities were thence normalised using the corresponding mechanical properties of the as-received material, which were obtained earlier in section 5.1.2 from the tensile tests on type-I specimens (*shown in figure 5.3a*). The results describing the effects of temperature and strain on the post-SPF properties are shown in figure 7.15. Figure 7.15a supports the previous observation that post-SPF yield strength is insensitive to the amount of superplastic strain, and shows a clear influence for forming temperature on it, which can be summarised in two main points. The first; as temperature increases, more drop in the post-SPF yield strength is resulted. The second; temperature's influence dampens as it increases and reaches the highest limits, which is 450 °C in this case. This point is clearly demonstrated by the large drop in post-SPF yield strength observed when heating up to 325 °C, compared to the subsequent drops as temperature approaches 450 °C. This behaviour can be related to the grain growth caused by heating at these temperatures; which makes sense as we expect the growth rate to increase with temperature, causing faster formation of larger grains, and hence lower yield strength.

Figure 7.15b on the other hand shows that apart from the warm forming temperature of 225 °C, temperature has a slight effect on post-SPF ultimate tensile strength. And since strain rate does not show a strong effect either, it can be generally stated that plastic strain is the main parameter influencing the room temperature tensile strength of the material following superplastic deformation.

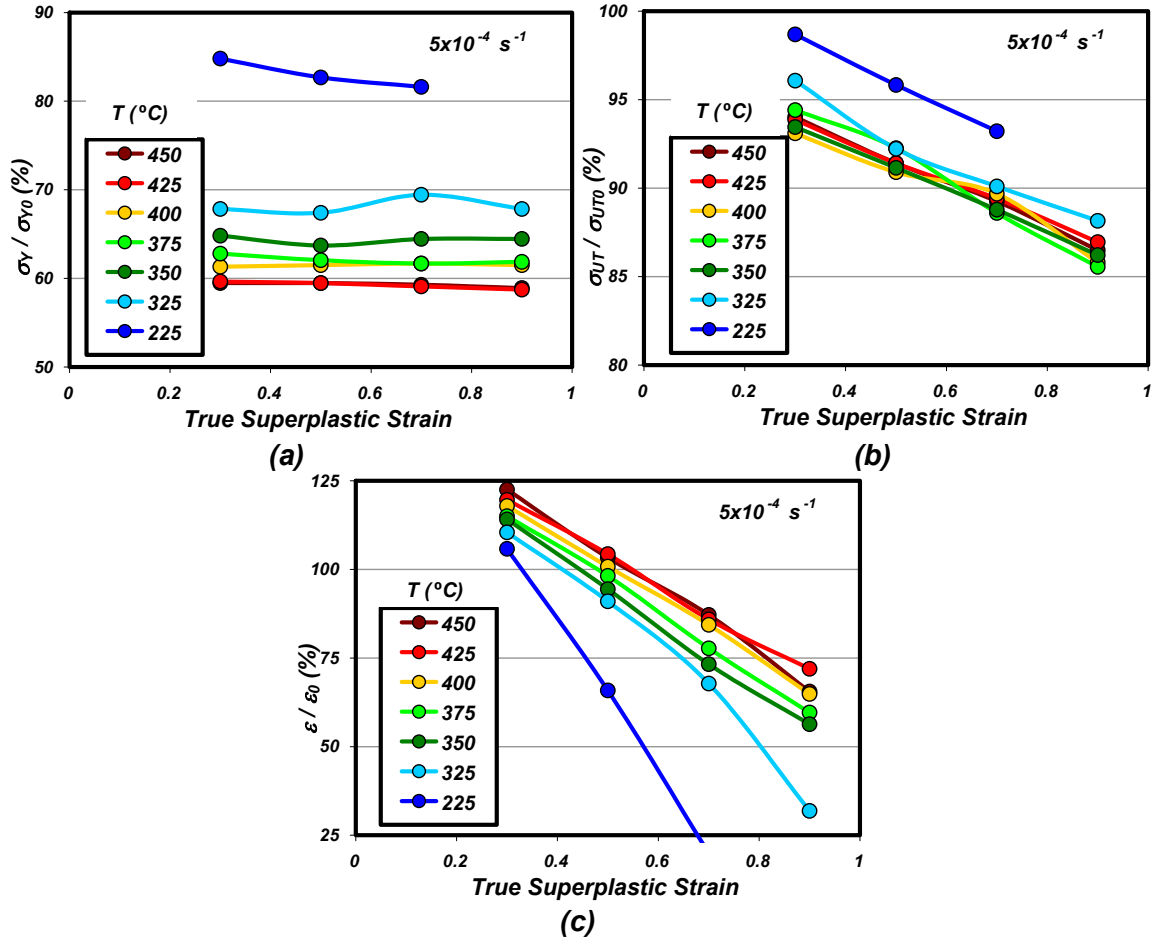


Figure 7.15: Normalised post-SPF mechanical properties for various strains and temperatures (a) Yield strength (b) Tensile strength (c) Fracture strain

An apparent effect for temperature on post-SPF fracture strain is depicted from figure 7.15c. The trend is somewhat similar to that observed in the yield strength case shown in figure 7.15a; in other words, temperature's effect is stronger at low temperatures and dampens as it increases. In fact, there is hardly any difference observed between the curves of 400, 425 and 450 °C, in figure 7.15c. Moreover, the high fracture strain ratios (ϵ/ϵ_0) that exceeded 100%, which were highlighted in the previous section at 400 °C, are observed here for a strain of 0.3, for all the other forming temperatures.

The explanation based on the thermal cycling analysis presented in the previous section can be expanded to justify this behaviour. Recall that heating to any of these temperatures (*for a certain amount of time*) means imposing some partial annealing on the material (*move it away from the H24 and closer to the O-temper*), which results in ductility enhancement. The higher the temperature, the more annealing is established, causing more ductility enhancement, as shown in figure 7.15c.

Since the variation with both superplastic strain and forming temperature is most significant in the case of fracture strain, a 3D surface post-SPF map of its values was generated, and it is plotted in figure 7.16. This map compliments the other one presented earlier in figure 7.10b by incorporating temperature as the third forming parameter. Together they demonstrate how the results of a post-SPF analysis would be used effectively for a proper selection of forming parameters, such that the desired mechanical properties in the formed part are achieved.

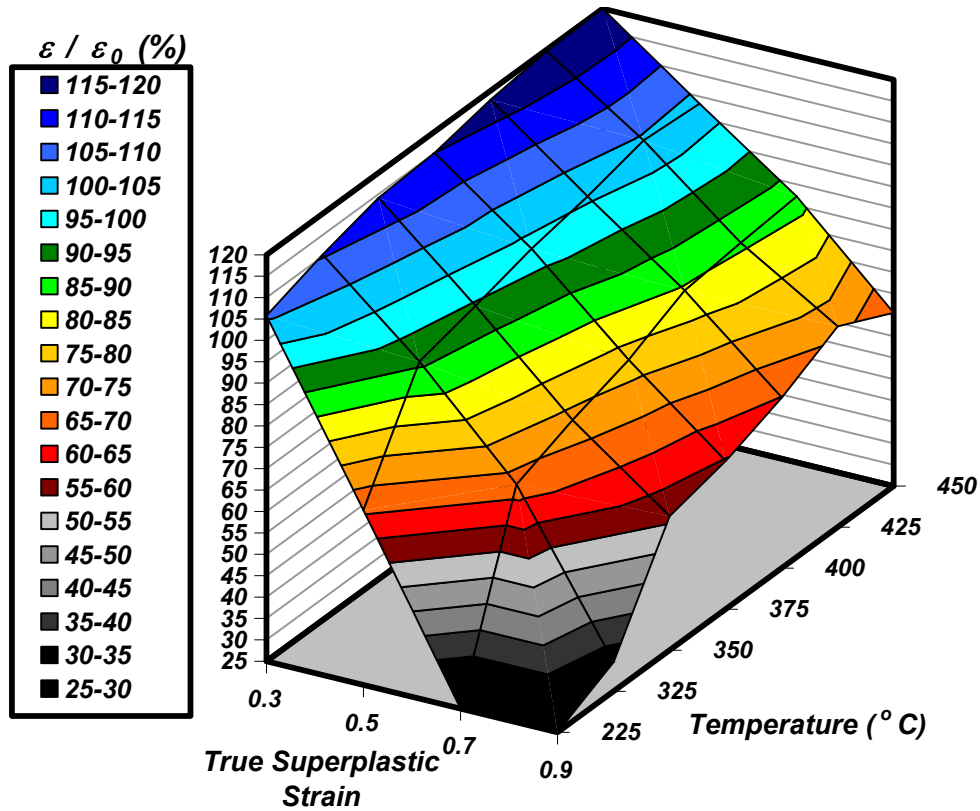


Figure 7.16: 3D post-SPF fracture strain map for various strains and temperatures

7.4 Post-SPF Mechanical Properties in 2D at 400 °C

During actual superplastic forming operations, biaxial stretching is the dominant loading condition. For this reason, this last section is dedicated to shed some light on how to expand the previously-covered 1D post-SPF analysis to the 2D case, where the mechanical properties of superplastically-deformed material under biaxial stretching are evaluated. Since the details of the approach were decently covered in section 7.2, they will not be repeated here; yet the main differences in expanding the 1D to the 2D case will be highlighted.

Circular disks, 80 mm in diameter, were cut out from the 1.65mm thick AZ31 magnesium alloy sheets. The sheets were superplastically-formed using the pneumatic bulge forming setup described in section 4.4, fitted with the cylindrical dies of the same diameter (63.5 mm) and three different heights; 12.70, 19.05 and 25.40 mm. The dies were shown earlier in figure 4.19. Forming was carried out at 400 °C, using the pressure-time profiles shown in figure 6.15a, which correspond to an average strain rate of $2 \times 10^{-4} \text{ s}^{-1}$ at the centre of the formed sheet. As a result, cups to the three different heights were formed, as was also shown in figure 6.15b.

After cooling down to the ambient temperature, a 12.5x9.5 mm tensile specimen was machined (*by milling*) out of the flat bottom part of each cup, along the rolling direction of the sheet. The produced tensile specimens were then subjected to uniaxial tensile tests at room temperature to evaluate the mechanical properties of the material. Figure 7.17 summarises the 2D approach in studying the post-SPF mechanical properties of the material, demonstrating the key steps each specimen (*circular sheet*) undergoes in the analysis.

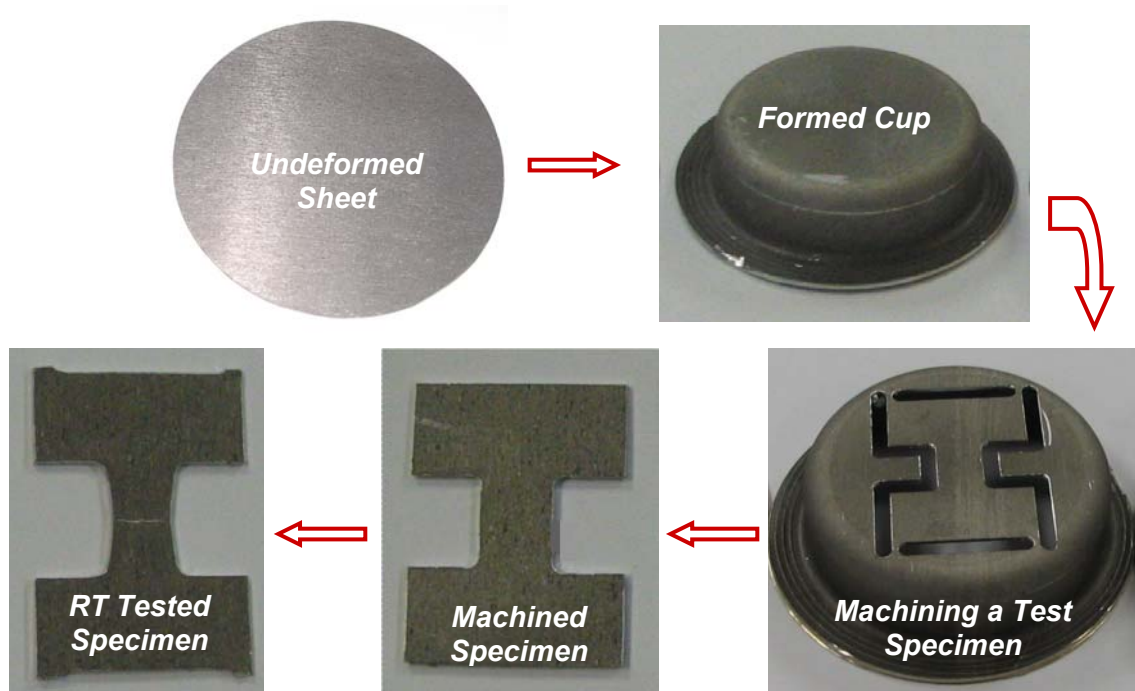


Figure 7.17: Post-SPF analysis in 2D mirrored by the changes underwent by test sheets

Forming the sheets to different heights implies imposing different strain levels at any specific location. An estimate to the amount of strain corresponding to each cup height was made by measuring thickness at the gauge section of the machined specimen, and thence evaluating the thickness strain based on the initial value of 1.65 mm; a summary of those estimates is shown in figure 7.18.

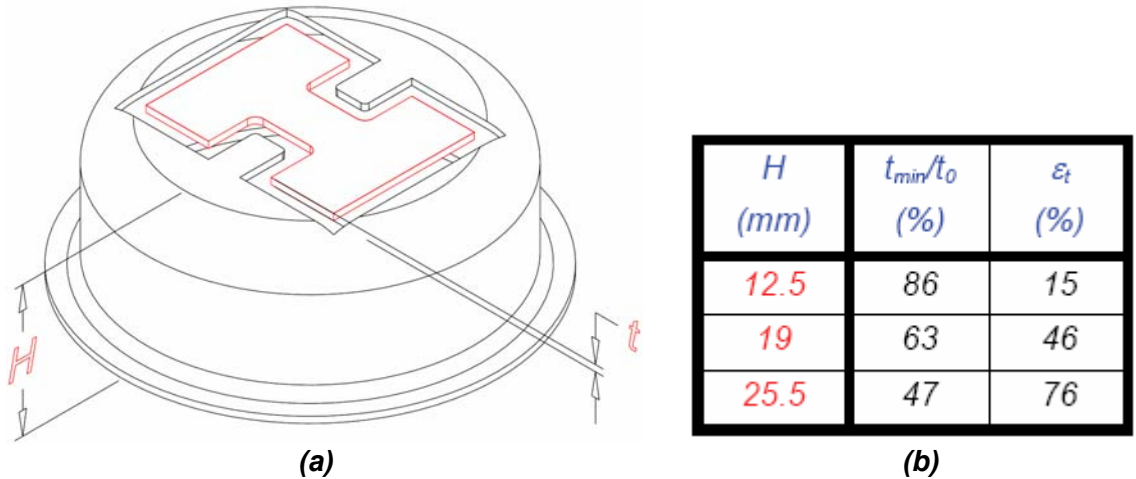


Figure 7.18: (a) A schematic plot for a tensile specimen machined out of the formed cup (b) Thickness strains corresponding to the three different cup heights

Room temperature testing of the machined specimens was repeated three times under the same conditions to ensure accuracy and repeatability of the results. The same three mechanical properties were targeted in each test; yield strength, ultimate tensile strength and fracture strain. Similarly, the obtained quantities were then normalised based on the mechanical properties of the as-received material, evaluated from tensile tests of specimens machined with the exact geometry (12.5x9.5 mm) from the original 1.65 mm thick sheet. The results of post-superplastic biaxial forming were combined for all the three mechanical properties as shown in figure 7.19 which shows a behaviour similar to the one obtained for the 1D case.

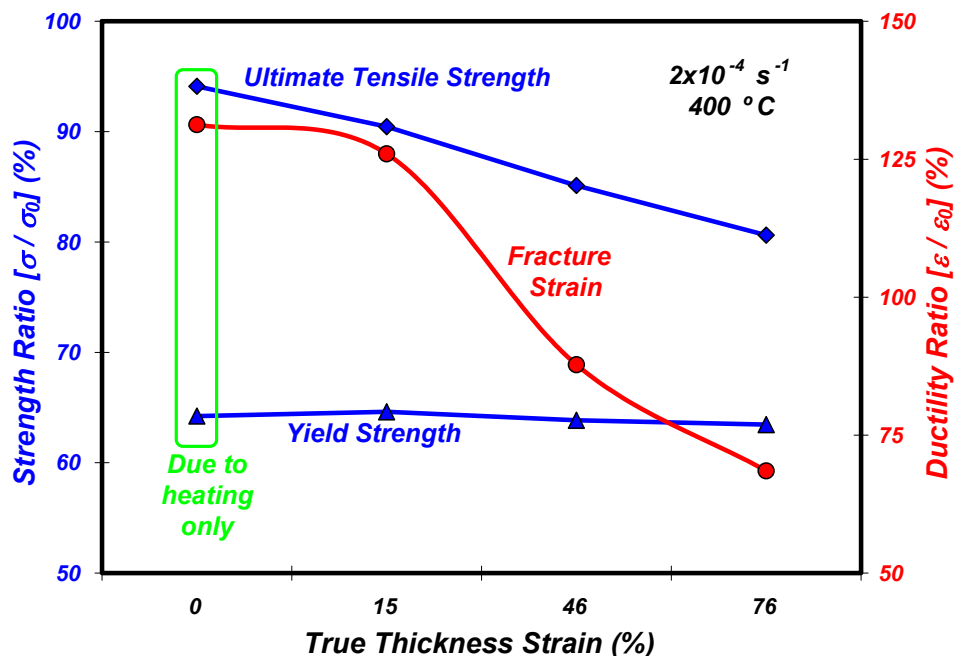


Figure 7.19: Effect of heating and strain on post-SPF mechanical properties in 2D

Ductility enhancement due to heating is observed here at low strain values, followed by gradual drop as strain increases. The ultimate tensile strength is lower for the heated specimens, and similarly decreases with superplastic strain. Note that large strains were not achieved in the cups, and therefore sharp drops in post-SPF ductility and ultimate strength were not observed. Finally, no effect of superplastic strain on the post-SPF yield strength was observed, coinciding with previous observations, which further indicates that post-SPF drop in yield strength is related to grain growth, which largely depends on heating that takes place prior to deformation.

8. CHAPTER EIGHT: REMARKS AND FUTURE RECOMMENDATIONS

8.1 Concluding Remarks

A multiaxial microstructure-based constitutive model, based on the continuum theory of viscoplasticity, was developed to describe the behaviour of superplastic materials. The model employs a dynamic anisotropic yield function, accounts for internal variables and microstructural evolution, including grain growth and cavitation. Using experimental data available in the literature, the model was calibrated and validated for the Pb-Sn superplastic alloy at three different loading conditions; simple tension, simple shear and combined tension-torsion. The model was shown to have the ability to capture the behaviour of the material in all the three cases to a very good extent.

Mechanical testing in superplastic studies is a topic that does not receive enough attention, mirrored by the lack of testing standards, even for the simplest type of all, the uniaxial tensile test. Detailed analysis was carried out and a comprehensive tensile testing methodology was presented, covering experimental setup, suitable grips and test specimens design, and proper testing procedures. In addition, a closer look on the commonly-ignored testing issues in superplasticity was given, and a trial to tackle those issues was presented.

Due to its great potential for weight savings in the transportation sector of applications, magnesium alloys were the main target material of this study. The AZ31 magnesium alloy was on focus in particular, where its superplastic behaviour was first characterised over a wide range of temperatures and strain rates using constant strain rate tensile and strain rate jump tests. The results related the material's mechanical behaviour in terms of flow stress, fracture strain and strain rate sensitivity on one side, to the forming parameters, of temperature, strain limit and strain rate, on the other side. In an effort to study the effect of loading biaxiality on the material's behaviour, a special fixture was designed and built, aiming at examining any possible deformation-induced anisotropy, and evaluating the microstructural evolution under the biaxial loading conditions. The preliminary results proved the fixture's ability to impose biaxial strains on the material, with the proper specimen design; yet, further work is needed to accurately measure stresses and strains.

In a collaborative work with another student, a systematic approach for controlling the superplastic forming process was presented. The developed constitutive model was first calibrated for the AZ31 magnesium alloy using the results of mechanical testing, combined with additional microstructural examination in terms of grain growth and cavitation. The capabilities of the calibrated model were tested using a specially-built bulge forming setup, by forming AZ31 magnesium sheets into different shapes, based on pressure-time

profiles generated by a FE code utilising the model. The results highlight the effectiveness of combining an accurate predictive tool with FE to control the deformation in actual superplastic forming practices.

The collaborative effort was taken a further step to tackle the problem of prolonged forming times in superplastic forming operations through optimisation. The calibrated model for the AZ31 magnesium alloy was combined with a stability criterion (*developed by the fellow student*) to generate the appropriate optimum loading path for the material. Experimental validation of the proposed optimisation scheme was carried out by both uniaxial tensile testing and bulge forming, and in both cases, results indicated significant reduction in forming time without sacrificing the integrity and uniformity of deformation.

Finally, the critical, yet virtually ignored, issue of post-superplastic forming was given a special attention, in a detailed comprehensive investigation of post-SPF properties of the AZ31 magnesium alloy. Following a systematic approach, the material's room temperature mechanical properties following uniaxial and biaxial superplastic deformation were evaluated, and thence related to those of the as-received material. The changes in mechanical properties were presented through a set of unique maps that quantify the effects of the various forming process parameters; temperature, strain rate and strain limit. Those changes were explained based on the corresponding microstructural evolution in the material as a result of the imposed heating and superplastic strain.

8.2 Importance and Contributions

- 1) Modelling anisotropy during superplastic forming. Most of the available models assume isotropic behaviour, though experimental observations indicated anisotropic behaviour during superplastic deformation.
- 2) Multiaxial loading. Most of the available models are based on the uniaxial loading condition. Special fixture for biaxial testing has been built for this purpose.
- 3) Characterising the superplastic deformation of the AZ31 magnesium alloy under wide-ranging temperatures and strain rates. Available data on the AZ31 magnesium alloy are scattered, cover limited ranges of temperatures and strain rates, and do not combine both the mechanical and microstructural aspects of deformation.
- 4) Model the superplastic behaviour of the AZ31 magnesium alloy. Bulge forming tests validated the model capabilities with the aid of FE.

- 5) Experimental validating of a proposed optimisation scheme. Both uniaxial tensile tests and bulge forming practices.
- 6) New procedure for high temperature tensile testing of superplastic materials. There is no published standard procedure for testing superplastic materials. Recommendations based on this work contributed to issuing an ASTM standard for testing superplastic materials.
- 7) Post-superplastic forming analysis. The issue of post-superplastic forming properties of superplastically-formed components has been ignored in superplastic studies, particularly for magnesium alloys.
- 8) Integrated multidisciplinary approach for the superplastic forming of lightweight alloys.

8.3 Recommendations for Future Work

Many targets were achieved in this work, yet there is a lot to be done:

- 1) Introduce some modifications and refinements to the biaxial testing fixture, particularly in terms of compliancy improvement and stress/strain measurements. Moreover, conduct additional controlled biaxial tests at elevated temperatures, and investigate microstructural evolution and failure in the material under actual loading conditions.
- 2) Incorporate advanced sensors and monitoring tools into the bulge forming setup, in order to produce in-situ data about the progress of deformation, which would then help controlling the forming process.
- 3) Develop hybrid forming technologies for lightweight alloys, by combining the superplastic forming technique with other forming and joining operations, in away that alleviates the limitations of the superplastic forming process (*slow forming*), yet take advantage of its attractions (*high uniform strain limits*).
- 4) Superplastic bulge forming of tube structures as an alternative approach to form particular parts.

REFERENCES

1. F. K. Abu-Farha & M. K. Khraisheh, (2004), "*Constitutive Modelling of Deformation-Induced Anisotropy in Superplastic Materials*", Materials Science Forum, vol. 447-448, pp. 165-170.
2. F. Abu-Farha and M. Khraisheh, (2005a), "*Modeling of Anisotropic Deformation in Superplastic Sheet Metal Stretching*", Journal of Engineering Materials and Technology, vol. 127, no. 1, pp. 159-164.
3. F. Abu-Farha and M. Khraisheh, (2005b), "*Deformation Characteristics of AZ31 Magnesium Alloy Under Various Forming Temperatures and Strain Rates*", Proceedings of the 8th ESAFORM Conference on Material Forming, Cluj-Napoca, Romania, pp. 627-630, April 27-29.
4. F. K. Abu-Farha and M. K. Khraisheh, (2006), "*On the Superplastic Forming of the AZ31 Magnesium Alloy*", Proceedings of the 7th International Conference on Magnesium Alloys and their Applications, Dresden, Germany, pp. 399-405, November 6-9.
5. F. Abu-Farha, N. Rawashdeh and M. Khraisheh, (2007), "*Superplastic Deformation of Magnesium Alloy AZ31 Under Biaxial Loading Condition*", Materials Science Forum, vol. 551-552, pp. 219-224.
6. F. Abu-Farha and M. Khraisheh, (2007a), "*On the High Temperature Testing of Superplastic Materials*", Journal of Materials Engineering & Performance, vol. 16, no. 2, pp. 142-149.
7. F. Abu-Farha and M. Khraisheh, (2007b), "*Mechanical Characteristics of Superplastic Deformation of AZ31 Magnesium Alloy*", Journal of Materials Engineering & Performance, vol. 16, no. 2, pp. 192-199.
8. F. Abu-Farha and M. Khraisheh, (2007c), "*Analysis of Superplastic Deformation of AZ31 Magnesium Alloy*", Journal of Advanced Engineering Material (JAEM), In Press.
9. E. Aghion, B. Bronfin and D. Eliezer, (2001), "*The Role of Magnesium Industry in Protecting the Environment*", Journal of Materials Processing Technology, vol. 117, no. 3, pp. 381-385.
10. S. R. Agnew and O. Duygulu, (2003), "*A Mechanistic Understanding of the Formability of Magnesium: Examining the Role of Temperature on the Deformation Mechanisms*", Materials Science Forum, vol. 419-422, pp. 177-188.
11. S. P. Agrawal and J. M. Tuss, (1985), "*Superplastic Forming and Post-SPF Mechanical Behaviour of an Aluminum Alloy for Airframe Applications*", Proceedings of the Superplasticity in Aerospace – Aluminium, Cranfield, England, pp. 296-325.
12. H. Ahmed and R. Pearce, (1985), "*Post-Forming Cavity Closure in Supral 150 by Hot Isostatic Pressing*", Proceedings of the Superplasticity in Aerospace – Aluminium, Cranfield, England, pp. 146-159.
13. N. Akkus, K. Manabe, M. Kawahara and H. Nishimura, (1997), "*A Finite Element Modelling for Superplastic Bulge Forming of Titanium Alloy Tube*

- and Pressure Path Optimisation*", Materials Science Forum, vol. 243-245, pp. 729-734.
14. D. Avery and W. Backofen, (1965), "A Structural Basis for Superplasticity", Transactions of ASM, vol. 58, pp. 551-556.
 15. M. Atkinson, (1997), "Accurate Determination of Biaxial Stress-Strain Relationships From Hydraulic Bulging Tests of Sheet Metals", International Journal of Mechanical Sciences, vol. 39, no. 7, pp. 761-769.
 16. C. C. Bampton and J. W. Edington, (1982), Metals Transactions, vol. 13A, pp. 1721.
 17. C. C. Bampton and J. W. Edington, (1983), Journal of Engineering Materials and Technology, vol. 105, pp. 55.
 18. D. Banabic, T. Balan and D.-S. Comsa, (2001), "Closed Form Solution for Bulging Through Elliptical Dies", Journal of Materials Processing Technology, vol. 115, pp. 83-86.
 19. D. Banabic, M. Vulcan and K. Siegert, (2005), "Bulge Testing under Constant and Variable Strain Rates of Superplastic Aluminium Alloys", Annals of the CIRP, vol. 54, pp. 205-208.
 20. K. Barnreiter and O. Eichberg, (1997), "Leichtbaumaßnahmen am manuellen Schaltgetriebe Audi B80", ATZ/MTZ-Sonderausgabe: Der neue Audi A6.
 21. A. Ben-Artzy, A. Shtechman, A. Bussiba, Y. Salah, S. Ifergan, M. Kupiec and R. Grinfeld, (2003), "Low Temperature Super-plasticity Response of AZ31B Magnesium Alloy with Severe Plastic Deformation", Magnesium Technology 2003, Proceedings of the 2003 TMS Annual Meeting, San Diego, California, pp. 259-263.
 22. J. Bonet, R. Wood, R. Said, R. V. Crutis and D. Garriga-Majo, (2000), "Numerical Simulation of the Superplastic Forming of Dental and Medical Prostheses"; Biomechanics and Modelling in Mechanobiology, vol. 1, pp. 177-196.
 23. J. R. Bradley and J. E. Carsley, (2004), "Post-Form Properties of Superplastically Formed AA5083 Aluminum Sheet", Advances in Superplasticity and Superplastic Forming 2004, Proceedings of the Symposium held during the 2004 TMS Annual Meeting, March 14-18, Charlotte, NC, pp. 149-157.
 24. T. Burk and W. Vogel, (2002), "Light Weight Materials for Automotive Structures", Materials Week 2002, International Congress Centre, Munich, Germany, September 30th - October 02nd.
 25. A. Bussiba, A. Ben Artzy, A. Shtechman, S. Ifergan and M. Kupiec, (2001), "Grain Refinement of AZ31 and AZ60 Mg Alloys – Towards Superplasticity Studies", Materials Science & Engineering A, vol. 302, no. 1, pp. 56-62.
 26. L. Carrino and G. Giuliano, (1997), "Modeling of Superplastic Blow Forming", International Journal of Mechanical Sciences, vol. 39, no. 2, pp. 193-199.
 27. Z. P. Chen and P. F Thomson, (2004), "A Study of Post-Form Static and Fatigue Properties of Superplastic 7475-SPF and 5083-SPF Aluminium Alloys", Journal of Materials Processing Technology, vol. 148, no. 2, pp. 204-219.

28. Y. Chino and H. Iwasaki, (2004), "*Cavity Growth Rate in Superplastic 5083 Al and AZ31 Mg Alloys*", Journal of Materials Research, vol. 19, no. 11, pp. 3382-3388.
29. M. Clark and T. Alden, (1973), "*Deformation Enhanced Grain Growth in a Superplastic Sn-1%Bi Alloy*", Acta Metallurgica, vol. 21, pp. 1195-1206.
30. G. S. Cole, (1999), "*How Magnesium Can Achieve High Volume Usage in Ground Transportation*", Magnesium into the Next Millennium, The 56th Annual Meeting of the International Magnesium Association, Rome, Italy, June 6-9, pp. 21-30.
31. M. Cope, D. Evetts and N. Ridley, (1987), "*Post-Forming Tensile Properties of Superplastic Ti-6Al-4V Alloy*", Material Science and Technology, vol. 3, no. 6, pp. 455-461.
32. R. V. Curtis, D. Garriga-Majo, A. S. Juszczak, S. Soo, D. Pagliaria and J. D. Walter, (2001), "*Dental Implant Superstructures by Superplastic Forming*", Material Science Forum, vol. 357-359, pp. 47-52.
33. R. V. Curtis, (2005), "Face On", Materials World, pp. 20-22.
34. Y. F. Dafalias, (1990), "*The Plastic Spin in Viscoplasticity*", International Journal of Solids and Structures, vol. 26, no. 2, pp. 149-163.
35. G. Davies, J. Edington, C. Cutler and K. Padmanabhan, (1970), "*Superplasticity: A Review*", Journal of Materials Science, vol. 5, pp. 1091-1102.
36. P. V. Deshmukh, N. V. Thuramalla, F. K. Abu-Farha and M. K. Khraisheh, (2004), "*Integrated Approach to Optimization of Superplastic Forming*", Advances in Superplasticity and Superplastic Forming, Proceedings of the 2004 TMS Annual Meeting, Charlotte, NC, March 14-18, pp. 361-369.
37. M. Dick, (1999), "*Das 3-Liter Lupo – Technologien für den Minimalen Verbrauch*", Technologien um das 3l-Auto, Brunswick, Germany, November 16-18.
38. X. D. Ding, H. M. Zbib, C. H. Hamilton and A. E. Bayoumi, (1995), "*On the Optimisation of Superplastic Blow-Forming Processes*", Journal of Materials Engineering & Performance, vol. 4, pp. 474-485.
39. X. D. Ding, H. M. Zbib, C. H. Hamilton and A. E. Bayoumi, (1997), "*On the Stability of Biaxial Stretching with Application to the Optimization of Superplastic Blow-Forming*", Journal of Engineering Materials and Technology, vol. 119, pp. 26-31.
40. E. Doege and K. Dröder, (1997), "*Processing of Magnesium Sheet Metals by Deep Drawing and Stretch Forming*", Materiaux et Techniques, vol. 7-8, pp. 19-23.
41. E. Doege, L-E. Elend and F. Meiners, (2000), "*Comparative Study of Massive and Sheet Lightweight Components Formed of Different Lightweight Alloys for Automotive Applications*", ISATA 33rd 2000; Automotive & Transportation Technology, Dublin, Ireland, pp. 87-94, September 25-27.
42. E. Doege and K. Dröder, (2001a), "*Sheet Metal Forming of Magnesium Wrought Alloys – Formability and Process Technology*", Journal of Materials Processing Technology, vol. 115, pp. 14-19.

43. E. Doege, W. Sebastian, K. Dröder and G. Kurz, (2001b), "*Increased Formability of Mg-Sheets Using Temperature Controlled Deep Drawing Tools*", Proceedings of the 02nd Global Symposium on Innovations in processing and Manufacturing of Sheet Materials, TMS 2001, pp. 53-60.
44. K. Dröder and St. Janssen, (1999), "*Forming of Magnesium Alloys – A Solution for Lightweight Construction*", Proceedings of the 1999 International Body Engineering Conference (SAE), Detroit, Michigan.
45. L. B. Duffy, J. B. Hawkyard and N. Ridley, (1988), "*Post-Forming Tensile Properties of Superplastically Bulge Formed High Strength α/β Ti-Al-Mo-Sn-Si Alloy (IMI 550)*", Materials Science and Technology, vol. 4, no. 8, pp. 707-712.
46. D. V. Dunford, A. Wisbey and P. G. Partridge, (1991), "*Effect of Superplastic Deformation on Microstructure, Texture, and Tensile Properties of Ti-6Al-4V*", Materials Science and Technology, vol. 7, no. 1, pp. 62-70.
47. A. Dutta and M. Mukherjee, (1992), "*Superplastic Forming: An Analytical Approach*," Materials Science and Engineering, vol. A157, pp. 9-13.
48. A. Dutta, (2004), "*Thickness Profiling of Initial Blank for Superplastic Forming of Uniformly Thick Domes*", Materials Science and Engineering A, vol. 371, pp. 79-81.
49. O. Duygulu and S. R. Agnew, (2003), "*The Effect of Temperature and Strain Rate on the Tensile Properties of Textured Magnesium Alloy AZ31B Sheet*", Magnesium Technology 2003, Proceedings of the 2003 TMS Annual Meeting, San Diego, California, pp. 237-242.
50. E. F. Emley, (1966), "*Principles of Magnesium Technology*", 01st edition, Pergamon Press.
51. D. Engelhart and C. Moedel, (1999), "*Die Entwicklung des Audi A2, ein neues Fahrzeugkonzept in der Kompaktklassenklasse*", Technologien um das 3l-Auto, Brunswick, Germany, November 16-18.
52. H. Friedrich and S. Schumann, (2000), "*The Second Age of Magnesium: Research Strategies to Bring the Automotive Industry's Vision to Reality*", The 2nd Israeli International Conference on Mg Science and Technology, Sdom, Israel, pp. 9-18.
53. H. Friedrich and S. Schumann, (2001), "*Research for a New Age of Magnesium in the Automotive Industry*", Journal of Materials Processing Technology, vol. 117, no. 3, pp. 276-281.
54. R. Gifkins and T. Langdon, (1970), "*Grain Boundary Displacement Due to Diffusional Creep*", Scripta Metallurgica, vol. 4, pp 563-567.
55. S. J. Hales and J. A. Wagner, (1992), "*Influence of Post-Forming Processing on Tensile Properties of Superplastic Al-Li Alloys*" NASA Technical Memorandum, no. 4331, pp. 125.
56. S. J. Hales and H. E. Lippard, (1994), "*Influence of Post-Superplastic Forming Practices on the Tensile Properties of Aluminium-Lithium Alloys*", Journal of Engineering Materials and Performance, vol. 3, no. 3, pp. 334-343.

57. C. Hamilton, H. Zbib, C. Johnson and S. Richter, (1991), "*Dynamic Grain Coarsening, its Effects on Flow Localization in Superplastic Deformation*", 2nd SAMPE Symposium, Chiba, Japan, pp 272-279.
58. E. Hart, (1967), "*A Theory for Flow of Polycrystals*", Acta Metallurgica, vol. 15, pp. 1545-1549.
59. R. Hill, (1950), "*The Mathematical Theory of Plasticity*", Oxford University Press, London.
60. C. Holste, D. Dikty, P. Freytag and B. Behrens, (2002), "*Innovative Lightweight Construction Concepts and Materials for Automotive Bodies*", Materials Week 2002, International Congress Centre, Munich, Germany, September 30-October 02.
61. D. Holt, (1970), "*An Analysis of the Bulging of a Superplastic Sheet by Lateral Pressure*", International Journal of Mechanical Sciences, vol. 12, pp. 491-497.
62. A. Jäger, P. Lukas, V. Gärtnerova, J. Bohlen and K. Kainer, (2004), "*Tensile Properties of Hot Rolled AZ31 Mg Alloy Sheets at Elevated Temperatures*", Journal of Alloys and Compounds, vol. 378, p 184-187.
63. A. Jambor and M. Beyer, (1997), "*New Cars – New Materials*", Materials & Design, vol. 18, no. 4-6, pp. 203-209.
64. C. Johnson, C. H. Hamilton, H. M. Zbib and S. Richter, (1993), "*Designing Optimized Deformation Paths for Superplastic Ti6Al4V*". Advances in Superplasticity and Superplastic Forming, edited by N. Chandra et al., Metals and Materials Society, pp. 3-15.
65. F. Jovane, (1968), "*An Approximate Analysis of the Superplastic Forming of a Thin Circular Diaphragm: Theory and Experiments*", International Journal of Mechanical Sciences, vol. 10, pp. 403-427.
66. F. Kaiser, D. Letzig, J. Bohlen, A. Styczynski, C. Hartig and K. Kainer, (2003a), "*Anisotropic Properties of Magnesium Sheet AZ31*", Materials Science Forum, vol. 419-422, pp. 315-320.
67. F. Kaiser, J. Bohlen, D. Letzig, K. Kainer, A. Styczynski and C. Hartig, (2003b), "*Influence of Rolling Conditions on the Microstructure and Mechanical Properties of Magnesium Sheet AZ31*", Advanced Engineering Material, vol. 5, no. 12, pp. 891-896.
68. M. A. Khaleel, M. T. Smith and A. L. Lund, (1997), "*Cavitation During Multiaxial Deformation of Superplastic Forming*", Materials Science Forum, vol. 243-245, pp. 155-160.
69. M. A. Khaleel, K. I. Johnson, C. H. Hamilton and M. T. Smith, (1998), "*Deformation Modeling of Superplastic AA-5083*", International Journal of Plasticity, vol. 14, no. 10-11, pp. 1113-1154.
70. M. A. Khaleel, H. M. Zbib and E. A. Nyberg, (2001), "*Constitutive Modelling of Deformation and Damage in Superplastic Materials*", International Journal of Plasticity, vol. 17, pp. 277-297.
71. A. Khan, (1996), "*Continuum Theory of Plasticity*", John Wiley & Sons, New York.
72. M. K. Khraisheh, A. E. Bayoumi, C. H. Hamilton, H. M. Zbib and K. Zhanz, (1995), "*Experimental Observations of Induced Anisotropy During the*

- Torsion of Superplastic Pb-Sn Eutectic Alloy*", Scripta Metallurgica et Materialia, vol. 32, no. 7, pp. 955-959.
73. M. Khraisheh, H. Zbib, C. Hamilton, and A. Bayoumi, (1997), "*Constitutive Modeling of Superplastic Deformation. Part I: Theory and Experiments*", International Journal of Plasticity, vol. 13, no. 1/2, pp. 143-164.
 74. M. K. Khraisheh and H. M. Zbib, (1999), "*Optimum Forming Loading Paths for Pb-Sn Superplastic Sheet Materials*", Journal of Engineering Materials & Technology, vol. 121, pp.341-345.
 75. M. K. Khraisheh, (2000-a), "*An Investigation of Yield Potentials in Superplastic Deformation*", ASME Journal of Engineering Materials and Technology, vol. 122, pp. 93-97.
 76. M. K. Khraisheh, (2000-b), "*Constitutive Modeling of Multiaxial Deformation and Induced Anisotropy in Superplastic Materials*", Recent Trends in Constitutive Modeling of Advanced Materials, AMD/ASME, vol. 239, pp. 79-94.
 77. M. K. Khraisheh and F. K. Abu-Farha, (2003), "*Microstructure-Based Modeling of Anisotropic Superplastic Deformation*", Transactions of NAMRI/SME, vol. 31, p41-47.
 78. M. K. Khraisheh, F. K. Abu-Farha, M. A. Nazzal and K. J. Weinmann, (2006), "*Combined Mechanics-Materials Based Optimization of Superplastic Forming of Magnesium AZ31 Alloy: Model Development and Experimental Validation*", Annals of the CIRP, vol. 55, pp. 233-236.
 79. M. K. Khraisheh, F. K. Abu-Farha and K. J. Weinmann, (2007), "*An Experimental Investigation of Post-Superplastic Forming Properties of AZ31 Magnesium Alloy*", Annals of the CIRP, In Press.
 80. W. Kim, S. Chung, C. Chung and D. Kum, (2001), "*Superplasticity in Thin Magnesium Alloy Sheets and Deformation Mechanism Maps for Magnesium Alloys at Elevated Temperatures*", Acta Materialia, vol. 49, no. 16, pp. 3337-3345.
 81. M. G. Kistner, (1998), "*SPF Challenges and Opportunities, A Manufacturer's Perspective*", Proceedings of the Symposium on Superplasticity and Superplastic Forming, edited by M. A. Khaleel, DOE, PNNL-SA-30406, pp. 23-25.
 82. G. Kurz, (2004), "*Heated Hydro-Mechanical Deep Drawing of Magnesium Sheet Metal*", Magnesium Technology 2004, Proceedings of the 2004 TMS Annual Meeting, Charlotte, NC, pp. 67-71, March 14-18.
 83. B. Lee, K. Shin and C. Lee, (2005), "*High Temperature Deformation Behavior of AZ31 Mg Alloy*", Materials Science Forum, vol. 475-479, pp. 2927-2930.
 84. C. Lee and J. Huang, (2004), "*Cavitation Characteristics in AZ31 Mg Alloys During LTSP or HSRSP*", Acta Materialia, vol. 52, p 3111-3122.
 85. E. H. Lee, (1969), "*Elastic-Plastic Deformations at Finite Strains*," ASME Journal of Applied Mechanics, vol. 36, pp. 1.
 86. J. Lubliner, (1990), "*Plasticity Theory*", Macmillan Publishing Co., New York.

87. D. S. McDarmid, (1985), "*Superplastic Forming and Post-Forming Tensile Properties of High Strength Titanium Alloy Ti-4Al-4Mo-2Sn-0.5Si*", Materials Science and Engineering, vol. 70, no. 1-2, pp. 123-129.
88. D. S. McDarmid and A. J. Shakesheff, (1985), "*Effect of Forming Parameters on the Superplastic Deformation and Post Formed Properties of 8090 and Supral 220 Aluminium Alloys*", Proceedings of the Advanced Materials Research and Development for Transports, November 26-28, Strasbourg, France, Les Editions de Physique, pp. 193-200.
89. A. Mertz, (2002), "*Improved Design Possibilities by Applying Magnesium Extrusions*", Materials Week 2002, International Congress Centre, Munich, Germany, September 30-October 02.
90. D. A. Miller, F. A. Mohamed and T.G. Langdon, (1979), "*An Analysis of cavitation failure incorporating cavity Nucleation with Strain*", Materials Science and Engineering, vol. 40, pp. 159-166.
91. M. P. Miller and D. L. McDowell, (1992), "*Stress State Dependence of Finite Strain Inelasticity*", Microstructural Characterization in Constitutive Modeling of Metals and Granular Media, ASME MD, vol. 32, pp. 27-44.
92. Y. Miyagi, M. Hino, T. Eto and Y. Hirose, (1987), "*Void Formation and its Effect on Post-Formed Mechanical Properties in Superplastic 7475 Aluminum Alloy*", Kobelco Technology Review, no. 2, pp. 45-48.
93. T. Mohri, M. Mabuchi, M. Nakamura, T. Asahina, H. Iwasaki, T. Aizawa and K. Higashi, (2000), "*Microstructural evolution and superplasticity of rolled Mg-9Al-1Zn*", Materials Science & Engineering A, vol. 290, no. 1-2, pp. 139-144.
94. W. L. Moore, M. Zelin and P. K. Chaudhury, (1995), "*Post-Formed Properties of Superplastic Aluminum Aerospace Alloys*", Superplasticity and Superplastic Forming, Proceedings of the Symposium Held During the 124th TMS Annual Meeting, Feb. 13-15, Las Vegas, NV, pp. 267-275.
95. A. Mukherjee, (1971), "*The Rate Controlling Mechanism in Superplasticity*", Materials Science and Engineering, vol. 8, pp. 83-89.
96. M. A. Nazzal, M. K. Khraisheh and B. M. Darras, (2004), "*Finite Element Modeling and Optimization of Superplastic Forming Using Variable Strain Rate Approach*", Journal of Materials Engineering and Performance, vol. 13, pp. 691-699.
97. M. Nazzal, F. Abu-Farha and M. Khraisheh, (2007), "*The Effect of Strain Rate Sensitivity Evolution on the Deformation Stability During Superplastic Forming*", Journal of Material Processing Technology, In Press.
98. P. D. Nicolaou, S. L. Semiatin and A. K. Ghosh, (2000), "*An Analysis of the effect of cavity nucleation rate and cavity coalescence on the tensile behavior of Superplastic Materials*", Metallurgical and Materials Transactions A, vol. 31A, pp. 1425.
99. K. Osada, (1997), "*Commercial Applications of Superplastic Forming*", Journal of Materials Processing Technology, vol. 68, no. 3, pp. 241-245.
100. K. A. Padmanabhan, R. A. Vasin & F. U. Enikeev, (2001), "*Superplastic Flow: Phenomenology and Mechanics*", Springer Verlag, Berlin.

101. J. Pilling and N. Ridley, (1989), "*Superplasticity in Crystalline solids*", The Institute of Metals, London.
102. M. S. Piltch, J. Bennett and K. Haberman, (1998), "*Numerical Simulation Requirements for SPF of an Industrial Titanium Part, The First Time Every Time*", Proceedings of the Symposium on Superplasticity and Superplastic Forming, edited by M. A. Khaleel, DOE, PNNL-SA-30406, pp. 49-51.
103. D. G. Sanders, (1998), "*Aerospace Manufacturing Challenges for Superplastic Forming in the Twenty-First Century*", Proceedings of a Symposium on Superplasticity and Superplastic Forming, edited by M. A. Khaleel, DOE, PNNL-SA-30406, pp. 13-14.
104. D. G. Sanders, (2001), "*The Current State-of-the-Art and the Future in Airframe Manufacturing Using Superplastic Forming Technologies*", Material Science Forum, vol. 357-359, pp. 17-22.
105. S. Schumann and F. Friedrich, (1998), "*The Use of Magnesium in Cars - Today and in the Future*", Mg Alloys and their Applications, Wolfsburg, Germany, April 28-30.
106. A. J. Shakesheff, (1985), "*The Effect of Superplastic Deformation on the Post-Formed Mechanical Properties of the Commercially Produced Supral Alloys*", Proceedings of the Superplasticity in Aerospace – Aluminium, Cranfield, England, pp. 36-54.
107. K. Siegert, S. Jäger and M. Vulcan, (2003), "*Pneumatic Bulging of Magnesium AZ 31 Sheet Metals at Elevated Temperatures*," Annals of the CIRP, vol. 52, pp. 241-244.
108. M. J. Stowell, (1983), "*Cavity growth and failure in superplastic alloys*", Metal Science, vol. 17, pp. 92.
109. M. J. Stowell, D. W. Livesey and N. Ridley, (1984), "*Cavity Coalescence in Superplastic Deformation*", Acta Metallurgica, vol. 32, no. 1, pp. 35-42.
110. M. Suery and B. Baudalet, (1978), "*Rheological and Metallurgical Discussion of Superplastic Behavior*", Revue de Physique Appliquee, vol. 13, no. 2, pp. 53-66.
111. Tabellenbuch Metall, (2001), 41st edition, 6th print, Verlag Europa Lehrmittel.
112. J. Tan and M. Tan, (2002), "*Superplasticity in a Rolled Mg-3Al-1Zn Alloy by Two-Stage Deformation Method*", Scripta Materialia, vol. 47, no. 2, pp. 101-106.
113. N. Thuramalla, P. Deshmukh and M. Khraisheh, (2004), "*Multi-Scale Analysis of Failure during Superplastic Deformation*", Materials Science Forum, vol. 447-448, pp. 105-110.
114. N. Thuramalla and M. Khraisheh, (2004), "*Multiscale-Based Optimization of Superplastic Forming*", Transactions of NAMRI/SME, vol. 32, pp. 637-643.
115. L. Tsao, C. Wu and T. Chuang, (2001), "*Evaluation of Superplastic Formability of the AZ31 magnesium Alloy*", Materials Research and Advanced Techniques, vol. 92, no. 6, pp. 572-577.
116. M. Vulcan, K. Siegert and D. Banabic, (2004), "*The Influence of Pulsating Strain Rates on the Superplastic Deformation Behaviour of Al-Alloy AA5083 Investigated by Means of Cone Test*", Materials Science Forum, vol. 447-448, pp. 139-144.

117. H. Watanabe, H. Tsutsui, T. Mukai, Y. Okanda, M. Kohzu and K. Higashi, (2000), "*Superplastic Behavior in Commercial Wrought Magnesium Alloys*", Materials Science Forum, vol. 350-351, pp. 171-176.
118. H. Watanabe, A. Takara, H. Somekawa, T. Mukai and K. Higashi, (2005), "*Effect of Texture on Tensile Properties at Elevated Temperatures in an AZ31 Magnesium Alloy*", Scripta Materialia, vol. 52, pp. 449-454.
119. D. Wilkinson and C. Caceres, (1984), "*Large Strain Behavior of a Superplastic Copper Alloy Deformation*", Acta Metallurgica, vol. 32, pp. 415-422.
120. A. Wisbey, M. Kearns, P. Patridge and A. Bowen, (1993), "*Superplastic Deformation and Post-formed Mechanical Properties of High Temperature Titanium Alloy IMI834*", Material Science and Technology, vol. 9, no. 11, pp. 987-993.
121. D. M. Woo, (1964), "*The Analysis of Axisymmetric Forming of Sheet Metal and Hydrostatic Bulging Process*", International Journal of Mechanical Science, vol. 6, pp. 303-317.
122. X. Wu, Y. Liu and H. Hao, (2001), "*High Strain Rate Superplasticity and Microstructure Study of a Magnesium Alloy*", Materials Science Forum, vol. 357-359, pp. 363-370.
123. X. Wu and Yi Liu, (2002), "*Superplasticity of Coarse-Grained Magnesium Alloy*", Scripta Materialia, vol. 46, no. 4, pp. 269-274.
124. H. Yang and Mukherjee, (1992), "*An Analysis of the Superplastic Forming of a Circular Sheet Diaphragm*," International Journal of Mechanical Science, vol. 34, no. 4, pp. 283-297.
125. D. Yin, K. Zhang, G. Wang and W. Han, (2004), "*Superplasticity of Fine-Grained AZ31 Mg Alloy Sheets*", Transactions of Nonferrous Metals Society of China, vol. 14, no. 6, pp. 1100-1105.
126. D. Yin, K. Zhang, G. Wang and W. Han, (2005), "*Superplasticity and Cavitation in AZ31 Mg Alloy at Elevated Temperatures*", Materials Letters, vol. 59, no. 14-15, pp. 1714-1718.
127. H. M. Zbib, and E. C. Aifantis, (1988), "*On the Concept of Relative and Plastic Spins and its Implications to Large Deformation Theories. Part I: Hypoelasticity and Vertex-Type Plasticity*", Acta Mechanica, vol. 75, pp. 15-33.
128. H. M. Zbib, and E. C. Aifantis, (1988), "*On the Concept of Relative and Plastic Spins and its Implications to Large Deformation Theories. Part II: Anisotropic Hardening Plasticity*", Acta Mechanica, vol. 75, pp. 35-56.
129. H. M. Zbib, (1993), "*On the Mechanics of Large Inelastic Deformation: Kinematics and Constitutive Modeling*", Acta Mechanica, vol. 96, pp. 119-138.
130. K. Zhang, C. H. Hamilton, H. M. Zbib and M. K. Khraisheh, (1995), "*Observation of Transient Effects in Superplastic Deformation of Pb-Sn Eutectic Alloy*", Scripta Metallurgica et Materialia, vol. 32, no. 6, pp. 919-923.
131. K. Zhang (1996), "*Transient Deformation Behavior and Modeling of Superplastic Pb-Sn Eutectic Alloy*", PhD Dissertation, Washington State University.
132. www.magnesium.com

133. www.superform-aluminium.com
134. www.wikipedia.org
135. ASTM E21, (2003), "*Standard Test Methods for Elevated Temperature Testing Tests for Metallic Materials*", American Society for Testing and Materials, pp. 139-146.
136. JIS H 7501, (2002) "*Method for Evaluation of Tensile Properties of Metallic Superplastic Materials*", Japanese Industrial Standard.
137. ASM Specialty Handbook, (1999) "Magnesium and Magnesium Alloys", Editors M. Avedesian and H. Baker, 1st print.

VITA

Fadi K. Abu-Farha

Date/Place of birth: 02nd of November, 1979 / Damascus (Syria).

Degrees already awarded: Baccalaureate of Science in Mechanical Engineering, Jordan University (2001)

Professional positions:

- i. Research Assistant: Mechanical Engineering Department and Center for Manufacturing, University of Kentucky (July 2002 – May 2007).
- ii. Teaching Assistant: Mechanical Engineering Department, University of Kentucky (January 2004 – May 2007).
- iii. Practicum (Traineeship): Research & Development Centre at Vorwerk Elektrowerke GmbH & Co. KG, Wuppertal, Germany (July - December 2001).

Scholastic and professional honours

1. Received the **Student Travel Grant** from *Arizona State University* to attend the 2006 NSF-DMII Grantees Conference, Saint Louis, MO, July 24-27, 2006.
2. Received the **Student Travel Assistantship** from the *University of Kentucky* to attend the 3rd International Conference on Structural Stability and Dynamics (ICSSD), Orlando, FL, June 20-22, 2005.
3. Awarded the **Young Researcher Fellowship** at The 3rd M.I.T. Conference on Computational Fluid and Solid Mechanics, Cambridge, MA, June 14-17, 2005.
4. Received the **Student Travel Grant** from Arizona State University to attend the 2005 NSF-DMII Grantees Conference, Scottsdale, AZ, January 3-6, 2005.
5. Received the **Student Travel Assistantship** from the University of Kentucky to attend the 133rd TMS Annual Meeting & Exhibition, Charlotte, NC, March 14-18, 2004.
6. *Microstructure-Based Modeling of Anisotropic Superplastic Deformation*, Marwan Khraisheh & Fadi Abu-Farha; Awarded the **Outstanding Paper Award** at the 31st Annual North American Manufacturing Research Conference (NAMRI/SME), McMaster University, Hamilton, Ontario, Canada, May 2003.
7. *Multiscale-Stability analysis on Superplastic deformation*, Naveen Thuramalla, Fadi Abu-Farha and Marwan Khraisheh: Awarded the **1st Prize** in the **Student Poster Competition**, in the 2003 TMS Annual Meeting & Exhibition, San Diego, CA, March 2-6, 2003.
8. Awarded the **2nd Prize** in the **Senior Design Project Competition** for the year 2001-2002, sponsored by the Jordanian Engineers Association, Amman, Jordan.

9. Awarded ***Al-Shami Honour Prize*** for ranking 1st in the Mechanical Engineering Department for the Year 2001-2002, University of Jordan, Amman, Jordan.
10. ***University of Jordan Scholarship*** recipient (1998,1999,2000).
11. ***United Nations 4-year Scholarship*** recipient (1997-2001).

Technical Publications:

Journal Papers:

1. **F. K. Abu-Farha** and M. K. Khraisheh, "*Analysis of Superplastic Deformation of AZ31 Magnesium Alloy*", Journal of Advanced Engineering Material (JAEM), In Press.
2. M.K. Khraisheh, **F.K. Abu-Farha** and K.J. Weinmann, "*An Experimental Investigation of Post-Superplastic Forming Properties of AZ31 Magnesium Alloy*", Annals of the CIRP, 2007, In Press.
3. B. M. Darras, M. K. Khraisheh, **F. K. Abu-Farha** and M. A. Omar, "*Friction Stir Processing of AZ31 Commercial Magnesium Alloy*", Journal of Material Processing Technology, In Press.
4. M. Nazzal, **F. Abu-Farha** and M. Khraisheh, "*The Effect of Strain Rate Sensitivity Evolution on the Deformation Stability During Superplastic Forming*", Journal of Material Processing Technology, In Press.
5. **F. Abu-Farha** and M. Khraisheh, "*Mechanical Characteristics of Superplastic Deformation of AZ31 Magnesium Alloy*", Journal of Materials Engineering & Performance, vol. 16, no. 2, pp. 192-199.
6. **F. Abu-Farha** and M. Khraisheh, "*On the High Temperature Testing of Superplastic Materials*", Journal of Materials Engineering & Performance, vol. 16, no. 2, pp. 142-149.
7. **F. Abu-Farha**, N. Rawashdeh and M. Khraisheh, "Superplastic Deformation of Magnesium Alloy AZ31 Under Biaxial Loading Condition", Materials Science Forum, Vol. 551-552, pp. 219-224 (2007).
8. M. K. Khraisheh, **F. K. Abu-Farha**, M. A. Nazzal and K. J. Weinmann, "*Combined Mechanics-Materials Based Optimization of Superplastic Forming of Magnesium AZ31 Alloy: Model Development and Experimental Validation*", Annals of the CIRP, Vol. 55/1, pp. 233-236 (2006).
9. **F. K. Abu-Farha** and M. K. Khraisheh, "*Modeling of Anisotropic Deformation in Superplastic Sheet Metal Stretching*", ASME Journal of Engineering Materials and Technology, Vol. 127, pp. 159-164 (2005).
10. **F. K. Abu-Farha** and M. K. Khraisheh, "*Constitutive Modeling of Deformation-Induced Anisotropy in Superplastic Materials*", Materials Science Forum, Vols. 447-448, pp. 165-170 (2004).
11. M. K. Khraisheh and **F. K. Abu-Farha**, "*Microstructure-Based Modeling of Anisotropic Superplastic Deformation*", Transactions of the North American Manufacturing Research Institute (NAMRI/SME), Vol. 31, pp. 41-47, (2003).

Refereed Conference Papers:

1. **F. K. Abu-Farha** and M. K. Khraisheh, "*On the Superplastic Forming of the AZ31 Magnesium Alloy*", Magnesium 2006, the 7th International Conference on Magnesium Alloys and their Applications, Dresden, Germany, November 6-9, 2006, pp. 399-405.
2. **F. Abu-Farha**, "*Constitutive Modeling of Anisotropy and Microstructural Evolution during Superplastic Deformation*", Proceedings of the 3rd M.I.T. Conference on Computational Fluid and Solid Mechanics, Cambridge, June 14-17, 2005, pp. 36-39.
3. **F. Abu-Farha** and M. Khraisheh, "*Deformation Characteristics of AZ31 Magnesium Alloy Under Various Forming Temperatures and Strain Rates*", Proceedings of the 8th ESAFORM (European Scientific Association for material FORMing) Conference on Material Forming, Technical University of Cluj-Napoca, Cluj-Napoca, Romania, April 27-29, 2005, pp. 627-630.
4. M. K. Khraisheh, **F. K. Abu-Farha** and P. V. Deshmukh, "*Microstructure-Based Modeling and Simulation of Superplastic Forming Process*", Proceedings of the 2004 European Conference on Superplastic Forming, edited by Gerald Bernhart, Thierry Cutard and Philippe Lours, Albi, France, 2004, pp. 75-80.
5. P. V. Deshmukh, N. V. Thuramalla, **F. K. Abu-Farha** and M. K. Khraisheh, "*Integrated Approach to Optimization of Superplastic Forming*", Proceedings of the Symposium on Advances in Superplasticity and Superplastic Forming, the 133rd TMS Annual Meeting and Exhibition, Charlotte, NC, March 2004, pp. 361-369.
6. **F. K. Abu-Farha**, P. V. Deshmukh, N. V. Thuramalla and M. K. Khraisheh, "*Superplastic Forming: Stretching the Limits of Fabricating Medical Devices and Implants*", Proceedings of the ASM Materials & Processing for Medical Devices Conference, Anaheim, CA, 8-10 September 2003, pp. 368-373.
7. N. Thuramalla, **F. Abu-Farha** and M. Khraisheh, "*A new failure criterion for Superplastic deformation*", Proceedings of the 10th International Symposium on Plasticity and its Current Applications, Quebec, Canada, 2003, pp.157-159.